# Analysis and modeling of thermodynamic fluctuations in canonical shock-turbulence interaction

Submitted in partial fulfillment of the requirements
for the degree of

**Doctor of Philosophy**

by


**Yogesh Prasaad M. S.**
(Roll No. 124010003)

Supervisor:
**Prof. Krishnendu Sinha**



Department of Aerospace Engineering
Indian Institute of Technology Bombay


2019

*Dedicated to my parents*

# Acceptance Certificate

**Department of Aerospace Engineering**

**Indian Institute of Technology Bombay**

The thesis entitled "Analysis and modeling of thermodynamic fluctuations in canonical shock-turbulence interaction" submitted by Yogesh Prasaad M. S. (Roll No. 124010003) may be accepted for being evaluated.

Date: 07|08| 2019

Prof. Krishnendu Sinha

# Approval Sheet

This dissertation entitled "Analysis and modeling of thermodynamic fluctuations in canonical shock-turbulence interaction" by Yogesh Prasaad M. S. is approved for the degree of Doctor of Philosophy.

Aniruddha Sinha

Examiners

Supervisor (s)

Chairman

Date: 6/8/2019

Place: Mumbai

# Declaration

I declare that this written submission represents my ideas in my own words and where others' ideas or words have been included, I have adequately cited and referenced the original sources. I declare that I have properly and accurately acknowledged all sources used in the production of this dissertation. I also declare that I have adhered to all principles of academic honesty and integrity and have not misrepresented or fabricated or falsified any idea/data/fact/source in my submission. I understand that any violation of the above will be a cause for disciplinary action by the Institute and can also evoke penal action from the sources which have thus not been properly cited or from whom proper permission has not been taken when needed.

Yogesh Prasaad M. S.
(Roll No. 124010003)

Date: 07/08/ 2019

# Abstract

Shock-turbulence interaction is a problem of interest where, the effects of the shock on the turbulence and vice versa could be studied in detail. A canonical case of one-dimensional mean flow convecting homogeneous isotropic turbulence across a normal shock wave provides a much cleaner environment for fundamental studies as it does not have any inhomogeneities or wall effects. Most of the earlier works on this problem were on quantities related to velocity and its derivatives such as turbulent kinetic energy and enstrophy. Data on thermodynamic quantities are sparse and limited in terms of analysis, and an attempt has been made in this work to close that gap. We focus only on the interaction of vortical turbulence with shocks, and the effect of acoustic/entropic turbulence on shocks is only described briefly with the help of available literature. We use numerical and theoretical tools to study the thermodynamic field generated by the shock-turbulence interaction. Direct numerical simulations (DNS) of homogeneous isotropic turbulence interacting with normal shocks of varying strengths, $M$ = 1.23, 1.50, 2.50 and 3.50 have been carried out. The turbulent Mach number immediately upstream of the shock is varied as $M_t \approx 0.05$, 0.15, 0.25 and 0.40 with Taylor lengthscale based Reynolds number of $Re_\lambda \approx 33$ for each of the shock strengths. Extensive grid convergence tests have been carried out to verify the simulations.

We investigate the post-shock thermodynamic field generated by the interaction with the help of a theoretical tool called linear interaction analysis (LIA) and the numerical simulations. Density, pressure and temperature variances attain large values at the shock, followed by, in general, a rapid decay in the downstream flow. The rapid variation immediately behind the shock makes it difficult to compare numerical results with theoretical predictions. A threshold method based on instantaneous shock dilatation (similar to a shock-sensor) is used to overcome this problem, and it gives excellent match between DNS and LIA. We find cases with non-monotonic variation with Mach number as well as local peaks in density fluctuations behind the shock for strong shocks. These are explained in terms of the contribution of the post-shock acoustic and entropy modes in the LIA solution and their cross-correlation. Far-field ($x \to \infty$) and near-field ($x = 0^+$) variations of the post-shock thermodynamic field have been analyzed for varying shock strengths and turbulence intensities.

The numerical solutions differ significantly from the LIA solution as $M_t$ is increased, in line with the assumptions used in the theory. The intensity of the post-shock thermodynamic field is found to be proportional to the upstream turbulent Mach number; monotonically increasing in strength as $M_t$ is increased. This is however, due to the increased levels of upstream thermodynamic fluctuations as $M_t$ is increased, which in turn results in an increased intensity of post-shock thermodynamic fluctuations. The effect of Taylor lengthscale Reynolds number is not easily deducible from the available data, and is not studied in detail. The shape of the energy spectrum, which is used in the generation of the homogeneous isotropic turbulence database has an effect on the post-shock evolution of thermodynamic fluctuations. The statistics computed in the near field and far field are, however, found to be independent of the shape of the spectrum.

Budget of the transport equations, for variances and fluxes of thermodynamic fluctuations, reveal interesting insight into the physics governing the thermodynamic field behind the shock wave. It is found that the variances are primarily determined by the competing effects of dilatational and dissipation mechanisms. The dominant mechanisms are identified for a range of conditions and their implication for developing predictive models is highlighted. Phenomenological models for the post-shock thermodynamic variances have been developed. The production mechanism of each of the thermodynamic variances is modeled using the existing models for turbulent heat flux and turbulent kinetic energy. Their decay mechanism is modeled from the physical insights obtained from the fundamental study. The models show excellent agreement with the available DNS data.

Keywords: direct numerical simulation, linear interaction analysis, homogeneous isotropic turbulence, shock waves, thermodynamic fluctuations, Kovásznay modes, budget analysis, predictive models

# Table of Contents

# List of Figures

# List of Tables

# List of Symbols

## Roman Symbols

| | |
|---|---|
| $(x_{sp}^{start}, x_{sp}^{end})$ | streamwise coordinate corresponding to the start and the end of the sponge region |
| $\bar{\mathbf{k}}$ | wavenumber corresponding to the vorticity/entropy wave behind the shock |
| $\lvert\mathbf{k}\rvert$ | magnitude of the wavenumber vector, $k$ |
| $\mathbf{k}$ | complex wavenumber vector, also denoted as $\vec{k}$ |
| $\mathcal{V}$ | volume |
| $\tilde{\mathbf{k}}$ | wavenumber corresponding to the acoustic wave behind the shock |
| $\tilde{\mathbf{k}}_i$ | imaginary component of the acoustic wavenumber |
| $\tilde{\mathbf{k}}_r$ | real component of the acoustic wavenumber |
| $\vec{V}$ | velocity vector |
| $a$ | speed of sound: $\sqrt{\dfrac{\gamma p}{\rho}}$ (or) $\sqrt{\gamma R T}$ |
| $A_v$ | amplitude of the vorticity wave |
| $c_p$ | gas specific heat capacity at constant pressure |
| $c_v$ | gas specific heat capacity at constant volume |
| $d$ | ordinary differential operator |
| $D(k)$ | dissipation spectrum function: $D(k) = \nu k^2 E(k)$, where $k$ is the wavenumber |

| | |
|---|---|
| $e$ | specific internal energy: $c_v T$ |
| $E(k)$ | energy spectrum function. Turbulent kinetic energy is obtained from the energy spectrum as, $TKE = \int_{k=0}^{\infty} E(k)dk$, where $k$ is the wavenumber |
| $E_0$ | total energy: $e + \dfrac{u_i^2}{2}$ |
| $F$, $G$, $H$, $I$, $K$, $Q$, $L$ | complex transfer functions relating the upstream fluctuations to the downstream fluctuations in LIA |
| $h$ | specific enthalpy: $c_p T$ |
| $k$ | turbulent kinetic energy: $\dfrac{\widetilde{u_i'' u_i''}}{2}$ (or) $\dfrac{\overline{u_i' u_i'}}{2}$ |
| $k_0$ | peak energy wavenumber |
| $k_{max}$ | Maximum wavenumber in the domain |
| $L_\epsilon$ | dissipation length scale: $\dfrac{(2\, R_{kk})^{3/2}}{\epsilon}$ (or) $\dfrac{k^{3/2}}{\epsilon}$ |
| $L_{db}$ | length of the isotropic turbulence database, usually $2\pi$ |
| $L_{sp}$ | length of the sponge region |
| $L_x$, $L_y$, $L_z$ | length of the numerical domain in the $x$, $y$, $z$ directions. Correspond to $L_{x_1}$, $L_{x_2}$, $L_{x_3}$ respectively, when written in tensor form |
| $M$ | Mach number: $\dfrac{\widetilde{u}}{\overline{a}}$ (or) $\dfrac{\overline{u}}{\overline{a}}$ |
| $M_t$ | turbulent Mach number: $\dfrac{\sqrt{\widetilde{u_i'' u_i''}}}{\widetilde{a}}$ (or) $\dfrac{\sqrt{\overline{u_i' u_i'}}}{\overline{a}}$ |
| $N_B$ | number of boxes used to create the final blended database |
| $p$ | pressure |
| $p^*$ | target back pressure |
| $p_{corr}$ | back pressure correction |
| $Pr$ | Prandtl number: $\dfrac{\mu\, c_p}{\kappa}$ |
| $q_i$ | heat conduction term in the $i^{\text{th}}$ direction: $-\kappa \dfrac{\partial T}{\partial x_i}$ |
| $R$ | Specific gas constant |

| | |
|---|---|
| $R_{ij}$ | Reynolds stress tensor: $\widetilde{u_i''u_j''}$ (or) $\overline{u_i'u_j'}$ |
| $R_{kk}$ | twice of turbulent kinetic energy |
| $Re$ | Mean flow Reynolds number: $\dfrac{\overline{\rho}\,\lvert\overline{u}_i\rvert\,L}{\overline{\mu}}$ |
| $Re_\lambda$ | Reynolds number based on Taylor lengthscale: $\dfrac{\overline{\rho}\,u'_{rms}\,\lambda}{\overline{\mu}}$ |
| $Re_{L_\epsilon}$ | Reynolds number based on dissipation length scale: $\dfrac{\overline{\rho}u'_{rms}L_\epsilon}{\overline{\mu}}$ |
| $s$ | entropy |
| $S^d_{ij}$ | deviatoric part of strain rate tensor: $S_{ij} - \left(S_{kk}\dfrac{\delta_{ij}}{3}\right)$ |
| $S_{ij}$ | strain rate tensor: $\dfrac{1}{2}\left(\dfrac{\partial u_j}{\partial x_i} + \dfrac{\partial u_i}{\partial x_j}\right)$ |
| $S_{u,i}$ | velocity derivative skewness: $\overline{\left(\dfrac{\partial u'_\alpha}{\partial x_\alpha}\right)^3} \Bigg/ \left[\overline{\left(\dfrac{\partial u'_\alpha}{\partial x_\alpha}\right)^2}\right]^{\frac{3}{2}}$ |
| $T$ | temperature |
| $t$ | Time |
| $T_{ref}$ | reference temperature for the gas |
| $u$, $v$, $w$ | velocity components in the $x$, $y$, $z$ directions. Corresponds to $u_1$, $u_2$, $u_3$, respectively, when written in tensor form |
| $u_i$ | velocity in the $i^{\text{th}}$ direction |
| $x$, $y$, $z$ | streamwise (shock-normal), transverse and spanwise directions. Corresponds to $x_1$, $x_2$, $x_3$, respectively, when written in tensor form |
| $x_i$ | spatial coordinate in the $i^{\text{th}}$ direction |
| $x_s$ | location of the instantaneous shock |

## Greek Symbols

| | |
|---|---|
| $\alpha_d$ | reflection coefficient for reflections from end of the domain |

| | |
|---|---|
| $\alpha_r$ | reflection coefficient for reflections from inside of the sponge region |
| $\delta_{ij}$ | Kronecker delta: 1 if $i = j$ and 0 otherwise |
| $\delta_n$ | numerical shock thickness |
| $\delta_s$ | physical shock thickness |
| $\Delta t$ | time step in the numerical simulations |
| $\Delta x$ | grid spacing in the streamwise direction |
| $\Delta y$ | grid spacing in the transverse direction |
| $\Delta z$ | grid spacing in the spanwise direction |
| $\epsilon$ | dissipation rate of turbulent kinetic energy: $\frac{1}{\bar{\rho}}\overline{\sigma_{ik}\frac{\partial u_j''}{\partial x_k}}$ |
| $\eta$ | Kolmogorov length scale: $\frac{\nu^{3/4}}{\epsilon^{1/4}}$ |
| $\gamma$ | Ratio of specific heats |
| $\kappa$ | thermal conductivity coefficient: $\frac{\mu\, c_p}{Pr}$ |
| $\lambda$ | Taylor lengthscale: $\overline{u_\alpha' u_\alpha'} \Big/ \overline{\left(\frac{\partial u_\alpha'}{\partial x_\alpha}\right)^2}$ (no summation) |
| $\mu$ | dynamic viscosity: $\mu_{ref}\, \frac{T}{T_{ref}}$ |
| $\mu_{ref}$ | reference dynamic viscosity for the gas |
| $\nu$ | kinematic viscosity: $\frac{\mu}{\rho}$ |
| $\Omega$ | temporal frequency of the wave |
| $\omega_m$ | Vorticity in the $m^{\text{th}}$ direction: $\varepsilon_{mji}\frac{\partial u_i}{\partial x_j}$ |
| $\partial$ | partial difference operator |
| $\psi$ | angle of incidence with respect to the streamwise direction of the incident wave |
| $\rho$ | density |

$\sigma_0$ sponge strength

$\sigma_{ij}$ viscous stress tensor: $2\,\mu\,S_{ij}^{d}$

$\tau_\epsilon$ dissipation time scale: $\dfrac{1}{2}\,\dfrac{R_{kk}}{\epsilon}$ (or) $\dfrac{k}{\epsilon}$

$\tau_{db}$ inflow turbulence database time period: $\dfrac{L_{db}\,N_B}{\overline{u}_{1,u}}$

$\tau_p$ pass-over time in STI: $\dfrac{L_{x,u}}{\overline{u}_{1,u}} + \dfrac{L_{x,d}}{\overline{u}_{1,d}} + \dfrac{L_{x,d}}{|\overline{u}_{1,d} - \overline{a}_d|}$

$\theta$ Dilatation: $\dfrac{\partial u_k}{\partial x_k}$

$\varepsilon_{ijk}$ Levi-Civita symbol

$\xi$ displacement of shock front in the instantaneous frame of reference

$\xi_t$ shock unsteadiness (or corrugation) velocity in the instantaneous frame of reference

$\xi_{y/z}$ slope of the shock front in the instantaneous frame of reference for the $(x, y)/(x, z)$ plane. Corresponds to $\xi_{x_2/x_3}$ and the respective planes are $(x_1, x_2)/(x_1, x_3)$, when written in tensor form

## Superscripts

$\overline{f}$ Reynolds average of the variable $f$, averaged over time and homogeneous directions

$\widetilde{f}$ Favre average of the variable $f$, mass-weighted average over time and homogeneous directions

$f'$ Reynolds fluctuation of the variable $f$

$f''$ Favre fluctuation of the variable $f$

$f^*$ indicates dimensional value of the variable $f$

## Subscripts

$\partial_i$ derivative with respect to index $i$. Implicitly denoted as derivative with respect to the spatial coordinate in the $i^{\text{th}}$ direction

| | |
|---|---|
| $\partial_t$ | derivative with respect to time |
| $f_0$ | value of $f$ at the initial time |
| $f_\alpha$ | to denote that the index $\alpha$ of the variable $f$ should not be summed up when repeated |
| $f_{db}$ | value of $f$ in the turbulent database |
| $f_d$ | downstream value of $f$, also indicated as $f_2$ in one-dimensional case |
| $f_{in}$ | value of $f$ at the inlet of the domain |
| $f_{rms}$ | root mean square value of variable $f$ |
| $f_u$ | upstream value of $f$, also indicated as $f_1$ in one-dimensional case |

## Abbreviations

| | |
|---|---|
| 1D, 2D, 3D | one-, two-, three-dimensional |
| CFD | **C**omputational **f**luid **d**ynamics |
| CFL | **C**ourant, **F**riedrich, **L**ewy number |
| DNS | **D**irect **n**umerical **s**imulation |
| ENO | **E**ssentially **n**on-**o**scillatory |
| GAR | **G**rid **a**spect **r**atio |
| LHS | **L**eft **h**and **s**ide |
| LIA | **L**inear **i**nteraction **a**nalysis |
| LODI | **L**ocal **o**ne **d**imensional **i**nviscid |
| MPI | **M**essage **p**assing **i**nterface |
| NS | **N**avier-**S**tokes |
| NSCBC | **N**avier **S**tokes **c**haracteristic **b**oundary **c**ondition |
| ODE | **O**rdinary **d**ifferential **e**quation |
| PDE | **P**artial **d**ifferential **e**quation |

| | |
|---|---|
| PDF | **P**robability **d**ensity **f**unction |
| RANS | **R**eynolds **a**veraged **N**avier-**S**tokes |
| RDT | **R**apid **d**istortion **t**heory |
| RH | **R**ankine-**H**ugoniot |
| RHS | **R**ight **h**and **s**ide |
| RK4 | $4^{th}$-order **R**unge-**K**utta method |
| RMS | **R**oot **m**ean **s**quare |
| SAT | **S**imultaneous **a**pproximation **t**erms |
| SBP | **S**ummation **b**y **p**arts |
| STI | **S**hock **t**urbulence **i**nteraction |
| SWTBLI | **S**hock **w**ave / **t**urbulent **b**oundary-**l**ayer **i**nteraction |
| TKE | **T**urbulent **k**inetic **e**nergy |
| WENO | **W**eighted **e**ssentially **n**on-**o**scillatory |

## Other Symbols

| | |
|---|---|
| $[f]$ | jump in value of $f$ across the shock |
| $\|\|\vec{f}\|\|$ | norm of the vector $f$, usually $L_2$-norm. Also denoted as $\|\|.\|\|_2$ |
| $\|\vec{f}\|$ | magnitude of the vector $f$ |

# Chapter 1

# Introduction

## 1.1 Motivation and background

Shock waves are characteristic features in high-speed compressible turbulent flows, specifically in the supersonic/hypersonic flow regime. In aerospace applications, the effect of shock waves on the turbulent features in a supersonic boundary layer is usually studied to understand the physical mechanisms responsible for boundary layer separation, increased heat transfer and high surface pressures, each of which are unique engineering problems. The interaction of free turbulence with a planar shock wave is a similar problem of interest, rich with physical insights on the effects of shock on turbulence and vice-versa without additional complexities such as mean shear, streamline curvature and wall effects. Shock-turbulence interaction has implications in a variety of applications, to name a few, supersonic/hypersonic propulsion systems, inertial confinement fusion, shock wave lithotripsy, and astrophysical shock waves. In this study, we focus on the interaction of a homogeneous isotropic turbulence interacting with a nominally planar shock wave, which is the most basic form of shock-turbulence interaction.

Compressible turbulent flows are characterized by appreciable changes in thermodynamic quantities such as density, pressure and temperature fluctuations, which can be drastically amplified / altered on interaction with shock waves. The importance of understanding the thermodynamic fluctuations is well known as they play a major role in turbulent mass flux, sound generation, turbulent heat flux, and most importantly, in the turbulent transport of energy between internal and kinetic energy components [89]. For example, consider the process of inertial confinement fusion, where a fuel capsule is to be compressed to its maximum limit, to generate energy by fusion mechanisms. The compression is achieved by a converging shock, which is set off by lasers heating the fuel capsule. At the initial stage, the fuel is separated from the lasers by an outer metal coating. An imploding shock is set off when the outer metal coating blows outwards due to the heat from the lasers. During this stage, the interface separating the fuel layers maybe subjected to either the Rayleigh-Taylor instability (RTI) or the Richtmyer-Meshkov instability (RMI) as the case maybe due to the traveling shock, resulting in non-uniform heating and compression of the fuel. The amount of density variations induced by the shock, describe the turbulent mass flux in the interface, which in turn determine the degree of mixing between the fluids. Mixing between the fuel layers needs to be avoided to ensure maximum compression and energy yield, which is unfortunately still an issue in ICF. Shock-compressible turbulence interaction has been used as a model problem to study the complex ICF process [10, 42, 59, 60, 101].

Compressible turbulence interacting with a shock wave has also been used as a model problem in astrophysics. The density variations in the interstellar medium due to accelerating astrophysical shocks (induced by supernovae explosions) is an example, where the interaction problem is investigated to understand the evolution of various cosmic phenomena (see [1, 2, 55, 171] and related works) and in atmospheric sciences (see [75] and related works). An understanding of the generation of pressure fluctuations behind the shock in a supersonic over-expanded nozzle (e.g., rocket nozzles of space vehicles) is necessary to mitigate jet noise (see [92, 126]). In a similar vein, the temperature fluctuations (and its gradients), which are amplified across the shock, increases the surface heat transfer (by $\approx 400\%$) and alter the skin friction coefficient at the shock impingement point in aerospace vehicles [138]. These examples indicate a necessity to understand the physical mechanisms (or dynamics) of shock-amplified compressible turbulence to model/design efficient systems that could benefit the application in consideration. The presence of a shock wave in front of a supersonic vehicle is detrimental since it introduces additional drag and increased aerodynamic heating, but is also very useful in the generation of lift as is the case in waveriders, which have high lift-to-drag ratios due to the compression lift produced by the shock waves (see Refs. [91, 153] for additional details). In the case of supersonic combustion, shock waves enhance the mixing of fuel and oxidizer [162], and thus are essential elements in scramjet combustion.

Initial studies of shock-turbulence interaction were theoretical, mostly employing linear analysis and were based on the Kovásznay's decomposition of turbulence [78]. The theory aptly called as the linear interaction analysis (LIA) was developed by Moore [108] and Ribner [123] to analyze the interaction of acoustic and vorticity waves, respectively with an unsteady normal shock. The theory was later made use of by many researchers to study problems involving shocks and free turbulence [35, 41, 59, 60, 85–87, 96, 98, 99, 165]. A number of physical experiments utilizing grid-generated turbulence interacting with a normal shock have been carried out [4, 8, 49, 54, 64] to study the underlying mechanisms responsible for amplification of turbulent kinetic energy (TKE) and the modification of length scales across the shock; purely driven by the need to understand mixing enhancement across the shock and shock wave/turbulent boundary layer interaction (SBLI). Several numerical simulations have also been carried out to study the canonical shock-turbulence interaction problem over the years due to its geometric simplicity and rich physics. Shock-resolved simulations, where the viscous shock-profile is resolved [66, 85, 87, 90, 132], shock-captured simulations, where the shock-profile is numerically estimated [45, 81, 83, 86, 98], and shock-fitting simulations, where the shock thickness is neglected by specifying Rankine-Hugoniot (RH) conditions [122, 141, 164] have been carried out to study this problem. The focus has been to understand the amplification of turbulent kinetic energy and vorticity variances (or enstrophy), reduction in length scales, and enhanced anisotropy in the post-shock Reynolds stresses, $R_{ij} = \widetilde{u_i'' u_j''}$.

The modification of the thermodynamic quantities behind the shock was explored by few researchers. Lee *et al.* [85–87] explored the validity of isentropic relations in the post-shock region, and Mahesh *et al.* [98, 99] studied the effect of upstream entropy fluctuations on the post-shock thermodynamic field using DNS and LIA. Quadros *et al.* [119] studied the interaction of purely vortical turbulence with a normal shock using LIA and data from the direct numerical simulation (DNS) of Larsson *et al.* [81] for understanding the turbulent heat flux correlation. The physical insights from the study has been used towards development of a simple model for the turbulent energy flux [117]. Tian *et al.* [159] studied the interaction of a Mach 2 shock wave with isotropic turbulence with (multi-fluid) and without (single-fluid) variable compositions. They compared the conditional expectation of density, pressure and temperature fluctuations amongst each other, and investigated whether they followed an isentropic scaling behind the shock. The earlier studies have looked at the amplification of thermodynamic fluctuations across relatively weak shocks and checked for the validity of Morkovin's hypothesis (see Ref. [147] for description) behind the shock [99]. By comparison, the current work aims to study the amplification of thermodynamic fluctuations across weak and strong shocks, and provide qualitative as well as quantitative insights using LIA and numerical simulations. In addition, the predictive capabilities of LIA would be explored by comparing with data from numerical simulations.

This requirement motivated us to pursue fundamental research into understanding the physics of shock-turbulence interaction. We make use of the LIA and the DNS data to study flow features in canonical shock-turbulence interaction. The focus of the current work is on the thermodynamic fluctuations generated by the shock. It is important to know the intensity of the thermodynamic fluctuations generated behind the shock, and the physical mechanisms that govern their evolution. The physical insights obtained herein, could aid in developing models for predicting the thermodynamic fluctuations in the shock-amplified turbulence.

## 1.2 Objective

The objective of the present study is to

- analyze the generation of density, pressure, temperature and entropy fluctuations across the shock wave using LIA and DNS,
- generate relevant data using numerical simulations for the required analysis,
- investigate the dominant mechanisms behind the evolution of thermodynamic fluctuations using Kovásznay mode decomposition (on the LIA data) and post-shock budget analysis (on the DNS data),
- develop modeling strategies to capture the essential physics of the thermodynamic fluctuations in canonical shock-turbulence interaction (STI).

Studying the four thermodynamic variances will also help explain the behavior of related quantities, like the turbulent mass flux, $\overline{\rho' u_i'}$ and heat flux, $\overline{h' u_i'}$ in the flow. A part of this work is also to fill in the gaps in existing literature, specifically for the analysis of thermodynamic fluctuations in the high Mach number regime. A wide range of Mach numbers and turbulent Mach numbers, from 'wrinkled shock' to 'broken shock' regimes are considered. The results are compared with the predictions from linear interaction analysis. Kovásznay mode decomposition of the LIA solution and the budget of transport equations computed using simulation data are used in a complementary way to bring out the dominant physical mechanisms. We develop advanced physics-based models for shock-turbulence interaction, similar to those in [144, 145] and other works. These models are validated against DNS data across a range of shock strengths.

## 1.3 Scope

This dissertation presents about the linear analysis and the numerical simulations of the canonical shock-turbulence interaction. DNS data of homogeneous turbulence with turbulent Mach numbers of $M_t$ = 0.05 to 0.40 and Taylor lengthscale Reynolds number of $Re_\lambda$ = 33 interacting with normal shock waves of varying strengths ($M$ = 1.23, 1.50, 2.50

and 3.50) are presented. The evolution of thermodynamic fluctuations behind the shock is discussed in detail using the LIA and the DNS results. The effect of shock strength (varying $M$) and turbulence intensity (varying $M_t$) on the thermodynamic fluctuations is studied using the present simulations. We also use the extensive DNS dataset of Larsson *et al.* [81, 83] covering a wide range of Mach numbers to complement the simulations performed as part of the current work. The data from Larsson *et al.* are also used to draw inferences, especially for the effect of viscous mechanisms (varying $Re_\lambda$) on the thermodynamic quantities. Dominant mechanisms responsible for the amplification and evolution of the thermodynamic fluctuations in the post-shock region are identified by performing a budget analysis on the DNS data. Models for the thermodynamic variances were developed using the LIA theory and the existing models for TKE [145] and the turbulent energy flux [117]. The models developed, herein, consider that the shock is only a source for production of the thermodynamic variances, and the evolution of turbulence behind the shock depends on the evolution of the respective Kovásznay modes. We find good predictions of the thermodynamic fluctuations by the developed models.

This dissertation is organized as follows,

- Chapter 2 covers the available literature addressing the shock turbulence interaction problem till date, and includes theoretical, experimental and computational studies. LIA has been the primary tool for the theoretical studies, and has been used for verifying the numerical simulations by many researchers. The limited experimental studies and the various computational studies using different types of numerical simulations are also provided. The scope of the earlier works with respect to the thermodynamic fluctuations is also discussed.

- Chapter 3 provides a brief review of the LIA framework used in the current work. The theory models the turbulence field upstream of the shock as a superposition of two-dimensional plane waves of varying amplitudes, orientations and wavenumbers. Each of the plane waves is considered to interact with the shock independently and generate post-shock fluctuations via the linearized RH relations. post-shock turbulent statistics are obtained by integrating over all of the post-shock waves.

- Chapter 4 describes the procedure and verification of the numerical simulations in detail. Details of the computational grid and the boundary conditions are provided in this chapter. The details of the cases that have been simulated along with the extensive grid independence tests are also provided. Procedures and verification tests for the temporally decaying homogeneous isotropic turbulence simulations are also discussed. The convergence of the DNS results towards LIA solutions is also discussed in this chapter.

- Chapter 5 describes the underlying physics of the post-shock thermodynamic field by comparing the LIA and the DNS solutions. A short description of the Kov'asznay mode decomposition of the thermodynamic variances in the LIA data is also provided. A new method for extracting variance values at the location immediately behind the shock without the mean shock effect is described in this chapter. The method is a threshold-based method and uses dilatation values as the threshold.

- Chapter 6 details the effect of the governing parameters ($M$, $M_t$ and $Re_\lambda$) on the post-shock thermodynamic field. The effect of the mean flow Mach number, the turbulent Mach number and the Taylor lengthscale Reynolds number on the evolution of thermodynamic fluctuations is provided. Far-field and near-field statistics (computed using the threshold method) for varying shock strengths and turbulence intensities are also presented. The effect of the Reynolds number is not clearly understood with the sparse data available for comparison. In addition to the governing parameters, the effect of the shape of the inflow turbulence energy spectrum on the post-shock thermodynamic variances is also discussed.

- Chapter 7 presents the dominant mechanisms responsible for the evolution of the thermodynamic fluctuations using a budget analysis on the DNS data. The correlation of density, pressure and temperature fluctuations with the fluctuating dilatation is found to be the dominant term in the post-shock region. At the shock, the production due to mean velocity gradients is responsible for the generation / amplification of the variances.

- Chapter 8 describes the model development procedure and the predictive capabilities of the model against the LIA and the DNS data. The models for the temperature, density, entropy and pressure variances were developed using the earlier works of Sinha *et al.* [145] and Quadros & Sinha [117]. The developed models predict the modification of turbulence (or the production of the thermodynamic variances) due to the passage of the shock accurately. The models were validated against the DNS data, both Larsson *et al.* [81] data and those that were developed as part of the current work. The models show a good match with the DNS data.

# Chapter 2

# Literature Survey

The physics of turbulence amplification in fluids due to the presence of shocks has been a subject of study for several researchers, both in the past and in the present, and is expected to continue in the future also. This is entirely due to the complicated nature of both the shock wave and the turbulence itself. Research in compressible turbulence in fluids dates back to the 1950s, where Moyal [111] studied the random noise generated by the fluctuating vorticity in a homogeneous fluid. In the past and in the recent times, compressible turbulence in fluids has been explained for many scenarios in the statistical sense only (see Refs. [33, 136]), and a deterministic description of its nature is found only in few idealized cases. In the case of shocks, its structure can only be formulated for weak cases ($M < 2$ [158]), and the supporting experimental evidence on its structure is also limited [143]. The incomplete description of the structure of a shock wave is due to the lack of techniques/methods to accurately measure the second coefficient of viscosity for the fluid. The following references [7, 32, 130, 172] are suggested for reading to know more about the second coefficient of viscosity and the difficulty in measuring this value for many fluids.

The study of a turbulent flow interacting with a shock wave, thus remains an active area of research, where various methods and techniques are employed to provide a description of the specific problem under consideration than the complete physics of the problem itself. The case of homogeneous isotropic turbulence interacting with a normal shock wave is considered in this work. This canonical configuration albeit being simple, is still not fully understood and has been studied by many using theoretical, numerical, and experimental methods. A comprehensive description of these works are presented in the following sections.

## 2.1 Theoretical analysis

Theoretical analysis of compressible turbulence interacting with a shock wave was made possible due to the seminal work of Kovásznay in 1953 [78]. Kovásznay [78] decomposed turbulence in a compressible, viscous and heat conductive gas into three fundamental modes: vorticity, entropy, and acoustic modes, which are governed by three independent equations. This decomposition is valid only for small fluctuations where linearization is possible, and breaks down for large fluctuations where interaction between each of the modes is highly probable. The vorticity mode consists of only solenoidal velocity fluctuations and the entropy mode has only non-isentropic density and temperature fluctuations. The acoustic mode comprises of irrotational velocity, isentropic density and temperature, and pressure fluctuations. The vorticity and entropy modes are 'frozen' (i.e., they have no mean convection velocity) in nature whereas, acoustic modes travel with the speed of sound.

Later in 1953-54, Moore [108] and Ribner [123] used this decomposition to study the interaction of acoustic and vorticity waves with a normal shock, and laid out the fundamentals of studying turbulence as a spectrum of these planar waves. Moore [108] followed a linearized framework to study the interaction of a single oblique acoustic wave and an oblique vorticity wave, each separately interacting with normal shocks of varying strengths ($M = 1, 1.5, \infty$). The interaction of acoustic waves was studied in detail for two different scenarios: (1) moving normal shock interacting with a sound wave in a stationary gas and (2) sound wave overtaking a shock from behind. In the former scenario, depending on the incident angle of the sound wave, the post-shock sound field is either propagating or attenuating whereas, the latter only shows reflection of the sound wave and no attenuation of sound waves is observed. However, the range of incidence angles for case (2) in his study was limited due to the problem definition that the sound wave must overtake the shock wave. Thus the absence of attenuation cannot be proved to be true for all incidence angles, though it is difficult to formulate a problem with the complete range of incidence angles for this case.

Ribner [123] analyzed the interaction of a single vorticity wave with a normal shock in the linearized sense with a different physical perspective than Moore. The unsteady interaction is transformed as a steady interaction by imposing a transverse velocity. The interaction results in refraction of the incident vorticity wave and simultaneously generates entropy and acoustic waves. The acoustic waves can be either propagating or attenuating depending on the incidence angle. In the second half of 1954, Ribner [124] extended the earlier analysis of single wave interaction to a spectrum of similar waves, and computed the post-shock root-mean-square (rms) values of various turbulent quantities. Expressions for spectra and correlations of various quantities in the post-shock turbulence field were provided. The noise generated by the shock-turbulence interaction was calculated for varying intensities and Mach numbers in this study. The analysis of the sound field generated by a shock-isotropic turbulence interaction was presented with special emphasis on the flux of acoustic energy in [125]. The post-shock acoustic energy flux is found to vary linearly with the shock strength. The results are found to match with Lighthill's theory, showing a similar asymptotic behavior for weak shocks and diverging significantly for strong shocks. In 1987, Ribner [127] applied LIA theory to represent the interaction of an infinite planar shock with a single three-dimensional spectrum component of turbulence (an oblique sinusoidal "shear wave" by his definition) and provided in parts of the three-dimensional spectrum analysis necessary to generalize the scenario to the interaction of a shock wave with convected homogeneous turbulence. Root-mean-square values of post-shock pressure, temperature and velocity fluctuations were calculated for an isotropic pre-shock turbulence in addition to the one-dimensional power spectra of these quantities. Ratios of the one-dimensional post-shock spectra of several quantities to the longitudinal pre-shock turbulence spectrum were presented for a wide range of Mach numbers. The major outcome of this theoretical work was that the STI is an excellent noise generator but the far field noise (pressure fluctuations) generated is low for strong shock interactions compared to weak shock interactions. The applicability of LIA to only weak fluctuations in the upstream becomes a restriction when analyzing for weak shock interactions.

Following the works of Ribner and Moore, Kerrebrock [74] carried out an extensive analysis of interaction of small perturbation fields with a normal shock and extended it to a flame, assuming the flame as a reactive gas dynamic discontinuity in the linear limit. The generation/refraction of three types of Kovásznay modes were observed for the shock and flame also in the presence of any one of the modes upstream of the discontinuity. A comprehensive set of expressions describing the post-shock statistics for the different types of upstream waves was provided for the first time. The case of shock wave being oblique was also analyzed with the necessary expressions provided. The limit of linear analysis for weak shocks was also pointed out, as the expressions were found to result in a singularity as the shock strength tend towards $M = 1$ limit. The case of only entropy disturbances interacting with a normal and an oblique shock wave was studied by Chang [17]. The effects of upstream entropy wave orientation on the sound generation was studied in detail to understand indirect noise generation processes. The shock front was found to be corrugated for planar entropy waves also, similar to the case of interaction of vorticity and acoustic waves, and was attributed to the generation of velocity fluctuations in the downstream region by the shock wave.

Higher order perturbation analysis based on the expansion of the disturbance field amplitude was presented for a supersonic compressible flow by Chu and Kovásznay [19]. An extension of the earlier work on the decomposition of turbulence into Kovásznay modes where nonlinear effects due to the interaction between the three Kovásznay modes were included in this study. The second order interactions such as vorticity-vorticity, vorticity-entropy, etc. are interpreted as source terms for the Euler equations and show significance only when all three Kovásznay modes have same orders of magnitudes in their intensities and lengthscales. Thus, for cases where only one of the mode is significantly dominant such as the case of largely vortical turbulence, linear analysis seems to be a valid approximation.

After Moore, Johnson and Laporte [72] investigated the interaction of cylindrical sound waves with a stationary normal shock using the method proposed by Weyl for radio waves in 1958. The cylindrical sound wave is represented as a superposition of planar sound waves of varying direction, and each plane wave independently interacts with the shock front. The resulting waves are superimposed to form the post-shock deformed sound wave (elliptic in shape) using the Fourier integrals approach. This is the first time, a composition of sound waves was studied, though initiated back in 1956 by Kerrebrock for this scenario. A decade later, McKenzie and Westphal [105] studied the interaction of a planar acoustic wave and a vorticity-entropy wave with an oblique shock wave. The effect of intensity and incident angles were studied in detail and the sound (and its energy flux) generated behind the shock was described in detail. For an incident sound wave, the post-shock sound wave was found to be $O(M^2)$ larger than the incident wave in amplitude, and if the waves are inclined close to the critical angle, the post-shock amplitude was of $O(M^3)$ larger. The analysis was applied to study the amplification of small disturbances in a solar wind on the interaction with a bow shock produced due to the earth's magnetic field. The linear perturbation analysis of the interaction of entropy, vorticity and acoustic disturbances with a weak normal shock was studied by Hardy and Atassi [46]. The interaction of acoustic waves was studied in detail and the amplification of an incident acoustic wave was larger compared to an incident vorticity or entropy wave. Weak-shock approximation was described to be valid for modeling of shock flows in complex geometries for the reason that the generated acoustic waves and the entropy waves are generally small in such scenarios.

Mahesh *et al.* in a series of articles compared LIA and numerical simulations of the STI problem. In [96], they studied the interaction of an isotropic field of acoustic waves interacting with a normal shock wave using LIA and computations. The effects of acoustic fluctuations were found to result in reduced amplification of turbulence at low Mach numbers ($M < 2$) against purely vortical case. However, larger amplifications than the vortical case was observed for high Mach numbers ($M > 3$). The computations were found to follow the trend of the results predicted by LIA. The combined interaction of vortical and acoustic waves with a normal shock was also discussed. In [99] and [98], they introduced the concept of adding entropy fluctuations on top of a vortical turbulent field and studied the combined interaction of vortical and entropy fluctuations. The upstream vorticity-entropy correlation is shown to strongly influence the evolution of the turbulence across the shock; positive correlation has a suppressing effect and vice versa. Morkovin's hypothesis was tested and was found to be invalid due to the shock-front oscillation. Comparison of LIA and numerical simulation solutions were found to be satisfactory. Similar type of study but with only vortical turbulence was carried out by Lee *et al.* in [85] and in [86].

Anyiwo and Bushnell [6] applied LIA to study the effect of shock wave on the turbulent boundary-layer by following a local STI approach. The study identified that the shock oscillation speed to be an important parameter along with the shock strength, incident angle of waves and fluid properties. Correction estimates with the help of LIA were suggested for the distortion in the turbulence spectra due to the shock-amplification. The turbulence closure models used in their period assumed spectral similarity in numerical simulations, and these corrections were found to bring the numerical results closer to experimental values. Robinet and Casalis [129] showed that the critical angle which appears as a singularity in the linearized Euler equations can be removed if the perturbations are not considered as normal modes. A different form for the perturbations deduced from the mathematical nature of the linearized Euler equations was proposed which resulted in non-singular values at the critical angles. This analysis was then applied to the shock wave oscillations occurring on a wing profile and in a nozzle. Good results were obtained in comparison with the available experimental data.

Fabre *et al.* [35] presented the LIA theory of planar waves interacting with a normal shock in the form of compact matrices, especially the transfer functions. The theory was then applied to study a cylindrical entropy spot with Gaussian entropy distribution interacting with a normal shock wave. Qualitative results for entropy, vorticity and noise generation were presented and compared with results from numerical simulation of the full nonlinear Euler equations. Griffond [41] extended the LIA theory to analyze the interaction of a gas concentration spot containing the mixture of two perfect gases with that of a normal shock in a similar fashion. The study was used to address the creation of vorticity, entropy and acoustic waves by the interaction and the refraction of the incident concentration wave without any amplification in itself. This single wave analysis of concentration waves was extended to the case of a shock wave traveling in a weakly inhomogeneous mixture [42] and in a Richtmyer-Meshkov instability (RMI) problem [101]. Lubchich and Pudovkin [94] studied the effect of acceleration of the shock corrugation due to the incident perturbations, and claimed that an additional inertial force was induced due to the acceleration. Suitable modifications to the Rankine-Hugoniot conditions for the unsteady and distorted normal shock wave was proposed accounting for this inertial force. Griffond's [41] numerical experiments and Tumin's [161] 'vanishing volume' concept showed that the effects of this inertial force to be negligible. One of the authors, Lubchich [93] refuted their arguments, and emphasized that the inertial force should indeed be included in the pressure term. Sinha [144] also argued that the effect of the inertial force to be negligible using theoretical arguments similar to Tumin's. Till date, no one has verified the effect of the inertial force due to frame acceleration.

Huete and his group studied the interaction of isotropic turbulent vorticity field [165], density field (a random pattern of density non-uniformities) [60] and acoustic field [59] with a normal shock in the linearized framework. Closed form analytical expressions for various correlations as a function of specific heat ratio, a new non-dimensional frequency and shock Mach number were presented. The non-dimensional frequency is a function of the incident wave's wavenumber, angle of inclination and the angular frequency. These expressions were simplified further in the asymptotic limits of weak and strong shocks, and highly compressible fluids. Various statistics including enstrophy amplification and acoustic energy flux generation are represented as functions of the three parameters. The difference in critical angles with respect to each of the cases (vorticity, entropy and acoustic) is discussed in detail along with the amplification ratios in each of their articles. The discussion was extended to the RMI problem, and the interface growth was described in detail with relevant formula. They have also explored the application of LIA in the field of astrophysics (discussed below).

Recently, Sinha [144] studied the evolution of enstrophy in shock/homogeneous turbulence interaction using LIA, and proposed models for the dissipation rate of turbulent kinetic energy accounting for the correlation between vorticity and entropy fluctuations (following [98]) in the upstream region. Quadros *et al.* [119] studied the generation of turbulent energy flux when homogeneous isotropic turbulence passes through a normal shock in the linear framework. The energy flux correlation was split into its respective Kovásznay modes using LIA to understand the rapid non-monotonic variation behind the shock. The various mechanisms responsible for the amplification and evolution of turbulent energy flux were identified, and the effect of compressible fluctuations was also explained using LIA. The study included the interaction of planar vorticity waves and a field of vortical turbulence with a normal shock using LIA, and supplemented the theory with computations of Larsson *et al.*, [81]. In [118], they decomposed the turbulent heat flux correlation ($\overline{u'T'}$) term into its respective Kovásznay modes using LIA, and explained the physical mechanisms responsible for the amplification and evolution of the velocity-temperature correlation. An extensive discussion on the validity of LIA and the range of Mach numbers for which viscous and nonlinear effects become important were provided.

The present work follows the methodology laid out by [99] (also mentioned in [119]) to study the thermodynamic fluctuations in STI using LIA. The earlier works of LIA [85, 86, 98, 99] emphasized on velocity fluctuations and its derivatives like turbulent kinetic energy and enstrophy, though some description about the thermodynamic field was also provided. In this study, we investigate the post-shock thermodynamic field using LIA and computations in detail, which is lacking in earlier studies.

Before proceeding, it is worth mentioning that Rapid Distortion Theory (RDT) has also been used to study the STI. One can look at the recent work of Kitamura *et al.* [76] for an extensive review of available literature where RDT has been used to study turbulence interacting with strong compressions [39, 97], but not limited to only shock waves. To the best of the author's knowledge Kitamura *et al.* [76] are the first ones to explicitly study the STI using RDT. Though, RDT supports sheared mean flow, which replicates shock/boundary-layer interactions, it does not include the shock-distortion effect. The importance of shock-distortion (or corrugation) effect, observed in STI scenarios is highlighted in [145], where the model developed by considering the distortion effect provides better predictions than standard turbulence closure models. The recent work of Braun and Gore [14] considers the shock-corrugation effect as an important physical feature in STI, and they found improvements in the prediction of Reynolds stresses when the distortion effects are considered. The applicability of RDT is thus, limited to weak interactions in sheared mean flows, where there are no perturbations on the shock front.

In this section, theoretical tools which represent only linear effects of the canonical shock-turbulence interaction were emphasized. There are weakly nonlinear and fully nonlinear statistical theories that are applied to compressible turbulence, which can be extended to study the post-shock field generated by the shock wave. In fact the canonical shock-turbulence interaction problem is a fully nonlinear problem and only a small parameter space can be approximated to be linear. For weak turbulence (characterized by very low $M_t$ values), linear theories such as LIA or RDT, which do not consider any triadic interactions can be used for analysis. Eddy-Damped Quasi Normal Morkovian (EDQNM) closure models and Direct Interaction Approximation (DIA) are some of the nonlinear theories which consider triadic interactions that can be used to investigate high-intensity turbulence flowfields. Turbulent flowfields, which have moderate intensities that cannot be considered as weak or strong are analyzed using ‘wave-turbulence’ (WT) theories. The WT theory consider only the resonant triadic interactions, i.e., interaction between waves of the same type (for example, same wavenumber) and not all of the triadic interactions possible. The book by Sagaut and Cambon [133] is a good reference to learn about the various weakly and fully nonlinear theories, which are used in practice by many to investigate compressible as well as incompressible turbulence. The recent article of Mittal and Girimaji [107] provides a mathematical framework for the analysis of internal energy dynamics in compressible turbulence (see Fig. 1 in their article), which can also be used to demarcate linear and nonlinear effects (see also the references therein). The parameter space, which demarcates linear and nonlinear effects varies among different problems, and the guidelines provided in Sagaut and Cambon [133] are helpful in the investigation of canonical (or idealized) problems at the least, if not for complex problems.

### 2.1.1 Other applications of LIA

LIA has been used mostly for providing a theoretical framework for the STI problem and to obtain first-order estimates of the post-shock field. There are many works where LIA was applied to study problems other than STI, some of which are provided below. Recently, LIA has been extensively used to study astrophysical problems.

Jackson *et al.* [62, 63] used LIA treatment for the interaction of a weak vorticity wave and a reactive normal shock wave (or detonation wave). Linearized Euler equations are used for the flow upstream and downstream of the shock whereas, the linearized Rankine-Hugoniot conditions with chemical heat-release term to accommodate for the reactions. Exothermic reactions were found to increase the amplification of the refracted waves, and the alteration of the shock front due to imposed perturbations in the upstream flow was also discussed. The effect of the chemical heat-release term on the post-shock turbulence statistics and the one-dimensional power spectra were studied as a function of the upstream Mach number. The significance of the Chapman-Jouguet Mach number with respect to the noise generated downstream was discussed in detail. Massa and Jha [101] followed their analysis to investigate the effect of the reactivity on the RMI supported by the density difference between burnt and fresh mixtures in a shock-flame interaction. This scenario is usually observed in hydrogen combustion engines and is studied specifically to address the safety issues of nuclear power plants. One can refer to this article where linear analysis was used for studying the RMI problem and the dissertation of Bhagatwala [10] for relevant references on RMI with shock-turbulence interaction as a major component.

Huete *et al.* [56–58] studied the passage of a planar detonation front through a gaseous mixture with nonuniform density perturbations using linear theory. Only the fast-reaction limit where the detonation thickness is much smaller than the density perturbations was studied. Explicit expressions were obtained using Laplace transforms, similar to their earlier works on conventional STI. The effects of the propagation Mach number, chemical heat-release and burn rate were analyzed in detailed for both the fast-reaction limit and the slow-reaction limit. Additional effects due to the reaction (or burn) rate is analyzed using numerical simulations, and were compared with the linear theory predictions. Similarly, Hejranfar and Rahmani [48] presented theoretical formula for the interaction of freestream disturbances with a normal shock considering real gas effects. They have used linearized RH conditions but with real gas state of equation to provide a relationship between the disturbance field at the two sides of the shock.

Recently, Abdikamalov, Huete and their collaborators [1, 2, 55] are studying the interaction of Mach $\geq 5$ shock with the vortical-entropy turbulence using linear interaction approximation/analysis. They study the effects of vortical and entropic disturbances (produced due to the nuclear shell burning in the core collapse of a supernovae) on the shock dynamics and on the post-shock flow field in the linearized sense. Effects of the generated pressure and entropy fluctuations behind the shock on the critical neutrino luminosity (a quantity which determines the possibility of supernova explosions) are discussed in detail, and the limits of the linear theory are discussed by comparing with results from 3D neutrino-hydrodynamics simulations. Upstream perturbations are found to decrease the critical neutrino luminosity required for producing an explosion by approximately 12% due to the additional pressure generated behind the shock. The first-order estimates obtained using LIA helps in careful selection of the parameters to study with numerical simulations, which would have been otherwise, a very expensive procedure, especially in the framework of astrophysics (a mesoscale problem).

## 2.2 Experimental works

Due to difficulties in generating canonical shock-turbulence interaction in a laboratory environment without wall effects (say, ‘parasitic’ shocks from the walls) has limited this study experimentally. Experiments on Shock-wave/turbulent boundary-layer interaction, on the other hand, have been carried out by a large number of researchers with problems such as oblique shock impinging on a flat plate, compression corners and conical flares. The reader can refer to the works of Delery [23, 24], Dolling [25], Holden [50], Souverein [149], Sandham [135], and the recent works of Giepman [37, 38] for the vast amount of experimental research carried in the field of SWTBLI with focus on aerospace applications. Experimental studies of canonical shock-turbulence interaction have been carried out in the past using shock tubes, wind tunnels and convergent-divergent (CD) nozzles. Velocity fluctuations and its derivatives such as Reynolds stresses are predominantly studied in experiments, and thus there are only few experiments which have studied or mentioned of thermodynamic fluctuations.

The earliest study of canonical shock-turbulence interaction in experiments can be traced back to the work of Sekundov [140], published in a Russian article around 1974 which was later translated in English. He studied the passage of turbulence generated by a screen (or grid) placed in front of a supersonic nozzle containing a standing shock wave. He observed amplifications in the instantaneous values of velocity and temperature, measured using wire and film sensors. Due to limitations in the experimental apparatus, the measurements in normalized amplifications (or 'growth coefficients' by his definition) of turbulence values were found to be approximately $8-14\%$. A decade later, experiments of STI were taken up by Trolier and Duffy [160], where they performed measurements of amplifications in mass flux and total temperature fluctuations across the reflected shock in a shock tube facility. One of their major findings within the limit of experimental limitations and uncertainties is that the amplification in the turbulence quantities vary non-monotonically against Reynolds number. The reflected shock amplified the turbulence intensities by a factor of approximately 3. This was later complemented by the experimental studies carried out by Hartung and Duffy [47]. They took turbulence measurements in a low pressure shock tube using hot-wire anemometry. Velocity and density fluctuations were obtained from mass flux and total temperature signals using low Mach number assumptions. Behind the partially reflected shock, the turbulence intensity of density increased to 0.2% from 0.1% and velocity increased from 0.6% to 0.8%. The finding of Trolier and Duffy [160] regarding the decrease of fluctuations with Reynolds number up to a 'critical' Reynolds number was also verified, and the rate of decrease was attributed to the shock tube driver diaphragm characteristics.

Debieve and Lacharme [22] studied the interaction of turbulent flowfield from an air injector with a $M = 2.3$ oblique shock generated by a compression ramp inside a CD nozzle. They compared the results using RDT and an intermittence diagram associating for the shock rippling phenomenon. Thermodynamic fluctuations (density and temperature) were found to be amplified across the shock and rapidly decayed in a monotonic fashion along the direction of the flow. This experimental work suggested the importance of including the effect of shock-ripple (or intermittency by their definition) while computing the production of turbulence. Later, Sinha *et al.* [145] arrived at the same conclusion from a theoretical perspective. Hesselink and Sturtevant [49] studied the propagation of weak shocks ($M = 1.007-1.1$) in a statistically uniform but random medium. They reported that the turbulent mixing is enhanced by the shock-induced Rayleigh-Taylor instability. The pressure fluctuations were amplified across the reflected shock, and that the amplification ratios increased for increasing shock strengths in their experiments. The first reporting of locally extinguished shocks (or the shock replaced by a series of compression waves) was made in this experiment which was verified by a subsequent ray tracing method to characterize the shock structure. Keller and Merzkirch [73] used a speckle photographic method, which is sensitive to changes of gradients in fluid density to study the grid generated turbulence interacting with a nominally normal shock wave (reflected from the end wall) in a shock tube. Spatial correlation coefficients, turbulent length scales, and energy spectra were determined under the assumption of homogeneous isotropic turbulence upstream of the shock. Amplification of the turbulence intensity by the shock interaction process was verified quantitatively and the spectrum shows that it to be restricted to the lower wave numbers.

Similar results were obtained by Honkan, Briassulis and Andreopoulos [16, 52–54] in their study on the effect of a $M = 1.24$ nominally normal shock interacting with grid generated turbulence. The amplification ratio was not the same for the range of lengthscales considered, and they reported that the transverse lengthscale increased across the shock. The change in the transverse lengthscale reported in these experiments are in disagreement with results from LIA and numerical simulations. Amplification of velocity and temperature fluctuations and dissipative length scales has been found in all experiments. Velocity fluctuations of large eddies were amplified more than the fluctuations of small eddies. The dissipative length scale, however, of the large eddies were found to be amplified less than the length scale of the small eddies. Xanthos *et al.* [166] conducted similar experiments and showed the dependence of amplification ratios to the grid sizes. Using spectral analysis they reported that the pressure fluctuations associated with large eddies were amplified the most compared to those associated with the small scales.

Barre *et al.* [8] developed a new method to generate a quasi-homogeneous isotropic turbulent supersonic flow at Mach number 3 using multiple nozzles. The interaction with a normal shock wave (generated by means of a wedge shaped shock generator) was analyzed by means of hot-wire anemometry and laser Doppler velocimetry. Results from their experiments showed that the usual behavior of unperturbed turbulence was observed (isotropy, spectra, integral scales, and decay) for this new method. The amplification ratio of longitudinal velocity fluctuations was about 2 in the near field and 1.5 in the far field, which is close to the values reported by Ribner's theory. The transverse lengthscale was, however, found to be decreasing across the shock which contradicts the findings of earlier experiments. They concluded that the homogeneous and isotropic initial turbulent field becomes axisymmetric after the shock interaction. Later, Larsson *et al.* [81] compares their numerical simulation results with that of Barre *et al.* [8] experiments and find good agreement for Reynolds stress amplification across the shock.

Agui *et al.* [4] studied the interaction of grid generated turbulence with normal shock waves generated in a shock-tube facility. In addition to studying the conventional statistics such as turbulent kinetic energy and lengthscales, they also investigated the validity of Morkovin's hypothesis. They found that the root mean square value of the fluctuating Mach number is significantly affected (almost as much as 100% variation) by changes in the thermodynamic fluctuations. The debate about the decrease in the transverse lengthscale was partially resolved by their experiments for a range of Mach numbers. They identified that the transverse lengthscale amplified for the low Mach numbers and decreased for the high Mach numbers, and thereby, proving that both Honkan and Co. as well as Barre *et al.* were correct in their own experiments. The reason for such a change was, however, not discussed and a hypothesis that the turbulent eddies were compressed in all directions for only stronger shocks was proposed.

Recently, Kitamura *et al.* [77] studied the characteristics of divergence-free grid turbulence interacting with a weak spherical shock wave of Mach number 1.05. Turbulence-generating grids were used to generate nearly isotropic, divergence-free turbulence. The turbulent Reynolds number based on the Taylor lengthscale was $49 \leq Re_\lambda \leq 159$ and the turbulent Mach number was of $O(10^{-3})$ respectively. The results showed that the root-mean-square value of streamwise velocity fluctuations increases and the streamwise integral length scale decreases after the interaction, which is in agreement with previous experiments. The change in both quantities, however, became small as the Reynolds number and the turbulent Mach number were increased for the same strength of the shock wave. They suggested that the changes in the Reynolds stresses (and so in TKE) is more significant for initial divergence-free turbulence than for curl-free turbulence. Takagi *et al.* [152] and Sasoh *et al.* [137] studied the statistical behavior of post-shock overpressure (i.e., larger than dynamic pressure) due to the shock oscillations in the presence of grid generated turbulence in a shock tube. The experiments were conducted to investigate the shock wave modulation by the turbulent field in detail, with an additional objective of relating the overpressure to the velocity fluctuations and its related lengthscales. In a separate study, Inokuma *et al.* [61] proposed an empirical model to account for the change in pressure due to the local shock oscillation for a similar experiment.

With the help of hot-wire measurements, experimental works reported on the change of density and temperature (instantaneous values) across the shock wave, yet no detailed analysis was carried out regarding the change in fluctuation levels. The amplification and evolution of thermodynamic fluctuations behind the shock is still an untouched area, except for the work by Agui *et al.* [4] and the recent works by the Japanese researchers [61, 77]. The former's objective was to check the validity of Morkovin's hypothesis and the latter attempted to quantify the increase in pressure due to shock wave modulation; however, their works were not aimed to understand the dynamics of the thermodynamic field generated by the shock wave upon interaction.

## 2.3 Numerical simulations

The first ever attempt of numerically simulating the interaction of turbulence (approximated as planar waves) with a normal shock dates back to the work of Zang *et al.* [170] where they simulated the interaction of two-dimensional vorticity, entropy and acoustic waves (each separately) with a normal shock in a shock tube. They found agreement between LIA and the simulations for cases with weak shocks and strong disturbances also, which is a limitation in LIA. However, their simulations did not cover Mach numbers greater than $M = 2$ and they found large discrepancies between the solutions obtained at near-critical angles of incidence. Numerical simulations of SWTBLI problems, on the other hand, were being performed from 1975 onward.

Lee *et al.* studied the interaction of temporally decaying isotropic turbulence with weak shocks using shock-resolved [85, 87] and shock-captured [86] numerical simulations for a perfect gas. They investigated the amplification of turbulence fluctuations and the change in various lengthscales by the shock, the effect of turbulence on the shock structure, and also checked the validity of LIA with their numerical solutions. They were the first to report of the distortions in the shock structure due to turbulence by numerical simulations and the possibility of localized shock extinguishment for high turbulence intensities in the upstream flow, which would later be identified and subsequently verified by Larsson *et al.* [81, 83]. Larsson *et al.* [81] showed by extensive numerical simulations that this phenomenon (termed as 'broken shock') is physically possible and not a numerical artefact. Recent theoretical works of Clavin [20] and Mostert *et al.* [109, 110] have also shown that 'broken shocks' are physically possible in hydrodynamic and electromagnetic shocks, respectively. The comparison of shock-captured and shock-resolved simulations by Lee *et al.* provided a criteria for the required grid spacing in the shock-capturing simulations to reproduce solutions equivalent to those of the shock-resolved simulations. They also studied the relation between downstream thermodynamic fluctuations by comparing with LIA solutions and investigated the change in the polytropic exponent relating density, pressure and temperature fluctuations. The major discrepancy in their work is the insufficient resolution in shock-parallel grid spacing for the Taylor-scale Reynolds number studied, which resulted in incorrect values for the vorticity component in the streamwise direction and the post-shock shock-normal Taylor lengthscale. An excellent match between the LIA and numerical solutions (comparison of velocity and thermodynamic statistics) was observed for low Mach number, low turbulence intensity simulations in their study. In our opinion, this agreement was indicative of the underprediction of nonlinear processes in their simulations, rather than confirmation of LIA theory. Nonetheless, their work was the starting point in a series of similar numerical experiments on STI, where the amplification of turbulence and the distortion of the shock structure for different conditions was studied.

The case of incoming turbulence with both vortical and dilatational (or acoustic) fluctuations interacting with a normal shock wave was investigated by Hannappel and Friedrich [45]. They showed that there is nearly an order of magnitude decrease in the amplification of turbulence fluctuations and in the change of lengthscales across the shock for an incoming turbulence with 50% dilatational energy component compared to the purely vortical turbulence case. They also studied the evolution of density variance in the computational domain and reported that the production mechanism is responsible for the enhancement across the shock wave while the density-dilatation correlation term balances the convection term.

Jamme *et al.* [66, 70] also performed a similar study in a shock-resolved framework with all three types of turbulence fields in the input data, i.e., with pure vorticity, vorticity/entropy, and vorticity/acoustic fluctuations. They reported that the downstream levels of the velocity statistics depend on the kind of turbulence which is introduced in the computational domain. The presence of upstream entropy fluctuations was found to enhance the amplification of the turbulent kinetic energy and transverse vorticity variances across the shock compared to the purely vorticity case. More reduction of the transverse Taylor lengthscale and integral scale was observed in the vorticity-entropy case while no influence was seen on the longitudinal Taylor lengthscale. When acoustic and vortical fluctuations were associated upstream, less amplification of the kinetic energy, less reduction of the transverse lengthscale and more amplification of the transverse vorticity variance were observed across the shock. These results agree with the findings of Ref. [45] and [98].

Jamme and his collaborators also explored the interaction of an anisotropic turbulence, a mean sheared flow and a combination of both, with that of a normal shock wave in a series of articles [21, 67–69]. They found no significant differences in the underlying mechanisms of second-order statistical quantities (such as TKE, enstrophy, etc.) between cases with isotropic and anisotropic turbulence, upstream of the shock. They have found, however, some differences in the evolution of vorticity variances [69] and thermodynamic fluctuations [68] between cases with uniform mean flow and sheared mean flow, upstream of the shock. Their article on the evolution of thermodynamic fluctuations in a sheared flow case [68] explores the mechanisms responsible for density fluctuations, where they proposed that the production of density fluctuations is due to the amplification of the transverse Reynolds stress. They commented that the mechanisms responsible for the post-shock evolution of the thermodynamic fluctuations remains the same, between the uniform mean flow and the sheared mean flow cases. The only difference between the cases is in the non-isentropic nature of the sheared flow case for the region upstream of the shock wave.

Mahesh *et al.* studied the amplification of various statistics across the shock with acoustic turbulent field [96] and vorticity-entropy turbulence[98, 99] in the upstream region. The effects of compressibility were found to result in reduced amplification of turbulence at low Mach numbers ($M < 2$) with respect to the purely vortical case, and larger amplifications for high Mach numbers ($M > 3$). The computations were found to follow the trend of the results predicted by LIA. The combined interaction of vortical and acoustic waves with a normal shock was also discussed but no results were shown. Apart from the conventional study on the amplification of turbulence, the effect of entropy fluctuations was also covered in detail [98, 99]. The upstream vorticity-entropy correlation is shown to strongly influence the evolution of the turbulence across the shock; positive correlation has a suppressing effect and vice versa. The validity of Morkovin's hypothesis was explored in their [98, 99] study, while in the presence of entropy fluctuations along with vortical field. Morkovin's hypothesis was found to be invalid due to the oscillation of the shock wave. Comparison of LIA and numerical simulations were found to be satisfactory.

Nearly a decade later, the numerical experiments with STI were revisited by Sesterhenn *et al.* [141] in which they investigated the amplification of Reynolds stresses and vorticity variances using shock-fitting methodology. A similar work was carried out by Rawat, Wang and Zhong [121, 122, 164], again using shock-fitting approach. Their results are in agreement with earlier studies carried out using shock-resolved and shock-capturing simulations. It is to be noted that the major purpose of these studies were to establish efficient numerical schemes to predict shock-dominated flows rather than to study the STI problem. Grube *et al.* [43, 44] studied the interaction of forced isotropic turbulence interacting with a normal shock and reported on the amplification of various turbulence quantities across the shock. They considered shock strengths of $M = 3.5$ to 5 in their simulations with turbulent Mach numbers as high as $M_t = 0.85$, and extensively studied the budget of terms in the transport equations of Reynolds stress and vorticity variances.

Larsson *et al.* [81, 83] carried out high-fidelity numerical simulations of the canonical STI problem. One of the discrepancies in the earlier simulations was the inadequate resolution in the grids considered, which led to incorrect amplification of vorticity variances, especially the streamwise component. They showed with extensive grid convergence tests that their simulations were well-resolved to predict the amplification of Reynolds stresses and the reduction in various lengthscales. They investigated the shock distortion due to turbulence and identified broken regimes in the shock for very high turbulence intensities. They provided a criterion which is used to identify the interaction regimes. Donzis [26, 27] independently arrived with the same criterion but using theoretical and similarity arguments. The highest *Re* based on Taylor lengthscale of 75 was investigated using numerical simulations for the STI problem by them. The methodology provided in their work is followed in our work.

Livescu and Ryu [90, 132] studied the turbulence structures in the post-shock region using shock-resolved numerical simulations. They used LIA extensively to verify their simulations. They used LIA post-shock statistics to compute post-shock spatially developing turbulence fields which mimic STI problem with high $Re_\lambda$ values in the upstream flow (approximately 200). This procedure of using LIA along with numerical simulations was proved to be cost-effective against very expensive simulations of similar order. However, the turbulent Mach number and the flow Mach number are restricted to low values in their study. The analysis of small scale turbulence structures and their dynamics rigorously proved the axisymmetric nature of the shocked turbulence.

Recently, Tian *et al.* [159] and Boukharfane *et al.* [13] studied the canonical STI problem independently with the objective of investigating the dynamics of a scalar field in the post-shock region. Their simulations are of the shock-capturing framework. Tian *et al.* [159] explored the velocity and the thermodynamic field generated by both a single-fluid and multi-fluid turbulence interacting with a normal shock. They reported that the TKE amplification was larger in a single-fluid case compared to the multi-fluid case whereas, the vorticity amplification was found to be larger in the multi-fluid case. For the range of turbulent Mach numbers and the Taylor lengthscale Reynolds number considered in their work, the modification of scalar statistics is found to be similar for both the single- and multi-fluid cases. They have also carried out extensive grid convergence tests and showed that the grid spacing in the shock-normal direction should be less than or equal to 1.4 times of the Kolmogorov lengthscale to obtain accurate results. Boukharfane *et al.* [13] explored the turbulence structures in the shocked turbulence similar to the works of Livescu and Ryu [90, 132] but for an upstream turbulence field containing an active scalar field. They quantified the changes induced due to the shock on the scalar field by separately performing spatially developing turbulence fields without a shock wave. Another recent numerical work on canonical STI is by Tanaka *et al.* [154], where they studied the modulation of pressure fluctuations for very low $M_t$ compressible turbulence interacting with a normal shock in the shock-capturing framework. They found qualitative agreements with the experiments of Inokuma *et al.* [61], which adds to the validity of shock-captured numerical simulations.

At the time of writing this dissertation, the latest articles on canonical STI were by Braun *et al.* [15], and Chen and Donzis [18]. Braun *et al.* [15] where they performed large eddy simulations (LES) of the canonical shock-turbulence interaction using a hybrid stretched-vortex model as the subgrid scale model (SGS) for the regions away from the shock. The SGS model was not used at the shock for reasons of excessive dissipation, and only the weighted essentially non-oscillatory (WENO) numerical scheme was applied at the shock but with a modified adaptive mesh refinement (AMR) procedure to ensure that the SGS kinetic energy is correct. They investigated the anisotropy in Reynolds stresses primarily, which was later used along with the LIA theory to develop a model for the same in [14], which would account for the shock-corrugation effects in Reynolds averaged Navier-Stokes simulations (RANS) of canonical STI. They also investigated spatial evolution of turbulence by LES with LIA generated post-shock fields similar to the procedure followed in [90]. One of their interesting findings is that the amplification in Reynolds stresses across the shock become independent of the Taylor-scale based Reynolds number when the upstream turbulence shows inertial range scaling, which was observed in their cases with $Re_\lambda > 100$. This is in agreement with the experiments of Kitamura *et al.* [77], where they also observed no discernible difference in the rms values of velocity fluctuations for $Re_\lambda > 100$. They have also discussed on the post-shock density fluctuations and on the turbulent mass flux, which is in agreement with the predictions of LIA.

Chen and Donzis [18] investigated the effects of forced turbulence interacting with a normal shock using shock-resolved simulations for a range of mean flow Mach numbers

($M$ = 1.07 − 1.4), turbulent Mach numbers ($M_t$ = 0.02 − 0.54) and Taylor-scale Reynolds numbers ($Re_\lambda$ = 4 − 65). They investigated the instantaneous jumps in thermodynamic variables and also the structure of the shock wave using the Quasi-Equilibrium (QE) theory of Donzis [26, 27]. According to the QE theory, the shock responds instantaneously to the local changes due to the presence of turbulent fluctuations in the upstream conditions. They found that the flow becomes subsonic locally, when the upstream turbulent fluctuations are strong enough. They have proposed functional forms for the statistical moments of thermodynamic variables using the QE theory and Gaussian probability density functions (PDFs). The moments predicted by the theory were found to match with the available DNS data. In addition, the effect of turbulence on the structure of the shock wave was quantified using the theory and DNS data. The criterion for 'wrinkled', 'broken' and 'vanished' were provided. New universal scaling laws were proposed for the amplification factors, which was found to collapse the available data and established the applicability of theoretical limits.

## 2.4 Summary

The majority of the earlier works reported above have focused on velocity fluctuations and its related statistics with limited and sparse data on thermodynamic fluctuations. The thermodynamic field investigated in these works were also limited to weak shock strengths and very low turbulence intensities. We attempt to close this gap as a part of this work by studying the thermodynamic field for shock strengths and turbulence intensities, which are relatively higher compared to these studies.

# Chapter 3

# Linear interaction analysis

A brief description of the LIA methodology used in the study is provided in this chapter. We consider the case of a 'quasi-vortical' turbulence interacting with a normal shock in this study, i.e., turbulence with mostly solenoidal energy. The fluid medium is a calorically perfect gas with $\gamma = 1.4$. The formulations developed by Mahesh *et al.* [99] for the case of vorticity waves interacting with a normal shock wave are reproduced here for completeness. The reader is referred to Refs. [35, 41, 99, 119] for additional details and for cases involving acoustic/entropy fluctuations.

## 3.1 Interaction of vorticity wave with normal shock

Turbulent flows can be decomposed as a linear combination of acoustic, vorticity and entropy modes under certain conditions [78]. The entropy mode, which is convected by the mean flow, is observed in the density and the temperature fluctuations only. The vorticity mode is only present in the solenoidal component of the velocity fluctuations, and is also carried by the mean flow. The acoustic mode travels at the speed of sound relative to the mean flow, and is found in pressure, isentropic temperature and density, and irrotational velocity fluctuations. According to the analysis of Ribner [123] and Moore [108], these modes evolve independently in the uniform mean flow behind the shock. The independent evolution of these modes in the inviscid limit implies that the fluctuating velocity field is a linear combination of the acoustic and the vortical modes. The density and the temperature fluctuations are combinations of the acoustic and the entropy modes. The pressure field is associated solely to the acoustic mode.

We consider a two-dimensional (2D) planar vorticity wave of amplitude, $A_v$, wavenumber of magnitude, $|\mathbf{k}|$ and orientation, $\psi$ with respect to the streamwise direction. The wave is being carried by an inviscid and uniform mean flow with velocity, $\overline{u}_1$

towards a normal shock, whose normal direction is aligned with the streamwise direction. A simple schematic of the single wave interaction is shown in Fig. (3.1).

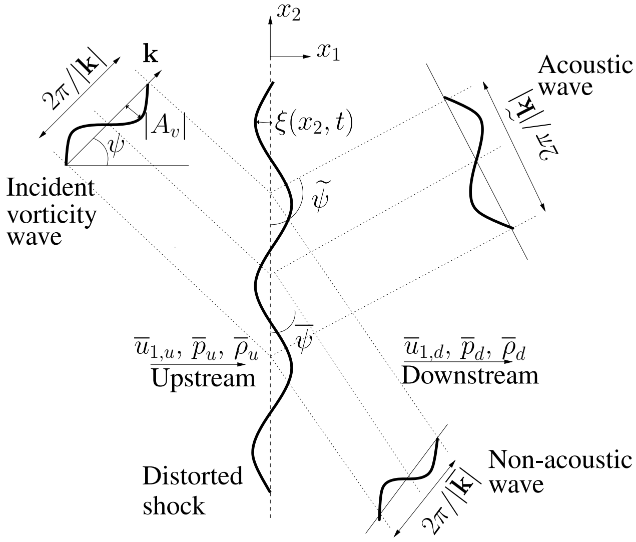


Figure 3.1: A schematic of a single vorticity wave interacting with a normal shock (in 2D) and yielding three types of Kovásznay's linear waves. Flow is from left to right

### 3.1.1 Linearized equations

The governing equations for the interaction are the 2D Euler equations,

$$\frac{\partial \rho}{\partial t} + u_1 \frac{\partial \rho}{\partial x_1} + u_2 \frac{\partial \rho}{\partial x_2} = -\rho \left( \frac{\partial u_1}{\partial x_1} + \frac{\partial u_2}{\partial x_2} \right), \tag{3.1a}$$

$$\frac{\partial u_1}{\partial t} + u_1 \frac{\partial u_1}{\partial x_1} + u_2 \frac{\partial u_1}{\partial x_2} = -\frac{1}{\rho} \frac{\partial p}{\partial x_1}, \tag{3.1b}$$

$$\frac{\partial u_2}{\partial t} + u_1 \frac{\partial u_2}{\partial x_1} + u_2 \frac{\partial u_2}{\partial x_2} = -\frac{1}{\rho} \frac{\partial p}{\partial x_2}, \tag{3.1c}$$

$$\frac{\partial s}{\partial t} + u_1 \frac{\partial s}{\partial x_1} + u_2 \frac{\partial s}{\partial x_2} = 0, \tag{3.1d}$$

which are linearized about a uniform mean flow ($\partial \overline{f}/\partial x_i = 0$) with finite mean velocity in the streamwise direction only ($\overline{u}_2 = \overline{u}_3 = 0$),

$$\frac{\partial \rho'}{\partial t} + \overline{u}_1 \frac{\partial \rho'}{\partial x_1} = -\overline{\rho} \frac{\partial u_1'}{\partial x_1}, \tag{3.2a}$$

$$\frac{\partial u_1'}{\partial t} + \overline{u}_1 \frac{\partial u_1'}{\partial x_1} = -\frac{1}{\overline{\rho}} \frac{\partial p'}{\partial x_1}, \tag{3.2b}$$

$$\frac{\partial u_2'}{\partial t} + \overline{u}_1 \frac{\partial u_2'}{\partial x_1} = -\frac{1}{\overline{\rho}} \frac{\partial p'}{\partial x_2}, \tag{3.2c}$$

$$\frac{\partial s'}{\partial t} + \overline{u}_1 \frac{\partial s'}{\partial x_1} = 0, \tag{3.2d}$$

where, the total energy term, $E_0 = \dfrac{p}{\rho\,(\gamma-1)} + \dfrac{(u_1^2+u_2^2)}{2}$ has been written in terms of the entropy, $s$. Entropy is given by the Gibb's equation as,

$$T\,ds = de + p\,d\left(\frac{1}{\rho}\right), \tag{3.3}$$

where $d$ represents the ordinary differential operator and $e = c_v T$ is the internal energy with $c_v$ being the gas specific heat capacity at constant volume. Reynolds decomposition is followed in the entire analysis, where the quantity, $f$ is decomposed into its mean component, $\overline{f}$ and the fluctuating component, $f'$.

In addition to the governing equations, relations for the linearized entropy and the linearized equation of state are required to make the system complete. The additional relations are,

$$\frac{s'}{c_p} = \frac{p'}{\gamma\overline{p}} - \frac{\rho'}{\overline{\rho}}, \tag{3.4a}$$

$$\frac{p'}{\overline{p}} = \frac{\rho'}{\overline{\rho}} + \frac{T'}{\overline{T}}, \tag{3.4b}$$

where the variables $c_v$ and $c_p$ are gas specific heat capacities at constant volume and constant pressure, respectively. The governing equations and the auxiliary relations are to be solved along with the boundary conditions at the shock to obtain the downstream flowfield.

### 3.1.2 Boundary conditions at the shock

The frame of reference is fixed to the stationary planar normal shock wave with coordinates $x_1$, $x_2$, and $x_3$. The corresponding velocities for these directions are denoted as $u_1$, $u_2$ and $u_3$. Though we started this analysis in 2D, we retain the spanwise velocity, $u_3$ to describe the problem in a generic sense. Subscript $u$ refers to values upstream of shock and $d$ represents downstream of the shock. The density, velocity in three directions, temperature and pressure fluctuations are represented by $\rho'$, $u_1'$, $u_2'$, $u_3'$, $T'$ and $p'$ respectively.

The upstream mean flow is one dimensional and steady ($\overline{u}_{1,u} \neq 0$, $\overline{u}_{2,u} = \overline{u}_{3,u} = 0$). The upstream turbulence is obtained as a linear superposition of Fourier modes comprising of only vortical fluctuations. Each of the vortical waves in the upstream turbulent field is characterized by the parameters, $(A_v, |\mathbf{k}|, \psi)$ as mentioned above. The frequency of each wave is given by $\Omega = |\mathbf{k}|\,\cos(\psi)\,\overline{u}_{1,u}$, which is due to the wave being carried by the upstream mean flow, and does not possess its own wave/phase velocity like the acoustic waves. The waves in the incident field upstream of the shock wave have the following form:

$$\frac{u'_{1,u}}{\overline{u}_{1,u}} = l\,A_v\,e^{i\,|\mathbf{k}|\,\left(m\,x_1 + l\,x_2 - \overline{u}_{1,u}\,m\,t\right)}, \tag{3.5a}$$

$$\frac{u'_{2,u}}{\overline{u}_{1,u}} = -m\,A_v\,e^{i\,|\mathbf{k}|\,\left(m\,x_1 + l\,x_2 - \overline{u}_{1,u}\,m\,t\right)}, \tag{3.5b}$$

where $m = \cos(\psi)$ and $l = \sin(\psi)$. In the case of purely vortical turbulent field, the upstream thermodynamic fluctuations are set to zero, $p'_u = T'_u = \rho'_u = 0$.

Upon interaction with the turbulent flow field, the normal shock is distorted from its mean position ($x_1 = 0$) by a distance $\xi(x_2, x_3, t)$ and at a shock-front speed of $\xi_t(x_2, x_3)$. The linearized Rankine-Hugoniot conditions are the boundary conditions at the shock, and should be applied at the instantaneous position of the shock. Consider a coordinate system, $(\hat{x}_1, \hat{x}_2)$ for the 2D interaction at the instantaneous shock front as shown in Fig. (3.2), such that the reference frame is stationary with respect to the shock front.

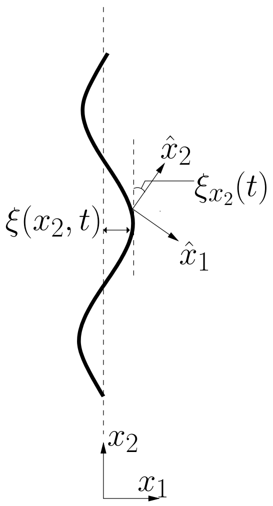


Figure 3.2: A schematic the distorted shock front showing the instantaneous frame of reference attached to the unsteady shock wave

For small shock distortions, the instantaneous reference frame is related to the inertial frame of reference as,

$$\hat{x}_1 = x_1 - \xi - x_2\,\xi_{x_2}, \tag{3.6a}$$

$$\hat{x}_2 = x_2 + x_1\,\xi_{x_2}, \tag{3.6b}$$

where $\xi_{x_2}$ [1] is the slope of the shock front in the $(x_1, x_2)$ plane. The corresponding instantaneous velocity components $(\hat{u}_1, \hat{u}_2)$ are given by,

$$\hat{u}_1 = u_1 - \xi_t - u_2\,\xi_{x_2} \approx \overline{u}_1 + u_1' - \xi_t, \tag{3.7a}$$

$$\hat{u}_2 = u_2 + u_1\,\xi_{x_2} \approx u_2' + \overline{u}_1\,\xi_{x_2}, \tag{3.7b}$$

where $\xi_t$ is the shock-distortion speed.

The analysis involves solution to the boundary value problem for the shock displacement, and the flow field behind the shock wave is given by the linearized RH relations,

$$\frac{u'_{1,d} - \xi_t}{\overline{u}_{1,u}} = \underbrace{\left[\frac{(\gamma-1)M_u^2 - 2}{(\gamma+1)M_u^2}\right]}_{B_1}\left(\frac{u'_{1,u} - \xi_t}{\overline{u}_{1,u}}\right), \tag{3.8a}$$

$$\frac{\rho'_d}{\overline{\rho}_d} = \underbrace{\left[\frac{4}{(\gamma-1)M_u^2 + 2}\right]}_{C_1}\left(\frac{u'_{1,u} - \xi_t}{\overline{u}_{1,u}}\right), \tag{3.8b}$$

$$\frac{p'_d}{\overline{p}_d} = \underbrace{\left[\frac{4\gamma M_u^2}{2\gamma M_u^2 - (\gamma-1)}\right]}_{C_1}\left(\frac{u'_{1,u} - \xi_t}{\overline{u}_{1,u}}\right), \tag{3.8c}$$

$$\frac{u'_{2,d}}{\overline{u}_{1,u}} = \frac{u'_{2,u}}{\overline{u}_{1,u}} + \underbrace{\left[\frac{2(M_u^2 - 1)}{(\gamma+1)M_u^2}\right]}_{E_1}\xi_{x_2}, \tag{3.8d}$$

where, Eq. (3.8a) is obtained from the Prandtl relation, $u_u u_d = a^{*2}$ with $a^*$ being the sound speed corresponding to the characteristic Mach number, $M^*$ (see Ref. [5]). Equations (3.8b) and (3.8c) are obtained from the linearized RH relations for mass and enthalpy conservation, respectively. Equation (3.8d) corresponds to the conservation of tangential velocity across a normal shock wave.

The boundary conditions given in Eqs. (3.8a) - (3.8d) are used to obtain the amplitude of the vorticity, entropy and acoustic modes downstream of the shock. Their corresponding waveforms are obtained as shown in the following section.

### 3.1.3 Downstream wave forms and regimes

The downstream solutions are obtained as a linear superposition of all the modes generated / refracted downstream of the shock [108, 123] for each incident wave. The downstream solutions are functions of the incidence angle of the incident wave, $\psi$, ratio of specific heats, $\gamma$ and the Mach number, $M$ of the shock wave. The downstream pressure

[1] For small angles of inclination, $\tan(\theta) \approx \theta$ and $\sin(\theta) \approx \theta$, with $\theta$ being the angle of inclination

field can be either propagating planar waves or exponentially decaying waves depending on the incidence angle. The angle which demarcates the propagating field and the decaying field is termed as the critical angle of incidence, $\psi_c$. The downstream vorticity and the entropy waves are planar stationary waves carried by the uniform mean flow for all incidence angles.

Firstly, we obtain the waveform for the pressure fluctuations generated downstream of the shock. The pressure fluctuations behind the shock must satisfy the acoustic-wave equation,

$$\frac{\partial^2 p'_d}{\partial t\,\partial t} + 2\overline{u}_d \frac{\partial^2 p'_d}{\partial x_1\,\partial t} - \left(\overline{a}_d^2 - \overline{u}_d^2\right) \frac{\partial^2 p'_d}{\partial x_1\,\partial x_1} - \overline{a}_d^2 \frac{\partial^2 p'_d}{\partial x_2\,\partial x_2} = 0, \tag{3.9}$$

where $p'_d$ is the downstream pressure fluctuation with $\overline{u}_{1,d}$ and $\overline{a}_d$ being the downstream mean flow velocity and speed of sound, respectively.

Considering the downstream pressure fluctuations to be in the form of planar waves,

$$p'_d \sim e^{i\,\tilde{\mathbf{k}}\,x_1}\, e^{i\,|\mathbf{k}|\left(l\,x_2 - m\,\overline{u}_{1,u}\,t\right)}, \tag{3.10}$$

and substituting in Eq. (3.9) yields a quadratic equation for the streamwise acoustic wavenumber, $\tilde{\mathbf{k}}$ in the region downstream of the shock as,

$$\left[\frac{\overline{a}_d^2}{\overline{u}_{1,u}^2} - \frac{\overline{u}_{1,d}^2}{\overline{u}_{1,u}^2}\right] \tilde{\mathbf{k}}^2 + 2\,|\mathbf{k}|\,m \frac{\overline{u}_{1,d}}{\overline{u}_{1,u}}\, \tilde{\mathbf{k}} - \left[m^2 - l^2\, \frac{\overline{a}_d^2}{\overline{u}_{1,u}^2}\right] |\mathbf{k}|^2 = 0, \tag{3.11}$$

where one of its roots is,

$$\frac{\tilde{\mathbf{k}}}{|\mathbf{k}|} = \frac{-2\,m\,\frac{\overline{u}_{1,d}}{\overline{u}_{1,u}} + 2\,l\,\frac{\overline{a}_d}{\overline{u}_{1,u}} \sqrt{\frac{m^2}{l^2} - \left(\frac{\overline{a}_d^2}{\overline{u}_{1,u}^2} - \frac{\overline{u}_{1,d}^2}{\overline{u}_{1,u}^2}\right)}}{2\left(\frac{\overline{a}_d^2}{\overline{u}_{1,u}^2} - \frac{\overline{u}_{1,d}^2}{\overline{u}_{1,u}^2}\right)}, \tag{3.12}$$

and the other root is rejected because it leads to an unphysical solution that increases exponentially behind the shock.

The critical angle which determines whether the acoustic wavenumber is real (propagating field) or complex (decaying field) is given by,

$$\psi_c = \cot^{-1}\left(\sqrt{\left(\frac{\overline{a}_d^2}{\overline{u}_{1,u}^2} - \frac{\overline{u}_{1,d}^2}{\overline{u}_{1,u}^2}\right)}\right), \tag{3.13}$$

and is a function of the Mach number only. For incident angles, $\psi > \psi_c$, the $\tilde{\mathbf{k}}$ becomes a complex quantity and the pressure fluctuations decay exponentially behind the shock (termed as the decaying regime). The other regime, where $\psi < \psi_c$, is called as the propagating regime and there is no attenuation of pressure fluctuations in this regime.

The vorticity and entropy fluctuations downstream of the shock are both convected by the mean flow. These fluctuations should be of the same form to satisfy continuity continuity across the shock. They follow the dispersion relation [105, 170],

$$\Omega = \overline{u}_{1,u}\,|\mathbf{k}|\,m = \overline{u}_{1,d}\,\bar{\mathbf{k}}, \quad \bar{\mathbf{k}} = |\mathbf{k}|\,m\,\frac{\overline{u}_{1,u}}{\overline{u}_{1,d}} = |\mathbf{k}|\,m\,r_\rho, \tag{3.14}$$

where $\bar{\mathbf{k}}$ is the downstream wave number for the vorticity as well as the entropy wave forms and $r_\rho = \overline{\rho}_d/\overline{\rho}_u = \overline{u}_{1,u}/\overline{u}_{1,d}$ is the density ratio across the shock wave. Note that across the normal shock, the transverse component of the wavenumber remains constant and the temporal frequency ($\Omega$) is kept constant, allowing only the streamwise component of the wavenumber to change across the shock.

The waveform for the vorticity and the entropy modes in the downstream region of the shock is given by,

$$e^{i\,\bar{\mathbf{k}}\,x_1}\,e^{i\,|\mathbf{k}|\,(l\,x_2 - m\,\overline{u}_{1,u}\,t)}, \tag{3.15}$$

and the waveform for the acoustic mode is,

$$e^{i\,(\tilde{\mathbf{k}}_r + i\,\tilde{\mathbf{k}}_i)\,x_1}\,e^{i\,|\mathbf{k}|\,(l\,x_2 - m\,\overline{u}_{1,u}\,t)} \tag{3.16}$$

As mentioned earlier, we define the fluctuations of density, pressure, temperature and velocity as a linear combination of the acoustic, vorticity and entropy modes with their corresponding amplitudes and the waveforms given in Eqs. (3.15) and (3.16).

### 3.1.4 Solutions across the shock

The expressions for the velocity and the thermodynamic fluctuations downstream of the shock as a linear combination of the Kovásznay modes are given below,

$$\frac{1}{A_v}\,\frac{u'_{1,d}}{\overline{u}_u} = \left(F_c\,e^{i\,\tilde{\mathbf{k}}\,x} + G_c\,e^{i\,\bar{\mathbf{k}}\,x}\right)\,e^{i\,|\mathbf{k}|\,(l\,y - m\,\overline{u}_u\,t)}, \tag{3.17a}$$

$$\frac{1}{A_v}\,\frac{u'_{2,d}}{\overline{u}_u} = \left(H_c\,e^{i\,\tilde{\mathbf{k}}\,x} + I_c\,e^{i\,\bar{\mathbf{k}}\,x}\right)\,e^{i\,|\mathbf{k}|\,(l\,y - m\,\overline{u}_u\,t)}, \tag{3.17b}$$

$$\frac{1}{A_v}\,\frac{p'_d}{\overline{p}_d} = K_c\,e^{i\,\tilde{\mathbf{k}}\,x}\,e^{i\,|\mathbf{k}|\,(l\,y - m\,\overline{u}_u\,t)}, \tag{3.17c}$$

$$\frac{1}{A_v}\,\frac{\rho'_d}{\overline{\rho}_d} = \left(\frac{K_c}{\gamma}\,e^{i\,\tilde{\mathbf{k}}\,x} + Q_c\,e^{i\,\bar{\mathbf{k}}\,x}\right)\,e^{i\,|\mathbf{k}|\,(l\,y - m\,\overline{u}_u\,t)}, \tag{3.17d}$$

$$\frac{1}{A_v}\,\frac{T'_d}{\overline{T}_d} = \left(\left(\frac{\gamma - 1}{\gamma}\right)K_c\,e^{i\,\tilde{\mathbf{k}}\,x} - Q_c\,e^{i\,\bar{\mathbf{k}}\,x}\right)\,e^{i\,|\mathbf{k}|\,(l\,y - m\,\overline{u}_u\,t)}, \tag{3.17e}$$

where the coefficients $F_c$, $G_c$, $H_c$, $I_c$, $K_c$ and $Q_c$ are the complex transfer coefficients normalized by the amplitude of the wave, $A_v$. Here, $F_c$, $H_c$ and $K_c$ are the coefficients associated with the acoustic component, $G_c$ and $I_c$ are for the vortical components and $Q_c$

is for the entropy component. The coefficients are functions of the upstream Mach number, $M_u$, the angle of incidence, $\psi$, and the wave amplitude $A_v$. The boundary conditions across the shock give the following expressions for the velocity and slope of the shock front,

$$\frac{1}{A_v}\frac{\xi_t}{\overline{u}_u} = L_c\, e^{i|\mathbf{k}|\,(l\,y - m\,\overline{u}_u\,t)}, \tag{3.18a}$$

$$\frac{1}{A_v}\,\xi_{x_2} = -\frac{l}{m}\,L_c\, e^{i\,|\mathbf{k}|\,(l\,y - m\,\overline{u}_u\,t)}, \tag{3.18b}$$

where $L_c$ is the normalized transfer coefficient associated with the shock-corrugation due to upstream fluctuations. Here, we have considered that the shock-corrugation velocity to be of the same form as the incident wave where the real part is the component in-phase with the incident wave and the imaginary part is the out-of-phase component with the incident wave.

The expressions for the complex transfer coefficients are obtained by substituting Eqs. (3.17a) - (3.18b) in the linearized Euler equations for the region behind the shock and by appropriate usage of the linearized boundary conditions at the shock front. Substituting the downstream solution for the velocity components in the linearized Euler equations and equating only the acoustic components yields the following relation,

$$F_c = \alpha\, K_c, \tag{3.19a}$$

$$H_c = \beta\, K_c, \tag{3.19b}$$

where we have introduced complex variables $\alpha$ and $\beta$ to relate the potential velocity field and the acoustic field. The complex variables are defined as,

$$\alpha = \frac{\overline{a}_d^2}{\gamma\,\overline{u}_u^2}\,\frac{\frac{\tilde{\mathbf{k}}}{|\mathbf{k}|}}{m - \frac{\tilde{\mathbf{k}}}{|\mathbf{k}|\,r}}, \tag{3.19c}$$

$$\beta = \frac{\overline{a}_d^2}{\gamma\,\overline{u}_u^2}\,\frac{l}{m - \frac{\tilde{\mathbf{k}}}{|\mathbf{k}|\,r}}, \tag{3.19d}$$

where the incident wave orientation changes the variables from real to complex numbers via the acoustic wavenumber, $\tilde{\mathbf{k}}$. The irrotational component of the velocity field is thus described now. By definition, the solenoidal component of the velocity field should satisfy the incompressible continuity equation, $\nabla.\vec{V} = 0$. Substituting the vortical components of the velocity field in the incompressible continuity equation results in,

$$I_c = -\frac{m\,r}{l}\,G_c, \tag{3.19e}$$

which completes the relations for the velocity field. The linearized boundary conditions at the shock front, Eqs. (3.8a) - (3.8d), relates the complex transfer coefficients as follows,

$$F_c + G_c - L_c = B_1\,(l - L_c), \tag{3.19f}$$

$$\frac{K_c}{\gamma} + Q_c = C_1\,(l - L_c), \tag{3.19g}$$

$$K_c = D_1\,(l - L_c), \tag{3.19h}$$

$$H_c + I_c = -m - E_1\,\frac{l}{m}\,L_c, \tag{3.19i}$$

which gives us seven equations for the seven transfer coefficients.

The complete equations for the complex transfer coefficients are as follows,

$$L_c = \frac{-m - \beta\,D_1\,l + \frac{m\,r}{l}\,[-\alpha\,D_1\,l + B_1\,l]}{E_1\,\frac{l}{m} - \beta\,D_1 - \frac{m\,r}{l}\,(1 - B_1 + \alpha\,D_1)}, \tag{3.20a}$$

$$K_c = -D_1\,(l - L_c), \tag{3.20b}$$

$$F_c = \alpha\,D_1\,(l - L_c) \tag{3.20c}$$

$$H_c = \beta\,D_1\,(l - L_c) \tag{3.20d}$$

$$G_c = L_c\,(1 - B_1 + \alpha\,D_1) - \alpha\,D_1\,l + B_1\,l, \tag{3.20e}$$

$$I_c = -\frac{m\,r}{l}\,(1 - B_1 + \alpha\,D_1)\,L_c - \frac{m\,r}{l}\,[-\alpha\,D_1\,l + B_1\,l]\,, \tag{3.20f}$$

$$Q_c = C_1\,(l - L_c) - \frac{K_c}{\gamma} \tag{3.20g}$$

where once the coefficient $L_c$ is known, the other coefficients can be obtained easily, completing the solutions for the 2D wave interaction problem.

## 3.2 Interaction of turbulence with normal shock

The turbulent field upstream of the shock is considered to be isotropic. The incident turbulent field is represented as a superposition of planar 2D waves and each of these waves interact independently with the shock wave in the linear analysis framework. Integration over all the waves behind the shock wave provides the turbulence statistics behind the shock. The three-dimensional problem is related to the 2D analysis by considering that the incident 2D wave lies in the plane, $x_1 - e_r$, and makes an angle of $\psi$ with the $x_1$ axis as shown in Fig. (3.3).

The solenoidal nature of the incident velocity field imposes that the velocity vector should be normal to the wavenumber vector and thus the velocity vector has a parallel component (which is normal to the wavenumber vector) in the $x_1 - e_r$ plane and a perpendicular component in the $\phi$ direction (normal to the $x_1 - e_r$ plane). The component

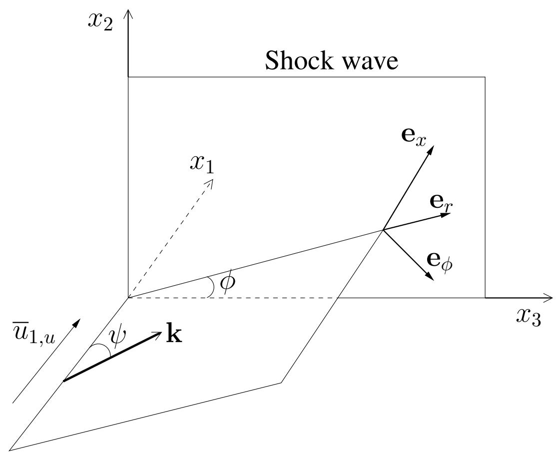


Figure 3.3: Coordinate system used in the 3D analysis of the interaction of isotropic turbulence with a steady shock wave

aligned with the $\phi$ direction will pass unchanged through the normal shock as tangential components of velocity across the shock are unchanged. With respect to this new frame of reference, the velocity field is given as,

$$u_1' = u_1', \tag{3.21a}$$

$$u_2' = u_r' \cos(\phi) - u_\phi' \sin(\phi), \tag{3.21b}$$

$$u_3' = u_r' \sin(\phi) + u_\phi' \cos(\phi), \tag{3.21c}$$

where $u_r'$ and $u_\phi'$ are the velocity components aligned with $e_r$ and $e_\phi$ directions respectively. This holds true for both the upstream and the downstream regions. The upstream velocity components in the new reference frame are related to the 2D analysis as,

$$\frac{u_{1,u}'}{\overline{u}_{1,u}} = l\, A_v\, e^{i\,|\mathbf{k}|\,\left(m\,x_1 + l\,\vec{r} - \overline{u}_{1,u}\,m\,t\right)}, \tag{3.22a}$$

$$\frac{u_{r,u}'}{\overline{u}_{1,u}} = -m\, A_v\, e^{i\,|\mathbf{k}|\,\left(m\,x_1 + l\,\vec{r} - \overline{u}_{1,u}\,m\,t\right)}, \tag{3.22b}$$

$$\frac{u_{\phi,u}'}{\overline{u}_{1,u}} = A_v\, e^{i\,|\mathbf{k}|\,\left(m\,x_1 + l\,\vec{r} - \overline{u}_{1,u}\,m\,t\right)}, \tag{3.22c}$$

where $\vec{r} = x_2\, \cos(\phi) + x_3\, \sin(\phi)$ is the vector related to the transverse component of the wavenumber in the new reference frame. Here, $u_{\phi,u}'$ is the shock-parallel component of velocity which remains unchanged across the shock wave. This definition of the velocity field ensures that the integration of the energy spectrum in the the upstream region over all the wavenumbers is equal to the turbulent kinetic energy of the incident turbulence.

The corresponding components of velocity downstream of the shock are given by,

$$\frac{u'_{1,d}}{\overline{u}_{1,u}} = \left(F\, e^{i\,\tilde{\mathbf{k}}\,x} + G\, e^{i\,\bar{\mathbf{k}}\,x}\right) A_v\, e^{i\,|\mathbf{k}|\,(l\,\vec{r}-m\,\overline{u}_u\,t)}, \tag{3.23a}$$

$$\frac{u'_{r,d}}{\overline{u}_{1,u}} = \left(H\, e^{i\,\tilde{\mathbf{k}}\,x} + I\, e^{i\,\bar{\mathbf{k}}\,x}\right) A_v\, e^{i\,|\mathbf{k}|\,(l\,\vec{r}-m\,\overline{u}_u\,t)}, \tag{3.23b}$$

$$\frac{u'_{\phi,d}}{\overline{u}_{1,u}} = A_v\, e^{i\,\bar{\mathbf{k}}\,x}\, e^{i\,|\mathbf{k}|\,(l\,\vec{r}-m\,\overline{u}_u\,t)}, \tag{3.23c}$$

where $u'_{\phi,d}$ component retains the amplitude but undergoes compression in streamwise wavenumber to ensure that the temporal frequency and the transverse component of the wavenumber remains the same.

Consider the integration of the statistic, $\overline{u'^2_{1,d}}$ to obtain the Reynolds stress in the streamwise direction behind the shock, which according to Ref. [99] is given by,

$$\frac{\overline{u'^2_{1,d}}}{\overline{u}^2_{1,u}} = \int_{|\mathbf{k}|=0}^{\infty} \int_{\psi=-\pi/2}^{\pi/2} \int_{\phi=0}^{2\pi} E_{11}\, d\mathcal{V}_k, \tag{3.24}$$

with the elemental volume of integration in the wavenumber space given by,

$$d\mathcal{V}_k = |\mathbf{k}|^2\ \sin(\psi)\, d\psi\, d|\mathbf{k}|\, d\phi, \tag{3.25}$$

and the function, $E_{11,d} \sim \overline{u'^2_{1,d}}$ [2] is related to the 2D analysis as,

$$E_{11,d} = \left(\frac{\overline{u'^2_{1,d}}}{\overline{u}^2_{1,u}}\right)_{2D} = \left[|F_c|^2\, e^{i\,(\tilde{\mathbf{k}}-\tilde{\mathbf{k}}^*)\,x_1} + F_c^*\, G_c\, e^{-i\,(\tilde{\mathbf{k}}^*-\bar{\mathbf{k}})\,x_1} + F_c\, G_c^*\, e^{i\,(\tilde{\mathbf{k}}-\bar{\mathbf{k}})\,x_1} + |G_c|^2\right] |A_v|^2, \tag{3.26}$$

where $|A_v|^2 = A_v\, A_v^*$ and $\tilde{\mathbf{k}}^*$ is the complex conjugate of $\tilde{\mathbf{k}}$.

The upstream streamwise kinetic energy is related to the wave amplitudes as,

$$|A_v|^2 = \frac{E_{11,u}}{l^2} \tag{3.27}$$

where $E_{11,u} \sim \overline{u'^2_{1,u}}$. The incident turbulence is isotropic and thus the upstream energy spectrum is given by,

$$E_{ij} = \frac{E(k)}{4\,\pi\,|\mathbf{k}|^2} \left(\delta_{ij} - \frac{|\mathbf{k}|_i\, |\mathbf{k}|_j}{|\mathbf{k}|^2}\right), \tag{3.28}$$

where $E(k)$ is the three dimensional energy spectrum. The upstream energy spectrum $E(k)$ is specified according to the form of von Kármán spectrum [80],

$$E(k) \sim \frac{1}{k_0} \frac{\left(\frac{|\mathbf{k}|}{k_0}\right)^2}{\left[\left(\frac{|\mathbf{k}|}{k_0}\right)^2 + \frac{5}{6}\right]^{\frac{11}{6}}}, \tag{3.29}$$

[2] Note that $\overline{f'^2} = \overline{f'\, f'^*}$ with $f'^*$ being the complex conjugate of $f'$

where the peak energy wavenumber $k_0$ is set at 4.

The wavenumbers in the Cartesian coordinates are given by,

$$|\mathbf{k}|_1 = |\mathbf{k}|\,\cos(\psi), \tag{3.30a}$$

$$|\mathbf{k}|_2 = |\mathbf{k}|\,\sin(\psi)\,\cos(\phi), \tag{3.30b}$$

$$|\mathbf{k}|_3 = |\mathbf{k}|\,\sin(\psi)\,\sin(\phi), \tag{3.30c}$$

and using the above relations in Eq. (3.27) yields,

$$|A_v|^2 = \frac{E(k)}{4\,\pi\,|\mathbf{k}|^2} \tag{3.31}$$

The other components of the turbulent kinetic energy downstream of the shock wave ($E_{rr,d}, E_{\phi\phi,d}$) are obtained as follows,

$$E_{rr,d} = \left(\frac{\overline{u'^2_{r,d}}}{\overline{u}^2_{1,u}}\right)_{2D} = \left[|H_c|^2\, e^{i\,(\tilde{\mathbf{k}}-\tilde{\mathbf{k}}^*)\,x_1} + H_c^*\, I_c\, e^{-i\,(\tilde{\mathbf{k}}^*-\bar{\mathbf{k}})\,x_1} + H_c\, I_c^*\, e^{i\,(\tilde{\mathbf{k}}-\bar{\mathbf{k}})\,x_1} + |I_c|^2\right] |A_v|^2, \tag{3.32a}$$

$$E_{\phi\phi,d} = \left(\frac{\overline{u'^2_{\phi,d}}}{\overline{u}^2_{1,u}}\right)_{2D} = |A_v|^2 = \frac{E(k)}{4\,\pi\,|\mathbf{k}|^2}, \tag{3.32b}$$

which due to the axisymmetric nature of the turbulence behind the normal shock wave is related to the Cartesian system as,

$$E_{22,d} + E_{33,d} = E_{rr,d} + E_{\phi\phi,d}, \tag{3.33}$$

and is true in the upstream region also.

For a purely vortical turbulence upstream of the shock, the problem is symmetric about $\psi$ and the function $E_{11,d}$ is independent of $\phi$. Thus the integration in Eq. (3.22a) reduces to,

$$\frac{\overline{u'^2_{1,d}}}{\overline{u}^2_{1,u}} = 4\,\pi \int_{|\mathbf{k}|=0}^{\infty} \int_{\psi=0}^{\pi/2} E_{11,d}\,|\mathbf{k}|^2 \sin(\psi)\,d\psi\,d|\mathbf{k}| \tag{3.34}$$

where $E_{11,d}$ is given by the expression in Eq. (3.22c). Similarly, the transverse components of the Reynolds stresses can be obtained as follows,

$$\frac{\overline{u'^2_{2,d}}}{\overline{u}^2_{1,u}} = \frac{\overline{u'^2_{3,d}}}{\overline{u}^2_{1,u}} = \frac{4\,\pi}{2} \int_{|\mathbf{k}|=0}^{\infty} \int_{\psi=0}^{\pi/2} \left[E_{rr,d} + \frac{E(k)}{4\,\pi\,|\mathbf{k}|^2}\right] |\mathbf{k}|^2 \sin(\psi)\,d\psi\,d|\mathbf{k}|, \tag{3.35}$$

where $E_{rr,d}$ is given by Eq. (3.28). Similar expressions can be obtained for other statistics by making use of their respective 2D correlations. For example, the evolution of scalar quantities like pressure variance is given by,

$$\frac{\overline{p'^2_d}}{\overline{p}^2_d} = 4\,\pi \int_{|\mathbf{k}|=0}^{\infty} \int_{\psi=0}^{\pi/2} E_{pp,d}\,|\mathbf{k}|^2 \sin(\psi)\,d\psi\,d|\mathbf{k}|, \tag{3.36}$$

where $E_{pp,d} = |K_c|^2 \, e^{i(\tilde{\mathbf{k}}-\tilde{\mathbf{k}}^*)x_1} \, |A_v|^2$. Note that the exponential term in $E_{pp,d}$ vanishes for the propagating regime, where $\tilde{\mathbf{k}}^* = \tilde{\mathbf{k}}$. Statistics involving derivatives such as vorticity variances, dilatation variances, etc. require additional steps but follow the same procedure as mentioned above. The reader is referred to Ref. [99] where required expressions for vorticity and Taylor lengthscales are provided.

## 3.3 Limitations of LIA and its implications

In the previous section (3.2), we derived the expressions for second-order statistical moments ($\overline{f'^2}$) of different flowfield variables for the case of vortical turbulence interacting with a planar normal shock. Mahesh *et al.* [96, 99] and Fabre *et al.* [35] have provided ample information for obtaining the post-shock field for single waves of each type interacting with a normal shock. The procedure mentioned above can be used to obtain second-order moments for upstream fields with entropy and acoustic modes also. The limitation is that the analysis assumes that there is no interaction between the different modes in the upstream turbulence, essentially the linearity assumption. Each mode is represented as a single wave, which independently interacts with the shock. Nonetheless, we would be able to obtain reasonable approximations of the higher-order moments as long as the intensity of the upstream turbulence ($f'/\overline{f}$) remains small. "How small or high is this limit?" is still an open question, yet to be addressed.

The assumption of linearity in the analysis obviously removes the nonlinearity of the problem, which is usually seen in the turbulent diffusion terms ($\overline{u'_k u'_i u'_j}$) of the Navier-Stokes equations (in the kinetic energy equation). In the wavenumber space, the triadic interaction of the turbulent diffusion terms characterizes the energy cascade from smaller wavenumbers (energy containing range - large lengthscale structures) to the larger wavenumbers (dissipation range - small lengthscale structures). It is to be recalled that in the present analysis, the upstream turbulence is not developed from a random state, but is specified using a known turbulent energy spectrum only ($E(k)$) or to be more specific only the shape of the turbulent energy spectrum is required. In essence, we do not require the details of how the turbulent flowfield achieved its fully developed state. The post-shock field is obtained as a product of the transfer function(s) and the upstream turbulent energy spectrum, where only the shape of the spectrum is provided as an input in the analysis. Therefore, it is not even essential that the specified shape of the energy spectrum corresponds to a fully developed turbulent flowfield, but it would be more meaningful to compare with DNS data only if it is so.

The post-shock fluctuations in the flowfield predicted by LIA are used to obtain statistical moments, and not to reconstruct a turbulent flowfield. Livescu [90] and Braun *et al.* [15] used LIA to obtain only the linear fluctuations immediately behind the shock, which along with a mean field was used as an inflow condition for a spatially developing turbulent flowfield. They did not use the LIA post-shock field to construct a turbulent flowfield. Livescu [90] compared higher-order statistics obtained from this exercise (referred to as Shock-LIA) with that of the full shock-turbulence interaction problem (referred to as Shock-DNS) and found a good match with negligible error for the low $M_t$ cases. The maximum upstream turbulent Mach number in Livescu's study was 0.05 and the post-shock $M_t$ was less than 0.1 for all of the cases, i.e., the assumptions of LIA were not violated. This ascertains that the post-shock field predicted by LIA is a reasonable approximation for low $M_t$ turbulence, at least for the region immediately behind the shock.

The other major limitation of traditional LIA is that it does not consider the viscous effects. By doing so, the shock can be considered as a discontinuity across which the linearized Rankine-Hugoniot conditions are valid. In addition to neglecting the turbulent diffusion effects due to the assumption of linearity, the removal of viscous effects in the analysis results in an inviscid evolution of the turbulent flowfield behind the shock. In the absence of production mechanisms, there is no decay of the fluctuations in the spatial direction. Important features such as the return-to-isotropy and the decay of turbulent kinetic energy are not predicted by LIA solutions accurately. This implies that reconstructing a turbulent flowfield from the fluctuations predicted by LIA would not be the same as the turbulent flowfield obtained from a DNS. Though the instantaneous flowfield may not be the same, the statistical moments (of 2nd order) predicted by LIA are similar to those obtained from the DNS, except for the quantities strongly affected by viscous decay. It is to be noted that no one has compared statistics of order three or higher as well as the reconstructed instantaneous post-shock turbulent field directly from LIA with the DNS data. In this study also, we do not compute moments of order greater than two from LIA.

The conventional LIA followed in this study assumes uniform mean flow ($\partial\overline{f}/\partial x_i = 0$), which restricts the class of problems that can be analyzed. This also limits any accurate reproduction of the post-shock turbulent flowfield, essentially for problems, which have mean shear. Production of turbulence due to mean shear is one of the major production mechanisms in boundary layers, and thus conventional LIA finds only limited applicability in such class of problems (those with mean gradients). For shock-turbulence interaction studies with a mean shear, RDT is preferred as the primary choice of a linear theoretical analysis [76]. The conventional LIA can be extended to include viscous effects (see Ref. [106]) and a preliminary framework for the same is described in Appendix (A). LIA with viscous effects has not been widely used by many due to the rather cumbersome procedure, which includes complexities such as solving for a nonlinear dispersion relation, estimating and using the correct shock thickness, balancing the viscous stresses at the shock, etc.

## 3.4 Summary

A concise description of the LIA procedure is provided in this chapter. LIA makes use of linearized Euler equations and linearized RH relations to compute solutions behind the shock. The interaction of a single planar vorticity wave with the shock wave is computed by solving the boundary value problem. The single wave solution is integrated in the wavenumber space for all the waves (as in a spherical shell) to obtain the statistics behind the shock for the interaction of isotropic turbulence with a normal shock wave. Purely vortical is considered upstream of the shock in the present analysis. Extension to entropy fluctuations requires modification in the transfer functions and the linearized RH relations only, whereas the other relations remain the same. The interaction with acoustic waves is slightly more involved but the methodology is the same as mentioned in this chapter (see Ref. [35, 96, 99] for more details). The 3D analysis can be easily extended to anisotropic turbulence also (see Ref. [69] for details). We compute the variances of density, pressure, temperature and entropy along with the Reynolds stresses and vorticity variances (or enstrophy), which are statistical moments of second-order determined from the linearized fluctuations (first-order) obtained from LIA. These second-order terms are compared with their DNS counterparts in Chapters (5) and (6) to assess the predictions of LIA.

# Chapter 4

# Numerical methodology and verification

A description of the numerical method and the simulations carried out are provided in this chapter. Computations are performed for the interaction of a temporally decaying homogeneous isotropic turbulence with a normal shock wave using the shock-capturing methodology. The turbulence database is generated in a separate precursor simulation. Code titled "*hybrid*" developed by Prof. Johan Larsson is used in this study. The code is written in C++ language and is parallelized using MPI with fully non-blocking communication. The code is highly scalable, and has shown excellent scalability in very large machines [9]. The code has been tested and verified extensively for the case of shock-turbulence interaction [81, 83]. Figure (4.1) shows the schematic of the computational domain with the shock-normal direction aligned with the streamwise direction ($x_1$).

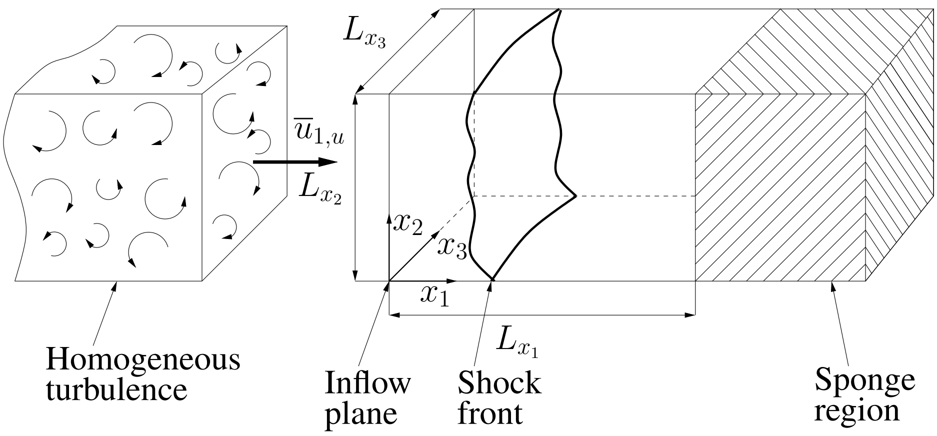


Figure 4.1: A schematic of the shock-turbulence interaction computational domain used in the numerical simulations

The accuracy of the simulations carried out in this work is established by extensive grid convergence tests and comparisons to LIA solutions; which are discussed at length in the subsequent sections. The list of simulations performed and other necessary details are provided in table (4.1). The upstream mean flow Mach number, $M_u = \dfrac{\widetilde{u}_u}{\widetilde{a}_u}$ is varied from 1.23 to 3.5 and the upstream turbulent Mach number, $M_{t,u} = \dfrac{\sqrt{R_{kk,u}}}{\widetilde{a}_u}$ for each of the mean flow Mach numbers is varied from 0.05 to 0.40 comprising a total of 16 cases. The tilde denotes Favre averages computed as $\widetilde{f} = \dfrac{\overline{\rho f}}{\overline{\rho}}$ and the double primes ($f''$) represent its corresponding fluctuations. The Reynolds stresses are $R_{ij} = \widetilde{u_i'' u_j''}$ and turbulent kinetic energy is given by $TKE = 0.5\, R_{kk} = 0.5\, \widetilde{u_k'' u_k''}$. The upstream Reynolds number based on Taylor lengthscale, $Re_{\lambda,u} = \dfrac{\overline{\rho}_u \sqrt{R_{kk,u}/3}\, \lambda}{\overline{\mu}}$ is approximately 33 for all of the cases. The upstream dissipation lengthscale, $L_{\epsilon,u} = \dfrac{(0.5\, R_{kk,u})^{3/2}}{\epsilon_u}$ and Taylor lengthscale, $\lambda_u = \sqrt{\dfrac{R_{22,u}}{\overline{(\partial u_{2,u} \,/\, \partial x_2)^2}}}$ are approximately 0.75 and 0.175, respectively. The dissipation rate of TKE is given by, $\epsilon = \dfrac{1}{\overline{\rho}} \overline{\sigma_{ik} \dfrac{\partial u_j''}{\partial x_k}}$. The Kolmogorov scale, $\eta = \overline{\nu}^{3/4}\, \epsilon^{-1/4}$ is approximately 0.015 upstream of the shock.

Table 4.1: List of simulations carried out in the present study along with the important parameters. The specific gas constant is given in the column under $R$ and the regime of interaction for the cases is provided in the last column

| $M_u$ | $M_{t,u}$ | $k_0\, \lambda_u$ | $Re_{\lambda,u}$ | $k_0\, L_{\epsilon,u}$ | $Re_{L_{\epsilon,u}}$ | $k_0\, \eta_u$ | $R$ | Regime |
|---|---|---|---|---|---|---|---|---|
| 1.23 | 0.05 | 0.68 | 33 | 2.78 | 136 | 0.06 | 117.5 | Wrinkled |
| 1.23 | 0.15 | 0.69 | 33 | 2.80 | 132 | 0.06 | 13.25 | Borderline |
| 1.23 | 0.25 | 0.73 | 33 | 2.96 | 135 | 0.06 | 4.7 | Broken |
| 1.23 | 0.40 | 0.77 | 32 | 3.08 | 130 | 0.07 | 1.85 | Broken |
| 1.50 | 0.05 | 0.68 | 33 | 2.78 | 136 | 0.06 | 117.5 | Wrinkled |
| 1.50 | 0.15 | 0.70 | 33 | 2.82 | 133 | 0.06 | 13.25 | Wrinkled |
| 1.50 | 0.25 | 0.70 | 32 | 2.77 | 127 | 0.06 | 4.7 | Borderline |
| 1.50 | 0.40 | 0.75 | 31 | 2.93 | 126 | 0.07 | 1.85 | Broken |
| 2.50 | 0.05 | 0.68 | 33 | 2.78 | 136 | 0.06 | 117.5 | Wrinkled |
| 2.50 | 0.15 | 0.69 | 33 | 2.82 | 134 | 0.06 | 13.25 | Wrinkled |
| 2.50 | 0.25 | 0.71 | 32 | 2.81 | 128 | 0.06 | 4.7 | Wrinkled |
| 2.50 | 0.40 | 0.75 | 32 | 3.03 | 129 | 0.07 | 1.85 | Wrinkled |
| 3.50 | 0.05 | 0.67 | 33 | 2.77 | 137 | 0.06 | 117.5 | Wrinkled |
| 3.50 | 0.15 | 0.69 | 33 | 2.82 | 135 | 0.06 | 13.25 | Wrinkled |
| 3.50 | 0.25 | 0.71 | 32 | 2.83 | 129 | 0.06 | 4.7 | Wrinkled |
| 3.50 | 0.40 | 0.75 | 32 | 3.07 | 130 | 0.07 | 1.85 | Wrinkled |

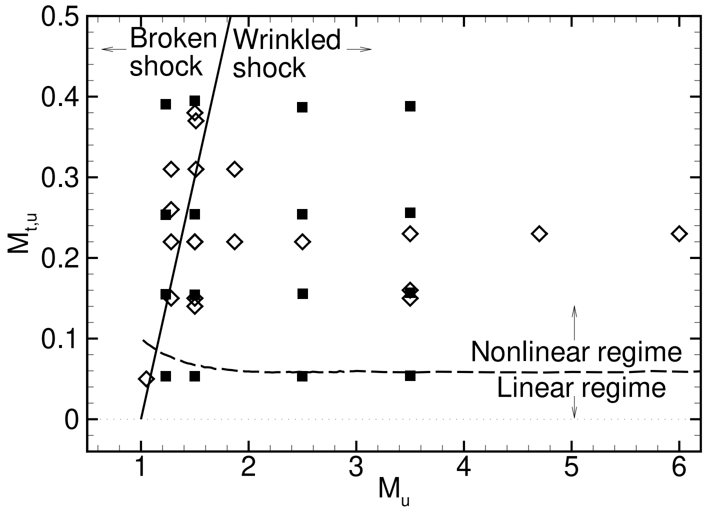


Figure 4.2: Parameter range for the present cases in the ($M_u$, $M_{t,u}$) domain (squares). The regimes of the interaction are demarcated by the solid line (left - broken shock, right - wrinkled shock) and the dashed line (below - linear effects, above - nonlinear effects). The solid line corresponds to $M_{t,u} = 0.6\,(M_u - 1)$ and the dashed line represents $M_{t,d} = 0.1\,M_d$. Additionally, the cases from Larsson *et al.* [81] are also shown for reference (diamonds)

Figure (4.2) depicts the regimes of interaction, 'wrinkled' and 'broken', based on the criterion provided in Ref. [81]. The linear and nonlinear regimes are distinguished by the criterion, $M_{t,d} = 0.1\,M_d$ [132], which assumes that fluctuations greater than 10% of their corresponding mean value fall in the nonlinear regime.

We follow the convention of Larsson *et al.* [81] to identify the interaction regime of our cases. They proposed the criterion, $M_{t,u} > 0.6\,(M_u - 1)$, for which the shocks are found to be extinguished locally. They termed such interactions as the 'broken' shock regime. In the 'broken' shock regime, the local shock surface disappears and through which the turbulence passes through without any significant change (see Figs. 9 and 16 in Ref. [83] and Fig. 19 in Ref. [81]). There is also another scenario in which the local shock surface is replaced by a series of very weak compression waves through which the shock undergoes a smoother compression rather than a very steep gradient as is the case for a normal shock. Larsson *et al.* [81] attributed this local extinguishment of the shock surface to the near-sonic or subsonic flow due to the intense turbulent fluctuations at the corresponding location in the upstream region. However, they also found that in the 'broken' shock regime, only 1% of the shock surface had holes, even for their most intense turbulence case. The reader is referred to their articles [81, 83] for more details on the local extinguishment of the shock.

Recently, Chen and Donzis [18] performed simulations of very high intense turbulence interacting with a normal shock and investigated cases with intensity as high as $M_{t,u} > (M_u - 1)$. They introduced a new regime called the 'vanished' shock regime, where they found no amplification in the Reynolds stresses but the mean quantities still displayed a shock-like behavior. This inconsistency in their naming convention prompts us to use the convention of Larsson *et al.* [81], which is followed throughout this study.

We term the cases as the 'wrinkled' shock regime when they satisfy criterion, $M_{t,u} < 0.6\,(M_u - 1)$, i.e., there are no local extinguishment(s) in the shock surface, but the shock could be strongly distorted (or corrugated). The 'borderline' regime is used for the cases in this study, which are ±0.05 of the criterion used to distinguish the 'wrinkled' and the 'broken' regime, though a much stricter criterion based on the PDFs (probability density functions) of the density difference across the shock should be used as mentioned in Ref. [81]. The regimes of the present cases are tabulated in the last column of table (4.1).

## 4.1 Governing equations

The governing equations are the three-dimensional, unsteady, compressible Navier-Stokes (NS) equations with the assumption of perfect gas. The equations are solved in the Cartesian coordinates for the conservative variables $\rho$, $\rho\, u_i$, $\rho\, E_0$ as shown below,

$$\frac{\partial \rho}{\partial t} + \frac{\partial(\rho\, u_k)}{\partial x_k} = 0, \tag{4.1a}$$

$$\frac{\partial(\rho\, u_i)}{\partial t} + \frac{\partial(\rho\, u_i u_k)}{\partial x_k} + \frac{\partial p}{\partial x_i} = \frac{\partial \sigma_{ik}}{\partial x_k}, \tag{4.1b}$$

$$\frac{\partial(\rho\, E_0)}{\partial t} + \frac{\partial(\rho\, u_k\, E_0)}{\partial x_k} + \frac{\partial(p\, u_k)}{\partial x_k} = \frac{\partial(u_i\, \sigma_{ik})}{\partial x_k} - \frac{\partial q_k}{\partial x_k}, \tag{4.1c}$$

where, $\rho$ is density, $u_i$ is the velocity vector, $p$ is the pressure, $E_0$ is the total energy, $\sigma_{ik}$ is the viscous stress tensor and $q_k$ is the heat conduction vector. The viscous stresses and the heat flux are modeled using Stokes hypothesis and Fourier's law of heat conduction, respectively. They are expressed as follows,

$$\sigma_{ik} = \mu \left( \frac{\partial u_i}{\partial x_k} + \frac{\partial u_k}{\partial x_i} - \frac{2}{3} \frac{\partial u_m}{\partial x_m}\, \delta_{ik} \right), \tag{4.2a}$$

$$q_k = -\frac{\mu\, c_p}{Pr} \frac{\partial T}{\partial x_k}. \tag{4.2b}$$

State equation for the perfect gas holds and thus pressure, $p = \rho R T$. The thermal conductivity, $\kappa$ is related to molecular viscosity, $\mu$ through the assumption of constant Prandtl number $Pr = \mu\, c_p/\kappa$, with $c_p$ being the gas specific heat at constant pressure. The molecular viscosity varies as a function of temperature, which according to a power law is given as, $\mu_{ref}(T/T_{ref})^{3/4}$. Here, $\mu_{ref}$ and $T_{ref}$ are the reference viscosity and temperature of the gas, respectively.

## 4.2 Numerical procedure

The compressible NS equations are solved using a solution-adaptive finite difference method for the perfect gas. The inviscid fluxes near the shock are calculated using a fifth order accurate weighted essentially non-oscillatory (WENO) numerical scheme with Roe flux splitting. The fluxes in the remainder of the domain are calculated using a sixth order accurate central difference scheme in the split form proposed by Ducros *et al.* [31]. The use of the split form is known to improve the nonlinear numerical stability, and no de-aliasing filter is required. The shock wave(s) are identified as regions where the negative dilatation is greater than the low pass-filtered vorticity magnitude i.e., where $-\frac{\partial u_k}{\partial x_k} > \sqrt{\omega_k \omega_k}$ [81]. This shock-sensor is a modified form of the well-known Ducros sensor [30], which is widely used in computations of shock-dominated flows in the recent years. The other widely used shock-sensor is the Jameson sensor [65, 151], which is based on pressure fluctuations. There are also shock-sensors based on empirical relations such as the one used in Refs. [112, 113, 146] and only with dilatation as in Ref. [134]. The present shock-sensor is inspired by the observation that shock waves are associated with large negative dilatation (compression), whereas turbulence is more typically associated with large vorticity. Since it is a modified form of the Ducros sensor, it inherits all the properties of the Ducros sensor such as Galilean invariance and the ability to distinguish weak compression waves from shock waves.

Having identified the grid points occupied by the shock wave(s), the WENO scheme is applied to the narrow region comprising those points as well as three additional grid points in every direction. This is carried out in order to ensure that the central scheme is never used across any shock wave(s). It is indeed a standard practice to use a sensor to identify shocks when hybrid numerical methods such as the one mentioned above are used in computations. Many have used shock-sensors (or switches) [3, 13, 15, 81, 83, 114, 154] in their computations to restrict the application of a numerical method to only a portion of the domain; though the sensors used are different amongst each other. The switching between the WENO and central differencing schemes, introduces internal ‘interfaces’ in the domain. The method devised by Pirozzoli [114] is used to ensure proper conservation across these interfaces and the linear stability of these interfaces has been verified by Larsson and Gustafsson [82]. Any spurious oscillations that are introduced due to the solution-adaptive switching of the numerical schemes are thus bounded. The entire system of equations is integrated in time using a fourth order accurate explicit Runge-Kutta (RK4) scheme.

This numerical procedure has been verified and validated on several problems of interest [71, 80, 81, 83]. It was also identified that the solution-adaptive method has no effect on the results provided that there is sufficient grid resolution [81]. The present study uses the term 'DNS' in the extended sense, where all scales of the turbulence are computed but the shock waves are captured numerically. This implies that the methodology assumes that there is sufficient separation between the turbulence lengthscale (usually $\eta$) and the shock lengthscale (its physical thickness $\delta_s$). In the shock-capturing framework, the interaction problem is accurately described if the numerical shock thickness, $\delta_n$ is sufficiently small than the Kolmogorov lengthscale, $\eta$. Larsson [80] has shown that any error induced by the shock-capturing scheme is of the $O(\Delta x_1^2)$ with $\Delta x_1$ being the grid spacing in the streamwise direction. When the streamwise grid spacing is sufficiently refined, the numerical errors in the statistics are found to decrease considerably.

Table 4.2: Table of initial conditions for each of the cases given in table (4.1). Values are truncated to two decimals for brevity

| $M_u$ | $M_{t,u}$ | $\overline{\rho}_u$ | $\overline{u}_{1,u}$ | $\overline{p}_u$ | $\overline{\rho}_d$ | $\overline{u}_{1,d}$ | $\overline{p}_d$ [1] |
|---|---|---|---|---|---|---|---|
| 1.23 | 0.05 | 1.00 | 15.81 | 118.01 | 1.39 | 11.34 | 188.88 |
| 1.23 | 0.15 | 1.00 | 5.40 | 13.75 | 1.39 | 3.87 | 22.21 |
| 1.23 | 0.25 | 1.00 | 3.32 | 5.19 | 1.39 | 2.38 | 8.48 |
| 1.23 | 0.40 | 1.00 | 2.22 | 2.33 | 1.39 | 1.59 | 3.91 |
| 1.50 | 0.05 | 1.00 | 19.28 | 118.01 | 1.86 | 10.35 | 290.24 |
| 1.50 | 0.15 | 1.00 | 6.58 | 13.75 | 1.86 | 3.53 | 33.91 |
| 1.50 | 0.25 | 1.00 | 4.04 | 5.19 | 1.86 | 2.17 | 12.73 |
| 1.50 | 0.40 | 1.00 | 2.71 | 2.33 | 1.86 | 1.45 | 5.63 |
| 2.50 | 0.05 | 1.00 | 32.13 | 118.01 | 3.33 | 9.64 | 840.77 |
| 2.50 | 0.15 | 1.00 | 10.97 | 13.75 | 3.33 | 3.29 | 97.97 |
| 2.50 | 0.25 | 1.00 | 6.74 | 5.19 | 3.33 | 2.02 | 37.10 |
| 2.50 | 0.40 | 1.00 | 4.51 | 2.33 | 3.33 | 1.35 | 16.58 |
| 3.50 | 0.05 | 1.00 | 44.99 | 118.01 | 4.26 | 10.56 | 1666.79 |
| 3.50 | 0.15 | 1.00 | 15.36 | 13.75 | 4.26 | 3.58 | 194.22 |
| 3.50 | 0.25 | 1.00 | 9.43 | 5.19 | 4.26 | 2.21 | 73.31 |
| 3.50 | 0.40 | 1.00 | 6.32 | 2.33 | 4.26 | 1.48 | 32.92 |

### 4.2.1 Initial conditions

The governing equations are solved in the dimensional form itself with upstream mean density, $\overline{\rho}_u$ and mean temperature, $\overline{T}_u$ being set at a value of 1. In essence, the upstream values are setup in the non-dimensional form instead of the governing equations. The results are always presented in the normalized sense and thus the present approach is acceptable to describe the shock-amplified turbulence quantities. The value of $\mu_{ref}$ = 0.002 yields a Taylor-scale Reynolds number of $Re_{\lambda,db} = 34$ in the turbulence database. The specific gas constant, $R$ determines the turbulent Mach number, $M_t$ of the turbulence database, and varies as shown in table (4.1). The Prandtl number and the ratio of specific heats are kept at a constant value of $Pr = 0.7$ and $\gamma = 1.4$, respectively for the perfect gas.

The upstream mean value of pressure, $\overline{p}_u$ is set up according to the mean pressure value in the turbulence database, and varies for each of the $M_{t,u}$ cases. The mean pressure in the turbulence database initially, $\overline{p}_{db,t=0} = R$ due to the mean density and temperature values being 1. As the turbulence develops in the temporal simulation, the mean value of pressure increases in the database, and is usually closer to the value of $R$. The upstream mean sound speed, $\overline{a}_u$ and the Mach number are used to calculate the upstream streamwise mean velocity, $\overline{u}_{1,u}$. The downstream mean values are specified using the laminar RH relations with slight adjustments to the pressure value, which will be explained later. The initial field in the STI computation is specified with the mean values of density, pressure and streamwise velocity as given in table (4.2) for each of the cases,

### 4.2.2 Computational grid

The schematic of the computational is shown in Fig. (4.1). The computational domain is $k_0 L_{x_1} = 9\pi$ long in the streamwise direction with the shock initially placed at $k_0 x_1 = 1\pi$. The length of the domain in the shock-parallel direction is $k_0 L_{x_2} = k_0 L_{x_3} = 8\pi$. The computational grid is stretched in the shock-normal direction to facilitate finer grid sizes near the shocks and relatively coarser sizes away from the shock. A uniform grid spacing in used in the shock-parallel directions. The grid sizes are varied to ensure that the anisotropically compressed post-shock turbulence is captured as the shock strength is varied. We note that the present simulations have grid resolution comparable to the viscous shock thickness estimate [132] for the low Mach number cases and vary by a factor of 4 to 5 for the high Mach number cases, when the same relation is used.

[1] The exact value is significant up to 5 decimal places, and is necessary to ensure that the shock drifting speed is minimal (elaborated in Appendix (D))

The grid used in shock-turbulence interaction needs to have the smallest grid spacing around the shock and larger grid spacings upstream and downstream of the shock. The grid index in the computational domain is defined as,

$$x_i = x_l + (x_r - x_l) f\left(\frac{i}{N-1}\right), \quad i = 0, ...., N-1 \tag{4.3}$$

where, $x_i$ is the discretized spatial coordinate in the stream wise direction with $x_l$ and $x_r$ being the end locations. The normalized coordinate is given by $f(s)$, a polynomial with multiple hyperbolic functions which varies as $f(0) = 0$, $f(1) = 1$, for $s \in [0, 1]$. Additional details on the formulas and relations used in the rectangular Cartesian grid generation are provided in Appendix (B). Variation of grid spacing against the shock-normal spatial coordinate is shown in Fig. (4.3).

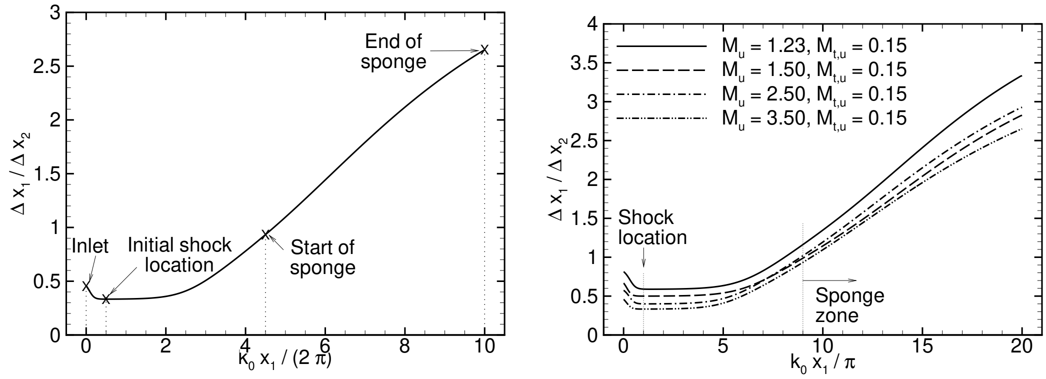


(a) Grid spacing: $M_u = 1.5$ and $M_{t,u} = 0.15$ (b) Grid spacing: $M_u = 1.23 - 3.5$ and $M_{t,u} = 0.15$

Figure 4.3: Grid spacing against streamwise coordinate, $x_1$. (a) Case of $1042 \times 384^2$. The grid points are clustered in the region of the shock located at $x = 0.25\pi$ with grid spacing equal to $0.5\Delta y$. Grid spacing in the transverse direction, $\Delta y = 2\pi/N_y$. The sponge has the coarsest grid spacing which varies from $\Delta y$ to $3\Delta y$ from its start to the end. (b) Grid spacing for the different Mach numbers in the $M_{t,u} = 0.15$ dataset

The grid spacing at the shock was varied to follow the approximate relation provided in Ref. [83] such that the post-shock Kolmogorov scale is sufficiently resolved as the shock strength is varied (see Sect. (4.4.1)). Figure (4.3b) highlights this variation, where the $M_u = 3.5$ case has the smallest grid spacing at the shock compared to the $M_u = 1.23$ case for $M_{t,u} = 0.15$ dataset. The transition of grid spacing in the useful domain to the grid spacing in the sponge region is also ensured to be 'gradual' such that no grid induced oscillations arise. Table (4.3) shows the details of the grid used in the simulations along with the number of grid points in the streamwise direction for each region in the computational domain. The sponge region has the coarsest grid spacing ($\approx 250-300$ grid points over a length of $k_0 L_{sp.} = 11\pi$). Unless stated otherwise, the data presented in the subsequent chapters use these grid sizes in the simulations.

Table 4.3: Details of grid spacing in each region of the computational domain. Columns 4 to 6 show the number of grid points in the shock-normal direction only. The number of grid points in the shock-parallel directions is 384 in each direction for all of the cases. Here, $x_i$ corresponds to the inlet, $x_s$ is the location of the shock, $x_{sp.}^{start}$ is the start of the sponge region and $x_{sp.}^{end}$ is the end of the sponge region

| $M_u$ | $M_{t,u}$ | Grid | $x_i \to x_s$ | $x_s \to x_{sp}^{start}$ | $x_{sp}^{start} \to x_{sp}^{end}$ |
|---|---|---|---|---|---|
| 1.23 | 0.05 | $882 \times 384^2$ | 70 | 558 | 254 |
| 1.23 | 0.15 | $882 \times 384^2$ | 70 | 558 | 254 |
| 1.23 | 0.25 | $888 \times 384^2$ | 65 | 569 | 254 |
| 1.23 | 0.40 | $888 \times 384^2$ | 65 | 569 | 254 |
| 1.50 | 0.05 | $1042 \times 384^2$ | 90 | 654 | 298 |
| 1.50 | 0.15 | $1042 \times 384^2$ | 90 | 654 | 298 |
| 1.50 | 0.25 | $1042 \times 384^2$ | 90 | 654 | 298 |
| 1.50 | 0.40 | $1046 \times 384^2$ | 80 | 667 | 295 |
| 2.50 | 0.05 | $1142 \times 384^2$ | 102 | 748 | 292 |
| 2.50 | 0.15 | $1142 \times 384^2$ | 102 | 748 | 292 |
| 2.50 | 0.25 | $1142 \times 384^2$ | 102 | 748 | 292 |
| 2.50 | 0.40 | $1142 \times 384^2$ | 102 | 748 | 292 |
| 3.50 | 0.05 | $1313 \times 384^2$ | 131 | 872 | 310 |
| 3.50 | 0.15 | $1313 \times 384^2$ | 131 | 872 | 310 |
| 3.50 | 0.25 | $1313 \times 384^2$ | 131 | 872 | 310 |
| 3.50 | 0.40 | $1313 \times 384^2$ | 131 | 872 | 310 |

### 4.2.3 Inflow and outflow conditions

The turbulence immediately upstream of the shock is needed to be realistic, fully developed and well-characterized. For this, the inflow turbulence is generated in several steps essentially following the technique proposed by Xiong *et al.* [169]. First, several independent but statistically identical fields of isotropic turbulence in periodic boxes are generated using the methodology proposed by Ristorcelli and Blaisdell [128]. These fields have been generated with initial energy spectra of the form similar to the von Kármán energy spectrum [80] with peak energy at wavenumber $k_0 = 4$ and Taylor lengthscale Reynolds number of $Re_{\lambda,t=0} = 114$. They are then allowed to decay temporally in periodic boxes for approximately $1-2$ units of the dissipation time scale, $t_\epsilon$, which ensures that the turbulence is fully developed and realistic. These independent realizations (or flowfields) of turbulence are then blended together into a longer inflow database [79], which is then used together with Taylor's hypothesis to specify the time-dependent inflow turbulence. This technique leads to very accurate spatially decaying turbulence immediately behind the inlet [82, 169]. A detailed study on the generation and analysis of isotropic turbulence databases is provided in the following section and in Appendix (E).

The resolved (or useful) part of the computational domain ends at an arbitrary length ($L_{x_1} = 2.25\pi$ in this study). A sponge region is appended beyond this length to gently damp the disturbances before reaching the outlet, thus minimizing spurious reflections towards the shock. In the sponge layer, source terms in the form of,

$$-\sigma_0 \left(\frac{x_1 - x_{sp}}{L_{sp}}\right)^2 \left(f - \overline{f}_{y,z}\right), \tag{4.4}$$

are added to the RHS of Eqs. (4.1a) - (4.1c), where $f$ denotes the conserved variable in each equation. Here, $\sigma_0$ is the strength coefficient, $x_{sp}$ is the location in the computational domain where the sponge begins, and $L_{sp}$ is the length of the sponge. The target state, $\overline{f}_{y,z}$ for all quantities is taken as the post-shock state obtained from laminar RH shock relations, except for pressure. The target state for pressure is taken as the backpressure specified at the outlet, and is usually closer to the RH value for pressure. Additional details on the sponge region and the verification tests to obtain an optimized sponge are provided in Appendix (C).

The formulation proposed by Poinsot and Lele [115] is used at the outflow boundary (or exit plane) following the sponge region, which is an extension of the characteristic boundary conditions developed for Euler equations by Thompson [157]. The non-reflecting Navier-Stokes characteristic boundary condition (NSCBC) with local one-dimensional inviscid (LODI) assumption is used to make the outflow boundary 'almost' non-reflecting. A perfectly non-reflecting NSCBC with LODI is possible, but is found to make the system of equations ill-posed in a multi-dimensional setting [115]. A similar procedure of using a sponge region before the non-reflecting outflow boundary with NSCBC was also followed in the work of Mahesh *et al.* [99].

The implementation of these boundary conditions is equivalent to specifying conditions on the derivatives of the flow variables normal to the boundary. The inviscid part of the NS equations (or Euler equations) display a hyperbolic behavior, which emanate waves that propagate both inward and outward of the computational domain at the outflow boundary. The characteristics of the outgoing waves are determined from the solution inside the computational domain, while that of the incoming waves are specified. The following is only a brief description of the boundary conditions and the complete details can be found in Poinsot and Lele [115].

The inviscid part of the NS equations (Eq. (4.1a) - (4.1c)) are written in the form of characteristic variables at the outflow boundary. Out of the five eigen values $(u - a, u, u, u, u + a)$ in the system of equations, the incoming wave that needs to be specified corresponds to the $u - a$ eigen value since the outflow boundary is subsonic. The amplitudes of the characteristic waves (denoted by $\mathrm{L}_i$ for $i = 1$ to 5) are related to the spatial derivatives of the physical variables in the linear limit. The amplitude of the incoming characteristic wave ($\mathrm{L}_1$) at the outflow boundary is determined by specifying the value of pressure, whereas the other characteristic variables ($\mathrm{L}_i$ for $i = 2$ to 5) are estimated from the interior solution. The viscous part of the NSCBC is satisfied by setting the gradients of the viscous stresses and the heat conduction terms to zero in the direction normal to the outflow boundary as suggested by Poinsot and Lele [115].

The issue of avoiding acoustic reflections from the outflow is common in literature; however, the more interesting issue is that of specifying the backpressure, $\overline{p}_\infty$ such that the shock is stationary in the mean. The RH relations are only valid instantaneously, but not on average in a turbulent flow. Lele [88] used RDT to develop approximate shock relations for turbulent flow, and found that the density and pressure jumps decrease in the presence of turbulence for a given shock Mach number. Thus, the value of $\overline{p}_\infty$ that yields a stationary shock for a given $M$ and $M_t$ should be slightly lower than that predicted by the laminar RH relations. Larsson *et al.* [81], however, showed that there is one additional effect that counteracts this decrease in jump across the shock. The decay of turbulence kinetic energy in the downstream region implies a spatially increasing internal energy, which causes the outlet state to be different from the state immediately downstream of the shock. More specifically, it suggests that the $p_\infty$ value which yields a stationary shock is slightly higher than that given by the turbulent shock jump. These two effects make it nearly impossible to find the exact $\overline{p}_\infty$ value that yields a stationary shock *a priori*. Multiple runs, possibly on a coarser grid, are required to identify the correct value of $\overline{p}_\infty$ that keeps the shock nearly stationary. The average shock speed, $\overline{u}_s$ is $< 0.001\overline{u}_{1,u}$ for all of the cases in the present study. A brief explanation of the procedure and additional details are provided in Appendix (D).

To ensure high accuracy at the boundaries as in the interior of the domain, the solution at the boundaries are calculated such that they satisfy the summation by parts (SBP) property using the simultaneous approximation terms (SAT) method [102, 103, 150]. This type of boundary treatment is found to be better than other high-order boundary treatments such as the projection method, injection method, etc., due to its superior numerical stability and an energy estimate that restricts the growth of instabilities at the boundaries. These properties are essential for turbulence resolving simulations to ensure that there is no additional dispersive errors and loss in resolution due to the reduction in order-of-accuracy at the boundaries. The SBP/SAT boundary treatment with additional artificial dissipation of Mattsson *et al.* [104] is used at the supersonic inflow of the computational domain and the subsonic outflow uses the regular SBP/SAT treatment of Mattsson [102]. The artificial dissipation in the SBP/SAT inflow treatment is set to zero for all of the cases, except for the $(M_{t,u}, M_u) = (0.25, 1.23), (0.40, 1.23)$ and $(0.40, 1.50)$ cases.

## 4.3 Homogeneous isotropic turbulence database

Decaying isotropic turbulence fields were generated with using the gas properties, $R = (117.5, 13.25, 4.7, 1.85)$ and $\mu_{ref} = 0.002$ for the cases provided in table (4.1) in a precursor simulation. First, initial fields of turbulence are generated as per the steps given below,

1. generate a random velocity field with chosen peak energy wavenumber and a decaying velocity spectra in Fourier space. We consider the von Kármán spectrum [80] given in Eq. (3.29) with peak energy wavenumber of $k_0 = 4$.

2. filter to avoid aliasing errors. When the product of two Fourier modes (say, $\hat{f} * \hat{g}$) with different wavenumber $k_f$ and $k_g$ is discretized, the resultant would have modes with wavenumbers of $k_f + k_g$, which are not resolved. On the discrete grid points, these modes will be identical to modes that lie within the range of resolved wavenumbers, leading to 'aliasing' errors [11].

3. normalize the velocity field such that the isotropic condition is satisfied. We now have a solenoidal isotropic turbulence.

4. solve a Poisson equation for pressure (see Eq. (3) in Ref. [128]) and ensure positive pressure by using limiter functions. The pressure field needs to be transformed to the physical space to check for positiveness.

5. solve a Poisson equation for time-derivative of pressure and use it in conjunction with the isentropic mass equation (see Eqs. (10) and (11) in Ref. [128]) to obtain the fluctuations of dilatation.

6. extract the irrotational velocity field from the fluctuations of dilatation and add them to the solenoidal velocity field. We now have the compressible velocity field in the wavenumber space.

7. transform to physical space by means of inverse Fourier transforms.

8. add the pressure fluctuations and the isentropic density fluctuations in physical space to the velocity field.

The initial field of compressible turbulence generated as mentioned above allows the flow to develop more naturally as the pressure field is associated with the vortical motions. The compressible NS equations are solved with these initial fields in a triply periodic box of length $2\pi$ to generate the isotropic turbulence fields. There are no forcing mechanisms added to the governing equations and the fields are allowed to decay temporally. The numerical procedure for these precursor simulations remains the same as provided in Sect. (4.2). The fluxes are solved using sixth-order central differencing scheme and the time integration is by the RK4 method. The boundary conditions are periodic in all directions. For the high $M_t$ cases, eddy shocklets are found in the turbulence fields [134], which are captured using the fifth-order accurate WENO scheme.

The turbulence field to be fed at the inflow of the STI domain is collected after $t \approx 0.8\,\tau_{\epsilon,0}$, at which time, the velocity derivative skewness has obtained a value of $-0.5$ [156] (approximately) and the dissipation lengthscale has started to increase [81]. Here, $\tau_\epsilon = 0.5\,R_{kk}\,/\,\epsilon$ is the dissipation timescale, which is used to characterize large scale motions. The small scale resolution in the turbulence field is represented by the parameter $k_{max}\,\eta$ and the fields are adequately resolved as per the criterion given in Ref. [34]. The grid size for the turbulence fields are finalized after a thorough grid independence test for the chosen $Re_\lambda$ value. The grid sizes considered for the test are: $128^3$, $192^3$, $256^3$ and $384^3$. The periodic boxes are uniformly spaced. The grid resolution only depends on the $Re_\lambda$ value and need not be changed for the different $M_t$ cases.

First, we compare the temporal variation of key quantities/parameters for the different grid sizes in Fig. (4.4). The case shown is that of $M_t = 0.15$ and $Re_\lambda = 35$ at the time of collection (denoted by $t_{collection}$). As the turbulence develops over time, enstrophy increases and reaches a peak value around $0.1\,\tau_{\epsilon,0}$ and then decreases continuously. The Kolmogorov scale, which is related to the vorticity variances, also has a similar trend, where it decreases and then increase after $0.1\,\tau_{\epsilon,0}$ units. The skewness and the dissipation lengthscale criterion are met at around $0.8\,\tau_{\epsilon,0}$ units, and the turbulence field to be fed into the STI domain is collected around this time. The grid sizes of $256^3$ and $384^3$ are found to satisfy the small scale resolution criterion of $k_{max}\,\eta > 1.5$ [34] for the chosen $Re_\lambda$ value. We finalize the turbulence field with $384^3$ grid size to be used as inflow turbulence and the same grid size is considered for the other $M_t$ cases also.

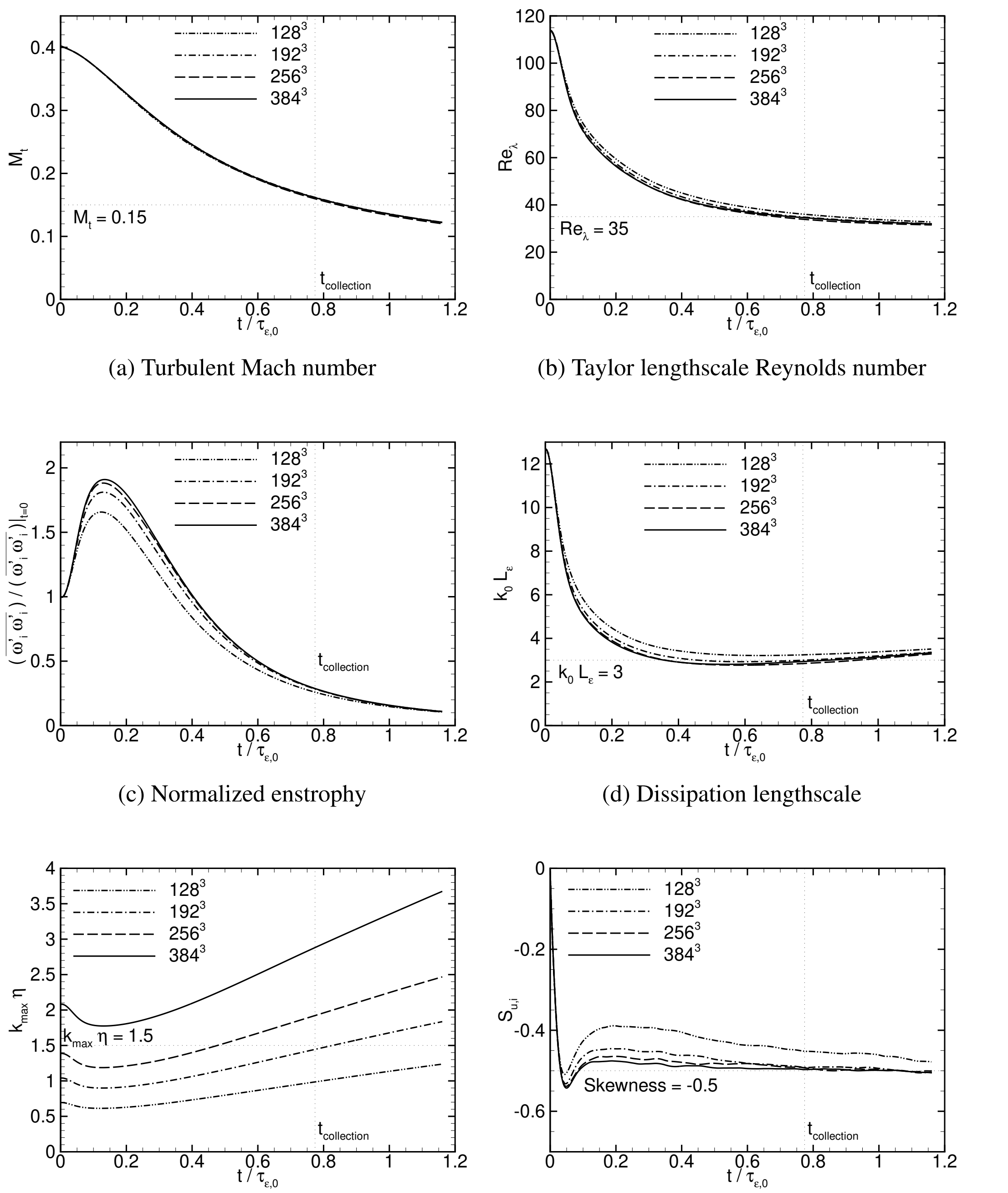


(a) Turbulent Mach number

(b) Taylor lengthscale Reynolds number

(c) Normalized enstrophy

(d) Dissipation lengthscale

(e) Kolmogorov lengthscale

(f) Velocity derivative skewness

Figure 4.4: Temporal variation of (a) turbulent Mach number, $M_t$, (b) Taylor lengthscale Reynolds number, $Re_\lambda$, (c) enstrophy, $\overline{\omega'_i \omega'_i}$ normalized by its initial value (denoted by subscript, $t = 0$), (d) dissipation length scale, $L_\epsilon$ normalized by the peak energy wavenumber, $k_0$, (e) Kolmogorov lengthscale, $\eta$ normalized by the maximum wavenumber, $k_{max}$ and (f) Skewness of velocity derivative, $S_{u,i}$. Time is normalized by the initial dissipation time scale, $\tau_{\epsilon,0}$ and the collection time is denoted by $t_{collection}$

Next, we check the energy spectrum of the turbulence fields at the time of collection. The compensated kinetic energy spectrum, $E(k)\,k^{5/3}\,\epsilon^{-2/3}$ and the normalized dissipation spectrum, $k\,D(k)\,\epsilon^{-1}$ [116] are shown for the $M_t = 0.15$ isotropic turbulence field in Fig. (4.5). The spectra show convergence as the grid is refined from $192^3$ to $384^3$. These spectra show that high-wavenumber fluctuations of both the velocity and vorticity fields are well resolved in our simulations; the same holds true for the other values of $M_t$ considered. For the low Reynolds number considered here, the spectra do not show an inertial subrange.

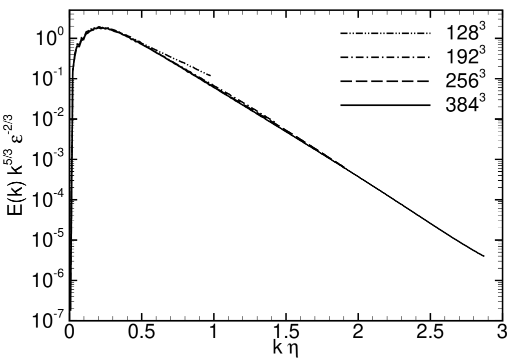


(a) Kinetic energy spectrum

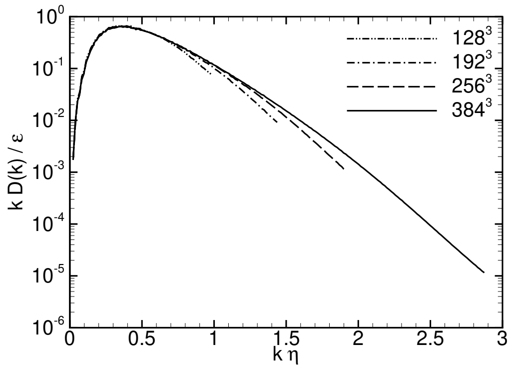


(b) Dissipation spectrum

Figure 4.5: Spectra of (a) total kinetic energy in its compensated form and (b) normalized dissipation. The spectra correspond to the $M_t = 0.15$ isotropic turbulence fields, collected at $t = 0.8\,\tau_{\epsilon,0}$ for the various grids shown in the legend. The wavenumber is normalized by the Kolmogorov lengthscale, $\eta$

Multiple realizations of the isotropic turbulence fields were generated and were blended together using the technique described by Larsson [79]. This method is based on the work of Xiong *et al.* [169] but with an additional procedure of dilatation removal using a least-squares method based optimization approach, which reduces memory requirements and increases parallelism. A total of 8 independent turbulence fields are 'stitched' together using the method of Larsson [79] to form the homogeneous turbulence database. This blending procedure introduces additional dilatation fluctuations and requires 'tweaking' of the blending region size to limit the added fluctuations.

The blending of multiple turbulence boxes is achieved by solving a constrained minimization problem, where the dilatation error is removed by solving a Poisson equation. Additional details of the blending procedure are provided in Appendix (F). In the present work, the length of the blending region ($l_b$) is set equal to the Taylor lengthscale ($\lambda$ at $t_{collection}$) of the developed turbulence box. The size of the region, where the Poisson equation is solved ($L_b$) is specified as five times the Taylor lengthscale (i.e., $5\,\lambda$) following a trial and error approach. These parameters are given in relation to the Taylor lengthscale, since velocity gradients in the turbulence box scale as $u_i'/\lambda$. The error due to the added dilatation fluctuations scale as $u_i'/l_b$ and so the blending region size should be proportional to the Taylor lengthscale. For easiness, the size of the blending region was fixed to one Taylor lengthscale and the region for the Poisson equation was varied until we achieved reasonable dilatation levels in the blended region. In this approach, we found the results to be not very sensitive to the values of $l_b$ and $L_b$, provided that the latter is at least 4 times larger than the former.

Figure (4.6) shows the normalized dilatation variance for each of the cases between two of the different isotropic fields and the final blended database. The discrepancy between the isotropic database and the blended database is within the limits of the actual variance. This indicates that the error introduced by the blending procedure is very small even for the highest $M_t$ case considered here.

It is to be noted that each individual realization is isotropic but the blended database is homogeneous due to the variations in the blending region. The use of a sufficiently longer database generated *a priori* as the inflow turbulence is cheaper than using one isotropic turbulence field and solving for multiple flow-through times in the STI domain. Additional details for the other $M_t$ cases are provided in Appendix (E).

## 4.4 Simulation parameters and verification

Simulations have been carried out for four different Mach numbers, $M_u = 1.23$, 1.50, 2.50 and 3.50 in the present study with Taylor lengthscale Reynolds number, $Re_{\lambda,u} = 33$ and with varying turbulent Mach numbers, $M_{t,u} = 0.05$, 0.15, 0.25 and 0.39 as given in table (4.1). Here, the subscripts $u$ and $d$ are used to denote the upstream and the downstream states, respectively. The slight reduction in the values of $M_t$ and $Re_\lambda$ compared to the inflow turbulence is due to the decay of turbulence as it traverses the upstream portion of the STI domain.

Taylor's hypothesis is used to specify the homogeneous isotropic database as the time-dependent inflow turbulence for the canonical STI problem. The blending procedure is found to have a very small effect on the realism of the turbulence, and changes the root-mean-square (rms) values of the thermodynamic fluctuations by less than 5% and that of the dilatational fluctuations by 10% for the highest $M_{t,db}$ case of 0.40. The assumption of Taylor's hypothesis when convecting the inflow database into the domain introduces much larger errors since it is inaccurate for the acoustic waves [84]. For example, it increases

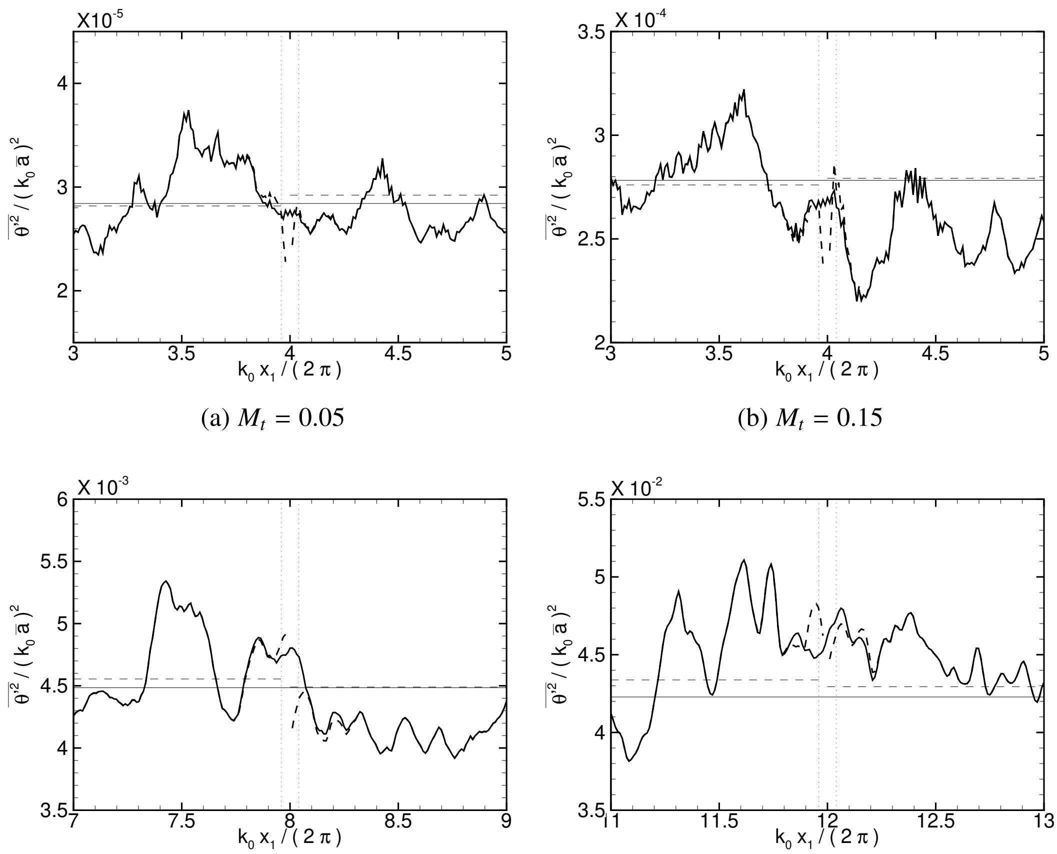


(a) $M_t = 0.05$ (b) $M_t = 0.15$

(c) $M_t = 0.25$ (d) $M_t = 0.40$

Figure 4.6: Variation of normalized dilatation variance against streamwise direction for the different $M_t$ cases. The streamwise direction is normalized by the peak energy wavenumber and additionally scaled by a factor of $2\pi$. The dilatation variance is normalized by the square of the product of the peak energy wavenumber, $k_0$ and the mean sound speed, $\overline{a}$. The dashed lines lines represent the isotropic fields and the solid line corresponds to the blended database. The thin dashed and solid lines represent the streamwise averaged values of the isotropic field and the blended database, respectively. Differences are observed only at the boundaries and in the blended regions

the rms of the thermodynamic fluctuations by 5% and that of the dilatational fluctuations by 25% in the case of $M_{t,u} = 0.15$. However, the resulting turbulence is at least 97% vortical with only a minimal amount of thermodynamic and compressible fluctuations for $M_{t,u} \leq 0.25$, and 90% vortical energy for the $M_{t,u} = 0.40$ case. The error introduced due to the use of Taylor's hypothesis is analyzed in Appendix (G).

Before proceeding, we note that the results (or statistics) presented throughout this dissertation are space averaged over the homogeneous directions $(x_2, x_3)$ and time averaged over one inflow turbulence time period, $\tau_{db} = \dfrac{N_B \times 2\pi}{\overline{u}_{1,u}}$, where $N_B$ is the number of turbulence fields 'stitched' in the blended database. The statistics are collected after the flow has reached a statistically steady state, which is achieved after the turbulence traverses the entire length of the domain and travels back to the shock wave. The time taken to achieve steady state is termed as the pass-over time [159], and is calculated as,

$$\tau_p = \frac{L_{x,u}}{\overline{u}_{1,u}} + \frac{L_{x,d}}{\overline{u}_{1,d}} + \frac{L_{x,d}}{|\overline{u}_{1,d} - \overline{a}_d|}, \tag{4.5}$$

where the wave from the outlet ($3^{rd}$ term) to the shock is the slow acoustic wave [81]. The wave from the inlet to the shock and then to the outlet is the vorticity wave. The pass-over time is approximately $2-3$ times of the inflow turbulence time period.

### 4.4.1 Grid convergence and verification

We consider the dataset of $M_{t,u} = 0.15$ and $Re_{\lambda,u} = 33$ for the grid convergence test. For each of the turbulent Mach numbers considered, a similar grid convergence test needs to be done. Due to computational resource limitations, we proceed with the same grid resolution verified in the subsequent discussion for the other $M_{t,u}$ values also. The simulations of Larsson *et al.* [81] also use similar grid resolution for the different $M_{t,u}$ values considered in their study, and thus we believe that the present simulations are indeed grid converged.

Table (4.2) provides the necessary details on lengthscales and the grid resolution for all of the cases in the $M_t = 0.15$ dataset including the cases considered in grid convergence tests. The upstream shock-turbulence intensity given by $M_{t,u}/(M_u - 1)$ varies from 0.65 to 0.06, which shows that the $M_u = 1.23$ case is in the 'broken shock' regime and the remaining cases are in the 'wrinkled shock' regime [26, 27, 81]. The reduction in Kolmogorov lengthscale is described with respect to the numerical shock thickness, $\delta_n$ [159] in the sixth and the seventh columns of the table, respectively. The pre-shock Kolmogorov

[2] Ratio of viscous shock thickness to Kolmogorov lengthscale, $\delta_s/\eta \approx 7.69 M_{t,u}/(\sqrt{Re_{\lambda,u}}(M_u - 1))$ [132]. This formulation is not valid for $M_u > 2$ [158]

Table 4.4: List of cases simulated in the present study including the cases considered in grid convergence tests. $\Delta x_{2/3}$ is the transverse grid spacing, $\Delta x_{1,s}$ is the shock-normal grid spacing at the shock, $\delta_n$ is the numerical shock thickness, $\delta_s$ is the viscous shock thickness and $\eta$ is the Kolmogorov lengthscale. Note that $k_{max}$ is based on the transverse grid-spacing. Cases denoted by bold characters are the finalized cases used for presenting the results

| $M_u$ | $\frac{M_{t,u}}{(M_u-1)}$ | Grid | $\Delta x_{2/3}/\Delta x_{1,s}$ | $\eta_u/\delta_n$ | $\eta_d/\delta_n$ | $(k_{max}\eta)_{min}$ | $\eta_u/\delta_s$ [2] |
|---|---|---|---|---|---|---|---|
| **1.23** | **0.65** | $\mathbf{882\times 384^2}$ | **1.66** | **0.71** | **0.57** | **2.38** | **1.11** |
| 1.50*a* | 0.30 | $695\times 256^2$ | 2.00 | 0.55 | 0.36 | 1.30 | 2.44 |
| 1.50*b* | 0.30 | $522\times 384^2$ | 1.00 | 0.45 | 0.30 | 1.98 | 2.44 |
| **1.50c** | **0.30** | $\mathbf{1042\times 384^2}$ | **2.00** | **0.95** | **0.61** | **1.91** | **2.44** |
| 1.50*d* | 0.30 | $1566\times 384^2$ | 4.00 | 1.69 | 1.08 | 1.90 | 2.44 |
| 1.50*e* | 0.30 | $1390\times 512^2$ | 2.00 | 1.15 | 0.75 | 2.55 | 2.44 |
| **2.50** | **0.10** | $\mathbf{1142\times 384^2}$ | **2.50** | **1.18** | **0.56** | **1.40** | **7.14** |
| 3.50*a* | 0.06 | $875\times 256^2$ | 3.03 | 0.72 | 0.33 | 0.90 | 12.5 |
| 3.50*b* | 0.06 | $658\times 384^2$ | 1.51 | 0.64 | 0.30 | 1.39 | 12.5 |
| **3.50c** | **0.06** | $\mathbf{1313\times 384^2}$ | **3.03** | **1.30** | **0.58** | **1.32** | **12.5** |
| 3.50*d* | 0.06 | $1844\times 384^2$ | 6.25 | 2.50 | 1.11 | 1.30 | 12.5 |
| 3.50*e* | 0.06 | $1750\times 512^2$ | 3.03 | 1.36 | 0.61 | 1.71 | 12.5 |

lengthscale varies from $0.7-1.3$ times the numerical shock thickness for the cases considered here and the post-shock Kolmogorov lengthscale is about half the numerical shock thickness. The normalized Kolmogorov lengthscale, $k_{max}\,\eta$ is usually taken to be $\geq 1.5$ to resolve features of small lengthscales in turbulence [116]. The post-shock Kolmogorov lengthscale based on the largest grid size among all three directions defined as $(k_{max}\,\eta)_{min}$ [159] (eighth column in the table), is satisfied for the low Mach number cases ($M_u = 1.23$ and 1.50) and is marginally less for the high Mach number cases of 2.50 and 3.50.

We show by a detailed grid convergence test that the chosen grid sizes for each of the case are sufficiently resolved for the statistics considered here. In all the cases, the ratio of the post-shock dissipation lengthscale to the Kolmogorov lengthscale ($L_{\epsilon,d}/\eta_d$) is $> 40$, which is sufficiently large enough to resolve the large scale quantities such as Reynolds stress [81]. The last column provides the ratio of upstream Kolmogorov lengthscale, $\eta_u$ to the viscous shock thickness, $\delta_s$ [132], which provides an estimate for the difference in grid spacing resolution between the shock-captured simulations in the current study and their corresponding shock-resolved simulations. The ratio of numerical shock thickness to the viscous shock thickness in the post-shock region is approximately 3 for the low Mach number cases and 10 for the high Mach number cases, assuming that the viscous shock formulation can also be applied to the stronger shocks. The statistics for the current simulations are computed by averaging over a time period of one flow-through time of the turbulence database, $\tau_{db}$, which is 8 isotropic boxes long.

Grid convergence test for various statistics has been carried out for the case of $M_u =$ 1.50 and 3.50 with $M_{t,u} = 0.15$ and $Re_{\lambda,u} = 33$ using grids varying from 256 to 512 grid points in the shock-parallel directions. Larsson and Lele [83] noted that the Kolmogorov lengthscale decreases behind the shock due to the increase in the viscous dissipation rate, which implies that the grid size behind and at the shock should be refined sufficiently to resolve the shock-modified turbulence. The grid aspect ratio (GAR) at the shock is given by the ratio, $\dfrac{\Delta x_{1,s}}{\Delta x_{2/3}}$, which has been varied to resolve the reduction in Kolmogorov lengthscale behind the shock. In the present work, the GAR at the shock is estimated using the relation,

$$\frac{\eta_d}{\eta_u} \approx \left(\frac{T_d}{T_u}\right)^{\frac{3}{8}} \left(\frac{\rho_d}{\rho_u}\right)^{-1} \approx \frac{\Delta x_{1,s}}{\Delta x_{2/3}}, \tag{4.6}$$

which is provided in Ref. [83]. Recently, Tian *et al.* [159] computed the numerical shock thickness as $\delta_n = (u_{1,u} - u_{1,d}) \Big/ \left|\dfrac{\partial u_1}{\partial x_1}\right|_{max}$, and noted that there are no significant errors in the post-shock statistics when the numerical shock thickness is 1.4 times smaller than the Kolmogorov lengthscale. Boukharfane *et al.* [13] used grid spacing which is $4-8$ times smaller than $\eta_u$ at the shock, and emphasized that such fine resolutions are required for accurate results. We show by a thorough grid refinement test that these values are not universal, and are dependent on the numerical methodology adopted.

Figure (4.7a) shows negligible differences ($\approx$ 2%) in the post-shock values of the Kolmogorov lengthscale as the grid spacing is refined in the shock-normal direction. Figure (4.7b) shows the ratio of Kolmogorov lengthscales as a function of shock strength obtained from the numerical simulations which closely follows the estimate obtained using the expression given in Eq. (4.6) [83]. We observed that the estimate in Eq. (4.6) to be sufficient (with a variation of 10%) for determining the required grid spacing in the shock-normal direction *a priori*. However, the importance of a thorough grid refinement test cannot be understated.

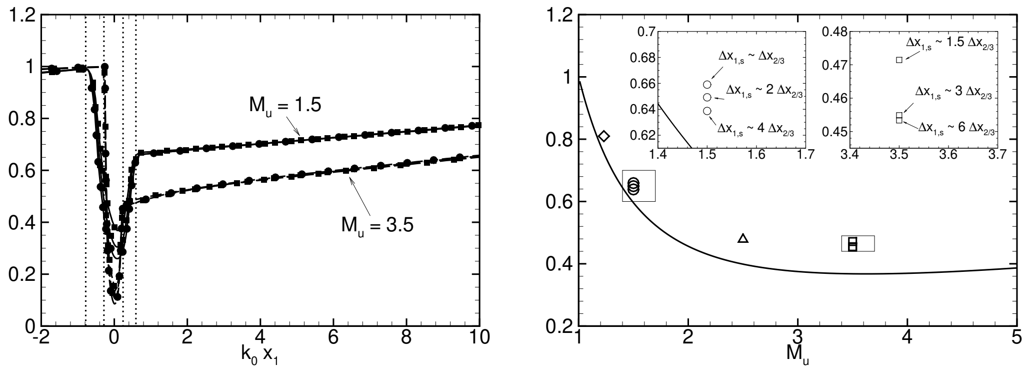


(a) $\eta_d/\eta_u$ against $k_0 x_1$

(b) $\eta_d/\eta_u$ against $M_u$

Figure 4.7: Variation of the Kolmogorov lengthscale ratio, $\dfrac{\eta_d}{\eta_u}$ (a) as a function of the shock-normal direction for the cases mentioned in Table (4.2): 1.5*b* (solid line with squares), 1.5*c* (solid line), 1.5*d* (solid line with circles), 3.5*b* (dashed line with squares), 3.5*c* (dashed line), 3.5*d* (dashed line with circles). The vertical lines around $k_0 x_1 = 0$ show the mean shock thickness for each of the cases, where the Mach 3.5 case has the shortest thickness, and (b) as a function of the upstream Mach number with symbols representing the values from the numerical simulations and the solid line represents the estimate for $\dfrac{\eta_d}{\eta_u}$ given in Eq. (4.6)

Figures (4.8) and (4.9) shows the grid convergence of statistics of interest for the case of $M_u = 3.50$, $M_{t,u} = 0.15$ and $Re_{\lambda,u} = 33$. The large scale features such as Reynolds stresses, $R_{\alpha\alpha} = \widetilde{u''_\alpha u''_\alpha}$ and small scale features such as the transverse vorticity variances, $\overline{\omega'_3\omega'_3}$ and the dissipation rate of TKE, $\overline{\rho}\epsilon = \overline{\sigma_{ij}\dfrac{\partial u''_i}{\partial x_j}}$ are shown in Fig. (4.8). The grid convergence of the thermodynamic variances are shown in Fig. (4.9). The maximum difference in various statistics between the grid sizes mentioned in 3.5*c*, 3.5*d* and 3.5*e* is found to be $\leq$ 2%. We find similar error values ($\leq$ 2%) between cases 1.5*c*, 1.5*d* and

1.5$e$ (not shown). The corresponding case of $M_{t,u} = 0.16$ and $Re_{\lambda,u} = 40$ from Larsson *et al.* [81] is also plotted for comparison. There are differences between the present cases and that of Larsson *et al.*, which are expected to be due to the differences in the inflow turbulence properties.

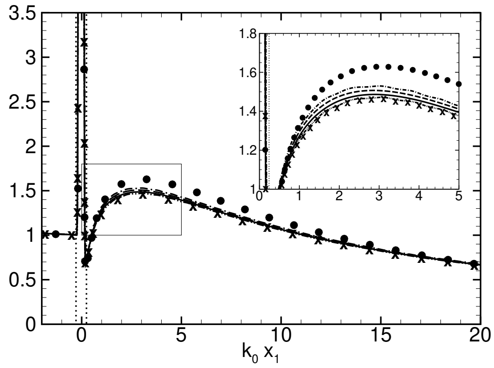


(a) $R_{11}/R_{11,u}$

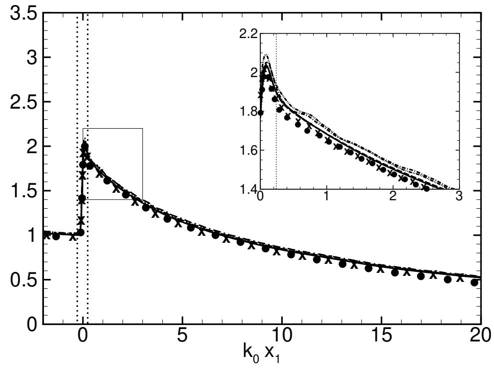


(b) $R_{22}/R_{22,u}$

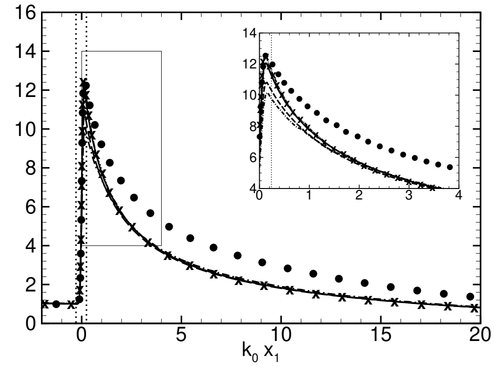


(c) $\overline{\omega_3'^2}/\overline{\omega_{3,u}'^2}$

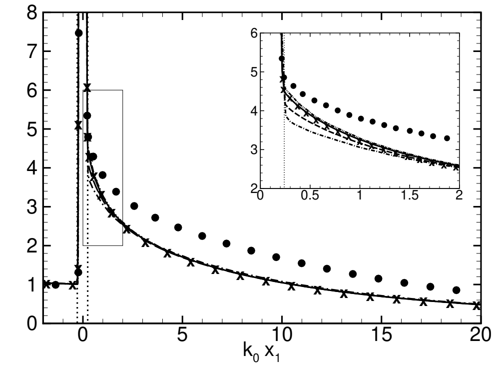


(d) $\epsilon/\epsilon_u$

Figure 4.8: Grid convergence for the case of $M_u = 3.50$, $M_{t,u} = 0.15$ and $Re_{\lambda,u} = 33$ on the grids $875 \times 256^2$ (dashed), $658 \times 384^2$ (dash-dotted), $1313 \times 384^2$ (solid), $1844 \times 384^2$ (x symbols), $1750 \times 512^2$ (dash-double dotted): (a) shock-normal Reynolds stress; (b) transverse Reynolds stress; (c) transverse vorticity variance; (d) dissipation rate of TKE. All the quantities are normalized by their corresponding values upstream of the shock. Corresponding data from [81] for the case of $M_u = 3.50$, $M_{t,u} = 0.15$ and $Re_{\lambda,u} = 40$ (circles) is also plotted for comparison. Inset shows the variation in the short region enclosed by the rectangle. Vertical dotted lines around $k_0x_1 = 0$ denote the region of unsteady shock movement

We present the results with grid resolution equal to the cases of 1.23, 1.5$c$, 2.5 and 3.5$c$ provided in table (4.4) only in the subsequent sections. These grid resolutions are used again for the different $M_{t,u}$ cases within the corresponding $M_u$ dataset. We found that

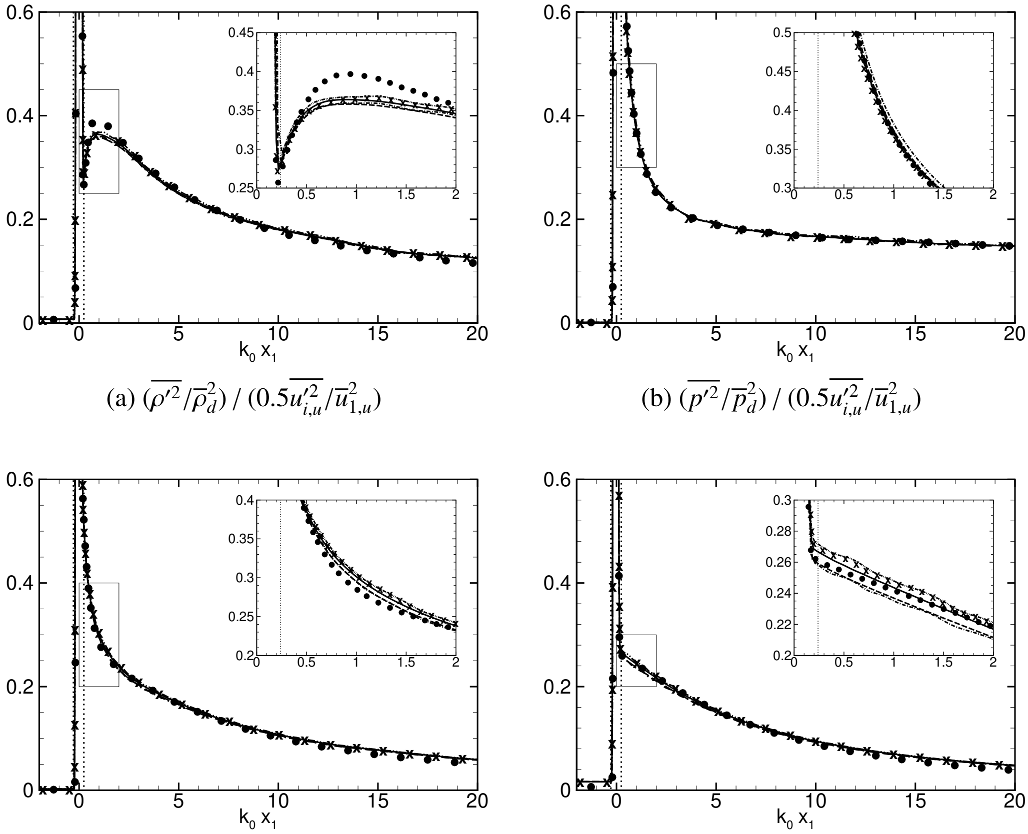


(a) $(\overline{\rho'^2}/\overline{\rho}_d^2)$ / $(0.5\overline{u'^2_{i,u}}/\overline{u}^2_{1,u})$

(b) $(\overline{p'^2}/\overline{p}_d^2)$ / $(0.5\overline{u'^2_{i,u}}/\overline{u}^2_{1,u})$

(c) $(\widetilde{T''^2}/\widetilde{T}_d^2)$ / $(0.5\overline{u'^2_{i,u}}/\overline{u}^2_{1,u})$

(d) $(\widetilde{s''^2}/c_p^2)$ / $(0.5\overline{u'^2_{i,u}}/\overline{u}^2_{1,u})$

Figure 4.9: Same as Fig. (4.8) but shown for the thermodynamic variances. (a) density variance; (b) pressure variance; (c) temperature variance; (d) entropy variance. All the quantities are normalized by the square of their corresponding mean values downstream of the shock ($\overline{\rho}_d$, $\overline{p}_d$ and $\overline{T}_d$) except for the entropy variance which is normalized by the square of the gas specific heat capacity at constant pressure ($c_p$). The quantities are additionally scaled by the normalized TKE $(0.5\overline{u'^2_{i,u}}/\overline{u}^2_{1,u})$. Lines and symbols are as mentioned in the caption of Fig. (4.8) with the insets showing the short region enclosed by the rectangle

the present numerical method produces very thin numerical shocks with refinement in the shock-normal grid spacing but very less changes in the post-shock turbulence. In a similar vein, we find the cases $1.5c$ and $3.5c$ to be grid-converged with the cases $1.5d, e$ and $3.5d, e$, respectively, though the former cases do not meet the scale separation criterion, which is $\frac{\eta}{\delta_n} \geq 1.4$ of Tian *et al.* [159].

## 4.5 Convergence to LIA values

Scale separation, defined as $\frac{\eta_u}{\delta_s}$ poses a physical problem in shock-resolved simulations and is necessary to ensure that the shock width and the turbulence scales do not overlap. In the shock-capturing simulations where the viscous shock profile is replaced by a numerical shock, a large scale separation would imply that the numerical shock-capturing methodology does not alter the post-shock turbulence i.e., the turbulence is resolved albeit the shock is captured [81, 86]. Recently, Tian *et al.* [159] discussed extensively on this scale separation ratio, where it was defined as $\frac{\eta_u}{\delta_n}$ and used the ratio as a measure to verify the shock-capturing framework of numerical simulations. By systematic variation of $M_t$ and $Re_\lambda$, Tian *et al.* [159] were able to show convergence of Reynolds stresses obtained from shock-captured simulations to the LIA solutions which are also in agreement with the results of low $M_{t,u}$ shock-resolved simulations of Ryu and Livescu [132]. Boukharfane *et al.* [13] took a different approach where they used the similarity scaling of Donzis [26, 27] to show scale separation in their simulations and subsequently, the convergence towards LIA solutions.

We adopt the approach of [159] to discuss on the convergence to LIA values as $M_{t,u} \to 0$ (negligible nonlinearity) and $Re_{\lambda,u} \to \infty$ (towards inviscid limit) for the numerical methodology used in the current work. Figures (6.6) - (6.8) in Sect. (6.3) of Chap. (6) shows the convergence of the thermodynamic variances towards the LIA solution as the upstream turbulent Mach number, $M_{t,u}$ is reduced for the different $M_u$ cases. The convergence towards LIA indicates that there exists a sufficient scale separation between the shock wave and the incoming turbulence [90, 132, 159], even for low Taylor lengthscale Reynolds number considered in this study.

The effect of Taylor lengthscale Reynolds number on the statistics related to velocity components are discussed in detail in [81] and for the turbulent heat flux in [119]. We found similar effect for the thermodynamic variances also (see Fig. (6.10) in Sect. (6.4) of Chap. (6)), where they converge towards the LIA solution as the Reynolds number is increased. The present simulations cover only $Re_{\lambda,u} = 33$, and thus we draw inferences from the comprehensive statistics of Larsson *et al.* [81].

## 4.6 Summary

A brief description of the DNS methodology is also provided. Temporally decaying homogeneous isotropic turbulence databases are generated separately and blended together to form a sufficiently long database for statistical convergence. Taylor's hypothesis is used to specify the turbulence database as inflow condition to the STI domain. The discretized governing equations are solved using a solution adaptive finite difference method with fifth order accurate WENO scheme in the shock region and sixth order accurate central differencing scheme with Roe flux splitting form for the rest of the domain. Time advancement is done by explicit fourth order Runge-Kutta scheme. Non-reflecting boundary conditions are used at the outflow with periodic boundary conditions on the shock-parallel directions. Grid-convergence study shows that the computational domain with 384 grid points in each of the transverse directions to be sufficient for the statistics of interest. The shock-normal grid spacing, however, changes for each of the shock strength considered.

# Chapter 5

# Evolution of thermodynamic fluctuations

In this chapter, the thermodynamic variances ($\overline{\rho'^2}$, $\overline{p'^2}$, $\widetilde{T''^2}$, $\widetilde{s''^2}$) obtained from the DNS of canonical shock-turbulence interaction are compared with the LIA predictions. The density, pressure and temperature variances are normalized by the square of their respective mean downstream values ($\overline{\rho}_d^2$, $\overline{p}_d^2$, $\widetilde{T}_d^2$). The entropy variance is normalized by the square of the gas specific heat capacity at constant pressure ($c_p^2$). Additionally, the variances are scaled by the upstream turbulent kinetic energy divided by the square of the upstream mean shock-normal velocity, $\dfrac{0.5\,\overline{u'^2_{i,u}}}{\overline{u}^2_{1,u}}$. This helps to compare different cases with varying upstream turbulence intensities, $\dfrac{M_{t,u}}{(M_u - 1)}$. The streamwise coordinate is normalized by the peak energy wavenumber ($k_0$) in the upstream field. This normalization is used throughout this dissertation unless otherwise stated. For comparisons between the LIA and the DNS data, we use $f'$ and $f''$ interchangeably since they are found to be the same for this problem. The Favre averaged variance $\widetilde{f''^2}$ can be expanded in terms of its Reynolds averaged counterpart as,

$$\widetilde{f''^2} = \overline{f'^2} - \left(\frac{\overline{\rho' f'}}{\overline{\rho}}\right)^2 + \frac{\overline{\rho' f'^2}}{\overline{\rho}}, \tag{5.1}$$

where the last two terms are higher order terms with respect to the variance. Comparison of the mean and variance of entropy is shown in Fig. (5.1) which clearly shows that the higher order terms are negligible, and that the Reynolds averaged and Favre averaged statistics are the same away from the mean numerical shock.

In this study, we compare results from purely vortical turbulence with the numerical simulations, which have finite thermodynamic fluctuations upstream of the shock. Table (5.1) shows the rms values of thermodynamic fluctuations just upstream of the shock.

The values are normalized as per isentropic relations and additionally scaled by the square of the upstream turbulent Mach number as mentioned in Ref. [83]. The thermodynamic fluctuations are approximately but not perfectly isentropic in each of the cases whereas, the entropy fluctuations are almost constant between the different cases as shown in the table. As noted in Appendix G, the error due to Taylor's hypothesis is very small for the thermodynamic fluctuations. The short length of the upstream region also prevents significant modification of the fluctuation levels due to the decay of turbulence. These imply that the levels of thermodynamic fluctuations just upstream of the shock are nearly the same as in the inflow turbulence.

Table 5.1: Table of normalized rms values of thermodynamic fluctuations upstream of the shock. Density, pressure and temperature fluctuation levels increase with $M_{t,u}$ but the entropy levels remain constant

| $M_u$ | $M_{t,u}$ | $\dfrac{\rho'_{rms}}{(\overline{\rho}_u\, M_{t,u}^2)}$ | $\dfrac{p'_{rms}}{(\gamma\, \overline{p}_u\, M_{t,u}^2)}$ | $\dfrac{T'_{rms}}{([\gamma-1]\, \overline{T}_u\, M_{t,u}^2)}$ | $\dfrac{s'_{rms}}{(c_p^2\, M_{t,u}^2)}$ | $\dfrac{\theta'_{rms}}{(k_0\, \overline{a}_u\, M_{t,u}^2)}$ |
|---|---|---|---|---|---|---|
| 1.23 | 0.05 | 0.44 | 0.38 | 0.51 | 0.17 | 0.89 |
| 1.23 | 0.15 | 0.52 | 0.46 | 0.57 | 0.17 | 0.98 |
| 1.23 | 0.25 | 0.70 | 0.66 | 0.74 | 0.16 | 1.66 |
| 1.23 | 0.40 | 0.70 | 0.67 | 0.74 | 0.16 | 1.88 |
| 1.50 | 0.05 | 0.42 | 0.35 | 0.48 | 0.17 | 0.83 |
| 1.50 | 0.15 | 0.50 | 0.44 | 0.55 | 0.17 | 0.73 |
| 1.50 | 0.25 | 0.68 | 0.64 | 0.72 | 0.16 | 1.50 |
| 1.50 | 0.40 | 0.69 | 0.66 | 0.72 | 0.15 | 1.89 |
| 2.50 | 0.05 | 0.40 | 0.32 | 0.46 | 0.17 | 0.96 |
| 2.50 | 0.16 | 0.47 | 0.41 | 0.52 | 0.17 | 0.50 |
| 2.50 | 0.25 | 0.65 | 0.61 | 0.69 | 0.16 | 1.14 |
| 2.50 | 0.40 | 0.69 | 0.66 | 0.73 | 0.15 | 1.50 |
| 3.50 | 0.05 | 0.39 | 0.32 | 0.46 | 0.17 | 1.10 |
| 3.50 | 0.16 | 0.46 | 0.40 | 0.51 | 0.16 | 0.47 |
| 3.50 | 0.25 | 0.63 | 0.59 | 0.67 | 0.16 | 1.05 |
| 3.50 | 0.40 | 0.68 | 0.65 | 0.72 | 0.15 | 1.40 |

## 5.1 Spatial profiles

Spatial variation of density, pressure, temperature and entropy from the dataset of $M_{t,u}$ = 0.15 and $Re_{\lambda,u}$ = 33 is shown in Fig. (5.2). The thermodynamic variances exhibits a large

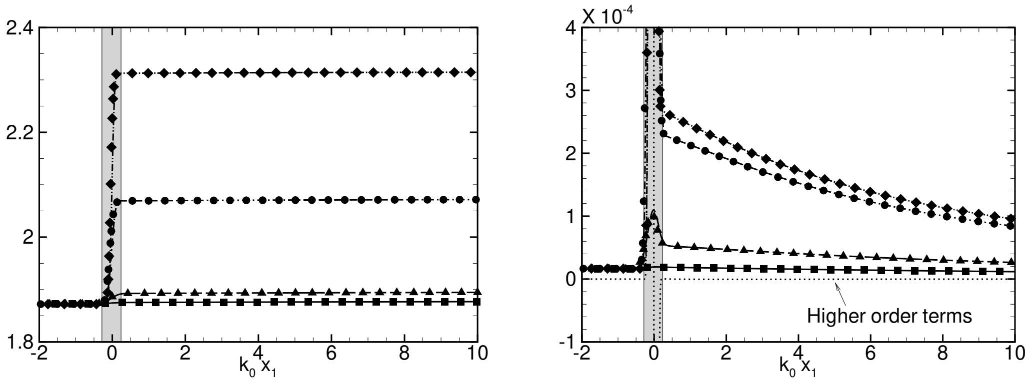


(a) Normalized mean entropy – $\overline{s}$ and $\widetilde{s}$ (b) Normalized entropy variance – $\overline{s'^2}$ and $\widetilde{s''^2}$

Figure 5.1: Spatial variation of normalized (a) mean entropy and (b) variance of entropy. The mean entropy is normalized by $c_p$ and the variance is normalized by $c_p^2$. The quantities are, however not additionally normalized by the upstream TKE as mentioned in the text. Lines represent Reynolds averaged quantities ($\overline{s}$, $\overline{s'^2}$) and symbols represent their Favre averaged counterparts ($\widetilde{s}$, $\widetilde{s''^2}$). Legend: $M_u$ = 1.23 (solid line and squares), $M_u$ = 1.50 (dashed line and triangles), $M_u$ = 2.50 (dash-dotted line and circles) and 3.5 (dash-double dotted line and diamonds). The sum of higher order terms in the variance (see (b)) is shown by a dotted line. Dataset corresponds to $M_{t,u}$ = 0.15 and $Re_{\lambda,u}$ = 33

jump at the shock wave, followed by a rapid decay in the downstream flow, except entropy variance which shows a gradual decrease in the entropy variance. There is a mismatch between LIA and DNS decay rates (prominent for the higher Mach number), but the DNS far-field values are found to be comparable to those obtained from LIA.

Figure (5.2a) presents the pressure fluctuations computed from simulations and LIA for two Mach numbers. The shocks are located at $k_0 x_1 = 0$, and the region of unsteady shock oscillations are marked by vertical lines. The pressure variance $\overline{p'^2}$ exhibits a large jump at the shock wave, followed by a rapid decay in the downstream flow. There is a mismatch between the LIA and the simulation decay rates (prominent for the higher Mach number), but the simulation far-field values are found to be comparable to those obtained from the LIA. The pressure variance obtained from the numerical simulation is higher than the LIA predictions in the range of $0^+ < k_0 x_1 < 6$. This is possibly due to non-linear effects at finite $M_t$, and are expected to vanish in the limit $M_t \to 0$. The pressure field is dominated by the pressure-dilatation effect, as per the budget data in Sect. (7.1.2), which is an inviscid mechanism. The fact that the pressure fluctuations approach a finite asymptotic value far away from the shock is entirely consistent with the notion that the shock produces a far-field radiating sound field. There are negligible pressure fluctuations in the flow upstream of the shock wave, and this is consistent with the purely vortical turbulence ($\rho_u'^{LIA} = p_u'^{LIA} = T_u'^{LIA} = s_u'^{LIA} = 0$) assumed in the linear theory.

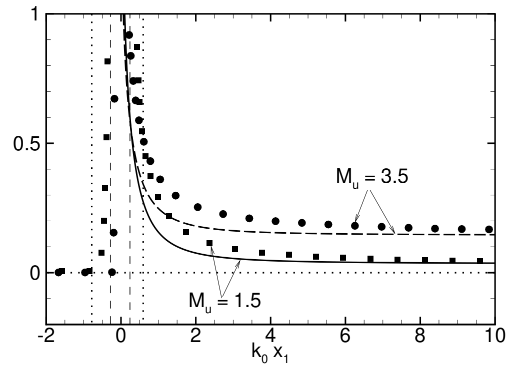


(a) Pressure

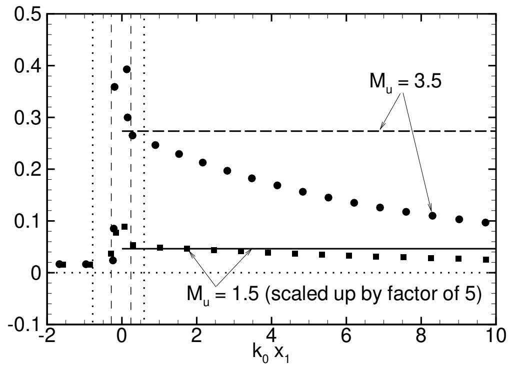


(b) Entropy

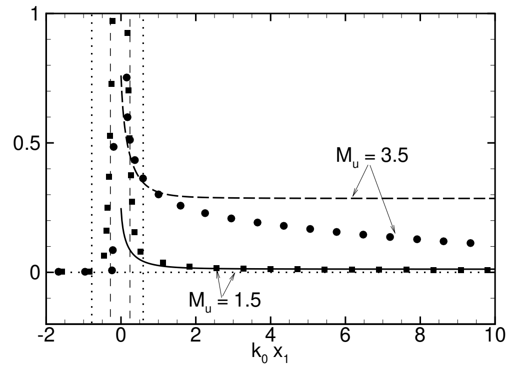


(c) Temperature

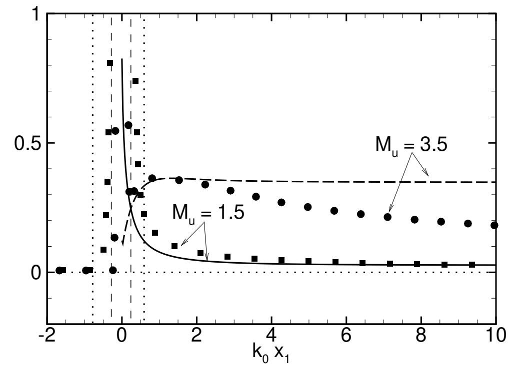


(d) Density

Figure 5.2: Spatial variation of normalized (a) pressure, (b) entropy, (c) temperature, and (d) density variances. Lines represent LIA solution and symbols represent results from the numerical simulations. Legend: $M_u = 1.50$ (solid line and squares) and 3.5 (dashed line and circles). The vertical dotted lines around $k_0 x_1 = 0$ correspond to the region of unsteady shock movement for the Mach 1.50 and 3.5 cases respectively. Dataset corresponds to $M_{t,u} = 0.15$ and $Re_{\lambda,u} = 33$

The post-shock variation of $\overline{s'^2}$ shown in Fig. (5.2b) is qualitatively different in the sense that it does not exhibit a rapid exponential decay as the pressure variance. There is a jump across the shock, as expected, followed by a gradual decrease in the downstream flow. The LIA predictions match the simulation values obtained immediately behind the shock, but do not reproduce the post-shock decay in the entropy variance. The interaction yields locally high values of $\overline{s'^2}$ in the shock region due to the unsteady oscillation of the shock wave. The same is true for the pressure variance in Fig. (5.2a).

The temperature variance shown in Fig. (5.2c) is similar to $\overline{p'^2}$ (Fig. (5.2a)), with high values across the shock that decay rapidly in the downstream flow. Additionally, the temperature fluctuations exhibit a slower but steady decrease farther away from the shock wave ($k_0 x_1 > 2$). This is more prominent in the higher Mach number case, and is akin to the decay of entropy fluctuations observed earlier. On the other hand, the temperature variance reaches an asymptotic far-field value in the LIA solution.

The density variances plotted in Fig. (5.2d) exhibit different qualitative variation at Mach 1.5 and 3.5. At the lower Mach number, it attains relatively high values across the shock, followed by a rapid decay in the downstream flow, similar to pressure and temperature variances presented earlier. LIA results, once again, compare well with the DNS data, similar to pressure and temperature variances presented earlier. At the higher Mach number, the simulation density variance has a non-monotonic variation behind the shock, with a peak value around $k_0 x_1 = 1$. The trend is similar to that of the shock-normal Reynolds stresses [81, 83, 86, 98] and the turbulent energy flux [119], and is also observed in LIA. The LIA gives low density fluctuations in the near-field ($k_0 x_1 = 0^+$) and it increases rapidly to high far-field values. As earlier, the linear theory results reach an asymptotic finite $\overline{\rho'^2}$ far away from the shock, whereas the simulation data shows a steady viscous decay downstream of the local peak behind the shock wave.

### 5.1.1 Comparison with viscous LIA

Reference is made to App. A for details on the viscous LIA used in this section. The framework of viscous LIA used here is a work in progress and thus used as a demonstrative tool than as a complete analysis of the problem. We consider the post-shock entropy fluctuations to be of the following form for the viscous fluid,

$$\frac{1}{A_v}\frac{s'_d}{c_p} = -Q_c \exp\left[i\,\bar{\mathbf{k}}\,x_1\right] \exp\left[-\left(\frac{4}{3}\right)\left(\frac{1}{\mathrm{Re}_{k_0}}\right)\left(\frac{\bar{\mathbf{k}}}{k_0}\right)\bar{\mathbf{k}}\,x_1\right] \tag{5.2}$$

where the effect of the viscous term is shown in the exponent containing $Re_{k_0}$. Here, $Re_{k_0} = \dfrac{\overline{u}}{\overline{\nu}\,k_0}$ is the Reynolds number based on the peak energy wavelength of the upstream turbulence. In essence, we have non-dimensionalized the argument of the viscous term in Eq. (5.2) as a Reynolds number. The post-shock entropy variance is then computed as

$$\frac{\overline{s'^2_d}}{c_p^2} = 4\,\pi \int_{|\mathbf{k}|=0}^{\infty} \int_{\psi=0}^{\pi/2} E_{ss,d}\,|\mathbf{k}|^2 \sin(\psi)\,d\psi\,d|\mathbf{k}|, \tag{5.3}$$

where

$$E_{ss,d} = |Q_c|^2 \exp\left[-\left(\frac{8}{3}\right)\left(\frac{1}{\mathrm{Re}_{k_0}}\right)\left(\frac{\bar{\mathbf{k}}}{k_0}\right)\bar{\mathbf{k}}\,x_1\right]|A_v|^2, \tag{5.4}$$

with $Re_{k_0}$ computed using post-shock values.

Figure 5.3 plots the spatial variation of entropy variance computed using constant values of $Re_{k_0}$ in the viscous LIA formulation (Eq. (5.3)) and compares the predictions against the DNS solutions for the case of $M_u = 3.50$. The upstream $Re_{k_0}$ from the DNS is approximately 45 for all of the cases and the post-shock $Re_{k_0}$ varies between 70 - 130 depending on the local $M_t$ value. The viscous LIA prediction for $Re_{k_0} = 1000$ matches the entropy variance of $M_{t,u} = 0.05$ case, whereas the predictions of $Re_{k_0} = 30$ are closer to the other $M_{t,u}$ cases, at least in the far-field region ($k_0 x_1 > 10$). A possible reason for this behavior is that the viscous dissipation for $M_{t,u} = 0.05$ is very small compared to the other $M_{t,u}$ cases ($\epsilon \sim O(M_t^3)$). However, we are not sure of the exact mechanism yet.

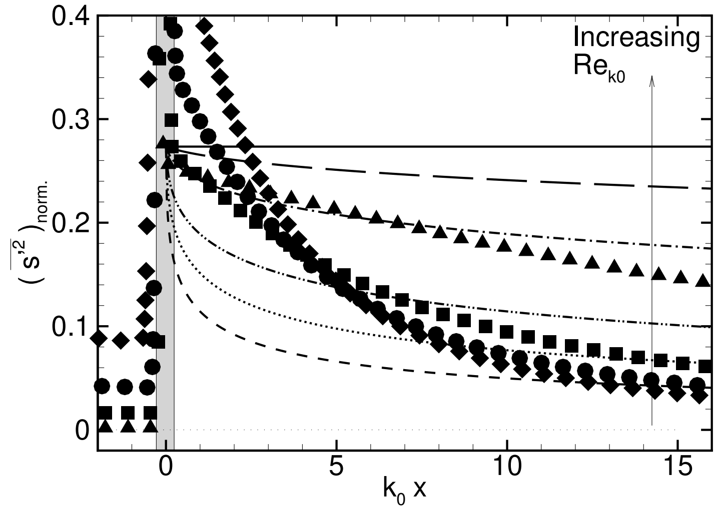


Figure 5.3: Spatial variation of the normalized entropy variance for the case of $M_u = 3.50$, $Re_{\lambda,u} = 33$ and varying $M_{t,u}$. The entropy variance is normalized by the square of the gas specific heat capacity at constant pressure ($c_p^2$) and the normalized upstream TKE. Symbols correspond to DNS solutions and the lines represent viscous LIA solutions computed as per Eq. (5.3) shown above. The region of unsteady shock movement for $M_{t,u} = 0.15$ is shown by the grey band. Legend: DNS - $M_{t,u} = 0.05$ (triangles), 0.15 (squares), 0.25 (circles), and 0.40 (diamonds). LIA - $Re_{k_0} = 10$ (dashed), 30 (dotted), 100 (dash-double dotted), 1000 (dash-dotted), 10000 (long dashed) and $\infty$ (solid)

The post-shock amplification (at $k_0 x_1 = 0^+$) predicted by the current formulation of the viscous LIA remains the same for all values of $Re_{k_0}$ and is slightly higher than its DNS counterpart for the $M_{t,u} = 0.05$ case. For increasing $M_{t,u}$ values, the DNS shows larger values than the LIA predictions. This is probably due to the effect of the neglected non-linear terms and also due to the consideration of only purely vortical turbulence in the viscous LIA. Including the effects of acoustic and entropy fluctuations in the upstream turbulence have been found to yield larger post-shock values compared to the purely vortical case [98, 99]. Similar results are obtained for the vorticity variances.

## 5.2 Kovásznay mode decomposition

Kovásznay showed that small perturbations in a compressible turbulent flow can be decomposed into vortical, entropy and acoustic components, which evolve independently in the linear inviscid limit. This forms the foundation of the LIA framework, and is used here to decompose the post-shock thermodynamic fluctuations namely, density ($\rho'$), pressure ($p'$), temperature ($T'$), and entropy ($s'$) into their respective component modes. The objective is to use the modal decomposition to gain insight into the thermodynamic fluctuations generated behind the shock wave and their variation with the shock Mach number.

In the linear limit, the post-shock thermodynamic field comprises of only the acoustic and the entropy modes. It is recalled that the acoustic mode consists of isentropic pressure, density and temperature fluctuations, and a dilatational velocity field. The entropy mode consists of isobaric temperature and density fluctuations. The post-shock entropy and the pressure fluctuations correspond to the pure entropy and the acoustic modes, respectively in the linear limit.

We note that the different Kovásznay modes are governed by different physical processes. Hence, identifying the modal contributions allows us to investigate the physics behind the observed trends in the post-shock thermodynamic field. A similar Kovásznay mode decomposition of the turbulent energy flux is reported in [118], where the modal decomposition is used to investigate the peak positive turbulent energy flux in the post-shock flow. The modal contributions are also used successfully to develop advanced turbulence models for the turbulent heat flux in canonical shock-turbulence interaction [117] and a variable turbulent Prandtl number model for shock-boundary layer flows [131].

The LIA solution in the post-shock region is a superposition of acoustic, entropy and vorticity waves (denoted by the subscripts $a$, $e$ and $v$, respectively), with a collection of orientation angles and wavelengths. The density variance is thus given by,

$$\overline{\rho'_d \rho'_d} = \overline{(\rho'_{d,a} + \rho'_{d,e})^2} = \overline{\rho'_{d,a}\rho'_{d,a}} + \overline{\rho'_{d,e}\rho'_{d,e}} + 2\,\overline{\rho'_{d,a}\rho'_{d,e}} \tag{5.5}$$

which allows us to decompose the full density variance into a pure acoustic contribution (the first term), a pure entropy contribution (the second term), and a combined acoustic / entropy contribution (the third term). There is no pure vorticity contribution ($\rho'_{d,v} = 0$) in the density variance. These correlations are hereby denoted as *aa*, *ee*, *ae*, respectively. A similar decomposition is possible for the other quantities that are defined by multiple modes.

The 2D planar wave solution of the post-shock density fluctuation is given by (same as Eq. (3.17d) in Chapter (3)),

$$\frac{1}{A_v}\frac{\rho'_d}{\bar{\rho}_d} = \left[\underbrace{\frac{K_c}{\gamma}\, e^{i\,\tilde{\mathbf{k}}\,x}}_{\text{acoustic}} + \underbrace{Q_c\, e^{i\,\bar{\mathbf{k}}\,x}}_{\text{entropy}}\right] e^{i\,|\mathbf{k}|\,(l\,y - m\,\bar{u}_u\,t)}, \tag{5.6}$$

and the post-shock density variance is obtained from the integration of all such waves,

$$\frac{\overline{\rho'^2_d}}{\bar{\rho}^2_d} = 4\,\pi \int_{|\mathbf{k}|=0}^{\infty} \int_{\psi=0}^{\pi/2} E_{\rho\rho,d}\, |\mathbf{k}|^2 \sin(\psi)\, d\psi\, d|\mathbf{k}|, \tag{5.7}$$

where

$$E_{\rho\rho,d} = \left[\frac{1}{\gamma^2}\,|K_c|^2 + |Q_c|^2 + \frac{1}{\gamma}\,|K_c\, Q_c^*|\, e^{i\,(\tilde{\mathbf{k}}-\bar{\mathbf{k}})\,x} + \frac{1}{\gamma}\,|K_c^*\, Q_c|\, e^{-i\,(\tilde{\mathbf{k}}-\bar{\mathbf{k}})\,x}\right] |A_v|^2, \quad \text{for} \quad 0 < \psi < \psi_c, \tag{5.8a}$$

$$E_{\rho\rho,d} = \left[\frac{1}{\gamma^2}\,|K_c|^2\, e^{i\,(\tilde{\mathbf{k}}-\tilde{\mathbf{k}}^*)\,x} + |Q_c|^2 + \frac{1}{\gamma}\,|K_c\, Q_c^*|\, e^{i\,(\tilde{\mathbf{k}}-\bar{\mathbf{k}})\,x} + \frac{1}{\gamma}\,|K_c^*\, Q_c|\, e^{-i\,(\tilde{\mathbf{k}}^*-\bar{\mathbf{k}})\,x}\right] |A_v|^2, \quad \text{for} \quad \psi_c < \psi < \frac{\pi}{2}, \tag{5.8b}$$

with $\tilde{\mathbf{k}}^*$ being the complex conjugate of the acoustic mode wavenumber and $\psi_c$ is the critical angle. In a similar fashion, the *aa*, *ee*, *ae* components of the density variance are obtained as,

$$\frac{\overline{\rho'^2_{\beta\beta,d}}}{\bar{\rho}^2_d} = 4\,\pi \int_{|\mathbf{k}|=0}^{\infty} \int_{\psi=0}^{\pi/2} E_{\rho_\beta\rho_\beta,d}\, |\mathbf{k}|^2 \sin(\psi)\, d\psi\, d|\mathbf{k}|, \tag{5.9}$$

where $\beta = a$ or $e$. The energy density functions ($E_{\rho_\beta\,\rho_\beta}$) for each of the correlations in Eq. (5.5) is given by,

$$E_{\rho_a\rho_a,d} = \frac{1}{\gamma^2}\,|K_c|^2\, e^{i\,(\tilde{\mathbf{k}}-\tilde{\mathbf{k}}^*)\,x}\, |A_v|^2, \tag{5.10a}$$

$$E_{\rho_e\rho_e,d} = |Q_c|^2\, |A_v|^2, \tag{5.10b}$$

$$E_{\rho_a\rho_e,d} = \frac{1}{2\,\gamma}\left[|K_c\, Q_c^*|\, e^{i\,(\tilde{\mathbf{k}}-\bar{\mathbf{k}})\,x} + |K_c^*\, Q_c|\, e^{-i\,(\tilde{\mathbf{k}}^*-\bar{\mathbf{k}})\,x}\right] |A_v|^2, \tag{5.10c}$$

with the superscript $*$ denoting the complex conjugate of the quantity. It is to be noted that $(\tilde{\mathbf{k}} - \tilde{\mathbf{k}}^*)$ is non-zero only for the waves, whose orientation angles ($\psi$) are greater than the critical angle ($\psi_c$). The same procedure is also applied to the temperature variance to obtain its corresponding *aa*, *ee*, *ae* components of the correlation.

The Kovásznay modes of entropy and acoustics are fundamentally different in terms of their evolution behind the shock wave. As per LIA, the majority of the acoustic energy decays with distance from the shock wave; in particular, those associated with the single-wave interactions exceeding the critical angle. On the other hand, the entropy mode generated at the shock propagates downstream without any change in amplitude as per the linear inviscid framework adopted by LIA. The thermodynamic field, with contribution from the acoustic and the entropy modes, exhibit a combination of these trends, as seen in the Kovásznay mode components of density and temperature variances shown in Fig. (5.4). The acoustic components have an exponential variation with $x_1$, while the entropy component is constant in the downstream flow. The acoustic-acoustic and entropy-entropy components are positive, while the correlation between the acoustic and the entropy modes can be positive or negative. In the acoustic-adjustment region ($0 < k_0 x_1 < 2$), the balance between all the three components determine the behavior of $\overline{\rho'^2}$ and $\overline{T'^2}$.

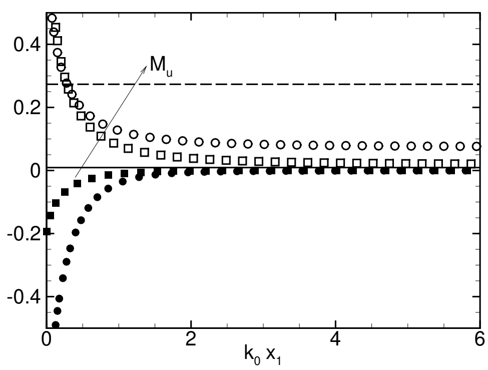


(a) Density

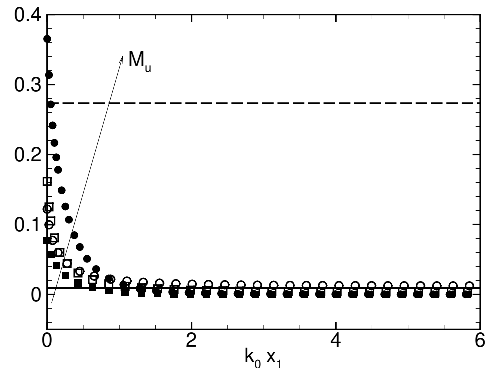


(b) Temperature

Figure 5.4: Spatial variation of normalized Kovásznay mode components of (a) density and (b) temperature variances. Legend: $M_u = 1.50$ (solid line and squares) and 3.5 (dashed line and circles). The entropy-entropy component is represented by solid lines, the acoustic-acoustic component is by open symbols, and the acoustic-entropy correlations is by filled symbols

The spatial variation of the temperature variance is explained in terms of the Kovásznay modes in Fig. (5.4b). The Kovásznay mode decomposition of the temperature variance is similar to the decomposition of density variance given by Eqs. (5.5) and (5.9). The energy density functions ($E_{T_\beta T_\beta}$) for the $aa$, $ee$, $ae$ components of the correlation are given by,

$$E_{T_a T_a,d} = \left(\frac{\gamma - 1}{\gamma}\right)^2 |K_c|^2 \, e^{i\,(\tilde{\mathbf{k}} - \tilde{\mathbf{k}}^*)\,x} \, |A_v|^2, \tag{5.11a}$$

$$E_{T_e T_e,d} = |Q_c|^2 \, |A_v|^2, \tag{5.11b}$$

$$E_{T_a T_e,d} = -\left(\frac{\gamma - 1}{2\gamma}\right) \left[ |K_c \, Q_c^*| \, e^{i\,(\tilde{\mathbf{k}} - \bar{\mathbf{k}})\,x} + |K_c^* \, Q_c| \, e^{-i\,(\tilde{\mathbf{k}}^* - \bar{\mathbf{k}})\,x} \right] |A_v|^2, \tag{5.11c}$$

which are similar to the energy density functions of the density variance, except for the additional factor of $(\gamma - 1)$. The results are qualitatively similar to that for Mach 1.5 provided in Ref. [118], except for the large entropy component at the higher Mach number. The farfield $\overline{T'^2}$ is almost entirely given by the entropy-entropy component, which is invariant in $k_0 x_1$ as per the inviscid analysis. The post-shock rapid decay in $\overline{T'^2}$ is due to the acoustic-acoustic and acoustic-entropic components, both related to the acoustic mode generated at the shock wave. All the components are positive for the temperature fluctuations, giving a large value at the shock and they together give a monotonic decay of $\overline{T'^2}$ to its far-field value due to the decrease in the acoustic components along the shock-normal direction.

The Kovásznay mode decomposition of the density variance shown in Fig. (5.4a) explains the non-monotonic behavior observed behind strong shocks. The components of the density variance are obtained from Eqs. (5.9) and (5.10a) - (5.10c). As expected the acoustic components have an exponential variation with $x_1$, while the entropy component is constant in the downstream flow. The acoustic-acoustic and entropy-entropy components are positive, while the correlation between the acoustic and the entropy modes has a negative contribution to the density variance. It is to be noted that the amplitude, $Q_c$ is negative, which results in a negative value for the acoustic-entropy correlation in the density variance and a positive value in the temperature variance. At low Mach numbers, the variation of $\overline{\rho'^2}$ in the post-shock field follows a monotonic decay due to the small magnitude of the acoustic-entropic component. By comparison, the large negative acoustic-entropic contribution to $\overline{\rho'^2}$ at Mach 3.5 counters the positive pure-acoustic component resulting in a non-monotonic variation behind the shock wave. This, along with the viscous decay in the farfield, results in the local peak in the density variance observed in the Mach 3.5 simulation data plotted in Fig. (5.2d).

## 5.3 Near-field and far-field values by spatial extrapolation

LIA yields solutions as a function of the upstream Mach number for a particular gas but neglects nonlinear and viscous mechanisms. DNS, on the other hand includes both of these effects, and provides solutions which are functions of $M_u$, $M_{t,u}$ and $Re_{\lambda,u}$. Thus, it is necessary to extract DNS data in a way that it makes sense when comparing with LIA data. Near-field ($x_1 = 0^+$) and farfield ($x_1 \to \infty$) are the two locations of practical interest where, the former is of interest to shock-induced mixing applications and the latter is for farfield noise predictions. Comparison of the near-field solutions between

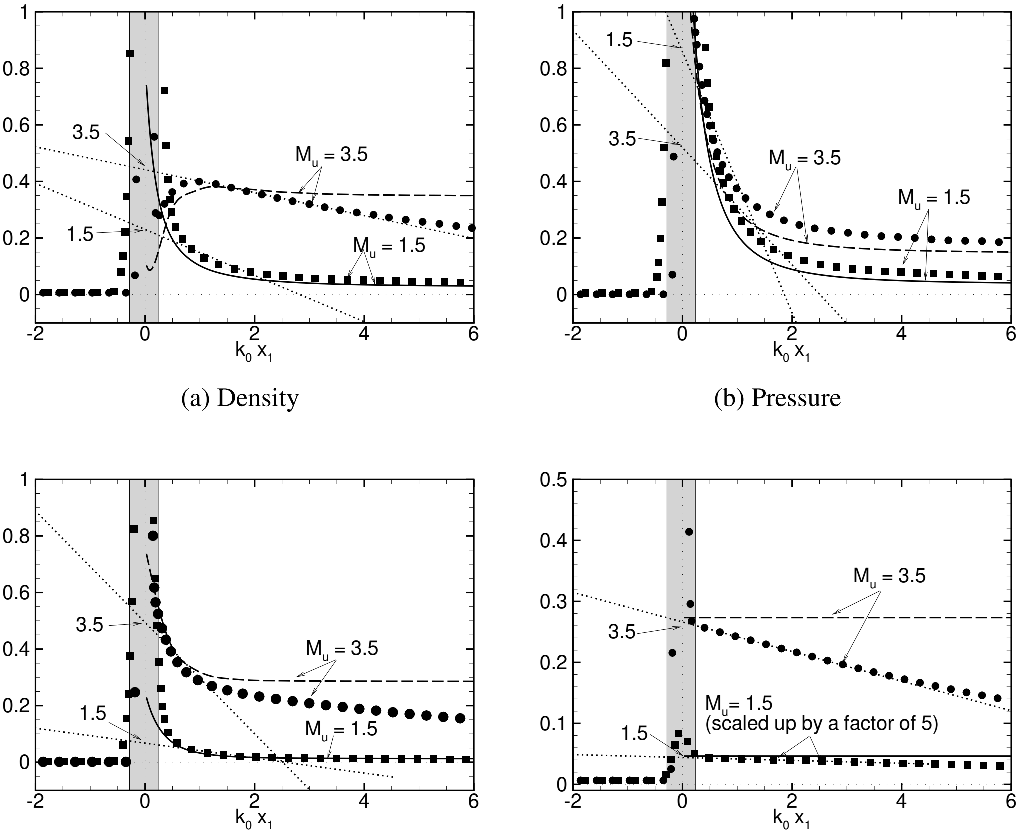


(a) Density (b) Pressure

(c) Temperature (d) Entropy

Figure 5.5: Spatial variation of normalized variances of (a) density, (b) pressure, (c) temperature and (d) entropy from the $M_u = 1.50$ and 3.50 of the $M_{t,u} = 0.15$ and $Re_{\lambda,u} = 33$ dataset. Solid lines correspond to LIA results and the symbols represent DNS data. The dotted lines extending to the center of the mean shock are the linear extrapolations. The grey band shows the region of mean shock movement for the $M_u = 3.50$ case

the two methods requires the shock to be approximated as a discontinuity in DNS and for the farfield solutions, the viscous effects in DNS should be neglected. The existing procedures are used to extract only farfield data by spatial extrapolation [81, 118, 119] or by identifying the location behind the shock where the acoustic transients have died out [26].

Figure (5.5) shows the spatial variation of normalized density, pressure, temperature and entropy variances from DNS and LIA along with extrapolated values obtained by performing a linear least-squares fit over the DNS data from $0.5\pi \leq k_0 x_1 \leq 2\pi$. The LIA solutions are obtained by integrating over all the waves in the post-shock field, similar to Eq. (5.7), with the respective energy density functions. The spatial extrapolation to the center of the mean shock is used extensively in the literature, for example [81, 118, 119], when comparing farfield values between LIA and DNS. This procedure works well for velocity related quantities which have a non-monotonic variation, i.e., a peak value behind the mean shock thickness and for profiles with gradual variations. It has been found to predict farfield values very well but not the values immediately behind the shock, especially when there is a rapid variation such as those found in the pressure and the temperature variances at low Mach numbers. The farfield values, thus estimated are also in fact the values, one would obtain when there is no viscous decay.

The true farfield value which is affected by the viscous decay has to be computed with a different method; one common procedure is to take average over the values in a small portion at the end of the domain considered. The near-field values, however, are poorly estimated by spatial extrapolation. There have been attempts to perform the linear extrapolation on a log-scale and estimate the near-field fluctuations, since the variances with rapid decay are very similar to exponential functions. The near-field variances were still poorly estimated. This indicates that a new procedure is required to estimate near-field values accurately, even though the farfield variances can be predicted (to a reasonable accuracy) using the spatial extrapolation method.

## 5.4 Statistics at the shock

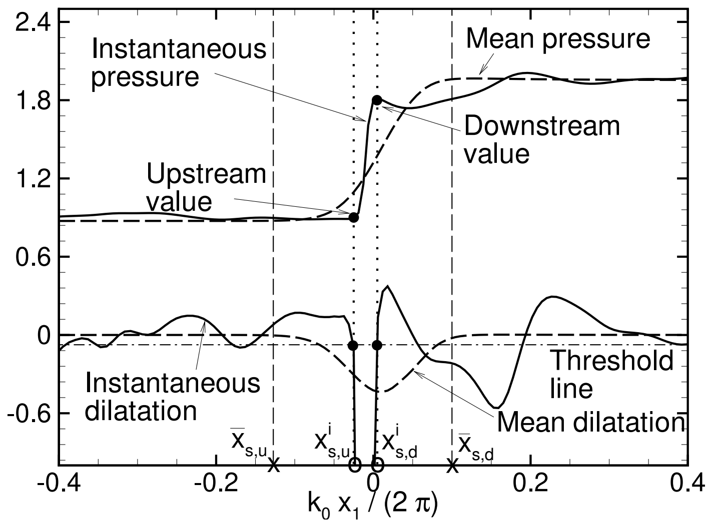


Figure 5.6: Representative schematic showing instantaneous (solid lines) and mean (dashed lines) profiles. The dilatation value used as the threshold to identify the extent of the instantaneous shock is shown by a horizontal dash-dotted line. The vertical dashed lines represent the mean shock thickness and the vertical dotted lines represent the instantaneous shock thickness. The edges of the instantaneous shock are denoted by $(x^i_{s,u}, x^i_{s,d})$ and that of the mean shock are shown by $(\overline{x}_{s,u}, \overline{x}_{s,d})$

The different statistics presented in Figs. (4.8) and (4.9) are computed at fixed $x_1$ by averaging over the transverse planes for a number of flow realizations. This conventional averaging gives a mean shock thickness determined by the unsteady oscillations of the shock. The turbulent statistics computed in the region of unsteady shock is governed by the Rankine-Hugoniot jump values across the unsteady shock wave. Larsson *et al.* [81] showed the contribution of the unsteady shock oscillations for the shock-normal Reynolds stress to be very large inside the shock. This effect is also seen in other statistics and the values are found to be large if one would compute them at the edges of the mean shock. By comparison, statistics conditioned by the local position of the instantaneous shock wave, is unaffected by the shock oscillations.

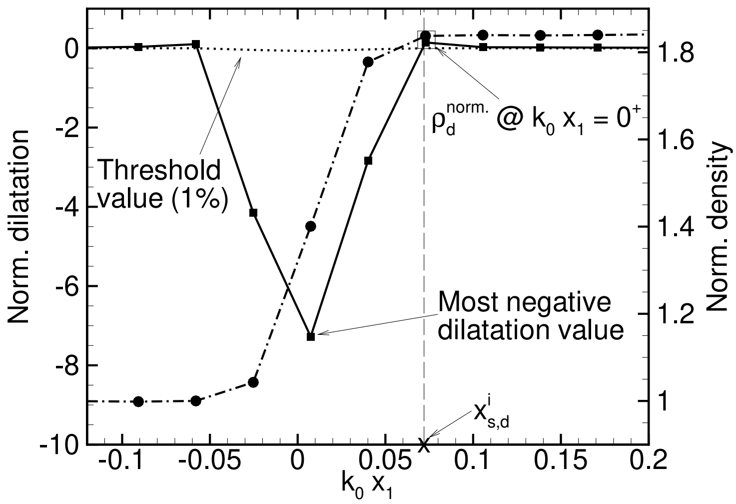


Figure 5.7: Schematic reproduced from a flowfield in the case of $M_u = 1.50$, $M_{t,u} = 0.15$ and $Re_{\lambda,u} = 33$ to elaborate on the threshold method. Dilatation (solid line with squares) is normalized by $k_0\overline{u}_{1,u}$ whose scale is given at the left axis. Density (dash-dotted line with circles) is scaled by $\overline{\rho}_u$ and its values are given at the right axis. The symbol $x$ marks the instantaneous downstream location ($x^i_{s,d}$) obtained using the 1% threshold value, and is extended to the density curve by a thin dashed line. The grid point enclosed by the hollow rectangle is the location from which the values are computed as $k_0x_1 = 0^+$ (or near-field) values

We employ a novel method to compute statistics at the instantaneous shock locations instead at the edge of the mean shock location. A threshold value based on the instantaneous dilatation is used to identify the shock thickness in the flowfield. This is similar to the dilatation-based shock-sensors used in the simulation, but in a much simpler form.

A threshold value of 1% of the most negative dilatation in an instantaneous flow field is used (see Fig. (5.7)) to identify the bounds of the shock ($x^i_{s,u}$, $x^i_{s,d}$). The instantaneous numerical shock thickness is much smaller than the mean shock thickness (see Fig. (5.6)) defined by $(\overline{x}_{s,u}, \overline{x}_{s,d})$. The post-shock statistics are then computed by obtaining values at the downstream edge ($x^i_{s,d}$) of the instantaneous shock wave for each $(x_2, x_3, t)$, and then by averaging suitably. This corresponds to the nearfield location defined in linear interaction analysis (discussed below) and is denoted by $k_0 x_1 = 0^+$.

Using this procedure, termed as the threshold method, we get finite values of the post-shock variances, instead of the very large values obtained in the conventional averaging method due to the inherent effect of unsteady shock oscillations (for example, Fig. (4.9)). We have assessed the accuracy / convergence of the method and found it to be about 10% in a series of consecutive grid spacings.

## 5.5 Summary

The spatial variation of the thermodynamic variances are compared between LIA and DNS solutions. Kovásznay mode decomposition of LIA statistics is used to explain the nature of the profiles. Far-field and nearfield fluctuation levels are of practical interest. The existing methods do not provide nearfield values correctly. A new method using dilatation value as a threshold is used to compute nearfield values from the DNS data. In the next chapter, we use this technique to precisely compute the nearfield values.

# Chapter 6

# Effect of the governing parameters

The post-shock thermodynamic field as a function of upstream flow Mach number $M_u$, turbulent Mach number $M_{t,u}$ and Taylor-scale Reynolds number $Re_{\lambda,u}$ is discussed in this chapter. The present simulations along with the DNS dataset of Larsson *et al.* [81, 83] are used to compare with the LIA predictions for varying shock strengths and turbulence intensities. The effect of $Re_\lambda$ on the thermodynamic variances is studied using the datasets presented in Refs. [83] and [81]. The present simulations cover 12 new cases with varying $M_t$ for the four different Mach numbers and $Re_{\lambda,u} \approx 30$, which are not available in the datasets of Larsson *et al.*

## 6.1 Effect of flow Mach number at various locations

Figure (6.1) shows the thermodynamic variances from LIA and DNS, taken at different locations. The LIA solutions are calculated using the integration,

$$\frac{\overline{f_d'^2}}{\overline{f}_d^2} = 4\pi \int_{|\mathbf{k}|=0}^{\infty} \int_{\psi=0}^{\pi/2} E_{ff,d}\, |\mathbf{k}|^2 \sin(\psi)\, d\psi\, d|\mathbf{k}|, \tag{6.1}$$

where $f$ could be either $\rho$, $p$, or $T$. The corresponding energy density functions for each of the thermodynamic quantities are,

$$E_{\rho\rho,d} = \left[\frac{1}{\gamma^2} |K_c|^2 e^{i(\tilde{\mathbf{k}}-\tilde{\mathbf{k}}^*)x} + |Q_c|^2 + \frac{1}{\gamma} |K_c\, Q_c^*| e^{i(\tilde{\mathbf{k}}-\bar{\mathbf{k}})x} + \frac{1}{\gamma} |K_c^*\, Q_c| e^{-i(\tilde{\mathbf{k}}^*-\bar{\mathbf{k}})x}\right] |A_v|^2, \tag{6.2a}$$

$$E_{pp,d} = |K_c|^2 e^{i(\tilde{\mathbf{k}}-\tilde{\mathbf{k}}^*)x} |A_v|^2, \tag{6.2b}$$

$$E_{TT,d} = \left[\left(\frac{\gamma-1}{\gamma}\right)^2 |K_c|^2 e^{i(\tilde{\mathbf{k}}-\tilde{\mathbf{k}}^*)x} + |Q_c|^2 - \left(\frac{\gamma-1}{\gamma}\right) |K_c\, Q_c^*| e^{i(\tilde{\mathbf{k}}-\bar{\mathbf{k}})x} \quad \ldots\right.$$

$$\left. \ldots - \left(\frac{\gamma-1}{\gamma}\right) |K_c^*\, Q_c| e^{-i(\tilde{\mathbf{k}}^*-\bar{\mathbf{k}})x}\right] |A_v|^2, \tag{6.2c}$$

$$E_{ss,d} = |Q_c|^2 |A_v|^2, \tag{6.2d}$$

where the term, $(\tilde{\mathbf{k}} - \tilde{\mathbf{k}}^*)$ is non-zero only for $\psi > \psi_c$ (non-propagative regime). Except for the entropy variance, which is constant in space, the other thermodynamic variables display an exponential variation along the streamwise direction. Note that the entropy variance is also similar to Eq. (6.1), except that it is normalized by $c_p^2$ instead of the square of its post-shock mean value.

Ideally, we would like to assess the far-field LIA predictions, but the viscous decay in the simulation data makes this difficult; we therefore perform the assessment at multiple $x_1$ locations between $k_0 x_1 = 1$ and farther downstream. The current DNS simulations are for an upstream turbulent Mach number of 0.15, which is lower than that in the Larsson *et al.* [81] cases ($M_{t,u} = 0.22$) used for comparison. The present simulations also differ in terms of the Taylor-scale Reynolds number from the cases of Larsson *et al.* [81] and thus, the spatial decay in the post-shock region between the two datasets are slightly different. The pressure and the entropy variances obtained from the current simulations (discussed below) are arguably closer to the LIA results, which are valid in the limit of $M_t \to 0$.

First, we study the post-shock pressure variance as a function of shock strength in Fig. (6.1a). The results show a monotonic increase in $\overline{p'^2}$ with shock strength, and the simulation data, irrespective of the location, match the trend observed in the LIA predictions (computed using Eq. (6.1) and (6.2b)). In fact, the higher $k_0 x_1$ values are closer to the LIA curves, which collapse to the asymptotic far-field solution predicted by the linear theory. There are discrepancies at lower Mach number, as well as at lower $k_0 x_1$ (for higher Mach numbers), which are similar to those presented in Fig. (5.2a). These discrepancies are attributed to the nonlinear effects due to finite $M_t$ in the simulations.

The entropy variance plotted in Fig. (6.1b) also shows a monotonically increasing trend with shock strength, but it seems to saturate at high Mach numbers. LIA predict a single value of $\overline{s'^2}$ for a given Mach number (computed using Eq. (6.1) and (6.2d)), whereas the entropy variance in the DNS continuously decreases with distance from the shock wave, owing to viscous effects. The far-field DNS data does not collapse, unlike the pressure variance; in fact, the decay appears to be stronger at high Mach number, indicating a higher viscous effect behind stronger shocks. Comparing the $k_0 x_1 = 1$ values of the entropy variance, there is excellent match between DNS data and LIA predictions, for the entire range of Mach numbers. The only exception is at low Mach numbers ($M = 1.23/1.27$), where the DNS data is under-predicted by the linear theory. This could possibly be a result of the small amount of entropy fluctuations in the upstream flow, which is not accounted for in the LIA predictions.

The variation of $\overline{p'^2}$ and $\overline{s'^2}$ at low Mach numbers show interesting differences. The post-shock entropy fluctuations take very low values for transonic shock waves, whereas

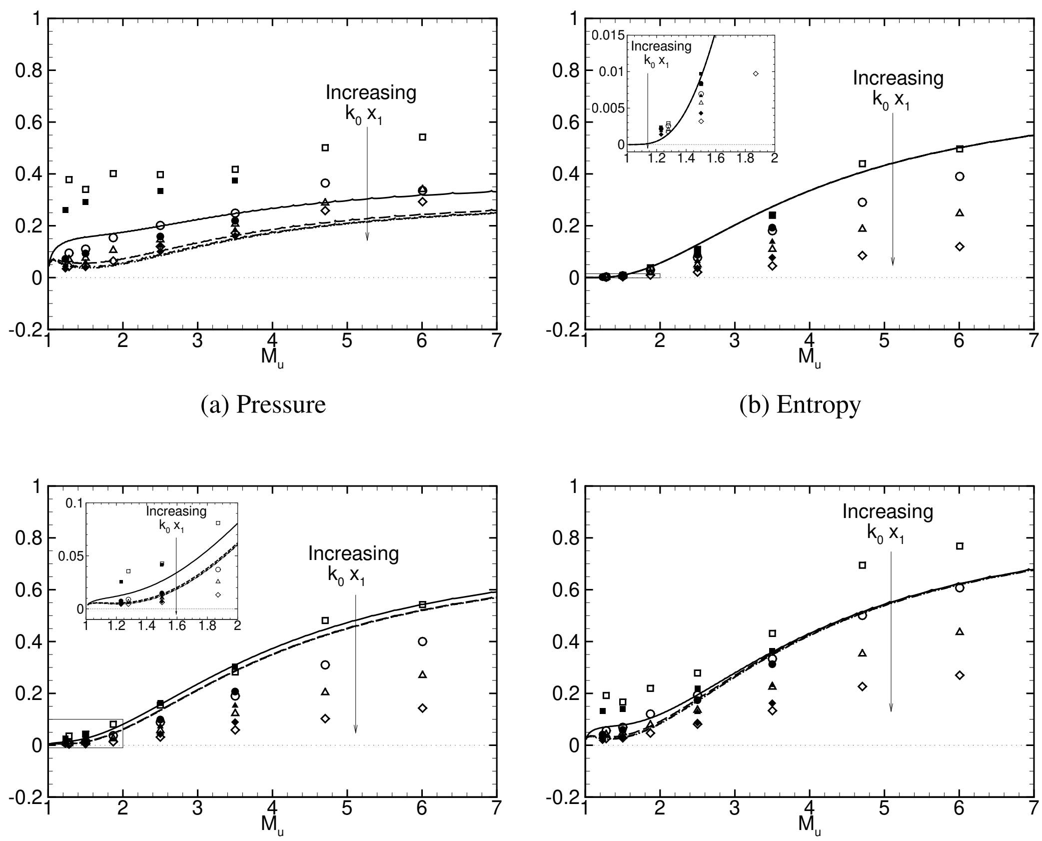


(a) Pressure

(b) Entropy

(c) Temperature

(d) Density

Figure 6.1: Variation of normalized (a) pressure, (b) entropy, (c) temperature, and (d) density variances at four different downstream locations from LIA (lines) and DNS (symbols): $k_0x_1 = 1$ (solid, squares), 3 (dashed, circles), 6 (dash-dotted, triangles), 12 (dash-double dotted, diamonds). Open symbols are from data of Ref. [81] for the cases of $M_{t,u} = 0.22$, $Re_{\lambda,u} = 40$ and filled symbols are from present simulations

the pressure fluctuations increase rapidly to values that are two or more orders in magnitude higher than $\overline{s'^2}$ at comparable Mach numbers. This has important consequences on the thermodynamic fluctuations, which have contributions from both the acoustic and the entropy modes. Further, the far-field pressure variance appears to saturate in the range $1.2 < M_u < 1.4$, before rising again for higher Mach numbers. Similar trends are also observed in other thermodynamic variances, as discussed subsequently.

A comparison of the temperature fluctuations computed at different streamwise locations in Fig. (6.1c) shows an increase with shock strength, except for a small range of non-monotonic variation near Mach 1.2. The LIA results (computed using Eq. (6.1) and (6.2c)) are qualitatively similar to the pressure variance, with the different $k_0x_1$ curves collapsing to the far-field value of $\overline{T'^2}$. The DNS data, by comparison, exhibits the steady decrease with $k_0x_1$, akin to the entropy variance plotted in Fig. (6.1b), especially at high Mach numbers. In spite of the scatter, the data points follows the trend in the LIA curves well, for the entire range of Mach numbers.

Figure (6.1d) plots the variation of density fluctuations with Mach number at different locations downstream of the shock. All the LIA curves (computed using Eq. (6.1) and (6.2a)) converge to the far-field $\overline{\rho'^2}$ values, except for minor variations at low Mach numbers. As expected, the density variance increases with shock strength, but saturates in the limit of $M_u \to \infty$. Interestingly, LIA predicts that the post-shock fluctuations in pressure, density and temperature scale with their respective post-shock mean values. For a fixed upstream thermodynamic state, the mean pressure and temperature continue to increase at high Mach numbers, and the same is true for the corresponding fluctuations. By comparison, a finite asymptotic density jump in the hypersonic limit results in a finite $\rho'/\overline{\rho}$ as $M_u \to \infty$.

The DNS data points at the different spatial locations follow the LIA trend with increasing Mach number. The variations are similar to that of the temperature fluctuations shown in Fig. (6.1c), such that the LIA values are lower than DNS for locations closer to the shock, and are larger than the DNS values further downstream. Once again, the scatter in the DNS data is due to viscous effects, which appear to increase with Mach number as the magnitude of the post-shock density variance increases.

## 6.2 Near-field variation of thermodynamic variances

Figure (6.2) presents the LIA near-field ($k_0x_1 = 0^+$) predictions, where the pressure variance shown in Fig. (6.2a) is the value prior to the exponential decay, and it is $4-5$ times larger than that at $k_0x_1 = 1$ presented in Fig. (6.1a), especially at low Mach numbers.

At high Mach numbers, the near-field pressure fluctuations are found to asymptote to a constant value. The near-field entropy variance (Fig. (6.2b)) is identical to the far-field values, owing to the zero streamwise variation in $\overline{s'^2}$ as predicted by LIA.

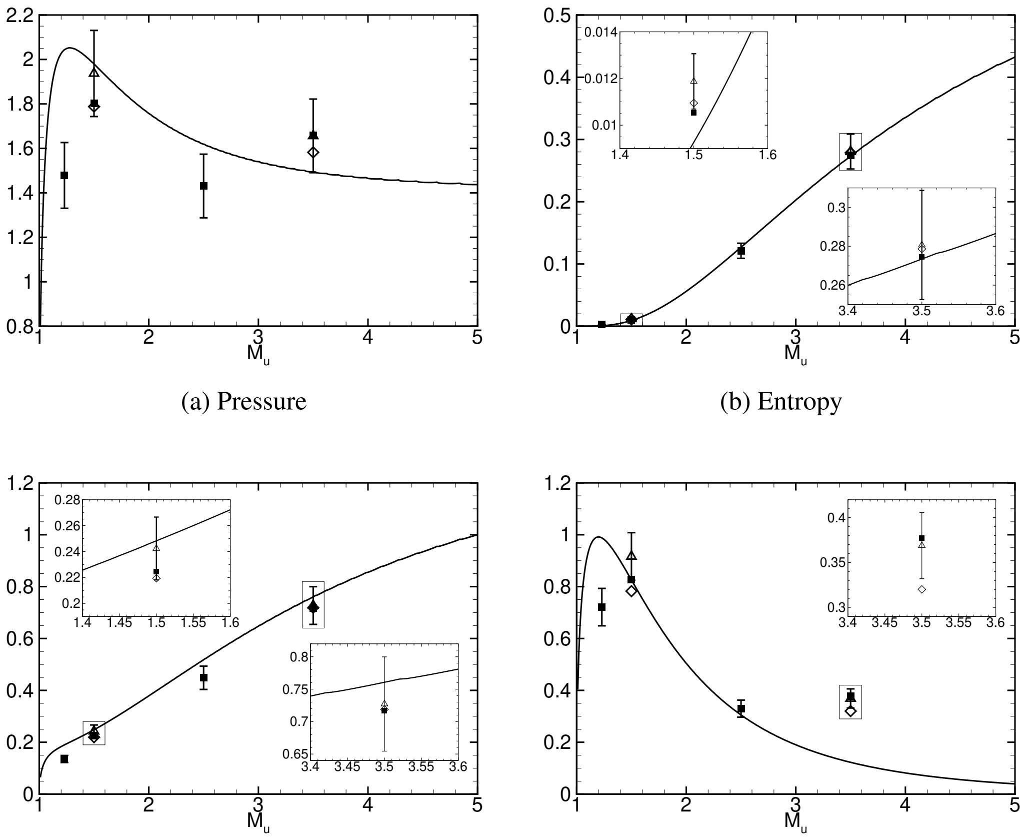


(a) Pressure (b) Entropy

(c) Temperature (d) Density

Figure 6.2: Variation of normalized (a) pressure, (b) entropy, (c) temperature, and (d) density variances at the near-field location ($k_0x_1 = 0^+$) from LIA (lines) and DNS (symbols). The symbols are 1.23, 1.5$c$, 2.5, 3.5$c$ (squares) ; 1.5$d$, 3.5$d$ (triangles) ; 1.5$e$, 3.5$e$ (diamonds). The error bars denote the $+/-$ 10% error, estimated between different grids

As noted earlier, it is difficult to obtain the near-field variances using conventional (fixed point) averaging of the DNS data. The high values of the thermodynamic fluctuations computed in the region of the shock wave are largely due to the unsteady shock oscillation. On the other hand, the statistics computed at the edge of the mean shock thickness is strongly affected by the rapid exponential decay, at least for the pressure variance. By comparison, the threshold method computes statistics based on the data at the edge of the instantaneous shock. It follows the idea of near-field LIA solution closely, and captures the fluctuation levels that are largely unaffected by the post-shock variations. It is found that the entropy variances obtained using the threshold method match the LIA results closely whereas, the pressure variances differ largely at low Mach numbers. Note that the DNS data corresponds to the STI cases computed in the current work, as the instantaneous shock data is not available from the earlier DNS cases of [81].

To show the effectiveness of the threshold method, an error estimate is obtained from the sequence of grids provided in table (4.2). The largest error in the statistics between two consecutive finer grid spacings in the shock-normal direction for the same transverse grid spacing is found to be slightly less than 10%. The statistics obtained using the threshold method, though having a relatively large error, are found to be close to the LIA near-field values presented.

The DNS statistics computed using the threshold method for the temperature variance in Fig. (6.2c) shows a much better match with the near-field LIA predictions. The values are, once again, higher by about an order in magnitude compared to the far-field $\overline{T'^2}$ at a given Mach number. The DNS data points are limited to Mach 3.5, corresponding to the current simulations, and it is lower than the LIA results.

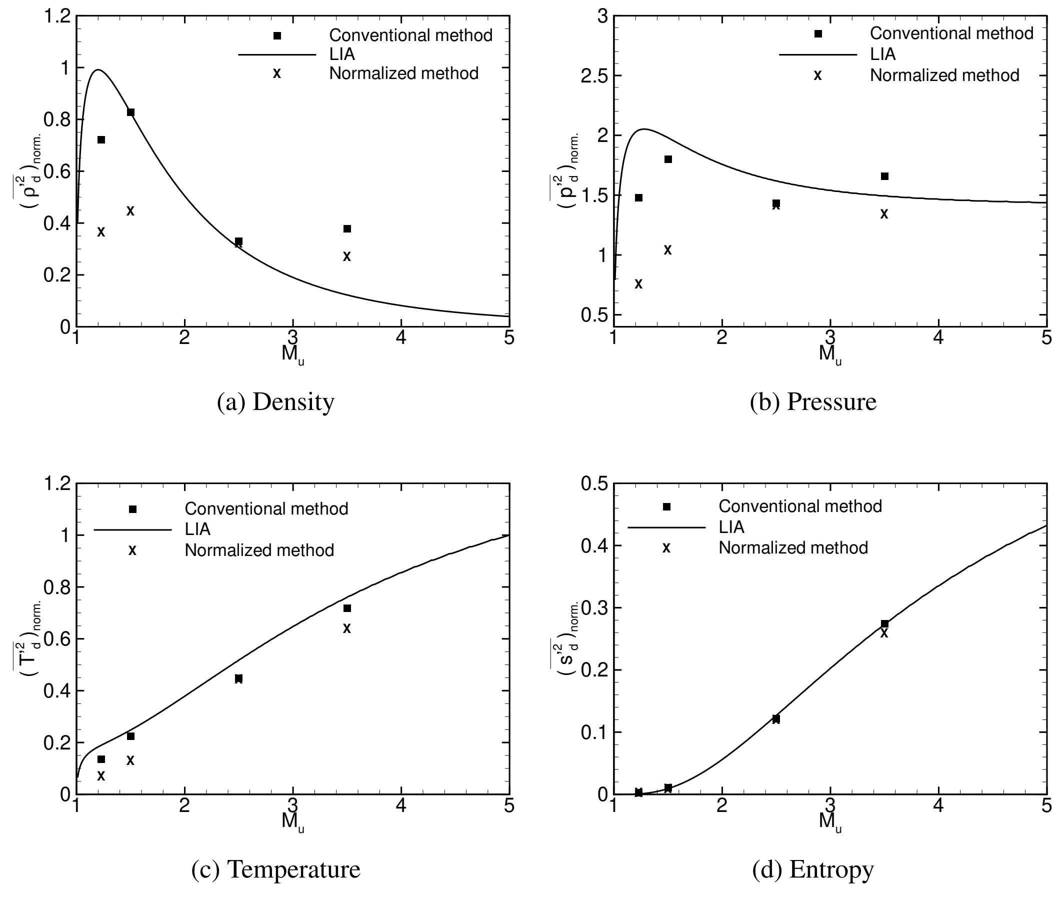


Figure 6.3: Variation of normalized (a) density, (b) pressure, (c) temperature, and (d) entropy variances at the near-field location ($k_0x_1 = 0^+$) from LIA (lines) and DNS (symbols)

Figure (6.3) plots the near-field variation of the thermodynamic variances computed using a modified version of the threshold method, where the shock location is identified using a normalized value of the instantaneous dilatation. The dilatation is normalized by the $L_2$ norm (denoted by $||.||_2$) of the local vorticity, which is also equivalent to the local solenoidal velocity gradient norm. The threshold measure is also normalized accordingly by the maximum value of the $L_2$ norm of the vorticity. The bounds of the instantaneous shock, are thus identified as the locations corresponding to the relation,

$$\frac{\theta}{||\omega_i||_2} < 0.01 \, \frac{min(\theta)}{max(||\omega_i||_2)}, \tag{6.3}$$

which essentially follows the procedure mentioned in Sect. (5.4), but with normalized values. The near-field predictions of the thermodynamic variances using the normalized threshold method are smaller than their non-normalized counterparts (or conventional threshold method) for the low Mach number cases and are comparable for the high Mach number cases. The reason for this behavior is currently unknown, however both the methods follow the same trend observed in the LIA as evident from Fig. (6.3a).

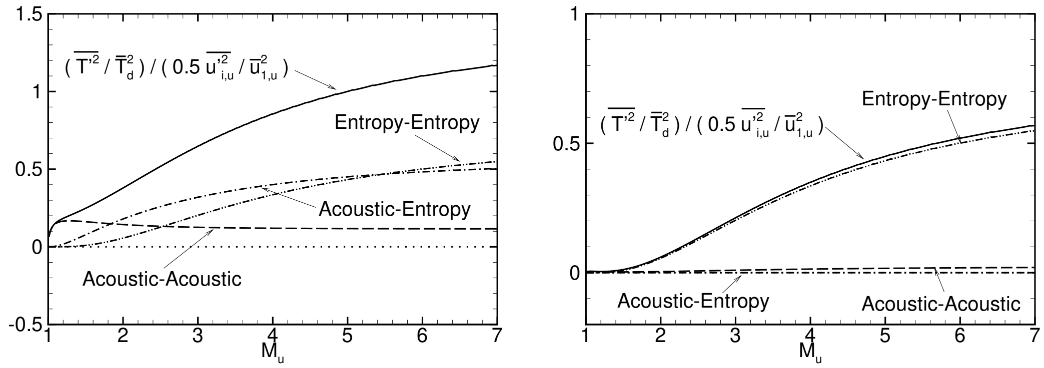


(a) at $k_0x_1 = 0^+$ (b) at $k_0x_1 = 2\pi$

Figure 6.4: Variation of Kovásznay mode components in temperature variance for the (a) near-field location ($k_0x_1 = 0^+$) and the (b) far-field ($k_0x_1 = 2\pi$) locations

Figure (6.4) presents the Kovásznay mode decomposition of the LIA temperature variance (computed using Eq. (6.1) and Eqs. (5.11a) - (5.11c)) and is plotted as a function of the shock Mach number. The far-field ($k_0x_1 = 2\pi$) and the near-field ($k_0x_1 = 0^+$) data are shown to contrast the variations at the two locations. The far-field data (in Fig. (6.4b)) shows that the temperature fluctuations at high Mach number are entirely due to the entropy mode, whereas the acoustic mode is dominant in the transonic range. This is similar to the observation in Ref. [118] in terms of the percentage contribution of each component to the temperature variance. Interestingly, the data presented here shows that the non-monotonic behavior of far-field $\overline{T'^2}$ with Mach number is caused by the switch (around $M_u = 1.4$) between the acoustic and the entropy contributions to the temperature field. The near-field data (in Fig. (6.4a)) has a similar trend, except for a large contribution from the correlation between the acoustic and the entropy modes for $M_u > 2$. The acoustic-entropy component dies down quickly, and has a vanishing magnitude in the far-field, owing to the different wave speeds of the acoustic and non-acoustic modes. For the propagating acoustic waves, the integration of the acoustic-entropy correlation term can be shown to algebraically decay with $x_1$ [41, 96].

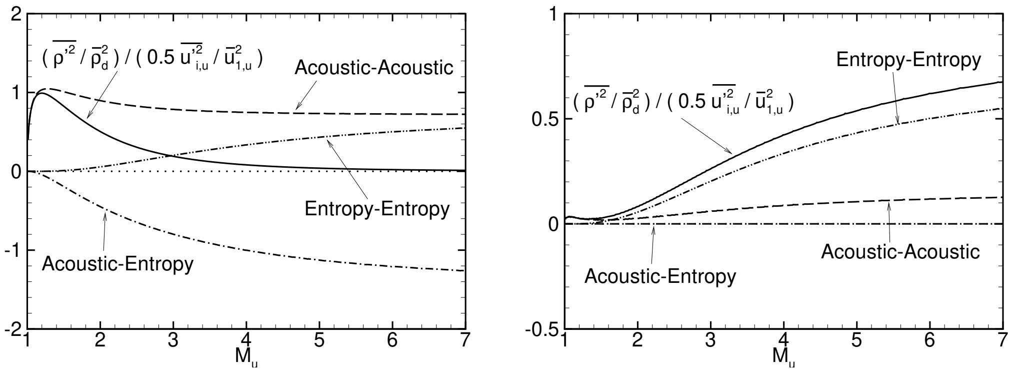


(a) at $k_0x_1 = 0^+$

(b) at $k_0x_1 = 2\pi$

Figure 6.5: Variation of Kovásznay mode components in Density variance for the (a) near-field location ($k_0x_1 = 0^+$) and the (b) far-field ($k_0x_1 = 2\pi$) locations

The LIA near-field density variance in Fig. (6.2d) show a unique variation with Mach number. It increases to attain a peak value for Mach 1.2 and then decreases at higher Mach number. As per the Kovásznay mode decomposition analysis (see Eqs. (6.1) and (5.10a) - (5.10c)) shown in Fig. (6.5a), this non-monotonic variation is caused by a rapid increase in the magnitude of the acoustic-entropy component at higher Mach numbers. It is found that the acoustic and the entropy components of the density field are out-of-phase with each other. A large negative acoustic-entropy component cancels the positive acoustic-acoustic and entropy-entropy contributions to result in vanishingly small near-field density fluctuations in the limit of infinite shock Mach number. The values computed at Mach 1.5 and 2.5 are comparable to the LIA results. On the other hand, the threshold method under-predicts the near-field density variance at the weakest interaction case (Mach 1.23) and over-predicts the LIA value for Mach 3.5. The reason for these discrepancies is not known.

Kovásznay mode decomposition for the far-field density variance is also plotted as a function of the shock Mach number in Fig. (6.5b) for comparison. The data corresponds to $k_0 x_1 = 2\pi$ and there are minimal changes beyond this value. Both the entropy and the acoustic contributions increase with Mach number, with a large entropy-entropy component in the high Mach number interactions and the acoustic-acoustic component dominating at low Mach numbers. The acoustic-entropy contribution to the far-field density variance is vanishingly small, as the correlation between the acoustic and the entropy modes decay away from the shock wave. A small plateau is visible in the lower Mach number range, and it is characteristic of the acoustic mode (in Fig. (6.1a)). The switch between the dominant acoustic-acoustic component to the large entropy-entropy component occurs near Mach 1.6, resulting in a further rise in $\overline{\rho'^2}$ with Mach number.

## 6.3 Effect of turbulent Mach number

The spatial variation of thermodynamic variances for different upstream turbulent Mach numbers is plotted in Fig. (6.6) - (6.8). The LIA solutions computed using Eq. (6.1) represents the $M_t \to 0$ limit in the figures. As expected, increasing the upstream turbulent Mach number results in increased amplification across the shock. For the case of $M_u = 1.50$ and $Re_{\lambda,u} = 33$ shown in Fig. (6.7), it is observed that the thermodynamic quantities decay rapidly behind the shock after attaining large values at the downstream end of the mean shock wave, except for entropy which decays gradually. This is similar to the effect of increasing shock strengths but with amplification proportional to $M_t^4$.

It is to be noted that the upstream turbulence in the DNS has thermodynamic fluctuations due to the usage of 'pseudo-sound relationships' for adding compressibility to the initially solenoidal turbulence,

$$p' \sim M_t^2, \quad \rho' \sim \frac{p'}{\overline{a}^2}, \quad T' \sim \frac{\gamma - 1}{\gamma} p' \tag{6.4}$$

This results in the variation of the thermodynamic fluctuations as $M_{t,u}$ is varied, with large thermodynamic fluctuations for the case of $M_{t,u} = 0.4$ and relatively small fluctuations for the $M_{t,u} = 0.05$ case. The non-monotonic variation of density variance observed for low $M_{t,u}$ values for the $M_u = 3.50$ case disappears at high $M_{t,u}$ values. This is due to the relatively larger component of acoustic fluctuations present in the $M_{t,u} = 0.25$ and 0.40 cases, which in turn is amplified largely across the shock. The amplification in the entropy component for a purely vortical upstream field is small compared to the amplification in the acoustic component (discussed in earlier sections using Kovásznay decomposition).

At very high turbulent Mach numbers, the amplification factor of the entropy fluctuations are found to be small compared to their low $M_{t,u}$ counterparts. It is hypothesized that the reduction in the amplification factor is due to the presence of shock holes, a phenomenon in which the local shock is replaced by multiple compression waves, and resulting in a smooth variation of the fluctuations inside the numerical shock instead of very large values. This is clearly observed in Figs. (6.6d), where there is no amplification for $M_{t,u} = 0.4$ and very small amplification for $M_{t,u} = 0.15$ and 0.25, and in (6.8b), where there is very small amplification for $M_{t,u} = 0.4$ case. These cases have the upstream shock-turbulence intensity defined as, $\dfrac{M_{t,u}}{(M_u - 1)}$ to be greater than 0.6, which is the criterion for broken shocks proposed in Refs. [27, 81]. For high $M_u$ cases, the amplification ratios increase with increasing $M_{t,u}$ values also, which supports the hypothesis that 'broken shocks' are due to the local shock-turbulence intensity than the $M_{t,u}$ value.

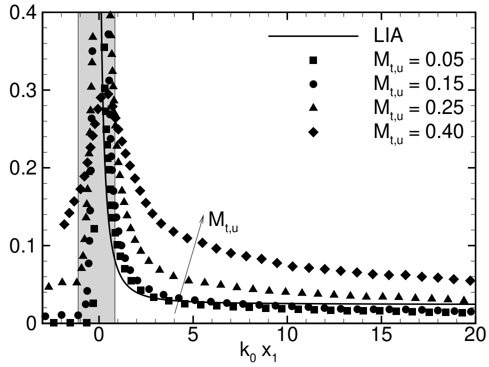


(a) Density

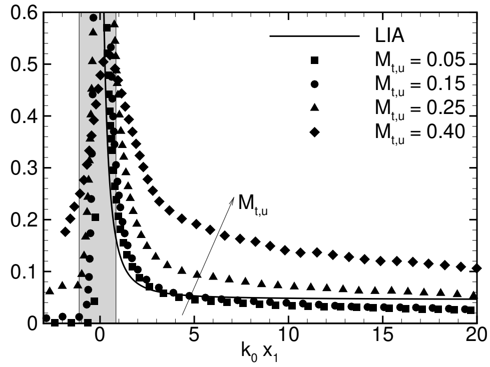


(b) Pressure

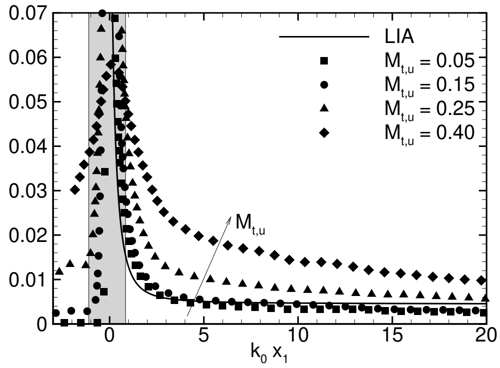


(c) Temperature

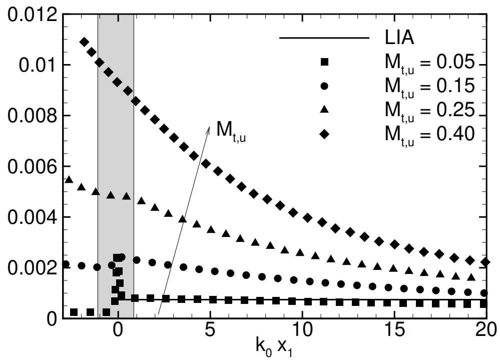


(d) Entropy

Figure 6.6: Spatial variation of normalized (a) density, (b) pressure, (c) temperature, and (d) entropy variances for varying upstream turbulent Mach numbers from the case of $M_u = 1.23$ and $Re_{\lambda,u} = 33$. The solid line is the LIA solution which is based on the $M_{t,u} \to 0$ assumption. The region of unsteady shock movement for $M_{t,u} = 0.15$ is shown by the grey band

The amplification of pressure and temperature fluctuations for the highest $M_{t,u}$ value is comparable to the amplification obtained at very high Mach numbers but with lower

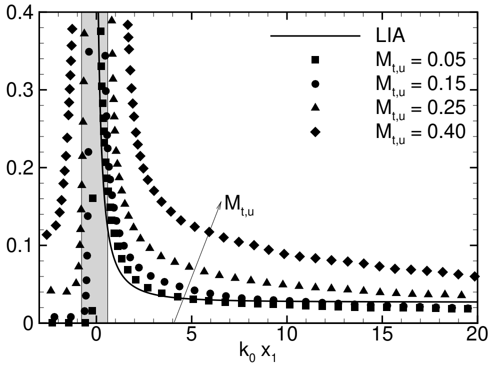


(a) Density - $M_u = 1.50$

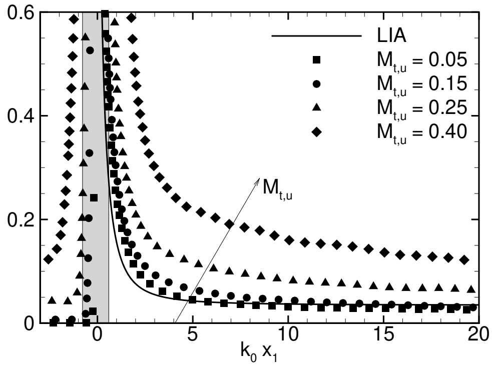


(b) Pressure - $M_u = 1.50$

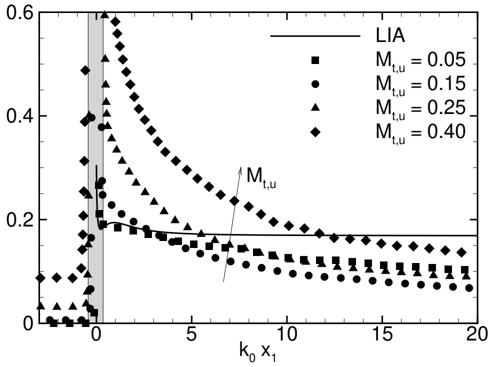


(c) Density - $M_u = 2.50$

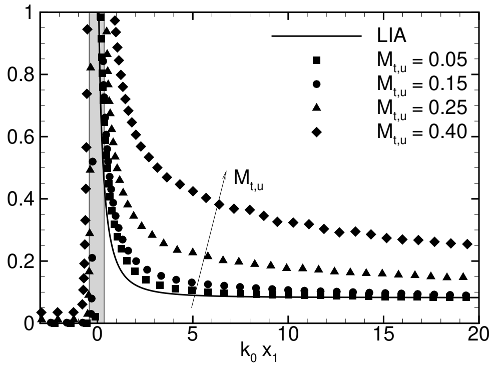


(d) Pressure - $M_u = 2.50$

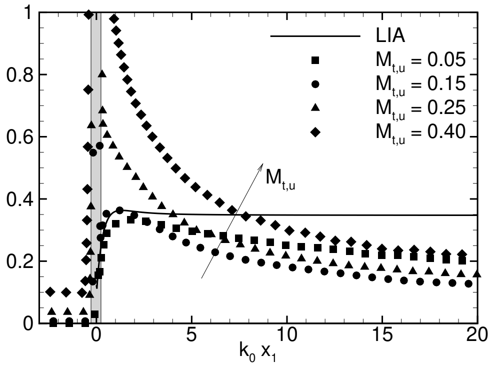


(e) Density - $M_u = 3.50$

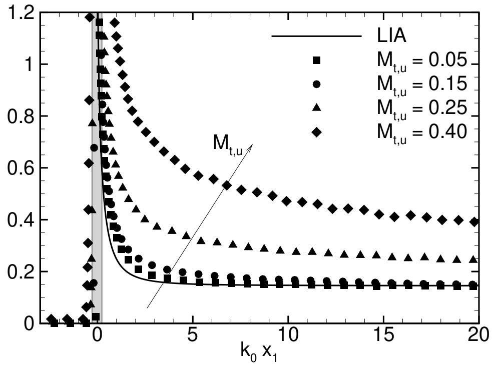


(f) Pressure - $M_u = 3.50$

Figure 6.7: Spatial variation of the normalized density variance for (a) $M_u = 1.50$, (c) $M_u = 2.50$ and (e) $M_u = 3.50$ in the dataset of $Re_{\lambda,u} = 33$ for all $M_{t,u}$ values. The corresponding pressure variances are shown in (b), (d) and (f). The solid line is the LIA solution and the symbols are DNS results. The region of unsteady shock movement for $M_{t,u} = 0.15$ is shown by the grey band

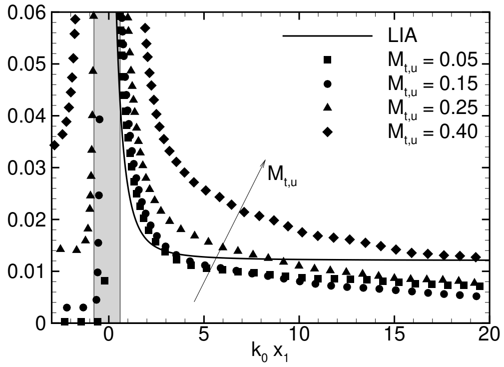


(a) Temperature - $M_u$ = 1.50

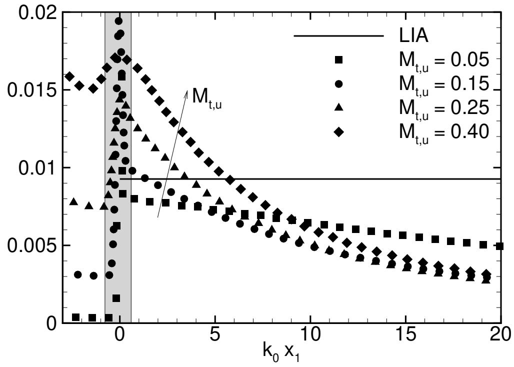


(b) Entropy - $M_u$ = 1.50

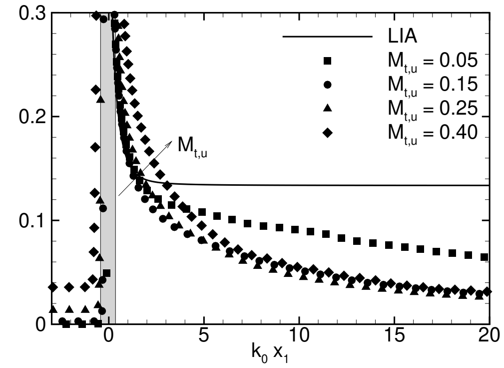


(c) Temperature - $M_u$ = 2.50

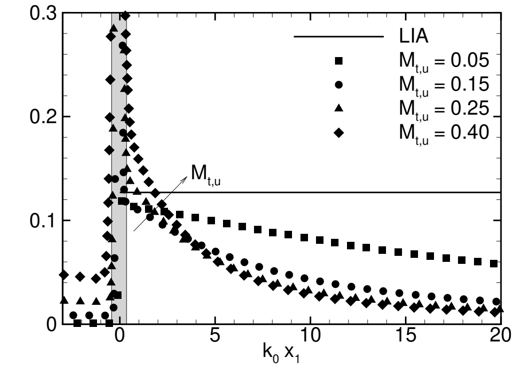


(d) Entropy - $M_u$ = 2.50

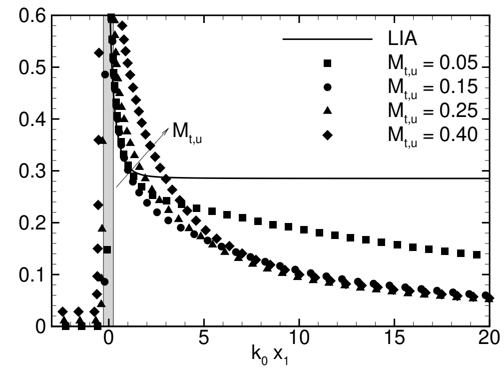


(e) Temperature - $M_u$ = 3.50

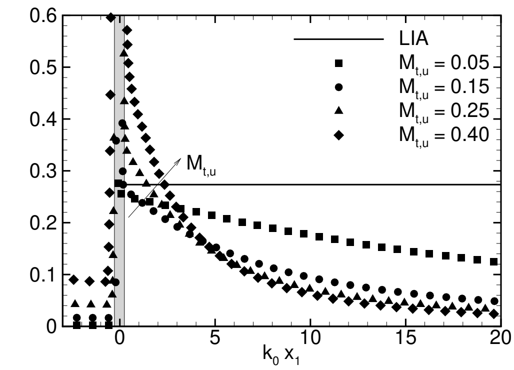


(f) Entropy - $M_u$ = 3.50

Figure 6.8: Spatial variation of the normalized temperature variance for (a) $M_u = 1.50$, (c) $M_u = 2.50$ and (e) $M_u = 3.50$ in the dataset of $Re_{\lambda,u} = 33$ for all $M_{t,u}$ values. The corresponding entropy variances are shown in (b), (d) and (f). The solid line is the LIA solution and the symbols are DNS results. The region of unsteady shock movement for $M_{t,u} = 0.15$ is shown by the grey band

$M_{t,u}$. The unsteady shock displacement is directly proportional to the $M_{t,u}$ value and the region of mean shock thickness increases in size for higher $M_{t,u}$. The broken shock cases have a very wide mean shock profile, which is actually due to the averaging of the distance between widely spaced compression waves over the time period of collection of flowfields.

Interestingly, the temperature variance for $M_{t,u} = 0.05$ and high Mach numbers ($M_u = 2.50$ and 3.50) decays at a much slower rate than the other $M_{t,u}$ values. This can be interpreted using the quasi-equilibrium assumption of Sarkar *et al.* [33, 136], where the acoustic component of the fluctuations have decayed at a very fast timescale (or short length of approximately $k_0 x_1 = 2$), leaving only the entropic component to decay the fluctuations.

At low $M_{t,u}$ values, the contribution from the entropy component is minimal, displaying a rather slow decay rate due to viscous effects compared to the exponential behavior observed for the other $M_{t,u}$ values. The tendency of equipartition between the pressure fluctuations and the dilatational component of the turbulent kinetic energy in contributing towards the total turbulent energy could explain the underlying mechanism for the dissipation effects.

### 6.3.1 Near-field variation for varying turbulent Mach number

Figure (6.9) shows the near-field values of the DNS cases computed using the threshold method in comparison to the LIA solution. The values are closer to the LIA predictions for up to $M_{t,u} = 0.15$, and significant deviations are observed for the higher $M_t$ values, especially for the temperature and entropy variances. The cases $M_u = 1.23$ with $M_{t,u} = 0.25$ and $M_u = 1.23$, 1.50 with $M_{t,u} = 0.4$ show different trends compared to the other cases. This is most probably due to their 'broken shock' nature, where the method was not able to find a proper shock.

The density, pressure and temperature variance values show an opposite trend compared to their counterparts shown in Figs. (6.6) - (6.8), where they were increasing with increasing $M_{t,u}$ values. It is to be noted that the increasing trend corresponds to the values beyond $k_0 x_1 > 1$, and not at the shock. The unphysical peak value observed in the center of the mean shock region (when computed in the conventional averaging procedure) decreases for increasing $M_{t,u}$ values. This implies that at each instant, the peak in the shock region is also decreasing for increasing $M_t$ values. This effect is reproduced in Fig. (6.9) by the threshold method, which finds lower peak values at the shock for increasing $M_t$ values. The entropy variance, on the other hand, is increasing with increasing $M_t$ value, since its peak in the numerical shock region is found increasing correspondingly.

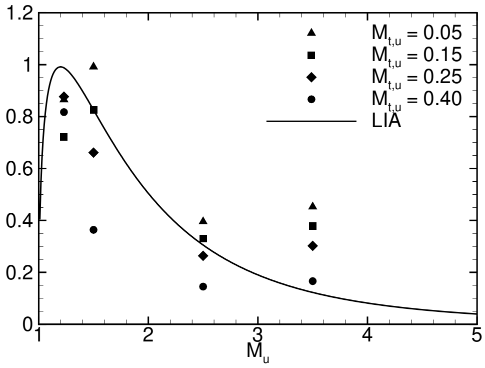


(a) Density

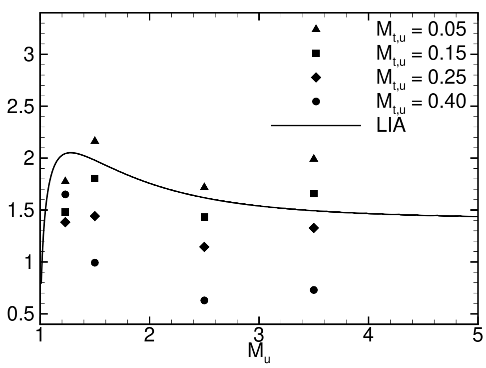


(b) Pressure

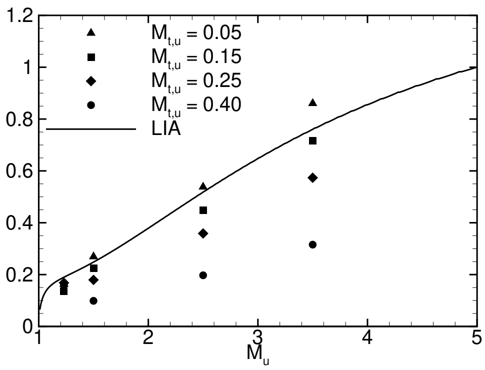


(c) Temperature

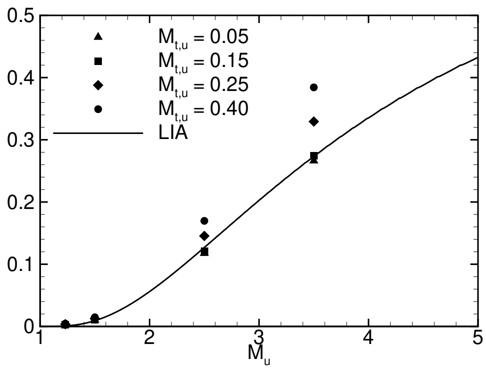


(d) Entropy

Figure 6.9: Variation of normalized (a) density, (b) pressure, (c) temperature, and (d) entropy variances at the near-field location ($k_0 x_1 = 0^+$) from LIA (lines) and DNS (symbols)

## 6.4 Effect of Reynolds number and spectrum shape

The effect of Taylor scale based Reynolds number and the shape of the upstream energy spectrum are investigated with the available DNS data in this section. Thermodynamic variances for low and high upstream Taylor scale Reynolds numbers are plotted in Fig. (6.10). The spatial variation of the variances is similar to the variations observed in Fig. (5.2) with large values in the shock region and rapidly decaying trend immediately behind the shock. The high Reynolds number case has a faster decay rate compared to the low Reynolds number flow, which is contradictory to the observations found for velocity and its related statistics.

The scaling of the spatial direction with the characteristic wavenumber ($k_0$) does not show this decay rate, but is used here since comparisons with LIA solutions have been made. Many reasons can be attributed to this discrepancy, but the most probable one is the difference between the turbulence spectrum used to generate the inflow turbulence. The effect of the shape of the upstream turbulence spectrum is also shown in the figure by comparing the LIA thermodynamic variances for two different turbulence spectrum.

The spectra used in this analysis are the exponential spectrum given by the expression,

$$E(k) \sim (k/k_0)^4 \, e^{-2(k/k_0)^2} \tag{6.5}$$

and the von Kármán spectrum [80], which is expressed as,

$$E(k) \sim \frac{(k/k_0)^2}{\left[(k/k_0)^2 + (5/6)\right]^{11/6}} \tag{6.6}$$

The variances are found to be independent at the locations immediately behind the shock ($x_1 = 0^+$) and at the far-field ($x_1 \to \infty$). In the rapidly decaying region ($1 < k_0 x_1 < 4$), there are significant variations between results from the two spectrum shapes. The von Kármán spectrum fairs better in comparison to the exponential spectrum since the initial spectrum in the DNS cases were also of the former type. There are still variations between LIA and DNS results, especially in the pressure fluctuations which implies that an exact match is possible only when the same energy spectrum used in the DNS is also applied in LIA. This was also verified in the work of [90] where the inflow turbulence from DNS is applied in LIA to obtain reliable post-shock flowfields for high Reynolds numbers, which are in general difficult to obtain using DNS.

The $Re_{\lambda,u} = 40$ cases from [83] used an exponentially varying turbulence spectrum whereas, a von Kármán type turbulence spectrum was used for the $Re_{\lambda,u} = 75$ cases [81]. As it is found that the decay rate of the variances depend on the inflow turbulence

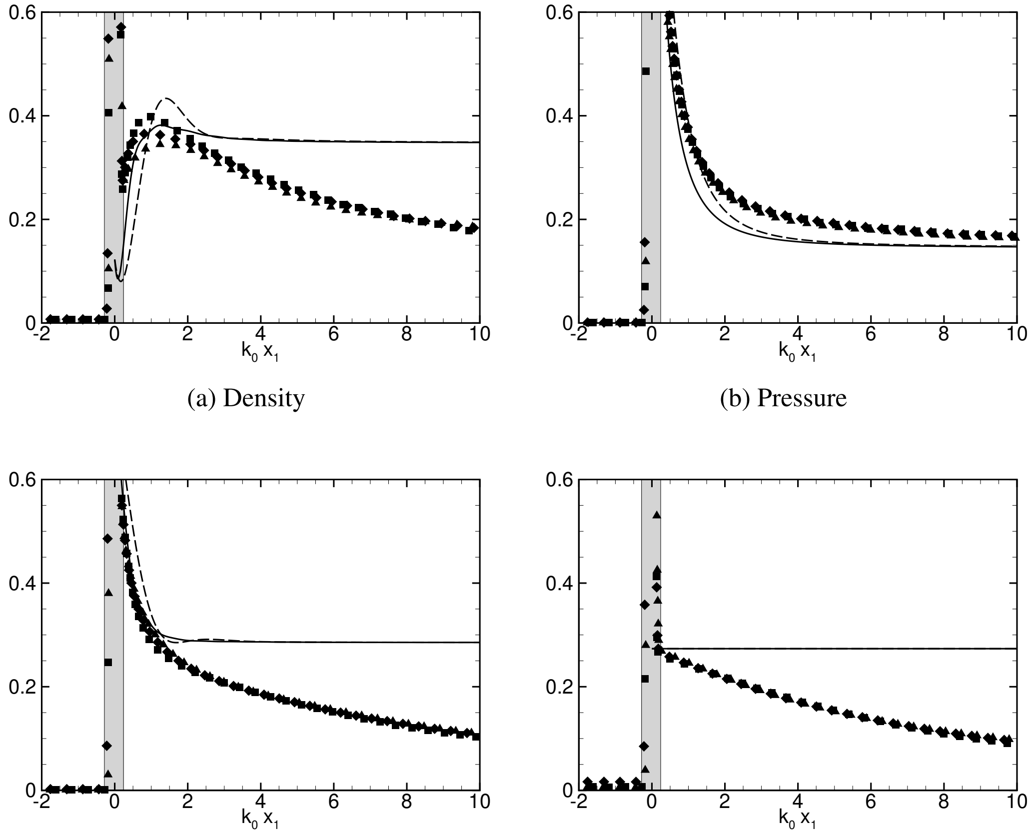


(a) Density (b) Pressure

(c) Temperature (d) Entropy

Figure 6.10: Spatial variation of normalized (a) density, (b) pressure, (c) temperature, and (d) entropy variances for varying upstream Taylor scale Reynolds number from the case of $M_u = 3.50$ and $M_{t,u} = 0.16$ in the dataset of [81] and the present simulations with $M_{t=0.15}$. Legend: $Re_{\lambda,u} = 40$ (squares), $Re_{\lambda,u} = 75$ (diamonds) and $Re_{\lambda,u} = 33$ (deltas). Lines represent LIA solution where the solid line is derived for an upstream von Kármán spectrum and the dashed line is for an exponential type of spectrum. The grey band corresponds to the region of mean shock motion

spectrum, it is necessary to have different $Re_{\lambda,u}$ cases generated using the same turbulence spectrum to make a meaningful comparison.

## 6.5 Summary

The effect of the shock strength on the thermodynamic variances is extensively analyzed, and the near-field and far-field predictions of LIA in comparison with the DNS are assessed. The effect of the turbulent Mach number is as expected; higher the upstream value, higher is the downstream value. Of the thermodynamic variances studied, the entropy field behind the shock is altered drastically whether the case is in the wrinkled shock regime (shock is highly displaced but with no holes locally) or in the broken shock regime (shock is replaced by multiple smooth compression waves locally). To understand the effect of Taylor-scale Reynolds number, additional data with the same inflow turbulence spectrum is required.

# Chapter 7

# Budget analysis

In this chapter, the significant terms responsible for the amplification and evolution of the post-shock thermodynamic field is investigated by computing the budget of the terms in their respective transport equations. The results are from the dataset of $M_t = 0.15$ and $Re_{\lambda,u} = 33$ for varying Mach numbers. The dominant terms for the variances and the fluxes are found to be the same for the other turbulent Mach number cases also, though their spatial evolution profile is different. The significant terms predicted by LIA are also the same terms found from the numerical simulations and show similarities qualitatively but the quantitative agreement is poor.

## 7.1 Budgets of thermodynamic variances

The different post-shock behavior exhibited by the different thermodynamic variances for varying Mach numbers is explored further in terms of their transport equation. DNS data is used to compute the budget of the source terms, so as to identify the dominant physical mechanisms responsible for a particular post-shock behavior. Note that the transport equations presented in this section are for steady one-dimensional mean flow encountered in canonical shock-turbulence interaction. A more detailed description of the transport equations for the thermodynamic variances can be found in [36]. For canonical shock-turbulence interaction with a steady mean shock ($\frac{\partial}{\partial t} = 0$) and one-dimensional mean flow, the averages are functions of the shock-normal direction $x_1$ only, i.e., the derivatives in the shock-parallel directions, $\frac{\partial \overline{f}}{\partial x_2} = \frac{\partial \overline{f}}{\partial x_3} = 0$. The thermodynamic variances are normalized as mentioned earlier; by the square of their downstream mean values ($\overline{\rho}_d^2$, $\overline{p}_d^2$ and $\overline{T}_d^2$), except for the entropy variance which is by the square of the gas specific heat capacity at constant pressure ($c_p^2$). Additionally the variances are scaled by the normalized upstream TKE, $\frac{0.5\,\overline{u_{i,u}'^2}}{\overline{u}_{1,u}^2}$. The spatial gradient operator ($\frac{\partial}{\partial x_1}$) is normalized by the peak energy wavenumber, $k_0$ and the velocity fluctuations are factored by their upstream mean values, $\overline{u}_{1,u}$. This normalization procedure is followed through out this chapter unless mentioned otherwise.

### 7.1.1 Density variance

The transport equation for density variance ($\overline{\rho'^2}$) can be obtained by multiplying $\rho'$ to the continuity equation and taking the respective averages. The transport equation for our problem reduces to,

$$\begin{aligned}\underbrace{\frac{\partial(\widetilde{u}_1\,\overline{\rho'^2})}{\partial x_1}}_{\text{Convection}} = \underbrace{-\frac{\partial(\overline{\rho'^2\,u_1''})}{\partial x_1}}_{\text{Diffusion}} &\underbrace{-2\,\overline{\rho'^2}\,\frac{\partial\widetilde{u}_1}{\partial x_1} - 2\,\overline{\rho'\,u_1''}\,\frac{\partial\overline{\rho}}{\partial x_1}}_{\text{Production}} \\ &\underbrace{-2\,\overline{\rho}\,\overline{\rho'\,\frac{\partial u_j''}{\partial x_j}} - \overline{\rho'^2\,\frac{\partial u_j''}{\partial x_j}}}_{\text{Dilatation}},\end{aligned} \tag{7.1}$$

where $\frac{\partial u_j''}{\partial x_j}$ is the fluctuation in dilatation.

Figure (7.1) shows the budget of the terms in the transport equation for density variance for the DNS cases computed as part of the current work. The term on the LHS of Eq. (7.1) is the convection term, which is the transport of density variance by the mean velocity field. The convection term is usually negative and for the sake of easy comparison, the negative of the convection term is shown in the figure. The last two terms represent dilatation effect on density fluctuations, with the second term being of higher order, and hence has negligible contribution. The first dilatation term is the primary source term in the post-shock evolution of density variance, and is comparable to the convection term. This is similar to that reported by [45] for a Mach 2 shock-turbulence interaction. In the absence of a strong mean compression outside the region of unsteady shock motion (shown by the vertical dotted lines near to $k_0x_1 = 0$), the fluctuating dilatation is the main contributor to the source terms as well as the overall budget. The density-dilatation correlation is positive for the first three cases resulting in a negative source term. It monotonically decreases in magnitude with increasing distance from the shock wave with a small exception for $k_0x_1 < 1$ in the $M_u = 2.5$ case. For the Mach 3.5 interaction, the convection and dilatation terms have a non-monotonic variation, similar to the spatial variation of the density variance in this case. The budget terms change sign behind the shock wave, and the zero crossing corresponds to the peak in the density variance observed in Fig. (5.2) for this particular turbulent Mach number. For high Mach numbers cases with high turbulent Mach numbers, there is no zero crossing, due to the acoustic component being much larger than the entropic component, and replicate the variation as observed at low Mach numbers with low turbulence intensities (say, $M_u = 1.5$ and $M_{t,u} = 0.15$).

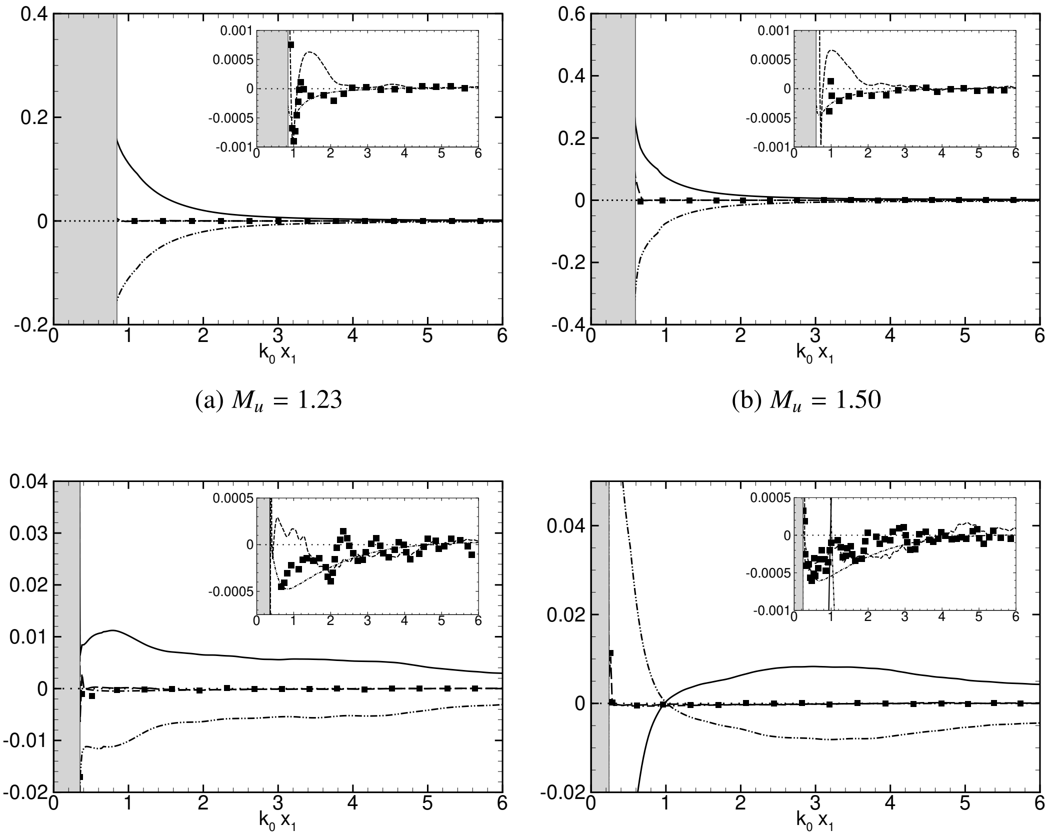


(a) $M_u = 1.23$

(b) $M_u = 1.50$

(c) $M_u = 2.50$

(d) $M_u = 3.50$

Figure 7.1: Budgets of terms in the transport equation of $\overline{\rho'^2}$ for different Mach numbers from the present simulations. Convection (solid), diffusion (dashed), production (dash-dotted), dilatation (dash-double dotted), and the sum of all terms (square symbols). The density variances are normalized as mentioned in the text whereas, the streamwise direction is normalized by the peak energy wavenumber in the inflow turbulence. Region of unsteady shock motion is shown by a grey band. Inset shows the contribution of the production and the diffusion terms which are at least an order of magnitude lesser than the dominant terms.

The diffusion term (first term on the right-hand side) represents the turbulent transport of density fluctuations in the post-shock flow. It is of an order higher than the convection term and is expected to have a small contribution. The production term generates density fluctuations through the gradient of mean quantities (density and velocity). [83]

report small variation in the mean velocity and density in the region immediately behind the shock. This is due to the fact that the jump conditions across a shock wave are slightly different for a turbulent flow than the standard RH conditions for flows without fluctuations [88]. Small variation in mean quantities behind the shock results in a finite gradient in the shock-normal direction, which in turn results in a non-zero production term behind the shock wave. The inset in each sub-figure of Fig. (7.1) shows a highly magnified view of the region immediately behind the shock, where the diffusion and production terms have non-negligible contribution. The diffusion and the production terms are indeed smaller than the dominant terms by at least an order of magnitude. The error computed as the sum of all the terms in the transport equation (with the convection term placed on the RHS) is also found to be small.

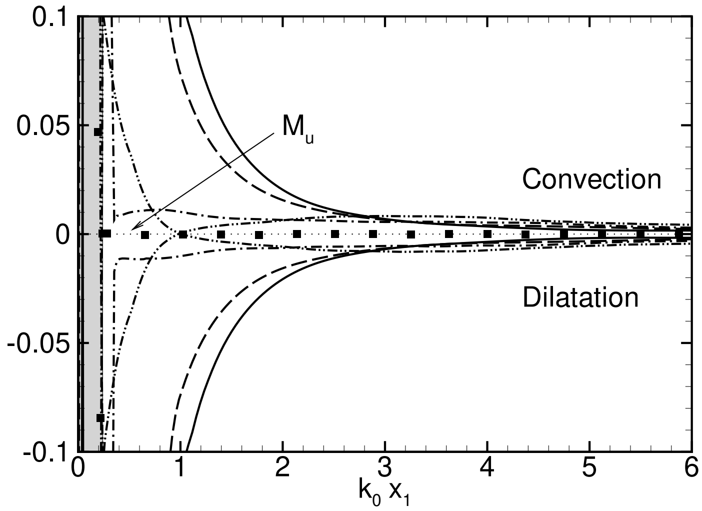


Figure 7.2: Same as Fig. (7.1) showing only the dominant terms for all the Mach numbers in the same plot. Legend: $M_u$ = 1.23 (solid), $M_u$ = 1.5 (dashed), $M_u$ = 2.5 (dash-dotted) and $M_u$ = 3.5 (dash-double dotted). The square symbols represent the sum of all the terms in Eq. (7.1). The grey band shows the region of unsteady shock motion for the case of $M_u$ = 3.50.

Figure (7.2) shows the variation of the significant terms for increasing Mach numbers. The convection (+ axis) and the dilatation (− axis) terms are only plotted against the shock-normal direction. For the turbulent Mach number of $M_{t,u} = 0.15$, the terms change sign after the acoustic adjustment region (around $k_0 x_1 = 1$). The plot indicates that the terms rapidly increase across the shock, followed by a rapid decrease in magnitude for increasing shock strengths. This seems to be counter-intuitive and requires clarification. Immediately behind the shock there is large amplification of density variance, followed by an acoustic decay and additional dissipation of entropy fluctuations for the stronger shocks. The rapid decay for stronger shocks is due to the variations in the mean shock thickness as the flow Mach number changes. The thin shock of $M_u = 3.5$, thus shows a rapid decay compared to the weak shock cases at a particular $k_0 x_1$ location behind the shock, but the decay rate of all the cases is almost similar. Beyond $k_0 x_1 \approx 10$ (range not shown), all the terms decay which implies that the convection of density variance is zero and that density variance asymptotes to a constant value.

### 7.1.2 Pressure variance

The transport equation for pressure variance ($\overline{p'^2}$) is obtained by taking a moment of the pressure transport equation with $p'$. The transport equation for instantaneous pressure can be obtained from the energy conservation equation using the relation $p = (\gamma - 1)\rho e^i$ where, $e^i = c_v T$ is the internal energy and $c_v$ is the gas specific heat capacity at constant volume. The simplified version of the pressure variance transport equation for the canonical shock-turbulence interaction is given by,

$$
\begin{aligned}
\underbrace{\frac{\partial(\widetilde{u}_1 \overline{p'^2})}{\partial x_1}}_{\text{Convection}} = & \underbrace{-\frac{\partial(\overline{p'^2 u_1''})}{\partial x_1} + 2(\gamma-1)\frac{\partial(\overline{p' q_1})}{\partial x_1}}_{\text{Diffusion}} \\
& \underbrace{-2\,\overline{p' u_1''}\frac{\partial \overline{p}}{\partial x_1} - 2(\gamma-1)\,\overline{p'^2}\,\frac{\partial \widetilde{u}_1}{\partial x_1} + 2(\gamma-1)\,\overline{p'\,\sigma_{i1}}\,\frac{\partial \widetilde{u}_i}{\partial x_1}}_{\text{Production}} \\
& \underbrace{-2\gamma\,\overline{p}\,\overline{p'\frac{\partial u_j''}{\partial x_j}} - (2\gamma-1)\,\overline{p'^2\frac{\partial u_j''}{\partial x_j}}}_{\text{Dilatation}} \\
& \underbrace{-2(\gamma-1)\,\overline{q_j\frac{\partial p'}{\partial x_j}}}_{\text{Dissipation}} \underbrace{+2(\gamma-1)\,\overline{p'\,\sigma_{ij}\frac{\partial u_i''}{\partial x_j}}}_{\text{Triple correlations}}\,.
\end{aligned}
\tag{7.2}
$$

The transport equation for pressure variance has a form similar to that of the density variance presented above, with terms representing mean convection, diffusion, production and dilatation. In addition, there is dissipation effect and a triple correlation including viscous stresses. The dissipation term consists of the product of the gradients in fluctuating pressure and temperature with the conductivity of the fluid, whereas the triple correlation can be interpreted as a correlation of the pressure fluctuations with the viscous work that contributes to the energy of the fluid element. Both the viscous correlation and the dissipation terms are found to be negligible in the $\overline{p'^2}$ budgets computed using the DNS data. On the other hand, the pressure dilatation correlation term is the main contributor to the budget, and it is about two orders in magnitude larger than the other source terms. The first part balances the convection term, as in the $\overline{\rho'^2}$ budget, while the second part of the dilatation term consists of higher order correlation, and is found to be comparatively small. Unlike earlier, the pressure-dilatation term is always negative, and it exponentially decreases with distance from the shock wave - a trend similar to $\overline{p'^2}$ at all Mach numbers.

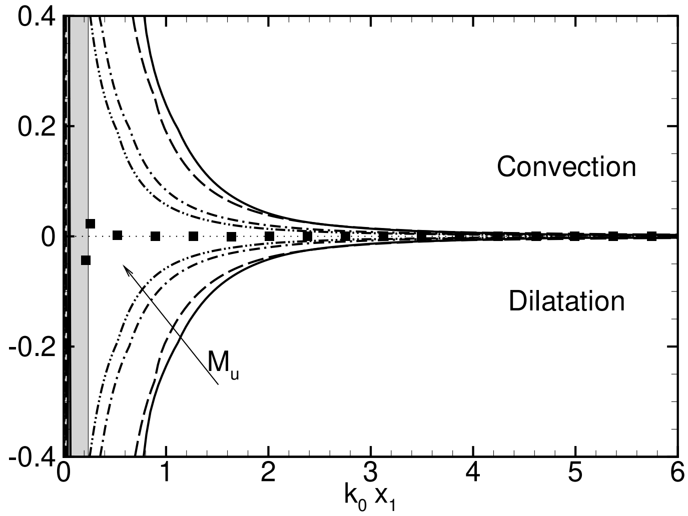


Figure 7.3: Budgets of terms in the transport equation of $\overline{p'^2}$ (Eq. (7.2)) for different Mach numbers: $M_u$ = 1.23 (solid), $M_u$ = 1.50 (dashed), $M_u$ = 2.50 (dash-dotted), $M_u$ = 3.50 (dash-double dotted) from the current simulations. Convection terms are represented on the positive axis and the dilatation terms are shown at the negative axis. Region of unsteady shock motion for $M_u$ = 3.50 (thinnest shock) case is shown by the grey band. Production, diffusion, dissipation and triple correlation terms (not shown) are very small in magnitude compared to the dominant terms. The square symbols represent the sum of all the terms in Eq. (7.2).

The production of pressure fluctuation due to mean pressure gradient depends on the pressure-velocity correlation. A second production term is given by the mean velocity gradient in the streamwise direction. These are, once again, found to be negligible, owing to the small magnitude of the post-shock mean field variation. Diffusion of pressure fluctuations are due to the turbulent transport of pressure fluctuations by the velocity field, as well as a correlation of the fluctuating pressure with the conduction heat flux. Both the diffusion terms are much smaller than the dominant dilatation effect, and this is similar to the density budget presented in Fig. (7.1).

Figure (7.3) plots the mean convection and the dilatation source term for varying Mach numbers. All the curves are qualitatively similar, and there is a clear trend of an increase in magnitude with increasing Mach number (to be interpreted as same as the density budget profiles. The effect of dissipation due to thermal conduction are found to be negligible for the case considered here. Thermal dissipation effects are observed for the $M_{t,u} = 0.4$ case due to the presence of relatively large amount of entropy fluctuations. However, they are still very small compared to the dilatation term and thus can be neglected to a certain degree of approximation.

### 7.1.3 Temperature variance

We follow the Favre averaging procedure for temperature and thus, the temperature variance transport equation, given in Eq. (7.3) is obtained by multiplying $\rho T''$ with the transport equation for temperature, followed by Reynolds averaging, and reducing it to the canonical shock-turbulence interaction case. The transport equation for temperature is obtained from the internal energy component of the total energy conservation equation and can also be obtained once the pressure transport equation is known.

$$\begin{aligned}
\underbrace{\frac{\partial(\widetilde{u}_1\,\overline{\rho\,T''^2})}{\partial x_1}}_{\text{Convection}} = & \underbrace{-\frac{\partial(\overline{\rho\,T''^2\,u_1''})}{\partial x_1} + \frac{2}{c_v}\frac{\partial(\overline{T''\,q_1})}{\partial x_1}}_{\text{Diffusion}} \\
& \underbrace{-2\,\overline{\rho\,T''\,u_1''}\,\frac{\partial\widetilde{T}}{\partial x_1} - (\overline{p}\,\overline{T''} + \overline{p'\,T''})\,\frac{\partial\widetilde{u}_1}{\partial x_1} + \frac{2}{c_v}\,\overline{T''\,\sigma_{i1}}\,\frac{\partial\widetilde{u}_i}{\partial x_1}}_{\text{Production}} \\
& \underbrace{-\frac{2}{c_v}\,\overline{p}\,\overline{T''\,\frac{\partial u_j''}{\partial x_j}} - \frac{2}{c_v}\,\overline{p'\,T''\,\frac{\partial u_j''}{\partial x_j}}}_{\text{Dilatation}} \\
& \underbrace{-\frac{2}{c_v}\,\overline{q_j\,\frac{\partial T''}{\partial x_j}}}_{\text{Dissipation}} + \underbrace{\frac{2}{c_v}\,\overline{T''\,\sigma_{ij}\,\frac{\partial u_i''}{\partial x_j}}}_{\text{Triple correlations}},
\end{aligned} \tag{7.3}$$

where $c_v = \dfrac{R}{\gamma - 1}$ is the specific heat capacity of the gas at constant volume and $R$ is the specific gas constant.

The above equation matches term-by-term to the pressure variance equation. There are minor differences in terms of $p'$ replaced by $\rho T$" and $c_v$ in place of the factors of $\gamma$ in Eq. (7.2). The budget of temperature variance is once again dominated by the acoustic effect, with a large dilatation source term balancing the convection term behind the shock wave (see Fig. (7.4)). The main difference is the dissipation term at higher Mach number. The dilatation effect decays rapidly to take very small values away from the shock, while the dissipation term shows a slow decrease in magnitude. So, the viscous dissipation of temperature fluctuations takes over the inviscid dilatation effect at some distance away from the shock wave. The location of this change moves closer to the shock with increasing shock strength as the dissipation becomes more negative with increasing

Mach number. Farther away from the shock, the budget is dominated by the negative dissipation term, which balances the dilatation and convection effects. Interestingly, the dilatation source term changes sign to become positive for $k_0 x_1 > 1$. This is true for all Mach numbers, and is not seen in the pressure and density budget plots, except for Mach 3.5 density budget, where the change in sign is associated with a local peak in the density variance downstream of the shock. The temperature variance has no such local peak in magnitude, and it is governed primarily by the viscous dissipation at large distances from the shock wave.

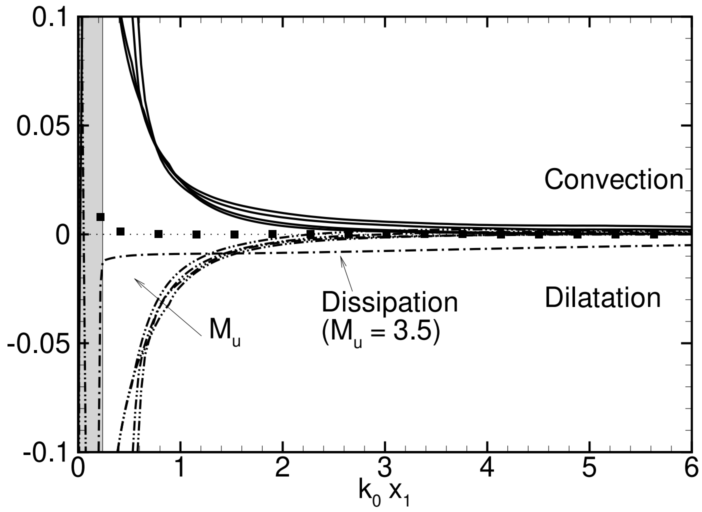


Figure 7.4: Budgets of terms in the transport equation of $\overline{\rho T''^2}$ (Eq. (7.3)) for the four different Mach numbers: $M_u = 1.23$ (solid), $M_u = 1.50$ (dashed), $M_u = 2.50$ (dash-dotted), $M_u = 3.50$ (dash-double dotted) from the current simulations. Region of unsteady shock motion from the $M_u = 3.50$ case is shown by the grey band. Production, diffusion, dissipation and triple correlation terms (not shown) are very small in magnitude compared to the dominant terms. The square symbols represent the sum of all the terms in Eq. (7.3). The thermal dissipation term is observable only for the $M_u = 3.5$ case and is shown by pink, dash-dotted line.

### 7.1.4 Entropy variance

Using the fundamental thermodynamic relation, specifically the form of Gibbs relation: $T\,ds = de - \dfrac{p}{\rho^2}\,d\rho$, the transport equation for entropy ($s$) can be obtained from the internal energy equation. The transport equation for its variance is obtained by taking a moment with $\rho s''$ similar to the procedure followed for temperature variance given in Eq. (7.3). For the case of canonical shock-turbulence interaction, the transport equation is written as,

$$
\begin{aligned}
\underbrace{\frac{\partial(\widetilde{u}_1 \overline{\rho\, s''^2})}{\partial x_1}}_{\text{Convection}} &= \underbrace{-\frac{\partial(\overline{\rho\, s''^2\, u_1''})}{\partial x_1} + 2\,\frac{\partial\overline{\left(\frac{q_1}{T}\, s''\right)}}{\partial x_1}}_{\text{Diffusion}} \\
& \underbrace{-2\,\overline{\rho\, s''\, u_1''}\,\frac{\partial \widetilde{s}}{\partial x_1} + 2\,\overline{\frac{\sigma_{i1}}{T}\, s''}\,\frac{\partial \widetilde{u}_i}{\partial x_1} + 2\,\overline{\frac{q_1}{T}\,\frac{s''}{T}}\,\frac{\partial \widetilde{T}}{\partial x_1}}_{\text{Production}} \\
& \underbrace{-2\,\overline{\frac{q_j}{T}\,\frac{\partial s''}{\partial x_j}}}_{\text{Dissipation}} \underbrace{+2\,\overline{\frac{\sigma_{ij}}{T}\, s''\frac{\partial u_i''}{\partial x_j}} + 2\,\overline{\frac{q_j}{T}\,\frac{s''}{T}\,\frac{\partial T''}{\partial x_j}}}_{\text{Triple correlations}}\,.
\end{aligned}
\tag{7.4}
$$

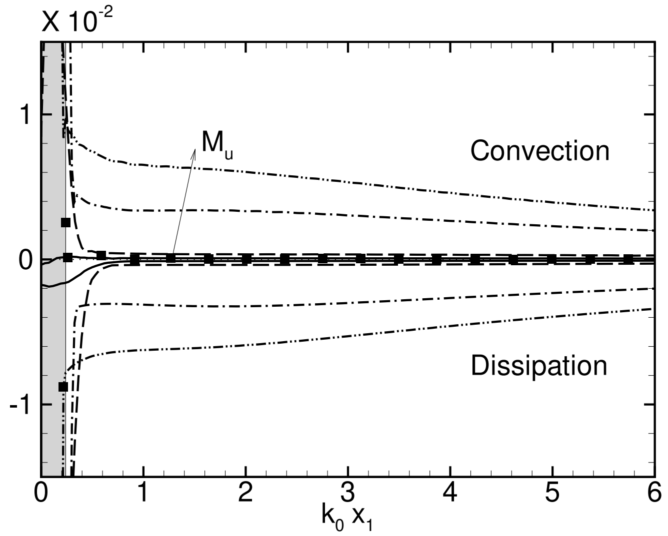


Figure 7.5: Budgets of terms in the transport equation of $\overline{\rho s''^2}$ (Eq. (7.4)) for different Mach numbers: $M_u$ = 1.23 (solid), $M_u$ = 1.50 (dashed), $M_u$ = 2.50 (dash-dotted), $M_u$ = 3.50 (dash-double dotted) from the current simulations. Convection terms are represented on the positive axis and the dissipation terms are shown at the negative axis. Region of unsteady shock motion for $M_u$ = 3.5 (thinnest shock) case is shown by the grey band. Production, diffusion and triple correlation terms (not shown) are very small in magnitude in comparison to the dominant terms. The square symbols represent the sum of all terms in the transport equation and indicates budget closure when zero.

The entropy variance transport equation and its budget plots in Fig. (7.5) are very different from those for the other thermodynamic fluctuations. The entropy budget is entirely governed by the thermal dissipation term, which includes a product of fluctuating heat flux vector and entropy gradients in the fluid. There is a slow monotonic decay in the dissipation rate and the steep gradient in the vicinity of the shock wave is due to unsteady shock oscillations. The triple correlation term has a non-negligible contribution to the overall budget, especially at low Mach numbers, indicative of high turbulence intensity resulting in entropy fluctuations. It has the usual correlation of the viscous work with the entropy fluctuations. There is an additional term consisting of the viscous dissipation of temperature fluctuations and the fluctuating entropy.

The dissipation effect balances the positive convection and small values of triple correlations for weaker interactions. The magnitude of viscous dissipation increases with Mach number. A similar increase in the dissipation of temperature fluctuations is reported in Fig. (7.4). We note that the entropy being a pure mode, has no contribution from the acoustic waves generated at the shock. This is evident from the absence of the dilatation effect in the $\widetilde{s''^2}$ transport equation. We also identify that the diffusion term has the same form as earlier, and is negligible except for the immediate vicinity of the shock wave. Production due to the post-shock gradients in mean entropy, mean temperature and mean velocity is also small and comparable to the error in the budget.

## 7.2 Modeling implications

It is identified that the transport of the thermodynamic variances in the post-shock region to be dominated by dilatational effects and dissipative mechanisms (see Sect. (7.1)). The full transport equations can be approximated to a suitable degree in the form of,

$$\widetilde{u}\,\frac{\partial \overline{\rho'^2}}{\partial x_1} \approx -2\,\overline{\rho}\,\overline{\rho'\,\frac{\partial u''_j}{\partial x_j}}, \tag{7.5}$$

$$\widetilde{u}\,\frac{\partial \overline{p'^2}}{\partial x_1} \approx -2\,\gamma\,\overline{p}\,\overline{p'\,\frac{\partial u''_j}{\partial x_j}}, \tag{7.6}$$

$$\widetilde{u}\,\frac{\partial \widetilde{T''^2}}{\partial x_1} \approx -\frac{2}{\overline{\rho}\,c_v}\,\overline{p}\,\overline{T''\,\frac{\partial u''_j}{\partial x_j}} - \frac{2}{\overline{\rho}\,c_v}\,\overline{q_j\,\frac{\partial T''}{\partial x_j}}, \tag{7.7}$$

$$\widetilde{u}\,\frac{\partial \widetilde{s''^2}}{\partial x_1} \approx -2\,\overline{\frac{q_j}{T}\,\frac{\partial s''}{\partial x_j}}, \tag{7.8}$$

where only the dominant source terms are retained on the right-hand side.

The dilatation source terms in the transport equations for density, pressure and temperature variance represent inviscid mechanism; they are devoid of any viscous or conduction effects. These source terms are also dominated by the acoustic mode, which has isentropic thermodynamic fluctuations. The isentropic relations between $p'$, $\rho'$ and $T'$ can thus be used for modeling the unclosed correlations in the respective dilatation source terms. Also note that the isentropic thermodynamic field is expected to correlate well with the dilatational velocity field, as both correspond to the acoustic waves generated at the shock wave. The fact that LIA is able to reproduce the acoustic mode, namely the pressure fluctuations, makes the linear inviscid framework appropriate for modeling the simplified transport equations given in Eqs. (7.5) - (7.8).

The dissipation term in the entropy equation shown in Eq. (7.8) has to be modeled differently, as the LIA theory does not provide information on the viscous and heat conduction effects. The entropy mode generated at the shock, and its isobaric nature can be exploited to develop closure models for the dissipation source terms in the entropy and temperature equations. The model equations can be cast in the $k - \epsilon$ framework, in line with the modeling of the vorticity variance and the solenoidal dissipation rate in Ref. [144]. Also, the variation of the mean conductivity across shock wave has to be accounted for, akin to the effect of the mean viscosity on the turbulent dissipation rate. The new physics-based models thus developed can be applied to canonical shock-turbulence interaction cases from the current DNS as well as those of Larsson *et al.* [81]. The magnitude of the thermodynamic variances generated for different Mach numbers and their post-shock evolution can be compared to the extensive DNS and LIA results presented in Chaps. (5) and (6).

## 7.3 Summary

For the region behind the shock. correlations of density-, pressure- and temperature-fluctuations with dilatation is found to be the dominant term in their respective variances. For entropy, the balance is due to the viscous dissipation term. The amplification at the shock, however, is found to be due to production mechanisms. These findings suggest that for the case of canonical STI, the thermodynamic field is governed by mostly inviscid mechanisms, the dilatation correlation, which is an acoustic effect that can be predicted using the LIA theory. Their implications for modeling the thermodynamic variances are highlighted.

# Chapter 8

# Modeling of thermodynamic fluctuations

In the previous chapter, the comparison of budget of terms for the thermodynamic variances showed that the dominant terms are linear in nature (mostly) and could be predicted by LIA. We follow the methodologies provided in the works of Sinha *et al.* [144, 145, 163], and Quadros and Sinha [117] to develop algebraic models for predicting the amplification (or production) of thermodynamic fluctuations across the shock. One of the important features of STI is the shock-corrugation effect (or shock-unsteadiness effect [145]), which is not incorporated in standard turbulence models such as $k-\epsilon$ and $k-\omega$ when used in shock-dominated problems. This results in an incorrect prediction of TKE which are mostly larger than those observed in DNS/LIA data. The inclusion of the shock-unsteadiness effect damps the excess (or incorrect measure) of the production of TKE, leading to an accurate prediction of the amplification of TKE across the shock. In this chapter, we explore the effect of shock-unsteadiness on the thermodynamic fluctuations via an integrated budget approach as followed in [145], and then follow up with the development of a model for the thermodynamic fluctuations.

Models for the temperature fluctuations [168] and for the density fluctuations (and also its flux) [139, 148, 155] in the differential equation form are available in literature for shock-dominated problems. Xiao *et al.* [168] proposed a differential equation based model for the turbulent enthalpy variance, which can be rewritten in terms of the temperature variance for perfect gases. Taulbee and VanOsdol [155] proposed models for the density variance and the turbulent mass flux using gradient diffusion hypothesis. Soulard *et al.* [148], on the other hand, proposed a model for the density variance based on pseudo-compressible approximation. Schwarzkopf *et al.* [139] proposed models for the unclosed second-moment terms in the transport equation of the Reynolds stress, which rely on a differential equation for the modeled turbulent lengthscale of the problem. Additional closures for the density variance and the turbulent mass flux were also provided based on the same turbulent lengthscale by them. These models are complex in nature comprising multiple effects such as diffusion and pressure gradients. Our objective is rather to develop simple, yet robust models for the post-shock thermodynamic fluctuations, which are also algebraic in nature.

We make use of LIA and the shock-unsteadiness $k-\epsilon$ model of Sinha *et al.* [145] (hereby, referred as SU $k-\epsilon$ model) to develop the models for the shock-amplified thermodynamic fluctuations. The proposed models have been developed in the phenomenological sense, and are compliant with the underlying physical mechanisms. DNS data from the $M_t = 0.22$ and $\mathrm{Re}_\lambda = 40$ dataset of Larsson *et al.* [81] are used to validate the proposed models. The models assume the inflow turbulence to be purely vortical, which implies that there are no thermodynamic fluctuations upstream of the shock wave. The DNS data, however, has some finite thermodynamic fluctuations in the upstream region but are very small compared to the vortical fluctuations [83]. We further consider that this canonical problem can be represented in a one-dimensional framework, since the averages (or moments in general) are functions of only the shock-normal direction ($x_1$ or just $x$ here). In this chapter, subscripts 1 and 2 are used to represent upstream and downstream values, respectively, instead of $u$ and $d$. It is to be noted that $k_{1/2}$ mean the upstream/downstream TKE in this chapter whereas, $k_0$ is still used to denote the peak energy wavenumber for consistency.

## 8.1 Linearized transport equations

The governing equations for the transport of thermodynamic variances and the budget analysis of the DNS data showing the dominant terms for each of the thermodynamic variances were already discussed in the previous chapter (also provided in Ref. [142]). In this section, the transport equations of the thermodynamic variances are linearized (about the uniform mean flow) and the budget of each term is computed using LIA. The differential form of the linearized equations is written in the frame of reference attached to the unsteady shock [99]. The equations are then integrated across the shock to identify the contribution of each term in the post-shock region (see [145, 163] for a detailed procedure).

### 8.1.1 Temperature variance

The conservation of total enthalpy in its linearized form,

$$c_p \frac{\partial T'}{\partial x} = -\overline{u}\frac{\partial u'}{\partial x} - u'\frac{\partial \overline{u}}{\partial x} + \xi_t \frac{\partial \overline{u}}{\partial x}, \tag{8.1}$$

is used to obtain the linearized transport equation for the temperature variance in the unsteady shock frame of reference. Here, $\xi_t$ is the shock-unsteadiness velocity. Taking a moment with $T'$ and neglecting higher order terms, the linearized equation is obtained as,

$$c_p \frac{\partial}{\partial x}\left(\frac{\overline{T'^2}}{2}\right) = -\overline{u'T'}\frac{\partial \overline{u}}{\partial x} + \overline{T'\xi_t}\frac{\partial \overline{u}}{\partial x} - \overline{u}\,\overline{T'\frac{\partial u'}{\partial x}}, \tag{8.2}$$

where the first term on the RHS is the production term due to the gradient of mean velocity. The second term is the shock unsteadiness term and the last term is the correlation between temperature and dilatation fluctuations. From the linearized Rankine-Hugoniot relation for enthalpy conservation across a normal shock, the change in temperature variance is written as,

$$\underbrace{c_p \frac{\left(\overline{T_2'^2} - \overline{T_1'^2}\right)}{2}}_{\text{Amplification}} = \underbrace{-\,\overline{u_1'T_m'}\,(\overline{u}_2 - \overline{u}_1)}_{\text{Production}} + \underbrace{\overline{T_m'\xi_t}\,(\overline{u}_2 - \overline{u}_1)}_{\text{Shock unsteadiness}} \underbrace{-\,\overline{u}_2\,\overline{T_m'\left(u_2' - u_1'\right)}}_{\text{Dilatation}}, \tag{8.3}$$

where $T_m' = \dfrac{(T_1' + T_2')}{2}$. Equation (8.3) is the integrated form of Eq. (8.2) across the shock, where the first term on the RHS is the production due to mean velocity gradient (*Production*), followed by the damping of the *Shock unsteadiness* term and the temperature-dilatation correlation term (*Dilatation*).

Figure (8.1) shows the budget of Eq. (8.3) for different Mach numbers where the terms are normalized by $c_p\,\overline{T}_2^2\left(\dfrac{k_1}{\overline{u}_1^2}\right)$. The integrated budget for the temperature variance across the shock show that the *Production* term to be the dominant term, contributing to the entirety of the amplification of temperature variance (*Amplification*) across the shock. The *Dilatation* term albeit small, is finite and is responsible for the amplification of temperature variance for the low Mach number cases. The *Shock unsteadiness* term is found to be negligible except for the high Mach number cases, where it balances out the contribution from the *Dilatation* term. The correlations such as $\overline{u'T'}$ and $\overline{T'\xi_t}$ are computed using the LIA theory, similar to Eq. (6.1) in chapter (6).

### 8.1.2 Density variance

The linearized transport equations for the density variance is obtained from the linearized mass conservation equation,

$$\overline{u}\frac{\partial \rho'}{\partial x} = -\overline{\rho}\frac{\partial u'}{\partial x} - \rho'\frac{\partial \overline{u}}{\partial x} - u'\frac{\partial \overline{\rho}}{\partial x} + \xi_t\frac{\partial \overline{\rho}}{\partial x}, \tag{8.4}$$

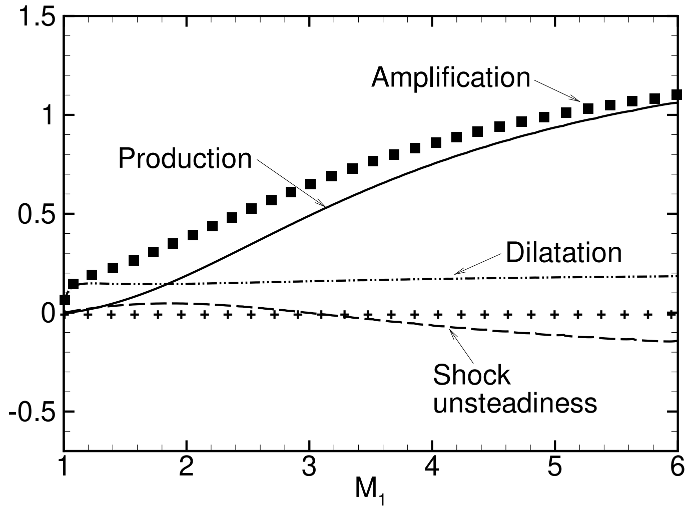


Figure 8.1: Budget of Eq. (8.3) for different Mach numbers. The terms are shown as they appear in the equation with the plusses denoting the balance between the LHS and RHS. All terms are normalized by $c_p \overline{T}_2^2 (k_1/\overline{u}_1^2)$

by taking a moment with $\rho'$ and neglecting higher order terms. The linearized equation is given by,

$$\overline{u}\,\frac{\partial}{\partial x}\left(\frac{\overline{\rho'^2}}{2}\right) = -\overline{u'\rho'}\,\frac{\partial\overline{\rho}}{\partial x} - \overline{\rho'^2}\,\frac{\partial\overline{u}}{\partial x} + \overline{\rho'\xi_t}\,\frac{\partial\overline{\rho}}{\partial x} - \overline{\rho}\,\overline{\left(\rho'\frac{\partial u'}{\partial x}\right)}, \tag{8.5}$$

where the first and the second terms on the RHS are production terms due to mean gradients of density and velocity, respectively. The third term accounts for the damping in production due to the unsteady shock and the last term is the correlation between density and dilatation fluctuations. From the linearized RH relation for conservation of mass, the change in density variance across the shock is written as,

$$\begin{aligned}\underbrace{\overline{u}_2\frac{\left(\overline{\rho_2'^2}-\overline{\rho_1'^2}\right)}{2}}_{\text{Amplification}} &= -\underbrace{\overline{\rho_m' u_2'}\,\left(\overline{\rho}_2-\overline{\rho}_1\right)}_{\text{Production-1}} - \underbrace{\overline{\rho_1'\rho_m'}\,\left(\overline{u}_2-\overline{u}_1\right)}_{\text{Production-2}} + \\ &\quad \underbrace{\overline{\rho_m'\xi_t}\,\left(\overline{\rho}_2-\overline{\rho}_1\right)}_{\text{Shock unsteadiness}} - \underbrace{\overline{\rho}_1\,\overline{\rho_m'\left(u_2'-u_1'\right)}}_{\text{Dilatation}},\end{aligned} \tag{8.6}$$

where $\rho_m' = \dfrac{(\rho_1' + \rho_2')}{2}$. Equation (8.6) can be interpreted as the integrated form of Eq. (8.5) across the shock. The term *Amplification* describes the change in density variance across the shock, *Production-1* is the production due to mean density gradients, *Production-2* is the production due to mean velocity gradients, *Shock unsteadiness* is the damping term due to the unsteady shock, and *Dilatation* corresponds to the density-dilatation correlation term.

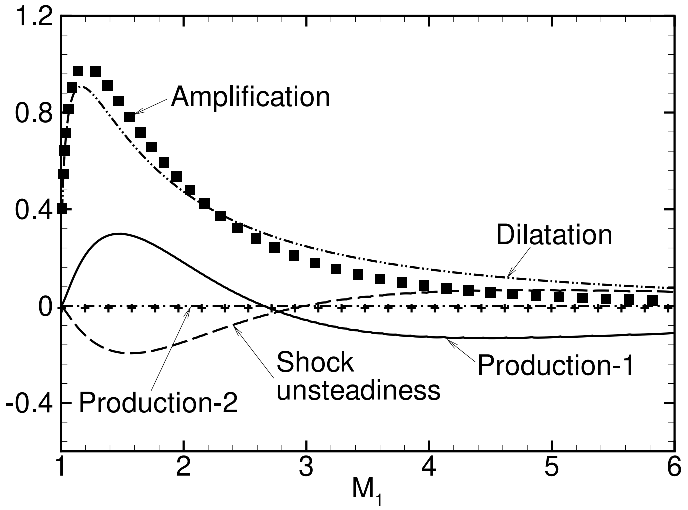


Figure 8.2: Budget of Eq. (8.6) for different Mach numbers. The terms are shown as they appear in the equation with the plusses denoting the balance between the LHS and RHS. All terms are normalized by $\overline{\rho}_2^2\,\overline{u}_2\,k_1/\overline{u}_1^2$

Figure (8.2) shows the budget of Eq. (8.6) against different Mach numbers for the case of purely vortical inflow turbulence, where the terms are normalized by $\overline{\rho}_2^2\,\overline{u}_2\left(\dfrac{k_1}{\overline{u}_1^2}\right)$. The integrated budgets across the shock show that the *Dilatation* term to be the dominant term matching the *Amplification* term. The effect of the *Shock unsteadiness* term is found to damp the *Production-1* term. The *Production-2* term is identically zero due to assumption of purely vortical turbulence upstream of the shock. The total density variance immediately behind the shock (or near-field density variance) tend towards zero at high Mach numbers, which is due to the balance between the acoustic and the entropy modes. The density variance away from the shock (or far-field density variance), however, is finite due to the entropy mode being larger than the acoustic mode [142]. For the case of upstream turbulence comprising of both vorticity and entropy fluctuations, the near-field density variance is found to be finite for the high Mach number interactions and strongly depends on the correlation between the vorticity and the entropy modes [99].

### 8.1.3 Pressure variance

The linearized transport equations for the pressure variance is also obtained in a similar way as that of the density variance. The linearized streamwise momentum conservation equation is,

$$\frac{\partial p'}{\partial x} = -\overline{\rho}\,\overline{u}\,\frac{\partial u'}{\partial x} - \rho'\,\overline{u}\,\frac{\partial \overline{u}}{\partial x} - u'\,\overline{\rho}\,\frac{\partial \overline{u}}{\partial x} + \xi_t\,\overline{u}\,\frac{\partial \overline{\rho}}{\partial x}. \tag{8.7}$$

Taking moment of the streamwise momentum conservation equation with $p'$ and neglecting higher order terms yields the linearized equation for pressure variance,

$$\frac{\partial}{\partial x}\left(\frac{\overline{p'^2}}{2}\right) = -\overline{\rho}\,\overline{p'u'}\,\frac{\partial \overline{u}}{\partial x} - \overline{u}\,\overline{p'\rho'}\,\frac{\partial \overline{u}}{\partial x} + \overline{\rho}\,\overline{p'\xi_t}\,\frac{\partial \overline{u}}{\partial x} - \overline{\rho}\,\overline{u}\,\overline{p'\frac{\partial u'}{\partial x}}, \tag{8.8}$$

which is similar to Eq. (8.5) with the first and the second terms in the RHS being the production terms, the third term is the shock unsteadiness term which damps the production due to mean velocity gradients and the last term is the correlation between pressure and dilatation fluctuations. The change in pressure variance across the shock is now obtained from the linearized RH relation for conservation of streamwise momentum,

$$\begin{aligned}\underbrace{\frac{\overline{p_2'^2} - \overline{p_1'^2}}{2}}_{\text{Amplification}} &= -\underbrace{\overline{\rho}_1\,\overline{p_m'u_1'}\,(\overline{u}_2 - \overline{u}_1)}_{\text{Production-1}} - \underbrace{\overline{u}_1\,\overline{p_m'\rho_1'}\,(\overline{u}_2 - \overline{u}_1)}_{\text{Production-2}} \\ &\quad + \underbrace{\overline{\rho}_1\,\overline{p_m'\xi_t}\,(\overline{u}_2 - \overline{u}_1)}_{\text{Shock unsteadiness}} - \underbrace{\overline{\rho}_1\,\overline{u}_1\,\overline{p_m'\left(u_2' - u_1'\right)}}_{\text{Dilatation}},\end{aligned} \tag{8.9}$$

where $p_m' = \dfrac{(p_1' + p_2')}{2}$. The above equation is analogous to Eq. (8.6) and can be taken as the integrated form of Eq. (8.8), with the first two terms representing the production of pressure variance, the third term represents the shock unsteadiness effect and the last term denotes the pressure-dilatation correlation.

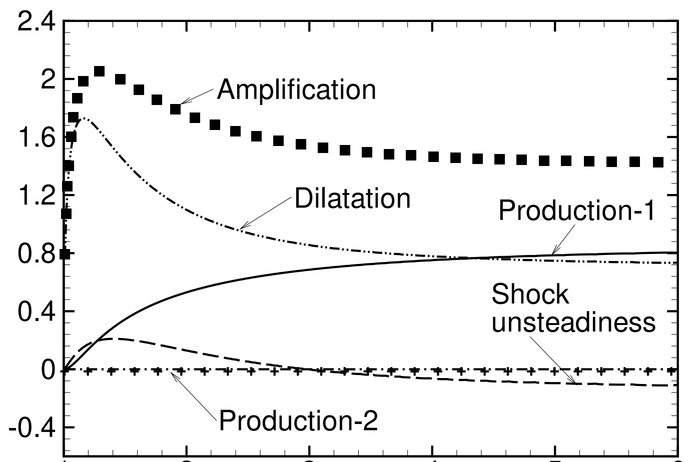


Figure 8.3: Budget of Eq. (8.9) for different Mach numbers. The terms are shown as they appear in the equation with the plusses denoting the balance between the LHS and RHS. All terms are normalized by $\overline{p}_2^2\,(k_1/\overline{u}_1^2)$

Figure (8.3) shows the budget of Eq. (8.9) for different Mach numbers where the terms are normalized by $\overline{p}_2^2\left(\dfrac{k_1}{\overline{u}_1^2}\right)$. The integrated budgets across the shock show that the

*Production-1* and the *Dilatation* term to be the dominant terms whereas, the effect of *Shock unsteadiness* is negligible except for low Mach numbers. The *Production-2* term which comprises of the correlation of pressure fluctuations with upstream density fluctuations is identically zero due to the consideration of purely vortical turbulence upstream of the shock. This term, however, would have significant contribution to the change in pressure variance if the upstream turbulence is of a mixed type such as vortical-entropy turbulence as considered in Refs. [98, 99] and [163].

The integrated budgets for the density, pressure and temperature variances indicate that the *Production* term in the form of $\overline{f'u'}\dfrac{\partial \overline{u}}{\partial x}$ and the *Dilatation* term in the form of $\overline{f'\left(\dfrac{\partial u'}{\partial x}\right)}$ to be the dominant terms. We, thus, model the production of thermodynamic variances at the shock as the product of the correlation $\overline{f'u'}$ and the mean velocity gradient $\left(\dfrac{\partial \overline{u}}{\partial x}\right)$. The effect of the dilatation term, as will be shown later, would be to damp the production at the shock and to model the decay of the thermodynamic variances in the region behind the shock.

## 8.2 Model development

The predictive models for temperature, density, pressure and entropy fluctuations are developed from the linearized equations in this section. The procedure used in the development of the models is analogous to the procedure followed in the works of Sinha *et al.* [145] and Quadros & Sinha [117]. We make use of the understanding of the underlying dynamics from earlier analysis on the thermodynamic fluctuations (previous chapters and also summarized in [142]) and on the turbulent energy flux [118, 119] for the model development. The following points consolidate the key messages from the previous studies:

- Thermodynamic variances obtained from LIA match well with the DNS data, and thus LIA predictions can be used to model the underlying physics (by providing closures for the generally unknown correlations).
- Reynolds and Favre averaged quantities were found to be approximately the same, i.e., $\overline{f} \approx \widetilde{f}$ and $\overline{f'^2} \approx \widetilde{f''^2}$.
- Density ($\overline{\rho'^2}$), pressure ($\overline{p'^2}$) and temperature ($\overline{T'^2}$) variances show a large amplification at the shock followed by a rapid decay. This rapid decay is mostly due to acoustic mechanisms.

- Entropy variance ($\overline{s'^2}$) also show a large amplification at the shock but a rather gradual decay compared to the other thermodynamic quantities. This slower decay is mostly due to viscous mechanisms.
- Decomposition of the post-shock thermodynamic variances in terms of their Kovásznay modes [78] (acoustic, entropy and vorticity modes) showed that the entropy-entropy correlation to be significant in the far-field ($x \rightarrow \infty$) and the acoustic-acoustic correlation to be dominant in the near-field ($x = 0^+$). Here, the shock is located at $x = 0$.
- At high Mach numbers, the effect of the acoustic mode in the variances is found to be small compared to the entropy mode in the thermodynamic fluctuations.

### 8.2.1 Temperature flux correlation

The model for turbulent temperature flux is derived here. This is similar to the model development procedure followed in Ref. [117]. First, we start with the linearized RH relation for the total enthalpy in the frame of reference attached to the instantaneous shock,

$$c_p \frac{\partial T'}{\partial x} = -\overline{u} \frac{\partial u'}{\partial x} - u' \frac{\partial \overline{u}}{\partial x} + \xi_t \frac{\partial \overline{u}}{\partial x}, \tag{8.10}$$

which upon taking a moment with $u'$ gives the linearized equation for temperature flux as,

$$c_p \frac{\partial}{\partial x} \left( \overline{u'T'} \right) = -\overline{u} \frac{\partial}{\partial x} \left( \frac{\overline{u'^2}}{2} \right) - \overline{u'^2} \frac{\partial \overline{u}}{\partial x} + \overline{u'\xi_t} \frac{\partial \overline{u}}{\partial x} + c_p \overline{T' \frac{\partial u'}{\partial x}}, \tag{8.11}$$

where the first two terms on the RHS are the production terms, the third term is the shock unsteadiness effect and the fourth term is the temperature-dilatation correlation.

Assuming $\overline{u'^2} = \dfrac{2k}{3}$ and $\overline{u'\xi_t} = b_1 \overline{u'^2}$, Eq. (8.11) is rewritten in terms of turbulent kinetic energy, $k$. Here, $b_1 = 0.4 + 0.6\, e^{2(1-M_1)}$ is the modeling coefficient obtained using LIA [145]. The modified equation reads as,

$$c_p \frac{\partial}{\partial x} \left( \overline{u'T'} \right) = -\frac{4}{9}\, (1 - b_1)\, k \frac{\partial \overline{u}}{\partial x} + c_p \overline{T' \frac{\partial u'}{\partial x}}, \tag{8.12}$$

where the model equation for $k$ from Ref. [145],

$$\overline{u} \frac{\partial k}{\partial x} = -\frac{2}{3} \left[ 1 - b_1 \right] k \frac{\partial \overline{u}}{\partial x}, \tag{8.13}$$

is used to solve for the turbulent kinetic energy.

Similar to the procedure used in Ref. [145] to determine the amplification of turbulent kinetic energy, we can compute the amplification of the turbulent temperature flux by considering the production term alone. The modeled equation for $\overline{u'T'}$ thus reduces to,

$$c_p \frac{\partial}{\partial x} \left( \overline{u'T'} \right) \approx -\frac{4}{9}\, (1 - b_1)\, k \frac{\partial \overline{u}}{\partial x}. \tag{8.14}$$

Integrating Eq. (8.13) across the shock yields the relation,

$$\frac{k_2}{k_1} = \left(\frac{\overline{u}_2}{\overline{u}_1}\right)^{-\frac{2}{3}(1-b_1)}. \tag{8.15}$$

which is a function of the upstream Mach number only, and can be used to obtain a closed form solution for the temperature flux across the shock. Upon substitution of Eq. (8.15) in Eq. (8.14) and integrating across the shock yields,

$$c_p\left(\overline{u_2'T_2'} - \overline{u_1'T_1'}\right) \approx \left[\frac{4}{9}(1-b_1)\right]\left(\frac{3}{2b_1+1}\right)\left[1-\left(\frac{\overline{u}_1}{\overline{u}_2}\right)^{-\frac{1}{3}(2b_1+1)}\right] k_1\,\overline{u}_1, \tag{8.16}$$

where $\overline{u_1'T_1'} = 0$ for the case of purely vortical turbulence upstream of the shock. Considering the incoming turbulence to be purely vortical in nature and normalizing Eq. (8.16) as shown below,

$$\left(\overline{u_2'T_2'}\right)_{norm.} = \frac{\overline{u_2'T_2'}}{\overline{u}_1\overline{T}_2\left(\frac{k_1}{\overline{u}_1^2}\right)} \approx \underbrace{\left[\frac{4}{9}(1-b_1)\right]\left(\frac{3}{2b_1+1}\right)\left[1-\left(\frac{\overline{u}_1}{\overline{u}_2}\right)^{-\frac{1}{3}(2b_1+1)}\right]}_{C_{uT}}(\gamma-1)\,\frac{M_1^2}{\left(\overline{T}_2/\overline{T}_1\right)}, \tag{8.17}$$

where the normalized downstream temperature flux is a function of the Mach number and the ratio of specific heats only. The coefficient $C_{uT}$ can thus be used to model the temperature flux as,

$$\overline{u'T'} = C_{uT}\,\frac{k\,\overline{u}}{c_p}, \tag{8.18}$$

where Eq. (8.17) is used as the guiding principle.

### 8.2.2 Temperature variance

The amplification of temperature fluctuations behind the normal shock is modeled using the *Production* term as,

$$\frac{\partial\overline{T'^2}}{\partial x} \approx -2\,\frac{1}{c_p}\,\overline{u'T'}\,\frac{\partial\overline{u}}{\partial x}, \tag{8.19}$$

where the unknown turbulent temperature flux correlation is closed using the model,

$$\overline{u'T'} = \underbrace{\left[\frac{4}{9}(1-b_1)\right]\left(\frac{3}{2b_1+1}\right)\left[1-\left(\frac{\overline{u}_1}{\overline{u}_2}\right)^{-\frac{1}{3}(2b_1+1)}\right]}_{C_{uT}}\frac{k\,\overline{u}}{c_p}. \tag{8.20}$$

The modeled equation for the amplification of temperature variance across the shock reads as,

$$\frac{\partial\overline{T'^2}}{\partial x} \approx -2\,\frac{C_{uT}\,k\,\overline{u}}{c_p^2}\,\frac{\partial\overline{u}}{\partial x}, \tag{8.21}$$

which depends on the accurate modeling of $k$. The SU $k-\epsilon$ model [145] is used for modeling the TKE. The above equation can be integrated across the shock to yield a closed form solution for the normalized temperature variance as,

$$\left(\overline{T_2'^2}\right)_{norm.} = \frac{\overline{T_2'^2}}{\overline{T}_2^2\left(\frac{k_1}{\overline{u}_1^2}\right)} \approx 2\,C_{uT}\left\{\left(\frac{3}{2(b_1+2)}\right)\left[1-\left(\frac{\overline{u}_1}{\overline{u}_2}\right)^{-\frac{2}{3}(2+b_1)}\right]\right\}(\gamma-1)^2\,\frac{M_1^4}{\left(\overline{T}_2/\overline{T}_1\right)^2}, \tag{8.22}$$

where the assumption of purely vortical turbulence upstream of the shock is also considered, which results in $\overline{T_1'^2} = 0$. The normalized temperature variance is a function of the upstream Mach number and the ratio of specific heats only, which makes it suitable to be compared with LIA data.

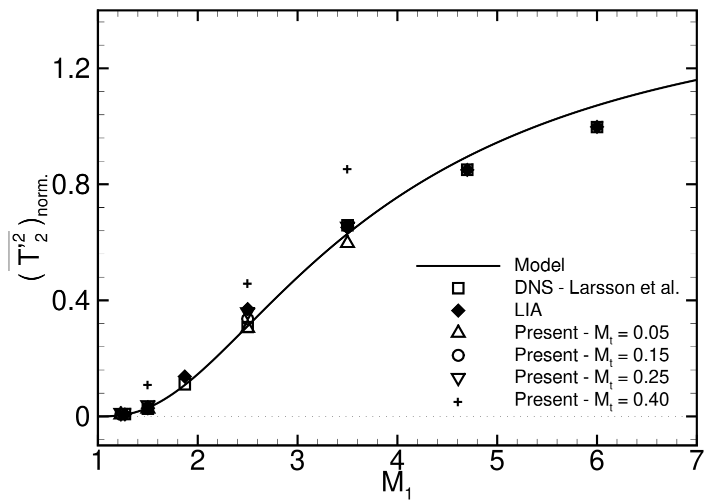


Figure 8.4: Variation of normalized temperature variance against Mach number. Normalization is as mentioned in Eq. (8.22). LIA and DNS values of Ref. [81] (taken by extrapolating to the mean shock center) are shown by a diamond and square symbols, respectively. The predictions from Eq. (8.22) is shown by a solid line. The data from the current simulations for $M_t$ = 0.05, 0.15, 0.25 and 0.4 values are shown by triangle, circle, gradient, and plus symbols, respectively

Figure (8.4) shows the closed-form solution of the normalized temperature variance (Eq. (8.22)) in comparison to the LIA and DNS results against a range of Mach numbers. The DNS dataset used for comparison is the $M_t = 0.22$ and $Re_\lambda = 40$ dataset of Larsson *et al.* [81, 83] which spans from $M_1 = 1.27$ to 6. DNS and LIA show a good match for the temperature variance till the location $k_0 x \approx 1$. Beyond $k_0 x = 1$, LIA predicts constant values whereas, DNS shows further decay towards zero, though gradual, due to the viscous effects. The closed-form solution of the model given in Eq. (8.22) predicts values that are closer to the LIA and DNS results, which were extrapolated to the mean shock center from $k_0 x = 1$.

The model predictions compare similarly for the present set of simulations also, except for the large deviations in $M_t = 0.4$ cases. This is expected since the model is based on LIA which assumes $M_t \to 0$ and also zero thermodynamic fluctuations, upstream of the shock. This model along with a modeled decay mechanism is shown in the next section (Sect. (8.3)) to have an excellent match with the DNS profile.

### 8.2.3 Density variance

The amplification of density variance can also be modeled in a similar fashion as that of the temperature variance shown above. The linearized equation is reduced to,

$$\frac{\partial \overline{\rho'^2}}{\partial x} \approx -2\,\frac{1}{\overline{u}}\,\overline{u'\rho'}\,\frac{\partial \overline{\rho}}{\partial x}, \tag{8.23}$$

where we have to model the unknown $\overline{\rho' u'}$ correlation to provide closure. We attempt to model the far-field density variance in similar lines as that of the model development of far-field $k$ in Ref. [145]. LIA suggests that the far-field acoustic mode becomes very small compared to the entropy mode at high Mach numbers. We make use of this understanding to model the turbulent mass flux in terms of the modeled $\overline{u'T'}$ through the following relations,

$$p' \approx 0 \quad \Rightarrow \quad \frac{\rho'}{\overline{\rho}} \approx -\frac{T'}{\overline{T}}, \tag{8.24}$$

$$\overline{\rho' u'} \approx -\frac{\overline{\rho}}{\overline{T}}\,\overline{u'T'} = -\frac{\overline{\rho}}{\overline{T}}\,C_{uT}\,\frac{k\,\overline{u}}{c_p}, \tag{8.25}$$

where $C_{uT}$ is the expression given in Eq. (8.20). The modeled production of density variance then becomes,

$$\frac{\partial \overline{\rho'^2}}{\partial x} \approx -2\,\frac{\overline{\rho}^2}{c_p\,\overline{T}}\,C_{uT}\,\frac{k}{\overline{u}}\,\frac{\partial \overline{u}}{\partial x}, \tag{8.26}$$

where the conservation of averaged mass,

$$\frac{\partial \overline{\rho}}{\partial x} = -\frac{\overline{\rho}}{\overline{u}}\,\frac{\partial \overline{u}}{\partial x} \tag{8.27}$$

is used to replace the mean density gradient in terms of the mean velocity gradient.

The following relations are used to rewrite Eq. (8.26) to be in terms of the mean velocity, $\overline{u}$ only,

$$\frac{\overline{\rho}_2}{\overline{\rho}_1} = \frac{\overline{u}_1}{\overline{u}_2}, \quad c_p\overline{T}_2 + \frac{\overline{u}_2^2}{2} = c_p\overline{T}_1 + \frac{\overline{u}_1^2}{2}, \quad \frac{k_2}{k_1} = \left(\frac{\overline{u}_1}{\overline{u}_2}\right)^{\frac{2}{3}(1-b_1)}, \tag{8.28}$$

which upon integration (across the shock) yields,

$$\left(\overline{\rho_2'^2}\right)_{norm.} = \frac{\overline{\rho_2'^2}}{\overline{\rho}_2^2\left(\frac{k_1}{\overline{u}_1^2}\right)} \approx 4\,\frac{C_{uT}}{\left(\overline{\rho}_2/\overline{\rho}_1\right)^2}\left[\frac{\left(\frac{\gamma-1}{2}\right)M_1^2}{1+\left(\frac{\gamma-1}{2}\right)M_1^2}\right]\left\{\left(\frac{3}{2\,(b_1-4)}\right)\left[1-\left(\frac{\overline{u}_1}{\overline{u}_2}\right)^{-\frac{2}{3}(b_1-4)}\right]\right.$$
$$\left.+\left[\frac{\left(\frac{\gamma-1}{2}\right)M_1^2}{1+\left(\frac{\gamma-1}{2}\right)M_1^2}\right]\left(\frac{3}{2\,(b_1-1)}\right)\left[1-\left(\frac{\overline{u}_1}{\overline{u}_2}\right)^{-\frac{2}{3}(b_1-1)}\right]\right\}, \tag{8.29}$$

which is an approximation of the exact closed form solution, since the Taylor series expansion of $(c_p\overline{T})^{-1}$ in Eq. (8.26) is limited up to the first order only. The upstream density variance, $\overline{\rho_1'^2} = 0$ due to the assumption of purely vortical turbulence upstream of the shock.

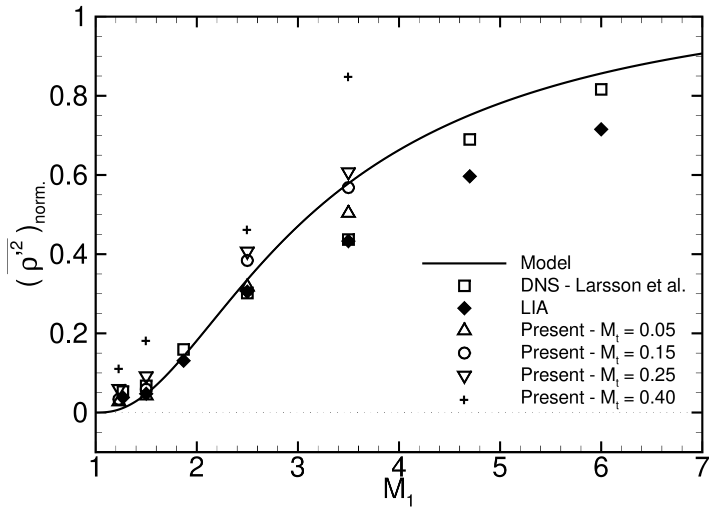


Figure 8.5: Variation of normalized density variance against Mach number. Normalization is as mentioned in Eq. (8.29). LIA and DNS values of Ref. [81] (extrapolated to the mean shock center) are shown by diamond and square symbols, respectively. The values from the closed-form solution given in Eq. (8.29) is shown by a solid line. The lines and symbols are the same as mentioned in caption of Fig. (8.4)

Figure (8.5) compares the closed-form solution of the normalized density variance given in Eq. (8.29) with the LIA and DNS results for a range of Mach numbers. For the high Mach number cases, both LIA and DNS show a non-monotonic variation in density variance with a post-shock peak located approximately at the location $k_0x = 1$. LIA predicts constant value of density variance beyond $k_0x = 3$ location after a short length of adjustment, whereas DNS shows a gradual decay towards zero similar to the temperature variance profile. The negative correlation between the acoustic and the entropy modes is found to be the reason for this non-monotonic behavior in density variance whereas, the correlation was found to be positive for the temperature variance giving it a monotonic profile. The model overpredicts, albeit slightly, both the DNS and the LIA data, whose values were taken by extrapolating to the mean shock center from the post-shock peak location at high Mach numbers, and underpredicts for the low Mach number cases. Similar to the variation observed in the temperature variance, the model underpredicts for $M_t = 0.4$ cases. This is also because of the change in the spatial variation of density variance, which do not show a non-monotonic variation at $M_t = 0.25$ and $M_t = 0.4$ values of the $M_1 = 3.50$ dataset.

### 8.2.4 Entropy variance

Entropy is defined as given in Ref. [51],

$$s = c_v \log\left(\frac{p}{\rho^\gamma}\right) = c_v \log\left(\frac{R\,T}{\rho^{(\gamma-1)}}\right) \tag{8.30}$$

which is a derived quantity based on the other thermodynamic quantities. The procedure used in the derivation of the linearized transport of density, pressure and thermodynamic variances is not directly applicable for the entropy variance, since entropy is not conserved across the shock. We make use of the transport equation of entropy variance (from previous chapter, Eq. (7.4) and in Ref. [142]), which is valid in the post-shock region to develop the model, assuming that the flowfield has been altered by the shock wave. The transport equation for the entropy variance with only the production term reads as,

$$\frac{\partial \overline{s'^2}}{\partial x} \approx -2\,\frac{1}{\overline{\overline{u}}}\,\overline{s'u'}\,\frac{\partial \overline{s}}{\partial x}, \tag{8.31}$$

where we have considered only the production term due to the mean entropy gradient across the shock as the source term. We model the entropy flux correlation in terms of the modeled temperature flux correlation,

$$\frac{s'}{c_p} = -\frac{\rho'}{\overline{\rho}} = \frac{T'}{\overline{\overline{T}}} \;\Rightarrow\; \overline{s'u'} = \frac{c_p}{\overline{\overline{T}}}\,\overline{u'T'} \tag{8.32}$$

where we have used the fact that $p'/\overline{p} << s'/c_p$ for the high Mach number cases considered in this study. We bring in the effect of the shock wave into Eq. (8.31) via the modeled $\overline{u'T'}$ term. The mean entropy gradient in Eq. (8.31) is written in terms of the mean velocity gradient by averaging Eq. (8.30) and computing its gradient,

$$\frac{\partial \overline{s}}{\partial x} = c_v\left[\frac{\gamma-1}{\overline{u}} - \frac{\overline{u}}{c_p\,\overline{\overline{T}}}\right]\frac{\partial \overline{u}}{\partial x}. \tag{8.33}$$

The modeled entropy variance equation is now written in terms of turbulent kinetic energy and mean velocity gradients as,

$$\frac{1}{c_p^2}\,\frac{\partial \overline{s'^2}}{\partial x} = -2\,\frac{C_{uT}}{\gamma}\,\frac{k}{c_p\,\overline{\overline{T}}}\left[(\gamma-1) - \frac{\overline{u}^2}{c_p\,\overline{\overline{T}}}\right]\frac{1}{\overline{\overline{u}}}\,\frac{\partial \overline{u}}{\partial x}, \tag{8.34}$$

where $C_{uT}$ is the same model coefficient given in Eq. (8.20). Integration of Eq. (8.34) across the shock results in,

$$\begin{aligned}
\left(\overline{s_2'^2}\right)_{norm.} &= \frac{\overline{s_2'^2}}{c_p^2\left(\frac{k_1}{\overline{u}_1^2}\right)} \approx 4\,\frac{C_{uT}}{\gamma}\left[\frac{\left(\frac{\gamma-1}{2}\right)M_1^2}{1+\left(\frac{\gamma-1}{2}\right)M_1^2}\right]\times \\
&\left\{(\gamma-1)\left(\frac{3}{2\,(b_1-1)}\right)\left[1-\left(\frac{\overline{u}_1}{\overline{u}_2}\right)^{-\frac{2}{3}(b_1-1)}\right]+\right. \\
&(\gamma-3)\left[\frac{\left(\frac{\gamma-1}{2}\right)M_1^2}{1+\left(\frac{\gamma-1}{2}\right)M_1^2}\right]\left(\frac{3}{2\,(b_1+2)}\right)\left[1-\left(\frac{\overline{u}_1}{\overline{u}_2}\right)^{-\frac{2}{3}(b_1+2)}\right] \\
&-4\left[\frac{\left(\frac{\gamma-1}{2}\right)M_1^2}{1+\left(\frac{\gamma-1}{2}\right)M_1^2}\right]^2\left(\frac{3}{2\,(b_1+5)}\right)\left[1-\left(\frac{\overline{u}_1}{\overline{u}_2}\right)^{-\frac{2}{3}(b_1+5)}\right] \\
&\left.-2\left[\frac{\left(\frac{\gamma-1}{2}\right)M_1^2}{1+\left(\frac{\gamma-1}{2}\right)M_1^2}\right]^3\left(\frac{3}{2\,(b_1+8)}\right)\left[1-\left(\frac{\overline{u}_1}{\overline{u}_2}\right)^{-\frac{2}{3}(b_1+8)}\right]\right\},
\end{aligned} \tag{8.35}$$

which is an approximation to the exact closure of the equation due to the truncation of the Taylor series expansion of $(c_p\overline{T})^{-2}$ to first order terms only.

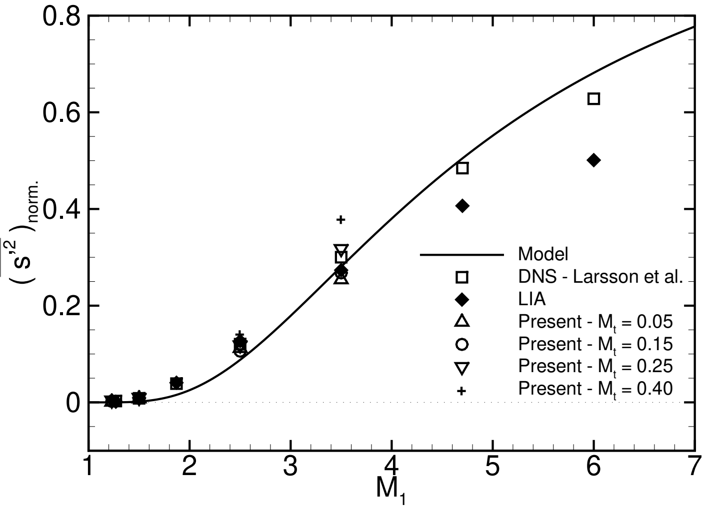


Figure 8.6: Variation of normalized entropy variance against Mach number. Normalization is as mentioned in Eq. (8.35). DNS values of Ref. [81], which are taken by extrapolating to the mean shock center, are shown by square symbols, and the LIA values are shown by diamond symbols. The closed-form solution given in Eq. (8.35) is shown by a solid line. The lines and symbols are the same as mentioned in caption of Fig. (8.4)

The production of the normalized entropy variance across the shock is given by the the closed-form solution of Eq. (8.35). The variation of Eq. (8.35) is shown in Fig. (8.6) along with the LIA and DNS results. The DNS predicts large amplification of entropy variance at the shock followed by a gradual decay. LIA, on the other hand, predicts constant entropy variance throughout the downstream region.

The model compares well with the DNS and the LIA data, although it slightly underpredicts for the low Mach number cases and overpredicts for the high Mach numbers. The DNS values are taken by extrapolating to the mean shock center from $k_0 x = 1$ location. The predictions grossly underpredict for the $M_t = 0.4$ cases as observed in the other variances.

### 8.2.5 Pressure variance

The model equation for the production of pressure variance is given by,

$$\frac{\partial \overline{p'^2}}{\partial x} \approx -2 \,\overline{p}\, \overline{p'u'}\, \frac{\partial \overline{u}}{\partial x}, \tag{8.36}$$

where only the production term in Eq. (8.8) is considered to be the source term.

The production of the density and entropy variances were obtained by considering that there are negligible pressure fluctuations for the high Mach number interactions. We attempt to develop the model for pressure variance with a different approach whereby, we use isentropic relations to relate the pressure flux correlation $\overline{p'u'}$ and the temperature flux correlation $\overline{T'u'}$ as,

$$\frac{p'}{\overline{p}} = \left(\frac{\gamma}{\gamma-1}\right)\frac{T'}{\overline{T}} \;\Rightarrow\; \overline{p'u'} = \left(\frac{\gamma}{\gamma-1}\right)\frac{\overline{p}}{\overline{T}}\,\overline{u'T'}. \tag{8.37}$$

Upon substitution of Eq. (8.37) in Eq. (8.36) we get,

$$\frac{\partial \overline{p'^2}}{\partial x} \approx -2 \overline{\rho}^2\, C_{uT}\, k\, \overline{u}\, \frac{\partial \overline{u}}{\partial x}, \tag{8.38}$$

where Eq. (8.20) is used to write the temperature flux correlation in terms of the turbulent kinetic energy. Integration of Eq. (8.38) yields,

$$\left(\overline{p_2'^2}\right)_{norm.} = \frac{\overline{p_2'^2}}{\overline{p}_2^2\left(\frac{k_1}{\overline{u}_1^2}\right)} \approx 2\, C_{uT}\left(\frac{3}{2(b_1-1)}\right)\left[1-\left(\frac{\overline{u}_1}{\overline{u}_2}\right)^{-\left(\frac{2}{3}(b_1-1)\right)}\right]\gamma^2\,\frac{M_1^4}{(\overline{p}_2/\overline{p}_1)^2}, \tag{8.39}$$

where the normalized pressure variance is found to approach an asymptotic value at high Mach numbers similar to the temperature variance.

Figure (8.7) shows the closed-form solution given in Eq. (8.39) along with the results from LIA and DNS for a range of Mach numbers. The model predicts amplifications slightly larger than the DNS values of Ref. [81] and slightly underpredicts for the present simulations with $M_t = 0.25$. The pressure variance values for the cases with $M_t = 0.4$, which were also taken by extrapolating to the mean shock center from the location $k_0x = 1$, are much larger than the model predictions. The LIA values are also computed in a similar fashion by extrapolating to the shock center. Unlike the DNS values which were increasing as the Mach number is increased, the LIA values were found to asymptote around the value of 1.5 for the high Mach number cases. This results in the model to be largely overpredicting compared to the LIA results at very high Mach numbers. Nonetheless, the model shows excellent agreement with the available DNS data.

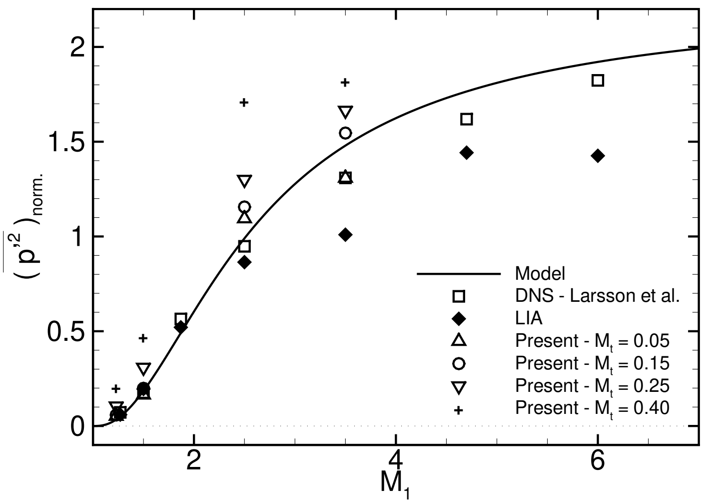


Figure 8.7: Variation of normalized pressure variance against Mach number. Normalization is as mentioned in Eq. (8.39). LIA and DNS values of Ref. [81] are taken by extrapolating to the center of the mean shock (see [118]). The LIA and DNS results are shown by diamond and square symbols, respectively. The closed-form solution given in Eq. (8.39) is shown by a solid line. The lines and symbols are the same as mentioned in caption of Fig. (8.4)

The closed-form solutions given in Eqs. (8.39), (8.35), (8.29) and (8.22) are indeed models for the post-shock normalized thermodynamic fluctuations obtained using LIA estimates. These solutions assume an inviscid shock similar to LIA, whose strength determines the intensity of the thermodynamic fluctuations. The post-shock fluctuation levels predicted by the model are comparable to the DNS and LIA values. In the following section, we extend these LIA-based models to include spatial decay in the post-shock region by adding dissipative terms. The dissipative terms include inviscid and viscous decay mechanisms. The inviscid decay mechanism is modeled with the help of LIA, while the viscous decay is similar to the dissipation effect in $k-\epsilon$ framework.

## 8.3 Modeling predictions

The averages (or moments) for this case of canonical shock-turbulence interaction are only dependent on the streamwise direction. This enables us to solve the transport equations for the thermodynamic variances given in Eqs. (8.21), (8.26), (8.34) and (8.38) in a one-dimensional framework. Since the equations are solved in the one-dimensional framework, the partial differential operator ($\partial$) and the ordinary differential operator ($d$) mean the same, and are used interchangeably. The equations are integrated in space using the classical $4^{th}$ order accurate Runge-Kutta method. The mean profile with the shock located at $k_0 x = 0$ is specified as follows,

$$\overline{u}(x) = \overline{u}_1 + (\overline{u}_2 - \overline{u}_1)\,\frac{1}{2}\,(1 + \tanh(x)), \tag{8.40}$$

$$\overline{\rho}(x) = \overline{\rho}_1\,\frac{\overline{u}_1}{\overline{u}(x)}, \tag{8.41}$$

$$\overline{T}(x) = \overline{T}_1 + \frac{1}{2c_p}\left(\overline{u}_1^2 - \overline{u}^2(x)\right), \tag{8.42}$$

$$\frac{d\overline{u}(x)}{dx} = \frac{\overline{u}_2 - \overline{u}_1}{\Delta x}\,\frac{1}{2}\left(1 - \tanh^2(x)\right), \tag{8.43}$$

$$\frac{d\overline{T}(x)}{dx} = -\frac{1}{c_p}\,\overline{u}(x)\,\frac{d\overline{u}(x)}{dx}, \tag{8.44}$$

where $\Delta x$ is the grid spacing in the one-dimensional grid.

The transport equations for the thermodynamic variances depend on the accurate modeling of TKE, $k$ and its dissipation rate, $\epsilon$. The model equations for $k$ and $\epsilon$ from Refs. [145] and [144], respectively, are also integrated along with the equations for the thermodynamic variances. The transport equations for the thermodynamic variances account only for the production of the thermodynamic variances, and their decay needs additional modeling. The spatial decay of the thermodynamic variances are modeled in a phenomenological sense, following the work of Ref. [117]. From LIA and DNS profiles of thermodynamic variances [142], the following points summarize the decay mechanisms for the thermodynamic variances:

- Temperature and density variances show acoustic decay till $k_0 x \approx 1 - 2$ and viscous decay is observed beyond that location,
- Pressure variance has only the acoustic decay mechanism
- Entropy variance has only the viscous decay mechanism

We model the decay profiles of the thermodynamic variances with the physical insights obtained from the earlier studies. The pressure and the entropy variance equations are implemented with an acoustic and a viscous decay mechanism, respectively. Temperature variance is modeled with a mixed type of decay profile with the acoustic mode being dominant behind the shock up to a certain distance and the entropy mode after that location. The production of density variance was modeled by considering the far-field variation of the density variance. The density variance is thus, modeled with only a viscous decay mechanism since the acoustic decay effects are minimal in the far-field. Additionally, the use of only a viscous decay mechanism in the density variance would also highlight the differences with the mixed type of decay model used in the temperature variance. The complete equations with the production and the decay terms for each of the thermodynamic variances along with the models for $k$ and $\epsilon$ are given in,

$$\frac{\partial}{\partial x}\begin{Bmatrix} \overline{\rho}\,\overline{u}\,k \\ \overline{\rho}\,\overline{u}\,\epsilon \\ \overline{T'^2} \\ \overline{\rho'^2} \\ \overline{s'^2} \\ \overline{p'^2} \end{Bmatrix} = \begin{Bmatrix} -\frac{2}{3}\overline{\rho}\,k\,\frac{\partial\overline{u}}{\partial x}\,(1-b_1') - \overline{\rho}\,\epsilon \\ -\frac{2}{3}\,C_{\epsilon 1}\,\overline{\rho}\,\epsilon\,\frac{\partial\overline{u}}{\partial x} - C_{\epsilon 2}\,\overline{\rho}\,\frac{\epsilon^2}{k} \\ -2\,C_{uT}\,\frac{k\overline{u}}{c_p^2}\,\frac{\partial\overline{u}}{\partial x} - \Phi \\ -2\,\frac{\overline{\rho}^2}{c_p\,\overline{T}}\,C_{uT}\,\frac{k}{\overline{u}}\,\frac{\partial\overline{u}}{\partial x} - C_\rho^{vd}\,\frac{1}{\overline{u}}\,\frac{\epsilon}{k}\,\overline{\rho'^2} \\ -2\,C_s^P\,\frac{C_{uT}}{\gamma}\,\frac{k}{c_p\,\overline{T}}\left[(\gamma-1) - \frac{\overline{u}^2}{c_p\,\overline{T}}\right]\frac{1}{\overline{u}}\,\frac{\partial\overline{u}}{\partial x} - C_\rho^{vd}\,\frac{1}{\overline{u}}\,\frac{\epsilon}{k}\,\overline{s'^2} \\ -2\overline{\rho}^2\,C_{uT}\,k\,\overline{u}\,\frac{\partial\overline{u}}{\partial x} - C_p^{ad}\left(\frac{\overline{p'^2} - \overline{p'^2}^{LIA}_{far-field}}{L_\epsilon}\right) \end{Bmatrix} \tag{8.45}$$

where the modeling parameters are defined as,

$$b_1 = 0.4 + 0.6\,e^{2(1-M_1)}, \quad b_1' = 0.4\,(1 - e^{(1-M_1)}), \tag{8.46}$$

$$c_{uT} = \left[\frac{4}{9}(1-b_1)\right]\left(\frac{3}{2(b_1+1)}\right)\left[1 - \left(\frac{\overline{u}_1}{\overline{u}_2}\right)^{-\frac{2}{3}(b_1+1)}\right], \tag{8.47}$$

$$\Phi = \left(C_T^{ad}\,\frac{\overline{T'^2}}{L_\epsilon}\right) + \left(C_T^{vd}\,\frac{1}{\overline{u}}\,\frac{\epsilon}{k}\,\overline{T'^2} - C_T^{ad}\,\frac{\overline{T'^2}}{L_\epsilon}\right)\frac{1}{2}\,(1 + \tanh(x - \lambda_0)), \quad \lambda_0 = \frac{1}{k_0}, \tag{8.48}$$

$$C_{\epsilon 1} = 1 + 0.21 M_1, \quad C_{\epsilon 2} = 1.2, \tag{8.49}$$

$$C_T^{ad} = 0.95 + 9.25\,e^{(1-M_1)}, \quad C_T^{vd} = 0.75 + 3.5\,e^{(1-M_1)}, \quad C_\rho^{vd} = 0.6 + 2.75\,e^{(1-M_1)}, \tag{8.50}$$

$$C_p^{ad} = 2 + 4.5\,e^{(1-M_1)}, \quad C_s^P = 0.15 + 2.5\,e^{(1-M_1)}, \quad C_s^{vd} = 0.75 + 3.7\,e^{(1-M_1)}. \tag{8.51}$$

where $C_f^{ad}$ and $C_f^{vd}$ are the acoustic and viscous decay model coefficient for the quantity $f$, respectively. Here, $k_0 = 4$ is the peak energy wavenumber used in the upstream turbulence energy spectrum, and $\lambda_0$ is the corresponding wavelength. The source terms in the equations for the thermodynamic variances are active only in the downstream region to be compliant with the purely vortical turbulence assumption. The source terms for $k$ and $\epsilon$ are active in the upstream as well as the downstream region.

The decay for the temperature variance is modeled to have a mixed decay profile as shown in Eq. (8.48), where the hyperbolic tangent function controls the transition from the acoustic decay to the viscous decay. This type of blending function based on lengthscales is similar to the blending functions proposed in the work of Xiao *et al.* [167], where they used a hyberbolic tangent to shift the numerical method from $k-\zeta$ RANS at the wall to LES with one-equation SGS model away from the wall. The transition location is identified using LIA as the location where the entropy modes become dominant over the acoustic modes. This requires *a priori* analysis of the problem using LIA to identify the transition location. It is to be noted that the blending function is grid-scale-dependent and the grid resolution should be sufficient to capture the characteristic lengthscale in the RANS framework.

Similar to the decay model for the turbulent energy flux proposed in Ref. [117], we also model the acoustic decay mechanism in the form of $\frac{\overline{f'^2}}{L_\epsilon}$, where $L_\epsilon = \frac{k^{(3/2)}}{\epsilon}$ is the dissipation lengthscale. The viscous decay mechanism is similar to the dissipation rate of TKE, and is of the form of $\left(\frac{\epsilon}{k}\right)\overline{f'^2}$. These forms of the acoustic decay and the viscous decay are used for the other variances also. It is shown in Fig. (8.8) that this type of mixed decay profile with the transition location set at $k_0 x = 1$, matches very well with the spatial variation of temperature variance observed in the DNS.

In the previous section, it was shown that the model equation for the entropy variance was developed in the phenomenological sense from its transport equation applicable to the downstream region. The modeled entropy variance varies in the $O(M^2)$ when integrated numerically, and thus requires an additional production coefficient, $C_s^P$ in the $O(-1)$ to control the values to be comparable to the post-shock predictions of LIA.

The pressure variance does not decay to zero in the far-field region like the other thermodynamic variances. To account for the non-zero far-field values of pressure variance, we use LIA to prescribe the lower limit of the model for the particular Mach number. For this, we are required to know the far-field pressure variance, $\overline{p'^2}^{LIA}_{far-field}$ *a priori* (see Ref. [99] for computing the far-field values). The decay coefficients range with Mach number as prescribed in Eqs. (8.50) and (8.51).

The equations are integrated in their non-dimensional form where the quantities are non-dimensionalized as shown below,

$$u = \frac{u^*}{a_1^*}, \quad T = \frac{T^*}{T_1^*(\gamma-1)}, \quad \rho = \frac{\rho^*}{\rho_1^*}, \quad p = \frac{p^*}{p_1^*\gamma}, \quad s = \frac{s^*}{c_p^*} \tag{8.52}$$

$$R = \frac{R^*}{c_p^*} = \frac{\gamma-1}{\gamma}, \quad c_p = \frac{c_p^*}{c_p^*} = 1, \quad c_v = \frac{c_v^*}{c_p^*} = \frac{1}{\gamma}, \quad x = k_0 x^*, \tag{8.53}$$

with the superscript $*$ denoting dimensional quantities. The values of $k$ and $\epsilon$ at the inlet of the 1D domain are obtained by linearly extrapolating DNS values from the location just upstream of the shock to the inlet station, as mentioned in Ref. [120]. For the homogeneous isotropic turbulence decaying in a steady, 1D mean flow, the governing equations for $k$ and $\epsilon$ are,

$$\overline{u}\frac{\partial k}{\partial x} = -\epsilon \tag{8.54}$$

$$\overline{u}\frac{\partial \epsilon}{\partial x} = -C_{\epsilon 2}\,\frac{\epsilon^2}{k}, \tag{8.55}$$

which when integrated simultaneously yields,

$$k(x) = k_{in}\left[1 + \frac{x\,\epsilon_{in}}{\overline{u}\,n\,k_{in}}\right]^{-n}, \quad n = \frac{1}{C_{\epsilon 2} - 1}, \tag{8.56}$$

$$\epsilon(x) = \epsilon_{in}\left[1 + \frac{x\,\epsilon_{in}}{\overline{u}\,n\,k_{in}}\right]^{-(n+1)}, \tag{8.57}$$

where $k_{in}$ and $\epsilon_{in}$ are the TKE and its dissipation rate at the inlet of the domain, respectively. The values of $k$ and $\epsilon$ at the location just upstream of the shock need to be known *a priori*, and are obtained as follows,

$$k_1 = \frac{M_t^2}{2}, \quad \epsilon_1 = \frac{5\,M_t^3}{\sqrt{3}\,(k_0\lambda^*)\,Re_\lambda}, \tag{8.58}$$

where $\lambda^*$ is the dimensional Taylor lengthscale. Equation (8.58) is used in Eqs. (8.56) and (8.57) to obtain the values at the inlet of the domain.

### 8.3.1 Temperature variance

Figure (8.8) compares the model prediction for temperature variance against DNS data for the four different Mach numbers. The switch between the acoustic decay mechanism and the viscous decay mechanism, enables us to capture the spatial variation observed in the DNS. The slope of the rapid decay is controlled by the $\lambda_0$ parameter, which is chosen to be $\frac{1}{k_0}$. Accurate representation of the rapid decay profile is possible if the lengthscale of transition is known already, which is possible with the use of LIA. It is to be noted that the length of the acoustic decay is usually found in the range of $\frac{1}{(2\,k_0)}$ to $\frac{3}{(2\,k_0)}$, and strongly depends on the shape of the inflow turbulence's energy spectrum. The acoustic decay coefficient is varied from 1 for $M_1 = 6$ to 3 for $M_1 = 2.5$ with the viscous decay coefficient kept around a value of 1. The model predicts the post-shock variation of temperature variance accurately.

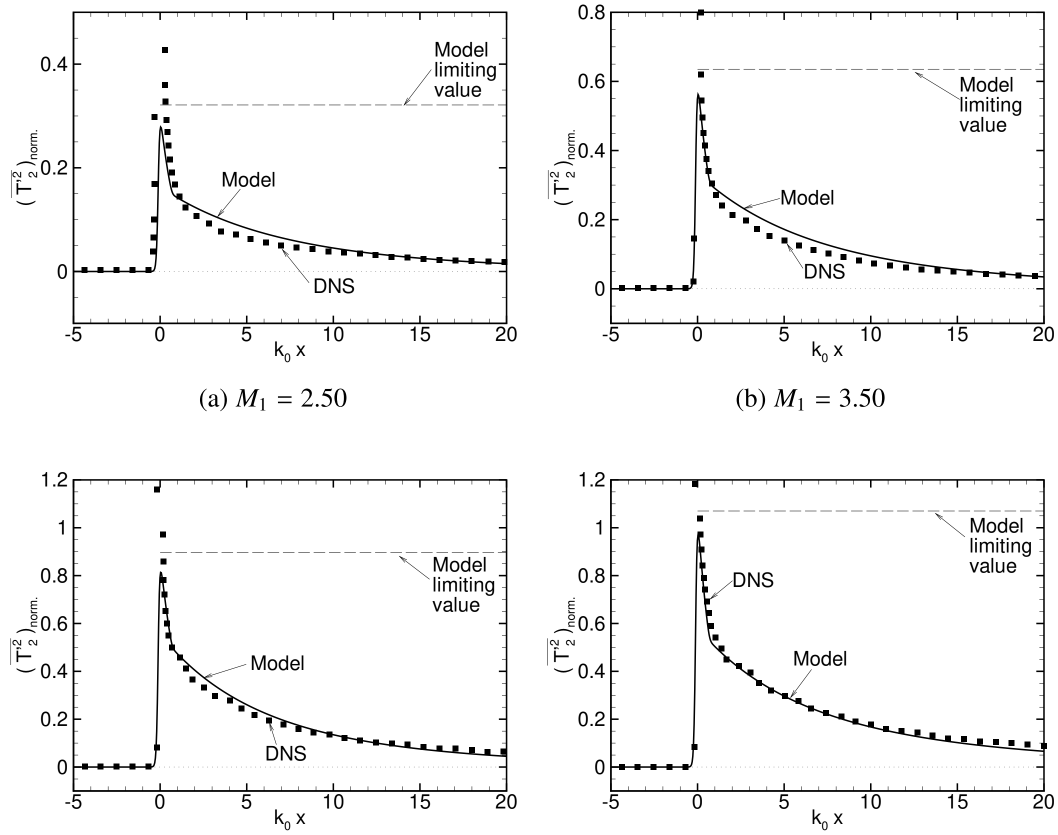


(a) $M_1 = 2.50$ (b) $M_1 = 3.50$

(c) $M_1 = 4.70$ (d) $M_1 = 6.00$

Figure 8.8: Variation of normalized temperature variance for the four different Mach numbers. The temperature variance is normalized by $\overline{T}_2^2\,(k_1/\overline{u}_1^2)$. Lines correspond to the solution of the RK4 integration of the temperature variance model equation in Eq. (8.45) and square symbols correspond to the DNS results of Ref. [81]. The horizontal dashed line is the limiting value for the model which is obtained by integrating Eq. (8.45) without the decay mechanisms

### 8.3.2 Density variance

Figure (8.9) plots the density variance model against DNS data for the four different Mach numbers. The viscous decay coefficient is varied from 0.6 to 1.2 with the highest value used for $M_1 = 2.5$ and the lowest value for the high Mach numbers. The excellent match at $M_1 = 6$ indicate that the viscous decay seems to be the sole decay mechanism for the density variance at high Mach numbers. The model without a mixed decay profile is found to show a reasonable match with the DNS data but would be more accurate if a mixed type is used, especially at low Mach numbers. Similar to Reynolds stress profiles, the density variance also show a non-monotonic variation with a post-shock peak value located at $k_0 x \approx 1$ but only for the high Mach number cases. The amplification behind the shock, predicted with only the production term as the source term matches well with the post-shock peak values for each of the cases considered here.

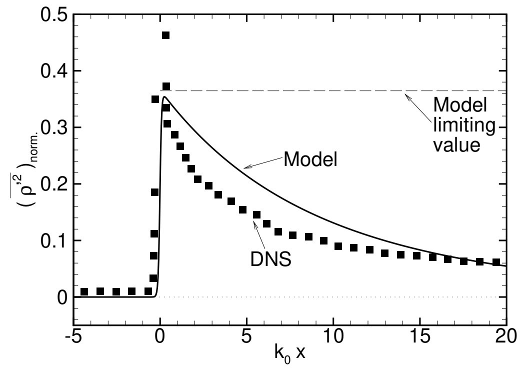


(a) $M_1 = 2.50$

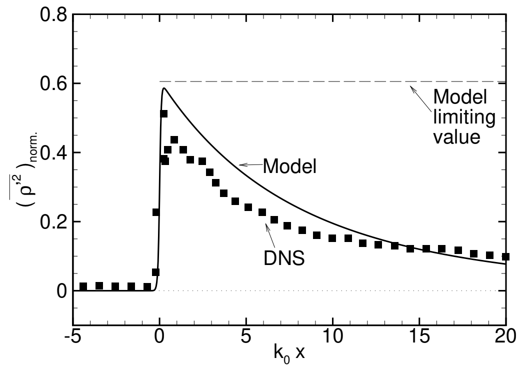


(b) $M_1 = 3.50$

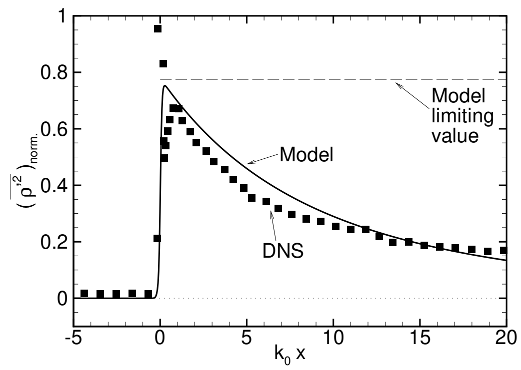


(c) $M_1 = 4.70$

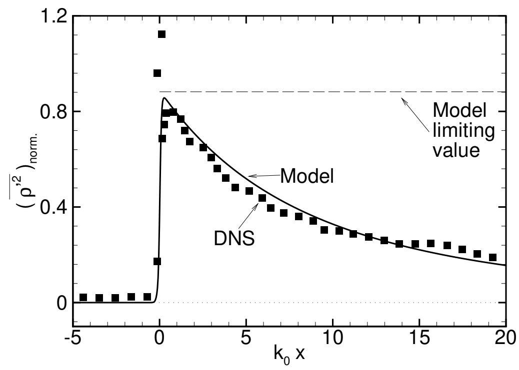


(d) $M_1 = 6.00$

Figure 8.9: Variation of normalized density variance for the four different Mach numbers. The density variance is normalized by $\overline{\rho}_2^2\,(k_1/\overline{u}_1^2)$. Lines and symbols are as mentioned in the caption of Fig. (8.8)

### 8.3.3 Entropy variance

The variation of the modeled entropy variance is compared with its corresponding DNS profile in Fig. (8.10) for the different Mach numbers. For the modeling coefficients used in the production term and the decay term, the predictions were found to match with the DNS data. The modeled production of entropy variance yields a sharp increase in entropy variance at the shock followed by a small decay. This is due to the quadratic dependence between the mean entropy gradient and the mean velocity gradient as given in Eq. (8.33). The model prediction without the decay mechanism is not the sharp peak but the value denoted by the horizontal dashed line. The model values match well with that of the DNS profiles.

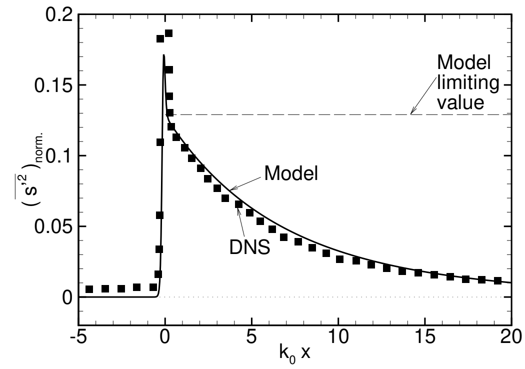


(a) $M_1 = 2.50$

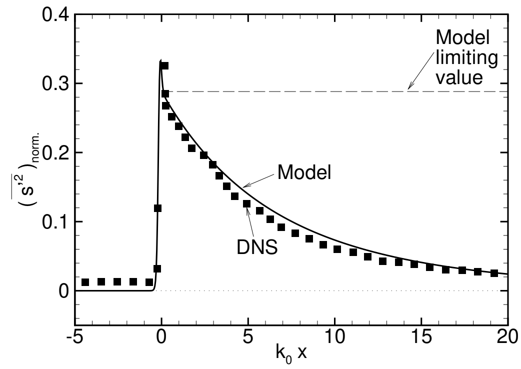


(b) $M_1 = 3.50$

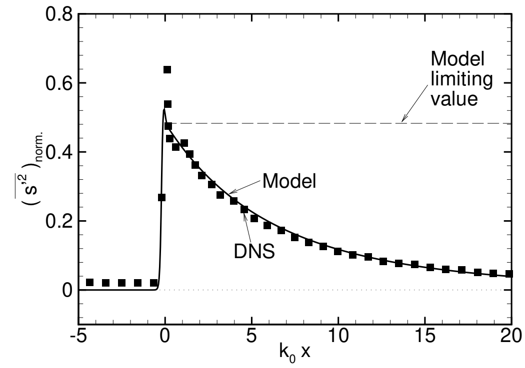


(c) $M_1 = 4.70$

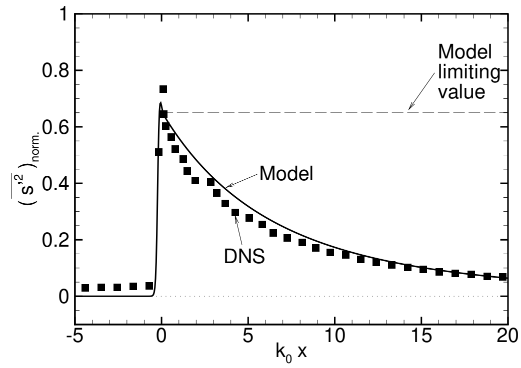


(d) $M_1 = 6.00$

Figure 8.10: Variation of normalized entropy variance for the four different Mach numbers. The entropy variance is normalized by $c_p^2\,(k_1/\overline{u}_1^2)$. Lines and symbols are as mentioned in the caption of Fig. (8.8)

### 8.3.4 Pressure variance

Unlike the other variances the model for pressure variance require a slightly different type of decay mechanism. Usage of acoustic decay mechanism in the form $\frac{\overline{p'^2}}{L_\epsilon}$ results in the pressure variance tending to zero in the far-field, however, LIA and DNS both show a finite value in the far-field region. We make use of LIA to prescribe the far-field value of pressure and apply a lower limit on the model. This type of modeling the pressure variance is found to match the spatial variation of the DNS data very well as shown in Fig. (8.11). The model follows the rapid decay of pressure variance behind the shock and asymptote to the LIA prescribed far-field value.

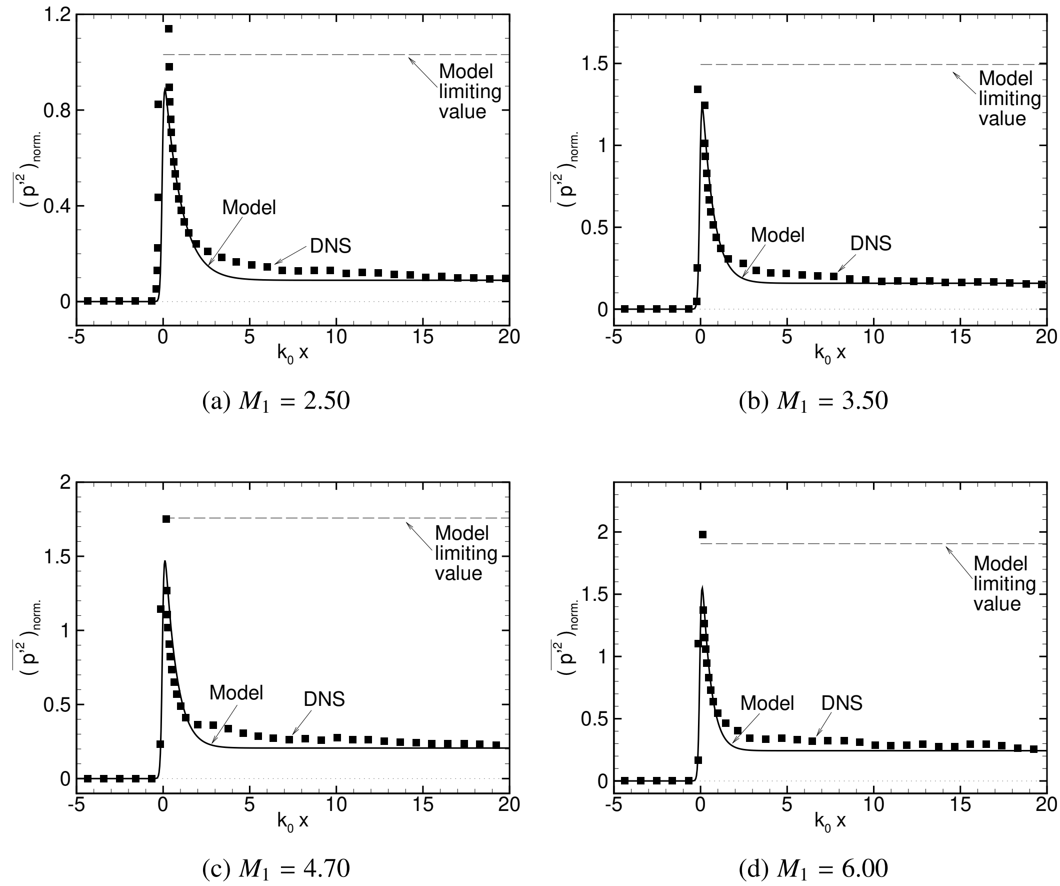


Figure 8.11: Variation of normalized pressure variance for the four different Mach numbers. The pressure variance is normalized by $\overline{p}_2^2\,(k_1/\overline{u}_1^2)$. Lines and symbols are as mentioned in the caption of Fig. (8.8)

The predictions of the models for high Mach number cases from the present set of simulations are shown in Appendix (I). The decay and the production coefficients for each of the cases are slightly different from those that were used for the dataset of [81] but, are not largely different from the expressions provided in Eqs. (8.50) and (8.51). The models show a good match with the DNS data.

## 8.4 Summary

Predictive models for density, pressure, temperature and entropy variances for the case of canonical shock-turbulence interaction were proposed. The models were developed as functions of the turbulent kinetic energy, and hence strongly depend on the accuracy of the model used for computing $k$ and $\epsilon$. The underlying physical mechanisms in the evolution of thermodynamic variances behind the shock were highlighted and modeled accordingly. The use of mixed type of decay mechanisms is found to predict variances composed of multiple Kovásznay modes accurately. A switching function based on the hyperbolic tangent function is used to employ the mixed type of decay mechanism. The proposed models predict the post-shock amplification and the decay of their respective variances very well for the range of Mach numbers considered in this study. Application in an actual CFD framework, effects of upstream entropy and acoustic fluctuations, corrections for the low Mach number cases ($M_1 < 2$), extension of model to three-dimensional framework, and modification for converging/moving spherical shocks (RMI due to shocks) are possible directions for future work.

# Chapter 9

# Conclusion and future work

In this dissertation, DNS data for thermodynamic fluctuations generated by canonical shock-turbulence interaction is presented. Exhaustive verifications have been carried out to ensure that the numerical simulations are well-resolved both in space and time. A large parameter space in terms of Mach number is also considered, and the available DNS data is complemented with new cases computed here. The linear interaction analysis based on Kovásznay mode decomposition of the disturbances is applied under the linear inviscid framework. LIA results are compared with the DNS data and are further used to investigate the thermodynamic field in terms of their component Kovásznay modes.

The DNS data shows that all thermodynamic fluctuations, except the entropy variance take large values across the shock and decay rapidly in the post-shock region. This is primarily associated with the acoustic mode, and reciprocates the well-known exponential decay of the acoustic energy generated at the shock. Various data extraction procedures and scaling factors have been employed to obtain meaningful inferences from the post-shock thermodynamic field. Computing statistics conditioned by the instantaneous shock location captures the large near-field values, whereas DNS statistics computed at a fixed location around $k_0 x_1 = 1$ follow the trends in the far-field LIA values. The far-field thermodynamic variances show steady increase in magnitude with increasing strength of interaction. There are interesting non-monotonic trends, for example, in the variation of the near field $\overline{\rho'^2}$ values with Mach number. The density variance generated by strong shocks ($M_u \geq 2.5$) also show a non-monotonic variation (and a local peak in magnitude) with distance from the shock wave. These are caused by the interplay between the acoustic and the entropy modes generated by the interaction.

The upstream turbulence intensity directly affects the amplification/generation of the thermodynamic fluctuations behind the shock. Interaction of higher $M_t$ turbulence databases generate larger amplification of the thermodynamic fluctuations downstream of the shock. The TKE is amplified across the shock for increasing upstream $M_t$ which in turn increases the post-shock thermodynamics. The effect of Reynolds number on the post-shock thermodynamics is analyzed. Due to the differences between the initial conditions, no meaningful inference of the Reynolds number effect was drawn from this analysis. The shape of the turbulence energy spectrum used to generate the temporally decaying turbulence database determines the spatial variation of the fluctuations behind the shock. It is found that an exponential type of energy spectrum results in a faster decay of the thermodynamic field compared to a von Kármán type energy spectrum. However, it is to be noted that the nearfield and far-field, the two regions of practical interest are not significantly affected by the spectrum shape.

Scaling the post-shock thermodynamic field with downstream mean values provides a measure of the intensity of the fluctuations. For the case of purely vortical (or quasi-vortical) turbulence upstream of the shock, the intensity of the thermodynamic fluctuations is the amplification/generation induced by the shock wave. Turbulent flowfields with entropy or acoustic fluctuations or mixture of the modes should be scaled by the upstream fluctuations to identify the actual amplification by the normal shock.

Transport equations are written to investigate the varying post-shock evolution of the different thermodynamic fluctuations and their fluxes. DNS data is used to compute the budget of the source terms in the flow downstream of the shock interaction for a range of Mach numbers. It is found that the budget is dominated by dilatation effect typical of the acoustics in the near field, whereas the far field variations are dominated by viscous dissipation and nonlinear effects. The only exception is the entropy fluctuation and its flux, which is independent of the acoustic decay behind the shock. The magnitude of the dissipation term is found to increase with shock strength, such that it prominently shows up for the temperature variance in the high Mach number interactions. Budget of the terms from the linearized transport equations also corroborate with the DNS data. The only contradiction is in the budget of the pressure variance obtained immediately behind the shock (or the integrated form across the shock) which showed comparable effects due to bulk compression. Nonetheless, the dominant mechanisms are found to be mostly linear in nature and can be modeled using LIA.

The budget data is used to write simplified transport equations governing the thermodynamics variances. These can form the foundation for developing physics-based turbulence models for the thermodynamic fluctuations generated by the shock waves. In addition, well-validated LIA results, along with the extensive data presented in this work, can be used effectively for modeling and validation of shock-dominated flows. Such an attempt has been undertaken and models for the production of thermodynamic variances across the shock were obtained with the help of existing models of [145] and [117].

Models for the thermodynamic fluctuations were developed using the SU $k-\epsilon$ model of Sinha *et al.* [145] and the turbulent energy flux model of Quadros *et al.* [117]. The developed models were found to predict the production at the shock with reasonable accuracy. The prediction of the decay mechanism in the post-shock region was found to be more accurate, thanks to the understanding of the physical dynamics obtained from the Kovásznay mode decomposition and the extensive budget analysis. The phenomenological models compare well with the available DNS data.

## 9.1 Contributions

Overall, this dissertation discusses in detail, how the thermodynamic fluctuations in homogeneous isotropic turbulence are altered by the passage of a normal shock wave. The important contributions of this work are:

- Using LIA and DNS, the enhancement in thermodynamic fluctuations across a normal shock were studied in detail. LIA has been found to match the DNS data well, and hence it can be a reliable tool to study the post-shock thermodynamic field in canonical STI.

- The numerical solutions add to the available database of DNS data of canonical STI. The inflow turbulence was developed using von Kármán type of energy spectrum, compared to the exhaustive data available for inflow turbulence with an exponential type of spectrum. This gives an opportunity to explore the variations in post-shock lengthscales and the redistribution of energy between the Reynolds stresses for the two types of inflow turbulence.

- The proposed threshold method based on dilatation provides a way to compare the nearfield values of DNS data directly with the nearfield values of LIA. The uncertainty of the method is within reasonable limits as investigated using different grids.

- Dominant mechanisms responsible for the post-shock evolution of thermodynamic fluctuations were identified using an extensive budget analysis of the respective transport equations. The thermodynamic variances were found to be governed by a combination of acoustic decay and viscous dissipation.

- Developed algebraic and differential equation-based models, which replicate the production and the decay mechanism of thermodynamic fluctuations in canonical STI. The model predictions match DNS data well over a range of shock Mach numbers.

## 9.2 Future work

Following are some of the avenues inspired by the present work that could be pursued in the future:

- LIA with upstream acoustic fluctuations can be investigated to explain the mismatch with the high $M_t$ DNS cases. An accurate framework to account for the correlation between velocity and pressure fluctuations in the upstream region needs to be developed. Additionally, the validity of the linearized RH conditions at the shock also needs verification for such cases.

- Budget analysis of the different thermodynamic fluctuations in the present work indicate that it is the compression by the shock via the correlation with dilatation fluctuations, which controls the evolution of thermodynamic fluctuations behind the shock. Existence of a different mechanism due to the addition of considerable amount of entropy/acoustic fluctuations upstream of the shock could be investigated in detail.

- A similar analysis for a range of parameters for a multi-fluid turbulence interacting with a normal shock could be carried out to explore the dynamics of the scalar field modified by the shock wave. This is directly relevant to problems involving RMI and RTI in ICF and nuclear physics.

- The proposed models were based on purely vortical turbulence upstream of the shock. Models accounting for upstream entropy/acoustic effects can be explored. Additional suggestions as provided in the summary of Chap. (8) could be also pursued.

- Turbulent fields interacting with reactive shocks (such as blast/detonation waves) have become problems of interest recently, and the present analysis can be extended to such studies.

# Appendix A

# Linear interaction analysis with viscous terms

The conventional LIA followed in this study (and described in chapter (3)) assumes that the flowfield is linear ($f' << \overline{f}$) and inviscid (Re $\rightarrow \infty$). In the DNS, the flowfield is both nonlinear ($f'^2$ and higher order fluctuations are not necessarily small) and viscous (Re is finite). The comparison between the two methods (LIA and DNS) brings out the effect of the nonlinear terms and the viscous terms collectively as a disagreement. To isolate each of the effects in the mismatch between LIA and DNS, the conventional LIA has to include the effect of viscous terms. In this appendix, we show that such an analysis is indeed possible, however we do not provide a complete framework. This work is at the most to be considered as a proof-of-concept and no more than that.

The analysis presented in this appendix essentially follows the approach of Refs. [78] and [19], where we retain the viscous terms in the governing equations for the Kovásznay modes instead of dropping them. The conventional LIA approach neglects the viscous stress terms in the momentum and energy equations, presumably for an easier analysis and also to support the argument of a very thin shock (discontinuity). The compressible Navier-Stokes equations are,

$$\frac{\partial \rho}{\partial t} + \frac{\partial (\rho\, u_k)}{\partial x_k} = 0, \tag{A.1a}$$

$$\frac{\partial (\rho\, u_i)}{\partial t} + \frac{\partial (\rho\, u_i u_k)}{\partial x_k} + \frac{\partial p}{\partial x_i} = \frac{\partial \sigma_{ik}}{\partial x_k}, \tag{A.1b}$$

$$\rho\, T \left( \frac{\partial s}{\partial t} + u_k \frac{\partial s}{\partial x_k} \right) = \sigma_{ik} \frac{\partial u_i}{\partial x_k} - \frac{\partial q_k}{\partial x_k}, \tag{A.1c}$$

where we use the entropy form of the energy conservation equation. The auxiliary equations of state, $p = \rho R T$ and Gibbs entropy, $T\, ds = de + p\, d(1/\rho)$ are used to close the system of equations.

Before proceeding, we make the following changes to our model problem of a three-dimensional turbulence carried by a one-dimensional uniform mean flow and interacting with a normal shock,

- the post-shock turbulent flowfield generated immediately behind the shock wave is isolated from the complete domain,
- the reference frame is attached to the isolated post-shock field,

and using these modifications, we emulate a temporally decaying turbulence box from the turbulent fluctuations generated by the shock in the conventional LIA. In essence, the amplitude of the fluctuations in the box are determined by the shock wave and the upstream turbulent field, and their temporal evolution governed by viscous diffusion effects. Decomposing the flowfield variables in Eqs. (A.1a) - (A.1c) into their mean ($\overline{f}$) and fluctuations ($f'$), and collecting only linear terms we get,

$$\frac{\partial \rho'}{\partial t} + \overline{\rho}\,\frac{\partial u_k'}{\partial x_k} = 0, \tag{A.2a}$$

$$\frac{\partial u_i'}{\partial t} + \frac{1}{\overline{\rho}}\,\frac{\partial p'}{\partial x_i} - \overline{\nu}\left[\frac{\partial^2 u_i'}{\partial x_k\,\partial x_k} + \frac{\partial^2 u_k'}{\partial x_i\,\partial x_k} - \frac{2}{3}\,\frac{\partial}{\partial x_i}\left(\frac{\partial u_k'}{\partial x_k}\right)\right] = 0, \tag{A.2b}$$

$$\frac{\partial s'}{\partial t} - \frac{1}{\overline{T}}\,\frac{4\,\overline{\nu}\,c_p}{3}\,\frac{\partial^2 T'}{\partial x_k\,\partial x_k} = 0, \tag{A.2c}$$

where the convective terms vanish due to the co-moving reference frame in the post-shock field. We have also assumed that the Prandtl number of the fluid to be equal to $3/4$, which is a reasonable assumption for air.

Two new variables,

$$P' = \frac{p'}{\gamma\,\overline{p}}, \quad S' = \frac{s'}{c_p}, \tag{A.3}$$

are introduced to represent all four of the thermodynamic fluctuations. The density and the temperature fluctuations are now written as,

$$\frac{T'}{\overline{T}} = (\gamma-1)\,P' + S', \quad \frac{\rho'}{\overline{\rho}} = P' - S'. \tag{A.4}$$

The continuity and the entropy equation are now written as,

$$\frac{\partial P'}{\partial t} - \frac{\partial S'}{\partial t} + \theta' = 0, \tag{A.5a}$$

$$\frac{\partial S'}{\partial t} - \frac{4\,\overline{\nu}}{3}\left[\frac{\partial^2 S'}{\partial x_k\,\partial x_k}\right] = \frac{4\,\overline{\nu}}{3}\left[(\gamma-1)\,\frac{\partial^2 P'}{\partial x_k\,\partial x_k}\right], \tag{A.5b}$$

where $\theta' = \partial u_k'/\partial x_k$. The momentum equation is manipulated to obtain the equations for vorticity and dilatation by taking a curl ($\varepsilon_{ijk}\,\partial u_k/\partial x_k$) and divergence ($\partial u_k/\partial x_k$) of the velocity field, respectively. The vorticity and the dilatation equations are,

$$\frac{\partial \theta'}{\partial t} + \overline{a}^2 \frac{\partial^2 P'}{\partial x_i \, \partial x_i} - \frac{4}{3}\,\overline{\nu}\,\frac{\partial^2 \theta'}{\partial x_i \, \partial x_i} = 0, \tag{A.6a}$$

$$\frac{\partial \omega_i'}{\partial t} - \overline{\nu}\left[\frac{\partial^2 \omega_i'}{\partial x_k \, \partial x_k}\right] = 0, \tag{A.6b}$$

where $\partial^2/\partial x_k x_k$ represents the Laplacean operator.

The governing equations for each of the Kovásznay modes are,

$$\frac{\partial \omega_i'}{\partial t} - \overline{\nu}\left[\frac{\partial^2 \omega_i'}{\partial x_k \, \partial x_k}\right] = 0, \tag{A.7a}$$

$$\frac{\partial S'}{\partial t} - \frac{4\,\overline{\nu}}{3}\left[\frac{\partial^2 S'}{\partial x_k \, \partial x_k}\right] = 0, \tag{A.7b}$$

$$\frac{\partial^2 P'}{\partial t^2} - \overline{a}^2 \frac{\partial^2 P'}{\partial x_i \, \partial x_i} - \left(\frac{4\,\gamma\,\overline{\nu}}{3}\right)\frac{\partial^2}{\partial x_i \, \partial x_i}\left(\frac{\partial P'}{\partial t}\right) = 0, \tag{A.7c}$$

where Eq. (A.7c) is obtained by using $d/dt$ of Eq. (A.5a) in Eq. (A.6a). It is to be noted that only the homogeneous part of Eq. (A.5b) is used as the governing equation for the entropy mode. The inhomogeneous equation has a special pressure-dependent solution, which varies as $1/Re$ and can be neglected for most flows [19, 78]. The corresponding solutions which satisfy Eqs. (A.7a) - (A.7c) are,

$$\omega_j' = A_j^{\omega}\ \exp\left[i\,k_i^{\omega}\,x_i - \overline{\nu}\,|k^{\omega}|^2\,t\right], \tag{A.8a}$$

$$S' = A^S\ \exp\left[i\,k_i^S\,x_i - \frac{4}{3}\,\overline{\nu}\,|k^s|^2\,t\right], \tag{A.8b}$$

$$P' = A^P\ \exp\left[i\,k_i^P\,x_i - \hat{C}\,t\right], \tag{A.8c}$$

where $A^{\omega/S/P}$ and $k^{\omega/S/P}$ represents the amplitude and wavenumber of each of the modes, respectively and the temporal frequency of the acoustic mode is given by,

$$\hat{C} = \overline{a}\,|k^P|\left(\frac{2\,\gamma}{3}\,\frac{\overline{\nu}\,|k^P|}{\overline{a}} - i\sqrt{1 - \frac{4\,\gamma^2}{9}\left(\frac{\overline{\nu}\,|k^P|}{\overline{a}}\right)^2}\right), \tag{A.9}$$

with $|k^{\omega/P/S}|^2$ denoting the square of the magnitude of the wavenumber vector of the corresponding mode.

The solutions given in Eqs. (A.8a) - (A.8c) represent the temporal decay of the fluctuations due to the viscous effects. We use Taylor's hypothesis, $t = x_1/\overline{u}_1$ to transform the temporally decay solution in to a spatially decaying solution, i.e., assume the turbulence is ‘frozen’. The solutions now read as,

$$\omega'_j = A_j^{\omega} \exp\left[ i\, k_i^{\omega}\, x_i - \overline{\nu}\, |k^{\omega}|^2\, \frac{x_1}{\overline{u}_{1,d}} \right], \tag{A.10a}$$

$$S' = A^S \exp\left[ i\, k_i^S\, x_i - \frac{4}{3}\, \overline{\nu}\, |k^s|^2\, \frac{x_1}{\overline{u}_{1,d}} \right], \tag{A.10b}$$

$$P' = A^P \exp\left[ i\, k_i^P\, x_i - \hat{C}\, \frac{x_1}{\overline{u}_{1,d}} \right], \tag{A.10c}$$

where it is to be noted that the usage of Taylor’s hypothesis also assumes the pressure fluctuations to be ‘frozen’, which is incorrect. We still proceed with this assumption since the current analysis is performed only to show that a viscous framework of LIA is feasible.

The current framework of viscous LIA is only a proof-of-concept and does not address the complete problem. We have considered only an inviscid shock in the present analysis and used the linearized Rankine-Hugoniot conditions to obtain the post-shock amplitudes for the fluctuations. The complete analysis is more involved and cumbersome, where we need to consider a viscous shock and balance the appropriate stresses across it to obtain the viscous amplitudes of the fluctuations in the post-shock region. The article by Miller and Ahrens [106] provides the details for such an analysis, where they used Laplace transforms to obtain the fluctuations immediately behind the shock. Their analysis was however to obtain an estimate for the viscosity of the fluid by the moving shock and does not include much information about the post-shock field. Thus, we can only expect the procedure with a viscous shock to yield a much better amplification value with respect to the DNS and also provide a better match with the viscous decay of the fluctuations observed in the DNS.

Additionally, we have also assumed that there is no mean flow due to the choice of the reference frame in this appendix. In our original model problem, the reference frame is attached to the mean shock and thus the complete analysis with the full domain has a finite mean flow, which has to be considered for the upstream and the downstream regions. Nonetheless, we have shown that it is possible to segregate the viscous and the non-linear effects in the disagreement by using the viscous variant of LIA.

# Appendix B

# Computational mesh

This appendix describes the methodology used in the generation of the numerical grid by the "*hybrid*" code. In Chap. (4), Sect. (4.2.2), the grid index in the computational domain is defined as,

$$x_i = x_l + (x_r - x_l) f\left(\frac{i}{N-1}\right), \quad i = 0, ...., N-1, \tag{B.1}$$

where $x_i$ is the discretized spatial coordinate in the stream wise direction with $x_l$ and $x_r$ being the start and the end locations, respectively. The normalized coordinate is given by $f(s)$, a polynomial function which varies as $f(0) = 0$ and $f(1) = 1$, for $s \in [0, 1]$.

The exact grid spacing is then given as,

$$\Delta x(s) = \frac{x_r - x_l}{N-1} f'(s), \tag{B.2}$$

where $f'(s)$ denotes the deviation from the uniform grid spacing.

Defining $f(s)$ as a combination of multiple hyperbolic functions such that it could accommodate different grid spacings at different regions of the domain. For this problem, we use three hyperbolic cosine functions to have different spacings at the inlet, the shock region and the sponge region.

$$\begin{aligned} f(s) = s &+ \frac{C_1}{2\gamma_1}\left[\log\left(\frac{\cosh\left(\gamma_1(s-t_1)\right)}{\cosh(-\gamma_1 t_1)}\right) - s\log\left(\frac{\cosh\left(\gamma_1(1-t_1)\right)}{\cosh(-\gamma_1 t_1)}\right)\right] \\ &+ \frac{C_2}{2\gamma_2}\left[\log\left(\frac{\cosh\left(\gamma_2(s-t_2)\right)}{\cosh(-\gamma_2 t_2)}\right) - s\log\left(\frac{\cosh\left(\gamma_2(1-t_2)\right)}{\cosh(-\gamma_2 t_2)}\right)\right] \\ &+ \frac{C_3}{2\gamma_3}\left[\log\left(\frac{\cosh\left(\gamma_3(s-t_3)\right)}{\cosh(-\gamma_3 t_3)}\right) - s\log\left(\frac{\cosh\left(\gamma_3(1-t_3)\right)}{\cosh(-\gamma_3 t_3)}\right)\right], \end{aligned} \tag{B.3}$$

where $\gamma_{1,2,3}$, $t_{1,2,3}$ and $C_{1,2,3}$ are constants which control the grid spacing at the inlet (index 1), the shock (index 2) and the sponge region (index 3).

The above equation satisfies the required boundary condition $f(0) = 0$ and $f(1) = 1$. The first derivative of the polynomial function, $f(s)$ [1] are,

$$\begin{aligned} f'(s) = 1 &+ \frac{C_1}{2}\left[\tanh(\gamma_1(s-t_1)) - \frac{1}{\gamma_1}\log\left(\frac{\cosh(\gamma_1(1-t_1))}{\cosh(-\gamma_1 t_1)}\right)\right] \\ &+ \frac{C_2}{2}\left[\tanh(\gamma_2(s-t_2)) - \frac{1}{\gamma_2}\log\left(\frac{\cosh(\gamma_1(1-t_2))}{\cosh(-\gamma_2 t_2)}\right)\right] \\ &+ \frac{C_3}{2}\left[\tanh(\gamma_3(s-t_3)) - \frac{1}{\gamma_3}\log\left(\frac{\cosh(\gamma_1(1-t_3))}{\cosh(-\gamma_3 t_3)}\right)\right], \end{aligned} \tag{B.4}$$

which is used in Eq. (B.2) to describe the grid spacing. Note that $f'(s) = 1$ corresponds to uniform grid spacing.

An iterative procedure is followed to solve for the constants $\gamma_{1,2,3}$, $t_{1,2,3}$ and $C_{1,2,3}$. The transition location, $s$ in the normalized coordinate, $f(s)$ is determined by the constants $t_{1,2,3}$ and the values of $C_{1,2,3}$ gives the jump in $f'(s)$ at those transition locations. Typical values of the constants used in the grid generation procedure for the various Mach numbers are provided in table (B.1).

Table B.1: Constants used in the grid generation procedure

| $M_u$ | Grid | $(\gamma_1, \gamma_2, \gamma_3)$ | $(t_1, t_2, t_3)$ | $(C_1, C_2, C_3)$ |
|---|---|---|---|---|
| 1.23 | $882 \times 384^2$ | $(40, 6, 6)$ | $(0.02, 0.675, 0.95)$ | $(-0.25, 0.6, 3.0)$ |
| 1.50 | $1042 \times 384^2$ | $(50, 6, 6)$ | $(0.01, 0.675, 0.95)$ | $(-0.25, 0.6, 3.0)$ |
| 2.50 | $1142 \times 384^2$ | $(40, 6, 6)$ | $(0.02, 0.675, 0.95)$ | $(-0.25, 0.6, 3.75)$ |
| 3.50 | $1313 \times 384^2$ | $(45, 6, 6)$ | $(0.01, 0.675, 0.95)$ | $(-0.25, 0.6, 4.0)$ |

The constants are slightly varied for the other grid sizes shown in table (4.4), in the range of $\pm 5$ for $\gamma_1$, $\pm 0.03$ for $t_3$ and $\pm 2$ for $C_3$. The other constants are kept the same as shown in table (B.1). A typical grid spacing distribution along the streamwise direction is shown in Chap. (4), Sect. (4.2.2), Fig. (4.3). It is to be noted that there are other functions and methodologies that could be used to obtain stretched grids (see Ref. [99]) and the method described above is only one such method.

[1] $\frac{d}{ds}(\log(\cosh(s))) = \tanh(s)$ and $\frac{d}{ds}(\tanh(s)) = 1 - \tanh^2(s)$

# Appendix C

# Optimized sponge

This appendix describes the procedure followed to obtain a sponge zone that is capable of restricting spurious oscillations from the outflow. In Chap. (4), Sect. (4.2.3), the source term in the form of,

$$-\sigma_0 \left(\frac{x_1 - x_{sp}}{L_{sp}}\right)^2 (f - \overline{f}_{y,z}), \tag{C.1}$$

is added to the RHS of each of the governing equations. Note that this source term is applicable only in the sponge region. Here, $f$ denotes the conserved variable in each equation, $\sigma_0$ is the strength parameter, $x_{sp}$ is the location where the sponge starts and $L_{sp}$ is the length of the sponge region. The target state, $\overline{f}_{y,z}$ for all quantities except for pressure, is taken as the post-shock state obtained from laminar RH shock relations. The target state for pressure is taken as the backpressure specified at the outlet. It is to be noted that for the case of canonical STI, the sponge region is required to prevent spurious reflections in the streamwise direction only.

If the strength coefficient of the sponge is high (or strong), the sponge would act as a hard wall, and if low (or weak), then it would allow spurious reflections from the outflow in to the domain. The length of the sponge also has similar significance. Thus, the sponge region must be of sufficient length and strength to reduce spurious reflections from the outflow boundary. There are two kinds of reflections that enter the useful domain, which are reflections from the outflow boundary and reflections from inside the sponge. To analyze the sponge, the following approximate scalar equation is considered,

$$\frac{\partial f'}{\partial t} + \lambda \frac{\partial f'}{\partial x_1} = -\sigma f', \tag{C.2}$$

where $\sigma$ is assumed constant, $f' = f - \overline{f}_{y,z}$ is the deviation of the solution from the target state, and $\lambda$ is the propagation velocity (either $\overline{u}_{1,d}$ or $\overline{u}_{1,d} \pm \overline{a}_d$ depending on the wave type). The analysis is restricted to the streamwise direction only for this case of STI.

Making the ansatz $f' = e^{i(|\mathbf{k}|\,x - \Omega\,t)}$, where $\Omega$ is taken as a real-valued frequency and $\mathbf{k}$ is taken as a complex wavenumber i.e., considering a spatially evolving problem that is steady in time, the following dispersion relation is obtained,

$$-\,i\,\Omega + i\,|\mathbf{k}|_r\,\lambda - |\mathbf{k}|_i\,\lambda + \sigma = 0, \tag{C.3}$$

from which $\Omega = |\mathbf{k}|_r\,\lambda$ and $|\mathbf{k}|_i = \dfrac{\sigma}{\lambda}$ is obtained by equating the real and the imaginary components. Here, $|\mathbf{k}|_r$ and $|\mathbf{k}|_i$ are the real and imaginary components of the wavenumber. The following inferences can be made from the above equation:

- the damping of the solution at the end of the domain depends on the parameters, $\sigma_0$ and $L_{sp}$, and the wavespeed, $\lambda$.
- reflections inside the sponge occur when the damping lengthscale is short compared to the wavelength of the reflections.

This allows us to define two reflection coefficients,

$$\alpha_d = \sigma_0\,\frac{L_{sp}}{\lambda}, \tag{C.4a}$$

$$\alpha_r = \frac{\frac{1}{|\mathbf{k}|_i}}{\frac{1}{|\mathbf{k}|_r}} = |\mathbf{k}|_r\,\frac{\lambda}{\sigma_0}, \tag{C.4b}$$

where $\alpha_d$ and $\alpha_r$ are the reflection coefficients at the end of the domain and from inside the sponge, respectively. When assessing a sponge layer, it is important to note that the coefficients, $\alpha_d$ and $\alpha_r$ are independent parameters, whereas the strength, $\sigma_0$ and length, $L_{sp}$ are not. Higher values of $\alpha_d$ and $\alpha_r$ are desirable to prevent reflections from entering the domain.

An extensive theoretical analysis of the sponge layer has been performed by Bodony [12] in similar lines. The dynamics of the original problem is definitely nonlinear (compressible NS equations) and thus, the above linear analysis is an approximation only. An optimized sponge region is therefore, identified in an iterative manner by varying the reflection coefficients in systematic order such that the strength and the length of the sponge region are varied accordingly.

The grid size of $336 \times 128^2$ is used for this analysis as it is easily affordable. The different sponges that have been analyzed are shown in table (C.1). Figure (C.1) plots various key parameters for measuring the performance of the sponge. The analysis is performed for the $M_u = 1.5$, $M_{t,u} = 0.15$ and $Re_{\lambda,u} = 33$ case. *Sponges 1* and *2* show significant amount of spurious reflections into the useful domain, and drastic alteration of the pressure and dilatation variances. *Sponge 3* is found to be the best sponge since the dilatational and pressure variances are found to be gradually decaying compared to

Table C.1: Parameters of different sponges. $\alpha_r$ and $\alpha_d$ are the reflection coefficients, $\sigma_0$ is the strength parameter and $L_{sp}$ is the length of the sponge

| Sponge | $\alpha_r$ | $\alpha_d$ | $\sigma_0$ | $L_{sp}$ |
|---|---|---|---|---|
| 1 | 2 | 2 | 13.1 | $0.25\pi$ |
| 2 | 4 | 4 | 6.6 | $0.75\pi$ |
| 3 | 8 | 8 | 3.3 | $2.75\pi$ |
| 4 | 8 | 4 | 3.3 | $1.5\pi$ |

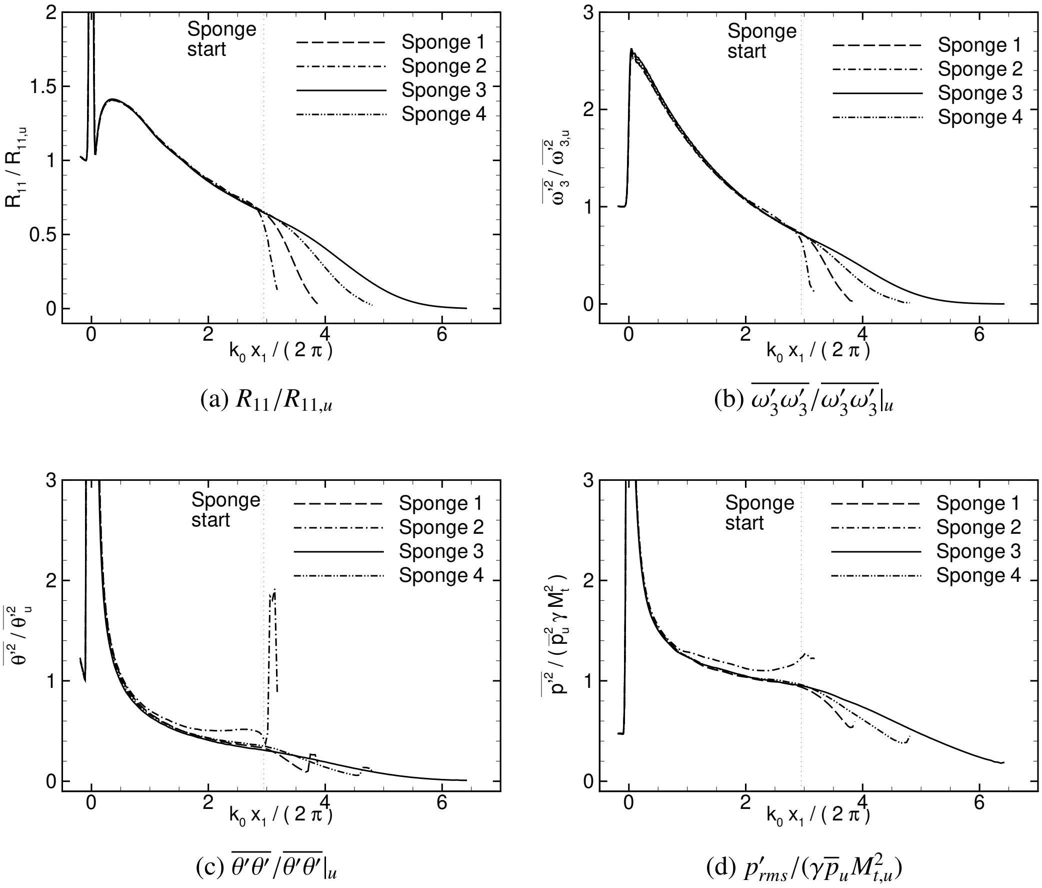


(a) $R_{11}/R_{11,u}$ (b) $\overline{\omega_3'\omega_3'}/\overline{\omega_3'\omega_3'}|_u$

(c) $\overline{\theta'\theta'}/\overline{\theta'\theta'}|_u$ (d) $p'_{rms}/(\gamma\overline{p}_u M_{t,u}^2)$

Figure C.1: Statistics of different quantities showing the performance of each sponge. (a) Reynolds stress, (b) spanwise vorticity variance, (c) dilatational variance, (d) rms of pressure fluctuations. Each quantity is normalized by its respective upstream values, except the rms of pressure. Pressure is normalized by a product of its upstream mean value and $\gamma M_t^2$

the other sponges. *Sponge 4* is also good; though not verified, it is expected that its performance would degrade for strong shocks (higher $M_u$) and high turbulence intensities (higher $M_{t,u}$). The length and strength of *Sponge 3* has been chosen for all other cases.

Figure (C.2) shows the performance of *Sponge 3* for the different $M_t$ values for the $M_u = 1.5$ and $Re_{\lambda,u} = 33$ dataset. This sponge was also found to reduce reflections sufficiently even for the high $M_t$ cases, as evident from Fig. (C.2b). There are reflections for the $M_{t,u} = 0.05$ case, which we believe is due to the damping strength parameter being too strong for this case. The length of the sponge is, however, sufficiently long enough to prevent the reflections from corrupting the statistics. We do note that the sponge is not perfect i.e., it does not completely prevent the reflections from the outflow, but the sponge is sufficient for the statistics investigated in this study. The sponge comprises of approximately 300 to 400 grid points in the shock-normal direction, which is relatively expensive. This issue, however, cannot be avoided due to the requirement of a 'gradual transition' in the grid spacing from the useful domain to the sponge region.

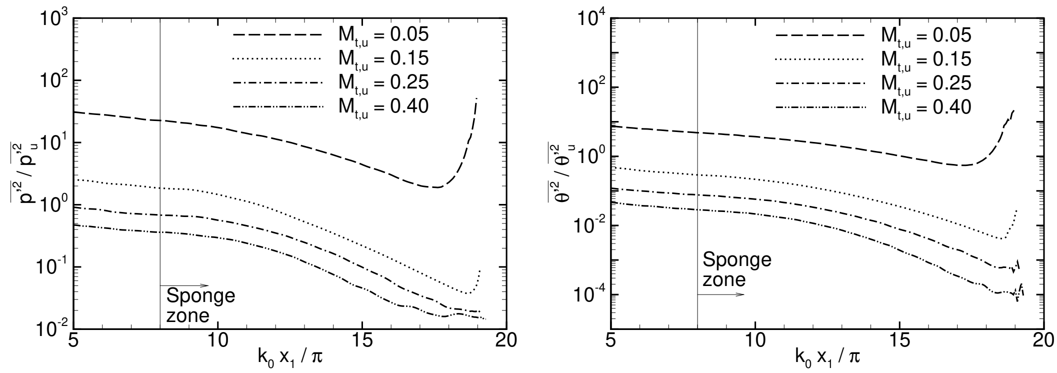


(a) Pressure variance　　(b) Dilatation variance

Figure C.2: Spatial variation of the pressure and dilatation variances for varying $M_t$ values in the $M_u = 1.5$ and $Re_{\lambda,u} = 33$ case. Semi-log plot of (a) normalized pressure variance and (b) density variance against the streamwise direction. The variances are normalized by their values just upstream of the shock. The streamwise direction is normalized by the peak energy wavenumber and additionally scaled by $\pi$. The sponge zone starts from $k_0 x_1/\pi = 8$ in this plot and is denoted by a vertical thin solid line. The variances are sufficiently damped for the high $M_{t,u}$ cases, and is found to be strongly constraining for the lowest $M_{t,u}$ case, however, the reflections do not affect the statistics significantly

# Appendix D

# Shock drift

This appendix addresses the issue with the drifting of the mean shock and the procedure followed to ensure a nearly stationary shock wave in the simulations. The work flow is proceeded by simulating each of the cases ($M_u$ and $M_{t,u}$) on a coarse grid with a back-pressure value, $\overline{p}_\infty$ and then computing the resulting average shock speed, $\overline{u}_s$. Based on the direction of the shock movement and its speed, the backpressure is adjusted to yield a stationary shock.

The backpressure in the first run (denoted by index 1) is usually set up as the value obtained from the laminar RH conditions. The average shock speed is obtained from the mean shock location at each instant of time. The mean shock location is obtained as the first location, where the mean pressure exceeds the arithmetic average of the upstream and the downstream mean pressure ($\overline{p}_u$ and $\overline{p}_d$) values (also known as pressure half-rise method [87, 99]).

We now formulate the relation for the change in backpressure that is required to correct the backpressure for a stationary shock [83]. Assuming the mean shock is moving downstream towards the outlet, the RH relation for the pressure jump becomes,

$$\frac{\overline{p}_d}{\overline{p}_u} = 1 + \frac{2\gamma}{\gamma+1}\left[\frac{(\overline{u}_{1,u} - \overline{u}_s)^2}{\overline{a}_u^2} - 1\right], \tag{D.1}$$

with $\overline{p}_{\infty,initial} = \overline{p}_d$ and $\overline{p}_d$ is the laminar RH value of pressure across the shock. For the specified value of initial backpressure, $\overline{p}_{\infty,initial}$, the resulting average shock speed, $\overline{u}_{s,initial}$ is computed. Expanding the pressure jump condition, Eq. (D.1) around a small shock speed, $\delta\overline{u}_s$ yields,

$$\delta\overline{p}_\infty \approx -\frac{4\,\overline{\rho}_u\,\overline{u}_{1,u}}{\gamma+1}\,\overline{u}_s, \tag{D.2}$$

where we have assumed that $\delta\overline{p}_\infty \approx \delta\overline{p}_d$, considering that the viscous decay is unaffected by the changes in the shock speed.

The backpressure is then adjusted as,

$$\overline{p}_\infty = \overline{p}_{\infty,initial} + \delta\overline{p}_\infty \approx \overline{p}_{\infty,initial} - \frac{4\,\overline{\rho}_u\,\overline{u}_{1,u}}{\gamma+1}\,\overline{u}_{s,initial}, \tag{D.3}$$

where in practice this adjustment is needed only once for low $M_{t,u}$ cases. For high $M_{t,u}$ values, $2-3$ adjustments may be required as necessary. An integral controller in the form,

$$\overline{p}^{n+1}_{corr} = \overline{p}^{n}_{corr} + b\,\Delta t\,(\overline{p}_\infty - \overline{p}_e) \tag{D.4}$$

is set up to ensure that the backpressure is appropriately controlled during the simulation. Here, $\overline{p}^{n}_{corr}$ is the backpressure correction at the $n^{th}$ timestep, $\overline{p}_\infty$ is the target backpressure value given by Eq. (D.3), $\overline{p}_e$ is the average pressure at the exit plane of the domain. The coefficient, $b$ is considered to be a constant timescale that controls the rate at which the backpressure is adjusted, and is usually set as the inverse of the time taken for an acoustic wave to travel from the shock to the outflow and back again to the outflow. It is difficult to keep the shock perfectly stationary but it can be ensured that the mean drift speed of the shock is as low as possible. The ratio of the mean drift velocity of the shock to the mean flow velocity is much less than 1% during the time of collection of statistics.

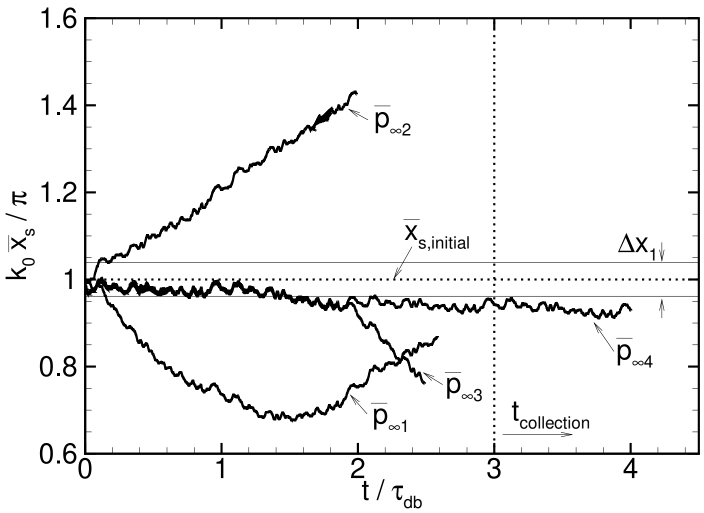


Figure D.1: Variation of mean shock location against time for the case of $M_u = 1.23$, $M_{t,u} = 0.25$, $Re_{\lambda,u} = 33$. Shock location is normalized by the peak energy wavenumber, $k_0$ and time is normalized by the inflow turbulence time period, $\tau_{db}$. The time at which statistics are computed is shown by the vertical line denoted by $t_{collection}$. The initial mean shock location is denoted by $\overline{x}_{s,initial}$ and the width of the grid spacing in the streamwise direction is shown by $\Delta x_1$. The different backpressure are $\overline{p}_{\infty,1} = 21.9777$, $\overline{p}_{\infty,2} = 22.1832$, $\overline{p}_{\infty,3} = 22.4064$, $\overline{p}_{\infty,4} = 22.2097$ with the index values denoting the runs. The mean shock drifts between two grid cells in the final run

Figure (D.1) shows the temporal variation of the mean shock location in time during the simulation runs. The case of $M_u = 1.23$, $M_{t,u} = 0.15$, $Re_{\lambda,u} = 33$ is considered to illustrate the multiple adjustments that are required to obtain a very slow shock drift speed. For the inflow conditions, the laminar backpressure value is 21.9777. During the first run, the shock is found to drift upstream and then moves downstream. The time at which the shock movement changes direction is approximately equal to the time at which an acoustic wave from the outlet reaches the shock. The results from the first run were used as input for the second run and the target backpressure was adjusted as per Eq. (D.3). This process is continued till the simulation yields an almost stationary shock, which for the case illustrated was at the value of $\overline{p}_{\infty,4} = 22.2087$ as shown. The statistically stationary state was achieved around 2.5 $\tau_{db}$ but the statistics were collected after 3 inflow turbulence time periods for this case. Additional time of 0.5 $\tau_{db}$ is allowed for the other cases also to ensure that the simulations are actually stationary in the statistical sense.

# Appendix E

# Additional details on the inflow turbulence

This appendix is an extension of Sect. (4.3) in Chap. (4). Here, the variation of different parameters in the decaying isotropic turbulence simulations for all of the $M_t$ cases are consolidated and analyzed. The isotropic boxes are of $384^3$ in size.

Figure (E.1a) shows the temporal variation of the skewness in velocity derivatives for all the $M_t$ cases. All of the cases have achieved a skewness value of $-0.5$, except for the $M_t = 0.4$ case, which was $-0.45$ at the time of collection of the turbulence field. The first instant where the skewness becomes $-0.5$ is approximately at $t = 0.4\,\tau_{\epsilon,0}$, however, the database was collected at $t = 0.78\,\tau_{\epsilon,0}$. This is due to the additional criteria on the dissipation lengthscale, which is required to increase after its decay in time. The dissipation lengthscale is an indirect measure of the development of large scale features. Figure (E.1b) plots the variation in the dissipation lengthscale, which clearly indicates a rise only after $t = 0.7\,\tau_{\epsilon,0}$ units, including the case of $M_t = 0.4$.

The slightly longer time due to the dissipation lengthscale criterion resulted in the increase of the mean temperature and pressure values as shown in Figs. (E.1c) and (E.1d). The increment in the mean values are especially very large for the $M_t = 0.4$ case compared to the other $M_t$ values. This subsequently results in an increased value in each of the thermodynamic variances in the blended database, and eventually in the upstream region of their corresponding STI cases. Figure (E.2) clearly shows this increment between the $M_t$ cases for the density and pressure variances, where they are approximately equal till the normalized time of 0.4, and then start to diverge rapidly, which is due to the increase in their corresponding mean values.

The dilatation variance (Fig. (E.2d)) is found to increase rapidly during the initial transient period for the high $M_t$ cases (0.25 and 0.40), whereas it remains almost constant

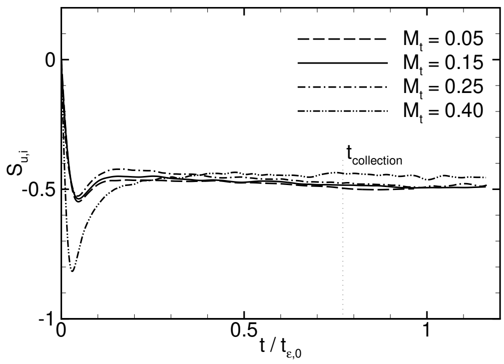


(a) Skewness of velocity derivatives

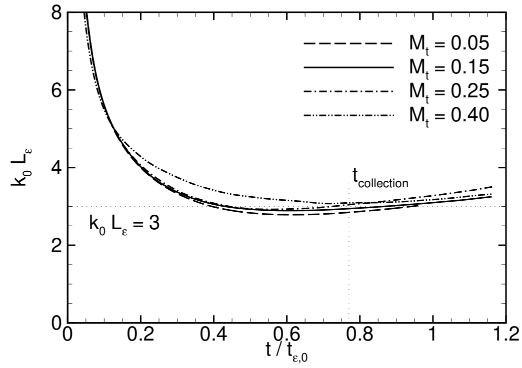


(b) Dissipation lengthscale

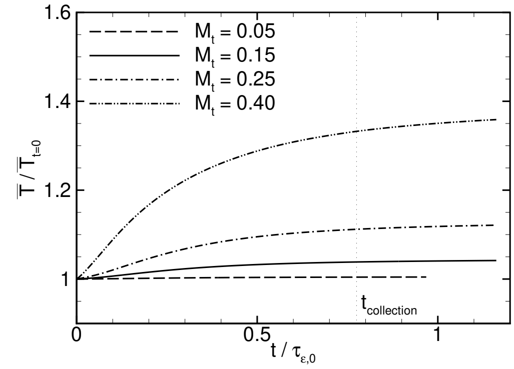


(c) Mean temperature

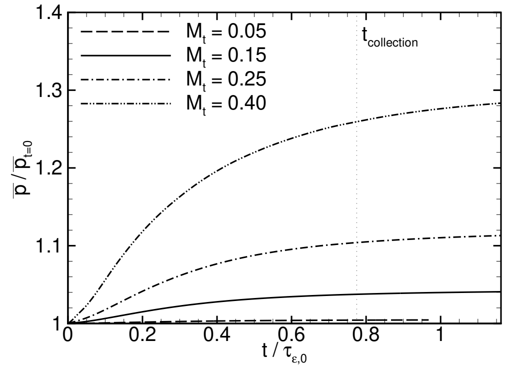


(d) Mean pressure

Figure E.1: Temporal variation of various parameters in the decaying turbulence for the different $M_t$ cases. Dissipation lengthscale is normalized by the peak energy wavenumber and the time is normalized by the initial dissipation timescale ($\tau_\epsilon = k/\epsilon$ computed at $t = 0$). Mean temperature and pressure are normalized by their corresponding mean values of the initial field (at $t = 0$). The line denoted by $t_{collection}$ marks the time at which the turbulence database is collected to be used as inflow turbulence in the STI domain

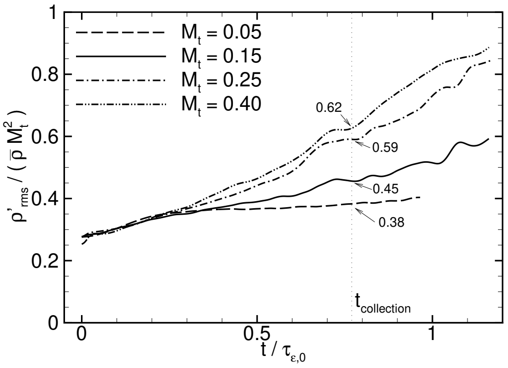


(a) Density

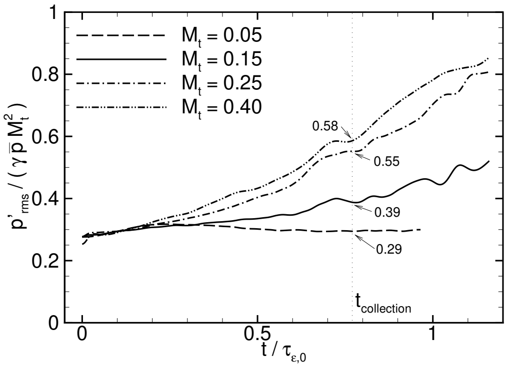


(b) Pressure

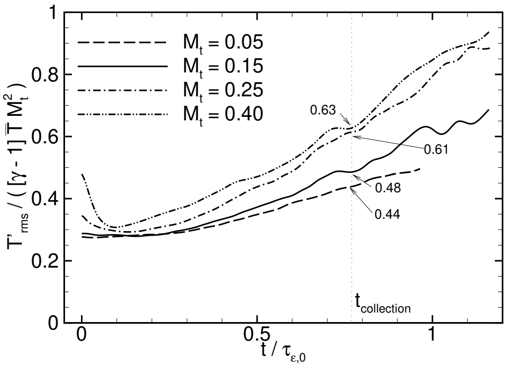


(c) Temperature

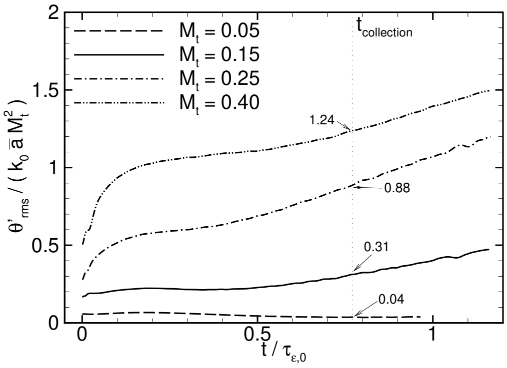


(d) Dilatation

Figure E.2: Temporal variation of rms values of thermodynamic fluctuations: (a) density, (b) pressure, (c) temperature, and (d) the rms value of dilatation fluctuations in the decaying turbulence fields for the different $M_t$ cases. Time is normalized by the initial dissipation timescale $\tau_\epsilon = k/\epsilon$ computed at $t = 0$. Density fluctuations are normalized by $\overline{\rho}\, M_t^2$, pressure by $\gamma\, \overline{p}\, M_t^2$, temperature by $[\gamma - 1]\, \overline{T}\, M_t^2$, and dilatation values are by $k_0\, \overline{a}\, M_t^2$. The line denoted by $t_{collection}$ marks the time at which the turbulence database is collected, which is to be used as the inflow turbulence in the STI domain for the low $M_t$ cases (0.05 and 0.15). The dilatation variance also shows an increase in time, possibly due to the combined increase of density and entropy fluctuations in the isotropic turbulent flowfield. For the low $M_t$ case of 0.05, the rms of dilatation fluctuations in the isotropic turbulence is almost negligible and becomes comparable to the vortical fluctuations at high $M_t$ values.

Figures (E.3a) and (E.3b) show the compensated energy spectrum for the total velocity fluctuations via $E(k)$ and that of its dilatational components via $E_d(k)$, respectively. The total energy spectra is similar to the low Reynolds number spectra observed in the forced isotropic turbulence simulations of Refs. [28, 40] with no 'flat region' indicating the lack of inertial range. The Kolmogorov constant is $C_K \approx 1.6$ which is consistent with the values found in incompressible flows [29]. As expected, intense (or high $M_t$) turbulence fields show increased dilatational component in the energy spectra. However, the Kolmogorov constant for the highest $M_t$ case of 0.4 is around $C_K = 0.12$, which indicates that the dilatational component is still an order of magnitude less than the solenoidal component of the energy spectra. Once again, no inertial scaling is found in the energy spectra, owing to the low Reynolds number. We note that there are some residual errors for the high wavenumbers in the dilatational energy spectra, however, they have no significant effect on the total energy [28].

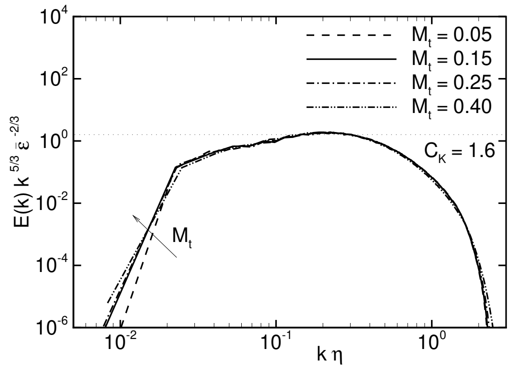


(a) Total kinetic energy spectrum

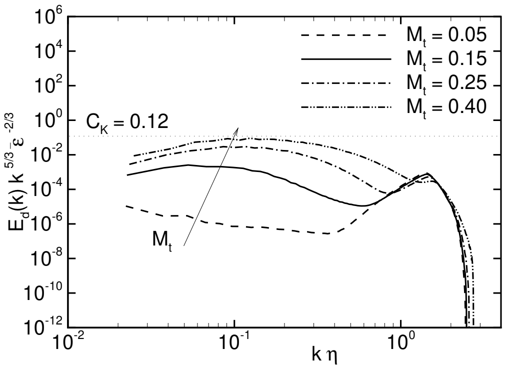


(b) Dilatational kinetic energy spectrum

Figure E.3: Compensated energy spectrum for (a) the total kinetic energy and (b) the dilatational component of the kinetic energy for varying $M_t$ values. The Kolmogorov constant for the highest $M_t$ case is 1.6 and 0.12 for the total and dilatation energies, respectively

# Appendix F

# Blending of turbulence flowfields

This appendix describes the mathematical framework of the blending procedure used to generate the longer inflow turbulence databases in Sect. (4.3) of Chap. (4). The details provided here are adapted from the work of Xiong *et al.* [169] and essentially follows the steps provided in Larsson [79].

In practice, the first step is to blend two independent but statistically identical turbulence boxes of size $[0, 2\pi)^3$ together in the streamwise direction $(x_1)$ to generate a longer turbulence box of size $[0, 4\pi) \times [0, 2\pi)^2$. To achieve this, the velocity fields from the two boxes are blended as,

$$u_i = u_i^1 \cos(\alpha) + u_i^2 \sin(\alpha) - \frac{\partial \Phi}{\partial x_i}, \quad |x_1| < l_b, \tag{F.1}$$

where $u_i^1$ and $u_i^2$ are the velocity fields of the first and the second box, respectively. The harmonic field, $\dfrac{\partial \Phi}{\partial x_i}$ is added to remove the erroneous dilatation in the subsequent steps. The parameter $\alpha$ is varied as,

$$\alpha = \frac{\pi}{4}\left[1 + \sin\left(\frac{\pi\, x_1}{2\, l_b}\right)\right], \quad |x_1| < l_b, \tag{F.2}$$

such that the velocity field is varied smoothly from $u_i^1$ to $u_i^2$ in the blending region of size $l_b$. It can be shown that the blended turbulence box retains the second-order single-point statistics ($R_{ij}(\vec{r}) = \overline{u_i(\vec{x})\, u_j(\vec{x} + \vec{r})}$) of the original fields. Note that $R_{ij}^1 = R_{ij}^2$ since the turbulence boxes are statistically identical. The transverse two-point correlations in the blended box are found to remain the same as the individual boxes, while the streamwise two-point correlation is lowered by an amount that depends on the size of the blending region, $l_b$ via the $\dfrac{d\alpha}{dx_1}$ term. It is recalled that the blended database is expected to be statistically identical to the individual isotropic boxes.

The gradients of the blended velocity field are given by,

$$\frac{\partial u_i}{\partial x_j} = \frac{\partial u_i^1}{\partial x_j} \cos(\alpha) + \frac{\partial u_i^2}{\partial x_j} \sin(\alpha) - \frac{\partial^2 \Phi}{\partial x_i\, \partial x_j} + \left(-u_i^1 \sin(\alpha) + u_i^2 \cos(\alpha)\right) \frac{d\alpha}{dx_1}\, \delta_{ij}, \tag{F.3}$$

where the last term is the error introduced due to the blending procedure. Larsson [79] observed that the blended database represents the vorticity reasonably with respect to the individual fields, but the dilatation has a large peak in the blended region. This error can be removed by solving the Poisson equation,

$$\frac{\partial^2 \Phi}{\partial x_i \, \partial x_i} = \left( -u_1^1 \, \sin{(\alpha)} + u_1^2 \, \cos{(\alpha)} \right) \frac{d\alpha}{dx_1} = \mathrm{Q}, \tag{F.4}$$

with Neumann and periodic boundary conditions in the streamwise and transverse directions, respectively.

The second step involves the removal of the erroneous dilatation by solving the Poisson equation (Eq. (F.4)) with the appropriate boundary conditions. This form of dilatation error removal was first suggested by Xiong *et al.* [169] and later shown to be correct by Larsson [79], whose blended database had a dilatation error within the variation of the individual fields. Instead of solving for the full domain size of $[0, 4\pi) \times [0, 2\pi)^2$, Larsson [79] suggested to solve only for the blended region, which is assumed to be decoupled from the rest of the blended database.

This is accomplished by imposing the constraint,

$$\frac{\partial \Phi}{\partial x_i} = 0, \quad |x_i| \geq L_b, \tag{F.5}$$

on the solutions of Eq. (F.3). Here, $L_b$ is an arbitrary length in the streamwise direction of the domain, which represents the isolated blended region. The size of $L_b$ need not be the exact size of the blending region, $l_b$ in the full domain. This additional constraint essentially makes the system (Eq. (F.3)) over-determined, which is solved by seeking a least-squares solution that is unique. The system of equations is most easily solved by first taking the Fourier transforms in the periodic directions, which results in,

$$\left( \frac{\partial^2}{\partial x_1 \, \partial x_1} - k_2^2 - k_3^2 \right) \hat{\Phi} = \hat{\mathrm{Q}}, \tag{F.6a}$$

$$\frac{\partial \hat{\Phi}}{\partial x_1} = 0, \quad |x_1| = L_b, \tag{F.6b}$$

$$\hat{\Phi} = 0, \quad |x_1| = L_b, \quad (k_2, k_3) \neq (0, 0), \tag{F.6c}$$

where $k_2$ and $k_3$) are the wavenumbers in the transverse directions $x_2$ and $x_3$, respectively. This system of equations can be written in a matrix form as $A\,X = B$, where $A$ is the matrix approximating $\left( \frac{\partial}{\partial x_1 \, x_1} - k_2^2 - k_3^2 \right)$ with $X$ and $B$ representing the vectors of $\hat{\Phi}$ and $\hat{\mathrm{Q}}$, respectively. The solution $X = A^{-1}\,B$ is obtained by a matrix inversion algorithm using Gaussian elimination in the present study.

The third and final step is to blend the density ($\rho$) and the pressure ($p$) fields, which have non-zero mean. This is achieved by,

$$f = \frac{1}{2}\left[1 - \sin\left(\frac{\pi\, x_1}{2\, l_b}\right)\right]\overline{f^1} + \frac{1}{2}\left[1 + \sin\left(\frac{\pi\, x_1}{2\, l_b}\right)\right]\overline{f^2} + f'^1\,\cos(\alpha) + f'^2\,\sin(\alpha), \quad |x_1| < l_b, \tag{F.7}$$

where $f = \overline{f} + f'$ is either density or pressure decomposed in its mean and fluctuating components. This method is found to preserve both first- and second-order statistics of the individual fields in the blended database [79].

The three steps are repeated to concatenate additional turbulence boxes to the blended field. This method of localized dilatation error removal (as a constrained minimization problem) reduces memory requirements and improves parallelism [79]. The blended database also has an accurate thermodynamic field compared to the longer databases generated using other methods available in literature [43, 86, 95, 99, 100]. Additional details about the blending procedure can be found in Larsson [79].

# Appendix G

# Error due to Taylor's hypothesis

In this appendix, we show that the errors introduced due to the usage of Taylor's hypothesis for convecting the turbulence box into the canonical STI domain [84], however, are much larger, specifically for the $M_t = 0.25$ and the $M_t = 0.4$ cases compared to the error introduced by the blending procedure. This is illustrated in Fig. (G.1), where the normalized thermodynamic variances (density, pressure, temperature and entropy) along with the transverse vorticity and dilatation variances from the region upstream of the shock are plotted for each of the $M_t$ values. The values from the blended database and from each of the isotropic turbulence boxes are also shown in the same plots.

It is clear that for increasing $M_t$ values, the normalized thermodynamic variances and the normalized dilatation variances increase in magnitude compared to the normalized vorticity variance, which remains almost constant. Note that the thermodynamic fluctuations increase by an order of magnitude as $M_t$ is increased. The normalized dilatation variance, however, becomes comparable to the vorticity variance upstream of the shock for the $M_{t,u} = 0.4$ case due to the error introduced via the Taylor's hypothesis. Interestingly, the upstream variances increase in the STI domain as $M_t/(M - 1)$ increases, i.e., they are dependent on the local turbulence intensity than the inflow turbulence intensity. This is clearly evident from the small departure of the $M = 3.5$ and $M_t = 0.4$ case from its corresponding value in the $M_{t,db} = 0.4$ blended database, but there are significant deviations for the cases of $M = 1.23$ and $M = 1.50$. On the other hand, the overlap of square symbols indicate that the blending procedure has introduced only a very small error in comparison to the original isotropic fields.

It is to be noted that there are other methods to feed the turbulence database into the STI domain other than the Taylor's hypothesis method. For example, in the work of Ryu and Livescu [132], the inlet turbulence was advected with the supersonic mean velocity to encounter a stationary shock wave. This method was found to be more accurate [90, 132] for high $M_t$ cases. In the present study, only the low Mach number cases with high $M_t$ values are affected by the error due to the Taylor's hypothesis, and the remaining are within reasonable limits.

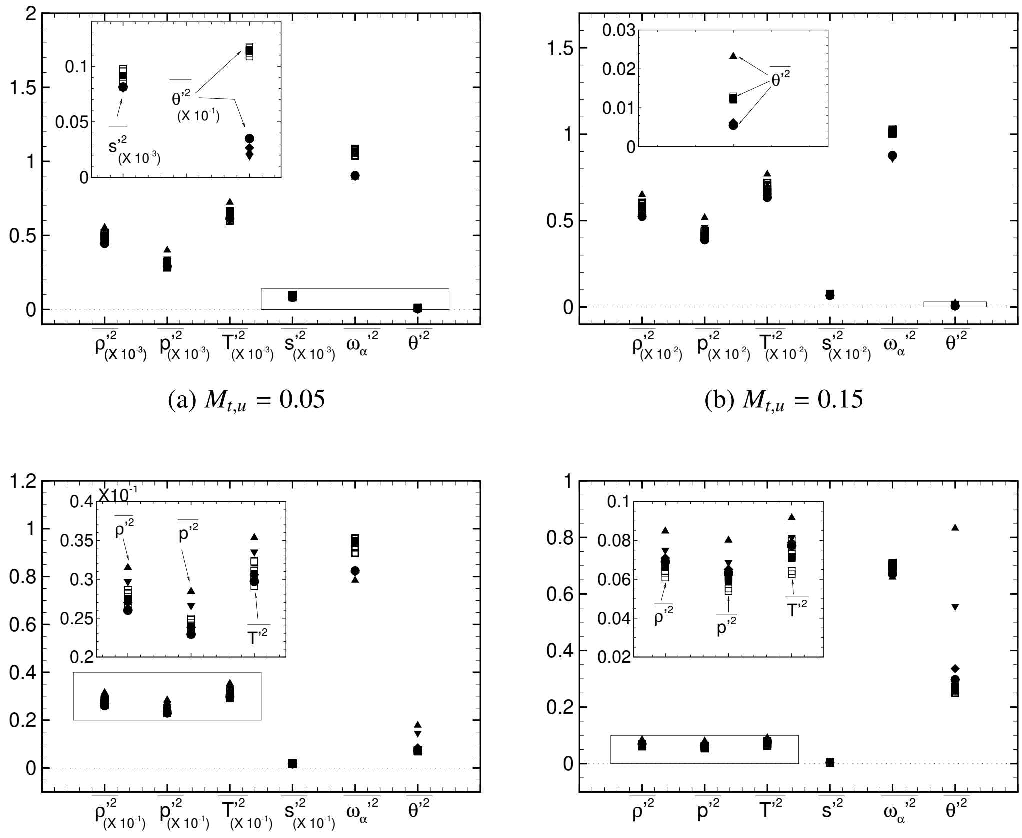


(a) $M_{t,u} = 0.05$ (b) $M_{t,u} = 0.15$

(c) $M_{t,u} = 0.25$ (d) $M_{t,u} = 0.40$

Figure G.1: Variation of normalized density, pressure, temperature, entropy, vorticity and dilatation variance for (a) $M_t = 0.05$, (b) $M_t = 0.15$, (c) $M_t = 0.25$ and (d) $M_t = 0.40$. Density variance is normalized by square of the mean density ($\overline{\rho}^2$), pressure by $(\gamma\overline{p})^2$, temperature by $[(\gamma-1)\overline{T}]^2$ and the entropy by $c_p^2$. Vorticity and dilatation variances are normalized by $(k_0\overline{a})^2$. The variances are additionally scaled by $M_t^2$. Values from the isotropic turbulence boxes are denoted by black hollow squares and the filled squares represent the blended box. Values taken upstream of the shock in the STI domain is shown by $M_u = 1.23$ (triangles), 1.50 (inverted triangles), 2.50 (diamonds) and 3.50 (circles). Thermodynamic fluctuations show 'almost isentropic' scaling

# Appendix H

# Normalization by upstream values

The post-shock thermodynamic field can be interpreted in different ways as per the normalizing factor. LIA considers normalizing with downstream quantities to provide the intensity of fluctuations immediately behind the shock. This can be considered as the amount of generated fluctuations due to the action of shock on the purely vortical turbulent field. The same quantities upon normalization with upstream quantities would indeed imply the actual amplification done by the shock. This appendix discusses the upstream normalization procedure and its inferences.

The evolution of the thermodynamic variances behind the shock is discussed in detail in Chaps. (5) and (6), where the quantities were normalized by their respective post-shock mean values. In this section, we discuss the effect of shock strength on the amplification of the post-shock thermodynamic field. As mentioned earlier, purely vortical turbulence is considered in LIA implying that there are no thermodynamic fluctuations upstream of the shock whereas, DNS has small amount of thermodynamics. Thus, the only meaningful way to normalize with upstream quantities is to use the mean values instead of fluctuations.

The results show a monotonic increase in $\overline{p'^2}$ with shock strength, and the DNS data, irrespective of the location, match the trend observed in the LIA predictions. In fact, the higher $k_0x_1$ values are closer to the LIA curves, which collapse to the asymptotic far-field solution predicted by the linear theory. There are discrepancies at lower Mach number, as well as at lower $k_0x_1$ for higher Mach numbers. The pressure variance is plotted on a logarithmic scale, so as to accommodate the large values of $\overline{p'^2}$ for the high Mach number cases. These high values are an artefact of the normalization, in the sense that the data is normalized by the turbulence intensity in the upstream flow, which usually takes low values.

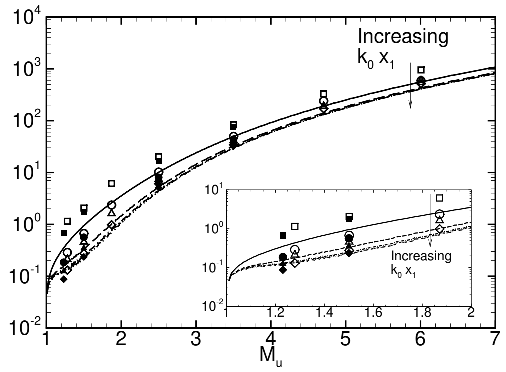


(a) Pressure variance at different locations

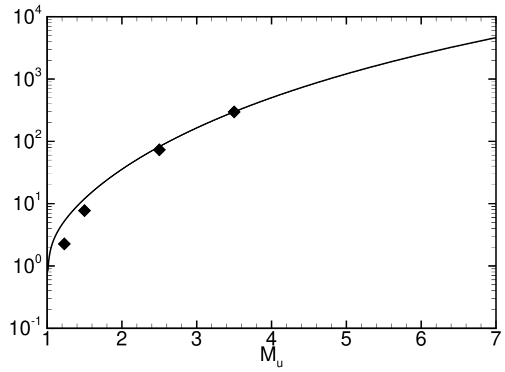


(b) Near-field pressure variance

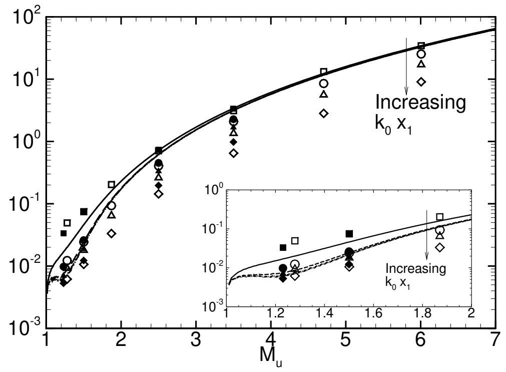


(c) Temperature variance at different locations

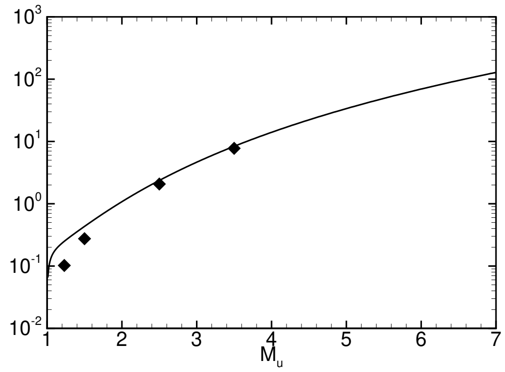


(d) Near-field temperature variance

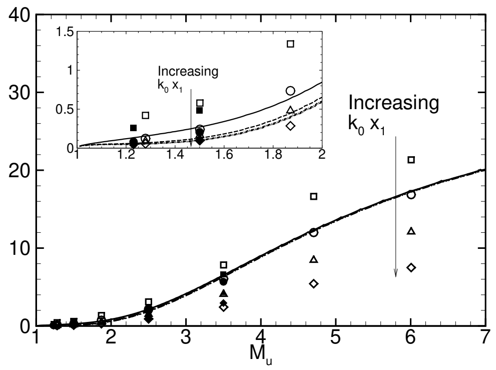


(e) Density variance at different locations

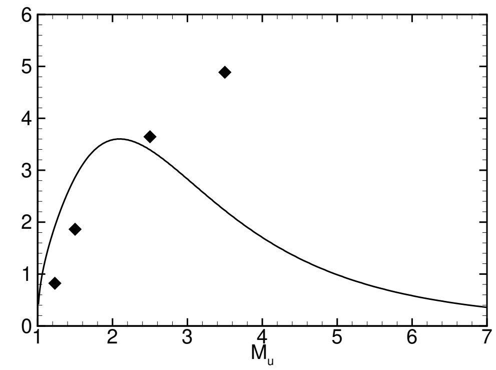


(f) Near-field density variance

Figure H.1: Semi-log plot of the normalized (a) pressure, (c) temperature, and the linear plot of normalized (e) density variances at four different downstream locations from LIA (lines) and DNS (symbols): $k_0 x_1 = 1$ (solid, squares), 3 (dashed, circles), 6 (dash-dotted, triangles), 12 (dash-double dotted, diamonds). Open symbols are from data of Ref. [81] for the cases of $M_{t,u} = 0.22$, $Re_{\lambda,u} = 40$ and filled symbols are from present simulations. The variances are normalized by the square of the upstream mean values and additionally by the normalized TKE. (b), (d) and (f) Same as mentioned above but shows the near-field values computed using the threshold method along with near-field LIA values

Similar trends are observed for the temperature variance. For density variance, all the LIA curves converge to the far-field $\overline{\rho'^2}$ values, except for minor variations at low Mach numbers. As expected, the density variance increases with shock strength, but saturates in the limit of $M_u \to \infty$. This is unlike temperature and pressure fluctuations presented earlier, which follow an $M_u^2$ scaling near the hypersonic range. For a fixed upstream thermodynamic state, the mean pressure and temperature continue to increase at high Mach numbers, and the same is true for the corresponding fluctuations. By comparison, a finite asymptotic density jump in the hypersonic limit results in a finite $\frac{\rho'}{\overline{\rho}}$ as $M_u \to \infty$. We therefore use a linear scale for the density variance, as opposed to the log scale in Figs. (H.1a) and (H.1c).

Figure (H.1b) - (H.1f) presents the LIA near-field predictions, where the variance is the value prior to the exponential decay, and it is $10 - 50$ times larger than that at $k_0 x_1 = 1$ presented in Fig. (H.1a) - (H.1e), especially at low Mach numbers. At high Mach numbers, both near-field and far-field pressure fluctuations increase quadratically with Mach number.

The near-field predictions of pressure variances obtained using the threshold method match the LIA results closely. The only exceptions are the minor under-predictions of $\overline{p'^2}$ at Mach numbers 1.23 and 1.5. The temperature variance shows a much better match with the near-field LIA predictions. The values are higher by about an order in magnitude compared to the far-field $\overline{T'^2}$ at a given Mach number. The LIA near-field density variance (Fig. (H.1f)) show a unique variation with Mach number. It increases to attain a peak value for Mach 2.2 as opposed to Mach 1.2 observed when normalized by downstream mean values, and then decreases at higher Mach number. However, the trend observed in LIA for density fluctuations is not reproduced by the threshold method as observed for the downstream normalization. The density statistics computed using the threshold method shows a monotonically increasing trend with Mach number with large discrepancies for strong shock waves. The reason for this behavior is, however not known.

# Appendix I

# Application of models to current data

In this appendix, we show the model predictions for each of the thermodynamic variances against their corresponding DNS data from the present set of simulations. We once again consider the high Mach number cases and the tested $M_t$ values are 0.15 and 0.25, for which the model predicted values closer to their DNS counterparts (see Figs. (8.4) - (8.7)). The modeling coefficients are slightly varied, since the present set of simulations use a different energy spectrum in the inflow turbulence and its decay rates are different from that of the cases from Ref. [81].

The model predictions for each of the thermodynamic variances are shown in Sects. (I.1) - (I.4). The models show a good match in the spatial variation against their corresponding DNS data. The decay rate of the pressure variance in the present simulations are slightly faster than those of the data presented in Ref. [81], and also deviate from LIA trends. Thus, the predictions for the pressure variance alone, are slightly poorer compared to the other thermodynamic variances.

## I.1 Temperature variance

Figure (I.1) shows the comparison of the model predictions for the temperature variance with that of the DNS data. They are found to be in excellent agreement for the high Mach number cases shown.

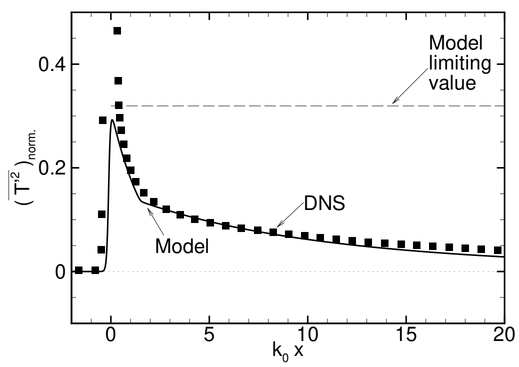


(a) $M_1 = 2.50$ and $M_t = 0.15$

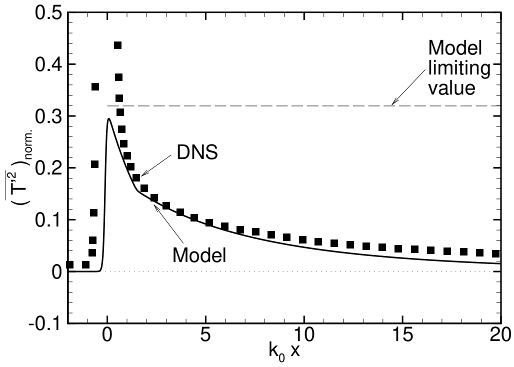


(b) $M_1 = 2.50$ and $M_t = 0.25$

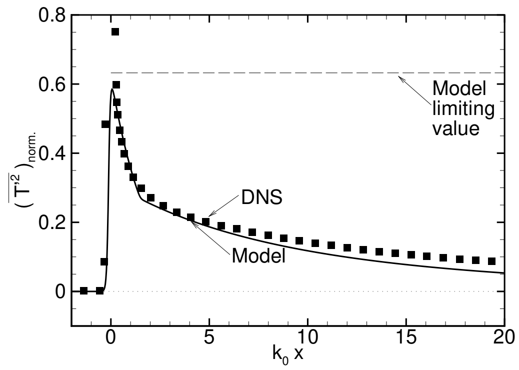


(c) $M_1 = 3.50$ and $M_t = 0.15$

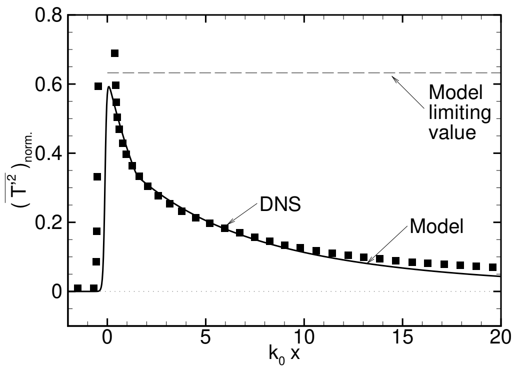


(d) $M_1 = 3.50$ and $M_t = 0.25$

Figure I.1: Variation of normalized temperature variance for the present simulations. The temperature variance is normalized by $\overline{T}_2^2\,(k_1/\overline{u}_1^2)$. Lines correspond to the solution of the RK4 integration of the temperature variance model equation in Eq. (8.45) and square symbols correspond to the present DNS results. The horizontal dashed line is the limiting value for the model which is obtained by integrating Eq. (8.45) without the decay mechanisms

# I.2 Density variance

Figure (I.2) shows the comparison of the model predictions for the density variance with the DNS data. Modeling the decay of density variance with only the entropy mechanism is found to be inadequate for the low $M_t$ cases, which have a non-monotonic variation at high Mach numbers. The mixed type of decay mechanism might help to improve the model predictions for the cases with non-monotonic spatial variation.

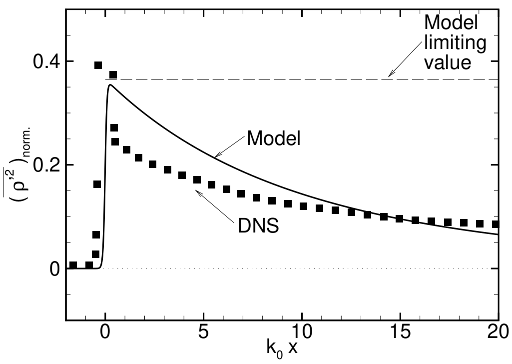


(a) $M_1 = 2.50$ and $M_t = 0.15$

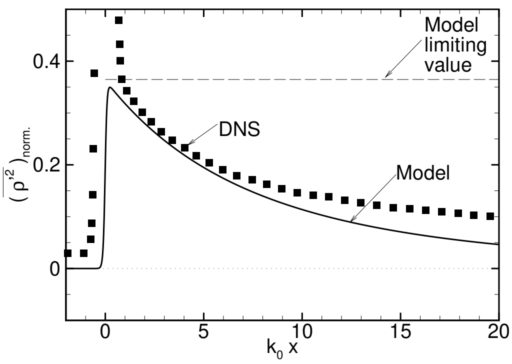


(b) $M_1 = 2.50$ and $M_t = 0.25$

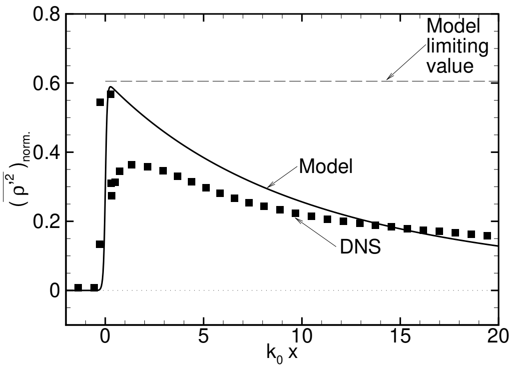


(c) $M_1 = 3.50$ and $M_t = 0.15$

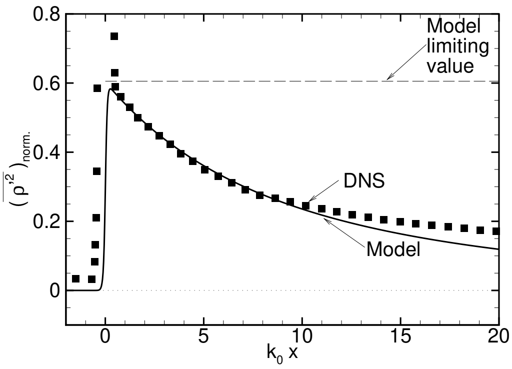


(d) $M_1 = 3.50$ and $M_t = 0.25$

Figure I.2: Variation of normalized density variance for the present simulations. The density variance is normalized by $\overline{\rho}_2^2\,(k_1/\overline{u}_1^2)$. Lines correspond to the solution of the RK4 integration of the density variance model equation in Eq. (8.45) and square symbols correspond to the present DNS results. The horizontal dashed line is the limiting value for the model which is obtained by integrating Eq. (8.45) without the decay mechanisms.

# I.3 Entropy variance

The model predictions for the entropy variance are in good agreement with the DNS data as shown in Fig. (I.3). The model seems to slightly underpredict the amplification at the shock for the high $M_t$ case. This is in agreement with Fig. (8.6), where the production across the shock is found to be lower than the DNS values.

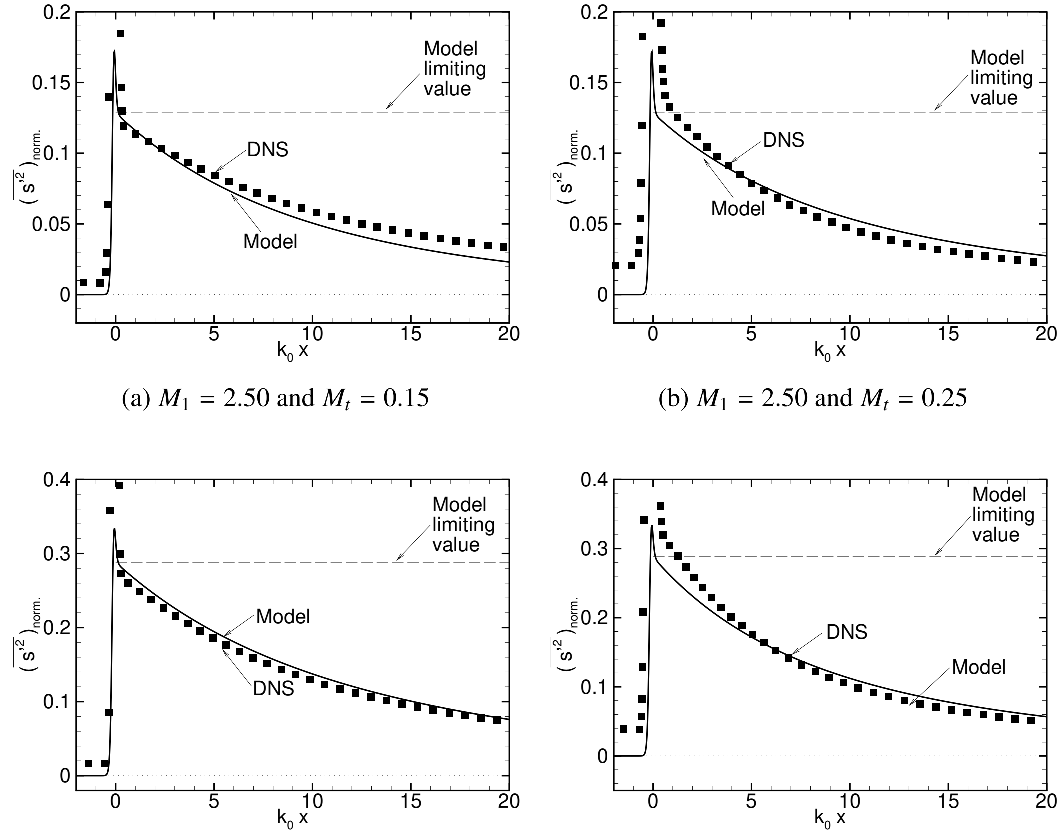


(a) $M_1 = 2.50$ and $M_t = 0.15$

(b) $M_1 = 2.50$ and $M_t = 0.25$

(c) $M_1 = 3.50$ and $M_t = 0.15$

(d) $M_1 = 3.50$ and $M_t = 0.25$

Figure I.3: Variation of normalized entropy variance for the present simulations. The entropy variance is normalized by $c_p^2\,(k_1/\overline{u}_1^2)$. Lines correspond to the solution of the RK4 integration of the model equation in Eq. (8.45) and square symbols correspond to the present DNS results. The horizontal dashed line is the limiting value for the model which is obtained by integrating Eq. (8.45) without the decay mechanisms.

# I.4 Pressure variance

Figure (I.4) shows the comparison of the model predictions for the pressure variance with the DNS data. The production across the shock and the decay rate are found to be in agreement with the DNS data. The discrepancy between the present DNS data and the LIA far-field pressure variance is found to affect the model predictions. The model overpredicts for the low $M_t$ case and underpredicts for the high $M_t$ case, which is similar to Figs. (6.7b) and (6.7d).

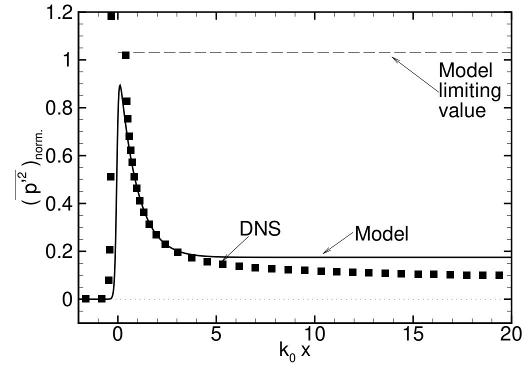


(a) $M_1 = 2.50$ and $M_t = 0.15$

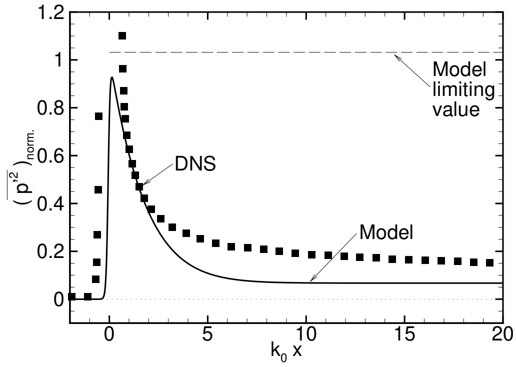


(b) $M_1 = 2.50$ and $M_t = 0.25$

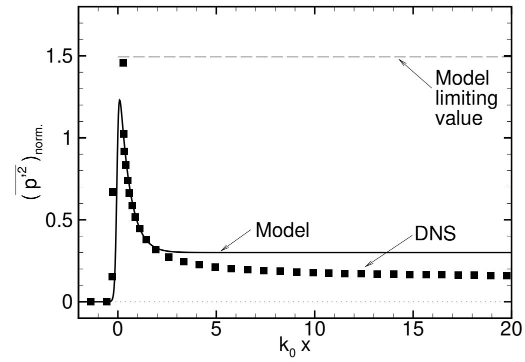


(c) $M_1 = 3.50$ and $M_t = 0.15$

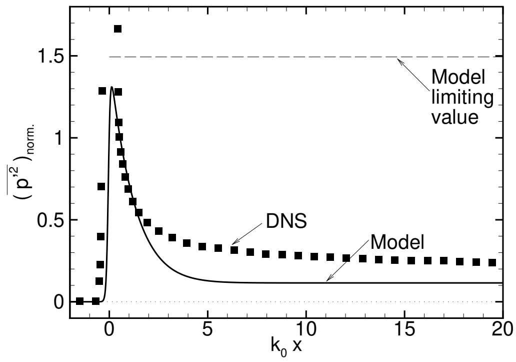


(d) $M_1 = 3.50$ and $M_t = 0.25$

Figure I.4: Variation of normalized pressure variance for the present simulations. The pressure variance is normalized by $\overline{p}_2^2\,(k_1/\overline{u}_1^2)$. Lines correspond to the solution of the RK4 integration of the model equation in Eq. (8.45) and square symbols correspond to the present DNS results. The horizontal dashed line is the limiting value for the model which is obtained by integrating Eq. (8.45) without the decay mechanisms.

# References


[1] Abdikamalov, E., Huete, C., Nussupbekov, A., and Berdibek, S., 2018, "Turbulence generation by shock-acoustic-wave interaction in core-collapse supernovae," *Particles* **1**, 97–110.

[2] Abdikamalov, E., Zhaksylykov, A., Radice, D., and Berdibek, S., 2016, "Shock-turbulence interaction in core-collapse supernovae," *Mon. Not. R. Astron. Soc.* **461**, 3864–3876.

[3] Adams, N. A., and Shariff, K., 1996, "A high-resolution hybrid compact-eno scheme for shock-turbulence interaction problems," *J. Comput. Phys.* **127**, 27 – 51.

[4] Agui, J. H., Briassulis, G., and Andreopoulos, Y., 2005, "Studies of interactions of a propagating shock wave with decaying grid turbulence: velocity and vorticity fields," *J. Fluid Mech.* **524**, 143–195.

[5] Anderson Jr., J. D., 2017, *Fundamentals of Aerodynamics* (McGraw-Hill Education. New York, USA).

[6] Anyiwo, J. C., and Bushnell, D. M., 1982, "Turbulence amplification in shock-wave boundary-layer interaction," *AIAA J.* **20**, 893 – 899.

[7] Ash, R. L., Zuckerwar, A. J., and Zheng, Z., 1991, *Second coefficient of viscosity in air*, Tech. Rep. NASA-CR-187783 (NASA).

[8] Barre, S., Alem, D., and Bonnet, J. P., 1996, "Experimental study of a normal shock / homogeneous turbulence interaction," *AIAA J.* **34**, 968 – 974.

[9] Bermejo-Moreno, I., Bodart, J., Larsson, J., Barney, B. M., Nichols, J. W., and Jones, S., 2013, "Solving the compressible navier-stokes equations on up to 1.97 million cores and 4.1 trillion grid points," in *Proc. Int. Conf. High Perform. Comput. Networking, Storage Anal.*, SC '13 No. 62 (ACM, New York, NY, USA). pp. 1 – 10.

[10] Bhagatwala, A. V., 2011, *Shock-turbulence interaction and Richtmyer-Meshkov instability in spherical geometry*, Ph.D. thesis (Stanford University).

[11] Blaisdell, G. A., Spyropoulos, E. T., and Qin, J. H., 1996, "The effect of the formulation of nonlinear terms on aliasing errors in spectral methods," *Appl. Num. Math.* **21**, 207–219.

[12] Bodony, D. J., 2006, "Analysis of sponge zones for computational fluid mechanics," *J. Comput. Phys.* **212**, 681 – 702.

[13] Boukharfane, R., Bouali, Z., and Mura, A., 2018, "Evolution of scalar and velocity dynamics in planar shock-turbulence interaction," *Shock Waves* **28**, 1117–1141.

[14] Braun, N. O., and Gore, R. A., 2018, "On primitive variable behaviour near shocks in ensemble-averaged methods," *J. Turbul.* **19**, 868–888.

[15] Braun, N. O., Pullin, D. I., and Meiron, D. I., 2019, "Large eddy simulation investigation of the canonical shock-turbulence interaction," *J. Fluid Mech.* **858**, 500–535.

[16] Briassulis, G., and Andreopoulos, J., 1996, "High resolution measurements of isotropic turbulence interacting with shock waves," in *34th Aerosp. Sci. Meet. Exhib.*, Aerospace Sciences Meetings No. AIAA-96-0042 (Reno, NV, USA).

[17] Chang, C. T., 1957, "Interaction of a Plane Shock and Oblique Plane Disturbances With Special Reference to Entropy Waves," *J. Aeronaut. Sci.* **24**, 675 – 682.

[18] Chen, C. H., and Donzis, D. A., 2019, "Shock-turbulence interactions at high turbulence intensities," *J. Fluid Mech.* **870**, 813–847.

[19] Chu, B. T., and Kovásznay, L. S. G., 1958, "Non-linear interactions in a viscous heat-conducting compressible gas," *J. Fluid Mech.* **3**, 494 – 514.

[20] Clavin, P., 2013, "Nonlinear analysis of shock-vortex interaction: Mach stem formation," *J. Fluid Mech.* **721**, 324–339.

[21] Crespo, M., Jamme, S., and Chassaing, P., ????, in *Fifth Int. Symp. Turbul. and Shear Flow Phenom. (TSFP5)* (TSFP5-1C-3, Munich, Germany).

[22] Debieve, J. F., and Lacharme, J. P., 1986, "A Shock-Wave/Free Turbulence Interaction," in *Turbulent Shear-Layer/Shock-Wave Interactions*, IUTAM Symposium,

Palaiseau, France, September 9-12, 1985, edited by Délery, J. (Springer Berlin Heidelberg, Berlin, Heidelberg). pp. 393 – 403.

[23] Délery, J. M., 1983, "Experimental investigation of turbulence properties in transonic shock/boundary-layer interactions," *AIAA J.* **21**, 180 – 185.

[24] Délery, J. M., 1985, "Shock wave/turbulent boundary layer interaction and its control," *Prog. Aero. Sci.* **22**, 209 – 280.

[25] Dolling, D. S., 2001, "Fifty years of shock-wave/boundary-layer interaction research: What next?." *AIAA J.* **39**, 1517 – 1531.

[26] Donzis, D. A., 2012, "Amplification factors in shock-turbulence interactions: effect of shock thickness," *Phys. Fluids* **24**, 011705.

[27] Donzis, D. A., 2012, "Shock structure in shock-turbulence interactions," *Phys. Fluids* **24**, 126101.

[28] Donzis, D. A., and Jagannathan, S., 2013, "Fluctuations of thermodynamic variables in stationary compressible turbulence," *J. Fluid Mech.* **733**, 221 – 244.

[29] Donzis, D. A., and Sreenivasan, K. R., 2010, "The bottleneck effect and the kolmogorov constant in isotropic turbulence," *J. Fluid Mech.* **657**, 171–188.

[30] Ducros, F., Ferrand, V., Nicoud, F., Weber, C., Darracq, D., Gacherieu, C., and Poinsot, T., 1999, "Large-eddy simulation of the shock/turbulence interaction," *J. Comput. Phys.* **152**, 517 – 549.

[31] Ducros, F., Laporte, F., Soulères, T., Guinot, V., Moinat, P., and Caruelle, B., 2000, "High-Order Fluxes for Conservative Skew-Symmetric-like Schemes in Structured Meshes: Application to Compressible Flows," *J. Comput. Phys.* **161**, 114 – 139.

[32] Dukhin, A. S., and Goetz, P. J., 2009, "Bulk viscosity and compressibility measurement using acoustic spectroscopy," *J. Chem. Phys.* **130**, 124519.

[33] Erlebacher, G., Hussaini, M. Y., Kreiss, H. O., and Sarkar, S., 1990, "The analysis and simulation of compressible turbulence," *Theor. Comput. Fluid Dyn.* **2**, 73 – 95.

[34] Eswaran, V., and Pope, S. B., 1988, "An examination of forcing in direct numerical simulations of turbulence," *Comput. Fluids* **16**, 257–278.

[35] Fabre, D., Jacquin, L., and Sesterhenn, J., 2001, "Linear interaction of a cylindrical entropy spot with a shock," *Phys. Fluids* **13**, 2403 – 2422.

[36] Gerolymos, G. A., and Vallet, I., 2014, "Pressure, density, temperature and entropy fluctuations in compressible turbulent plane channel flow," *J. Fluid Mech.* **757**, 701 – 746.

[37] Giepman, R. H. M., Louman, R., Schrijer, F. F. J., and van Oudheusden, B. W., 2016, "Experimental study into the effects of forced transition on a shock-wave/boundary-layer interaction," *AIAA J.* **54**, 1313 – 1325.

[38] Giepman, R. H. M., Schrijer, F. F. J., and van Oudheusden, B. W., 2015, "High-resolution piv measurements of a transitional shock wave–boundary layer interaction," *Exp. Fluids* **56**, 1 – 20.

[39] Girimaji, S. S., Jeong, E., and Poroseva, S. V., 2003, "Pressure-strain correlation in homogeneous anisotropic turbulence subject to rapid strain-dominated distortion," *Phys. Fluids* **15**, 3209–3222.

[40] Gotoh, T., and Fukayama, D., 2001, "Pressure spectrum in homogeneous turbulence," *Phys. Rev. Lett.* **86**, 3775–3778.

[41] Griffond, J., 2005, "Linear interaction analysis applied to a mixture of two perfect gases," *Phys. Fluids* **17**, 086101.

[42] Griffond, J., and Soulard, O., 2012, "Evolution of axisymmetric weakly turbulent mixtures interacting with shock or rarefaction waves," *Phys. Fluids* **24**, 115108.

[43] Grube, N., Taylor, E., and Martin, M. P., 2009, "Direct Numerical Simulation of Shock-wave/Isotropic Turbulence Interaction," in *39th AIAA Fluid Dyn. Conf.*, Fluid Dynamics and Co-located Conferences No. AIAA 2009-4165 (San Antonio, TX, USA).

[44] Grube, N., Taylor, E., and Martin, M. P., 2011, "Numerical Investigation of Shock-wave/Isotropic Turbulence Interaction," in *49th AIAA Aerosp. Sci. Meet. Incl. New Horizons Forum Aerosp. Expo.*, Aerospace Sciences Meetings. No. AIAA 2011-480 (Orlando, FL, USA).

[45] Hannappel, R., and Friedrich, R., 1995, "Direct Numerical Simulation of a Mach 2 shock interacting with isotropic turbulence," *Appl. Sci. Res.* **54**, 205 – 221.

[46] Hardy, B., and Atassi, H. M., 1997, "Interaction of acoustic, entropic, and vortical waves with a plane shock," in *3rd AIAA/CEAS Aeroacoustics Conference*, Aeroacoustics Conferences No. AIAA-97-1614 (Atlanta, GA, USA).

[47] Hartung, L. C., and Duffy, R. E., 1986, "Effects of pressure on turbulence in shock induced flows," in *24th Aerosp. Sci. Meet.*, Aerospace Sciences Meetings No. AIAA-86-0127 (Reno, NV, USA).

[48] Hejranfar, K., and Rahmani, S., 2019, "An assessment of shock-disturbances interaction considering real gas effects," *J. Fluids Eng.* **141**, 011201:1–16.

[49] Hesselink, L., and Sturtevant, B., 1988, "Propagation of weak shocks through a random medium," *J. Fluid Mech.* **196**, 513 – 553.

[50] Holden, H. A., and Babinsky, H., 2005, "Separated shock-boundary-layer interaction control using streamwise slots," *J. Aircraft* **42**, 166 – 171.

[51] Honein, A. E., and Moin, P., 2004, "Higher entropy conservation and numerical stability of compressible turbulence simulations," *J. Comput. Phys.* **201**, 531–545.

[52] Honkan, A., and Andreopoulos, J., 1990, "Experiments in a Shock Wave / Homogeneous Turbulence Interaction," in *21st AIAA Fluid Dyn. Conf.*, Plasma Dyn. and Lasers Conf. Ser. No. AIAA-90-1647 (Seattle, WA, USA).

[53] Honkan, A., and Andreopoulos, J., 1992, "Rapid compression of grid-generated turbulence by a moving shock wave," *Phys. Fluids A* **4**, 2562 – 2572.

[54] Honkan, A., Watkins, C. B., and Andreopoulos, J., 1994, "Experimental Study of Interactions of shock wave with free-stream turbulence," *J. Fluids Eng.* **116**, 763 – 769.

[55] Huete, C., Abdikamalov, E., and Radice, D., 2018, "The impact of vorticity waves on the shock dynamics in core-collapse supernovae," *Mon. Not. R. Astron. Soc.* **475**, 3305–3323.

[56] Huete, C., Jin, T., MartÃŋnez-Ruiz, D., and Luo, K., 2017, "Interaction of a planar reacting shock wave with an isotropic turbulent vorticity field," *Phys. Rev. E* **96**, 053104.

[57] Huete, C., Sánchez, A. L., and Williams, F. A., 2013, "Theory of interactions of thin strong detonations with turbulent gases," *Phys. Fluids* **25**, 076105.

[58] Huete, C., Sánchez, A. L., and Williams, F. A., 2014, "Linear theory for the interaction of small-scale turbulence with overdriven detonations," *Phys. Fluids* **26**, 116101.

[59] Huete, C., Wouchuk, J. G., and Velikovich, A. L., 2012, "Analytical linear theory for the interaction of a planar shock wave with a two- or three-dimensional random isotropic acoustic wave field," *Phys. Rev. E* **85**, 026312.

[60] Huete Ruiz de Lira, C., Velikovich, A. L., and Wouchuk, J. G., 2011, "Analytical linear theory for the interaction of a planar shock wave with a two- or three-dimensional random isotropic density field," *Phys. Rev. E* **83**, 056320.

[61] Inokuma, K., Watanabe, T., Nagata, K., Sasoh, A., and Sakai, Y., 2017, "Finite response time of shock wave modulation by turbulence," *Phys. Fluids* **29**, 051701.

[62] Jackson, T. L., Hussaini, M. Y., and Ribner, H. S., 1993, "Interaction of turbulence with a detonation wave," *Phys. Fluids A: Fluid Dyn.* **5**, 745–749.

[63] Jackson, T. L., Kapila, A. K., and Hussaini, M. Y., 1990, "Convection of a pattern of vorticity through a reacting shock wave," *Phy. Fluids A: Fluid Dyn.* **2**, 1260–1268.

[64] Jacquin, L., Blin, E., and Geffroy, P., 1993, "An Experiment on Free Turbulence/Shock Wave Interaction," in *Turbulent Shear Flows 8*, Selected Papers from the Eighth International Symposium on Turbulent Shear Flows, Munich, Germany, September 9 - 11, 1991, edited by Durst, F., Friedrich, R., Launder, B. E., Schmidt, F. W., Schumann, U., and Whitelaw, J. H. (Springer Berlin Heidelberg, Berlin, Heidelberg). pp. 229 – 248.

[65] Jameson, A., Schmidt, W., and Turkel, E., 1981, "Numerical solution of the euler equations by finite volume methods using runge kutta time stepping schemes," in *14th Fluid and Plasma Dynamics Conference*, AIAA 81-1259

[66] Jamme, S., Cazalbou, J.-B., Torres, F., and Chassaing, P., 2002, "Direct numerical simulation of the interaction between a shock wave and various types of isotropic turbulence," *Flow, Turbul. Combust.* **68**, 227 – 268.

[67] Jamme, S., Crespo, M., and Chassaing, P., 2005, "Direct Numerical Simulation of the Interaction Between a Shock Wave and Anisotropic Turbulence," in *35th AIAA Fluid Dyn. Conf. Exhib.*, AIAA 2005-4886 (Toronto, Ontario Canada).

[68] Jamme, S., Crespo, M., and Chassaing, P., 2010, "Thermodynamic fluctuations behaviour during a sheared turbulence/shock interaction," in *Turbulence and Interactions*, Notes on Numerical Fluid Mechanics and Multidisciplinary Design, Vol. 110, edited by Deville, M., Thien-Hiep, L., and Sagaut, P. (Springer Berlin Heidelberg, Berlin, Heidelberg). pp. 175–181.

[69] Jamme, S., Crespo, M., and Chassaing, P., 2014, “A study of sheared turbulence/shock interaction: velocity fluctuations and enstrophy behaviour,” in *Turbulence and Interactions*, Notes on Numerical Fluid Mechanics and Multidisciplinary Design, Vol. 125, edited by Deville, M., J.-L., E., Gleize, L., , V. .and Thien-Hiep, Terracol, M., and Vincent, S. (Springer Berlin Heidelberg, Berlin, Heidelberg). pp. 107–114.

[70] Jamme, S., Torres, F., and Cazalbou, J.-B., 1997, “Direct Numerical Simulation of Compressible Isotropic Turbulence Interacting With a Normal Shock Wave,” in *13th Comput. Fluid Dyn. Conf.*, Fluid Dynamics and Co-located Conferences No. AIAA-97-2070 (Snowmass Village, CO, USA).

[71] Johnsen, E., Larsson, J., Bhagatwala, A. V., Cabot, W. H., Moin, P., Olson, B. J., Rawat, P. S., Shankar, S. K., Sjögreen, B., Yee, H. C., Zhong, X., and Lele, S. K., 2010, “Assessment of high-resolution methods for numerical simulations of compressible turbulence with shock waves,” *J. Comput. Phys.* **229**, 1213 – 1237.

[72] Johnson, W. R., and Laporte, O., 1958, “Interaction of Cylindrical Sound Waves with a Stationary Shock Wave,” *The Phys. Fluids* **1**, 82–94.

[73] Keller, J., and Merzkirch, W., 1990, “Interaction of a normal shock wave with a compressible turbulent flow,” *Exp. Fluids* **8**, 241 – 248.

[74] Kerrebrock, J. L., 1956, *The interaction of flow discontinuities with small disturbances in a compressible fluid*, Ph.D. thesis (California Institute of Technology).

[75] Kimura, T., and Tosa, M., 1993, “Shock propagation in a turbulent cloud,” *The Astrophys. J. Part I* **406**, 512 – 519.

[76] Kitamura, T., Nagata, K., Sakai, Y., Sasoh, A., and Ito, Y., 2016, “Rapid distortion theory analysis on the interaction between homogeneous turbulence and a planar shock wave,” *J. Fluid Mech.* **802**, 108 – 146.

[77] Kitamura, T., Nagata, K., Sakai, Y., Sasoh, A., and Ito, Y., 2017, “Changes in divergence-free grid turbulence interacting with a weak spherical shock wave,” *Phys. Fluids* **29**, 065114.

[78] Kovásznay, L. S. G., 1953, “Turbulence in Supersonic Flow,” *J. Aeronaut. Sci.* **20**, 657 – 674, 682.

[79] Larsson, J., 2009, “Blending technique for compressible inflow turbulence: Algorithm localization and accuracy assessment,” *J. Comput. Phys.* **228**, 933 – 937.

[80] Larsson, J., 2010, "Effect of Shock-Capturing Errors on Turbulence Statistics," *AIAA J.* **48**, 1554 – 1557.

[81] Larsson, J., Bermejo-Moreno, I., and Lele, S. K., 2013, "Reynolds- and Mach-number effects in canonical shock-turbulence interaction," *J. Fluid Mech.* **717**, 293 – 321.

[82] Larsson, J., and Gustafsson, B., 2008, "Stability criteria for hybrid difference methods," *J. Comput. Phys.* **227**, 2886 – 2898.

[83] Larsson, J., and Lele, S. K., 2009, "Direct numerical simulation of canonical shock/turbulence interaction," *Phys. Fluids* **21**, 126101.

[84] Lee, S., Lele, S. K., and Moin, P., 1992, "Simulation of spatially evolving turbulence and the applicability of Taylor's hypothesis in compressible flow," *Phys. Fluids A* **4**, 1521 – 1530.

[85] Lee, S., Lele, S. K., and Moin, P., 1993, "Direct numerical simulation of isotropic turbulence interacting with a weak shock wave," *J. Fluid Mech.* **251**, 533 – 562.

[86] Lee, S., Lele, S. K., and Moin, P., 1997, "Interaction of isotropic turbulence with shock waves: effect of shock strength," *J. Fluid Mech.* **340**, 225 – 247.

[87] Lee, S., Moin, P., and Lele, S. K., 1992, *Interaction of isotropic turbulence with a shock wave*, Tech. Rep. TF-52 (Thermosciences Division, Department of Mechanical Engineering, Stanford University, Stanford, California 94305).

[88] Lele, S. K., 1992, "Shock-jump relations in a turbulent flow," *Phys. Fluids A* **4**, 2900 – 2905.

[89] Lele, S. K., 1994, "Compressibility Effects on Turbulence," *Annu. Rev. Fluid Mech.* **26**, 211 – 254.

[90] Livescu, D., and Ryu, J., 2016, "Vorticity dynamics after the shock-turbulence interaction," *Shock Waves* **26**, 241 – 251.

[91] Lobbia, M. A., and Suzuki, K., 2015, "Experimental investigation of a mach 3.5 waverider designed using computational fluid dynamics," *AIAA J.* **53**, 1590–1601.

[92] Lowson, M. V., 1968, "Pressure fluctuations resulting from shock interactions," *J. Sound Vib.* **7**, 380–392.

[93] Lubchich, A. A., 2009, "Response to "Comment on 'Interaction of small perturbations with shock waves'" [Phys. Fluids 21, 079101 (2009)]," *Phys. Fluids* **21**, 079102.

[94] Lubchich, A. A., and Pudovkin, M. I., 2004, "Interaction of small perturbations with shock waves," *Phys. Fluids* **16**, 4489–4505.

[95] Lund, T. S., Wu, X., and Squires, K. D., 1998, "Generation of turbulent inflow data for spatially-developing boundary layer simulations," *J. Comput. Phys.* **140**, 233 – 258.

[96] Mahesh, K., Lee, S., Lele, S. K., and Moin, P., 1995, "The interaction of an isotropic field of acoustic waves with a shock wave," *J. Fluid Mech.* **300**, 383 – 407.

[97] Mahesh, K., Lele, S. K., and Moin, P., 1994, "The response of anisotropic turbulence to rapid homogeneous one-dimensional compression," *Phys. Fluids* **6**, 1052–1062.

[98] Mahesh, K., Lele, S. K., and Moin, P., 1997, "The influence of entropy fluctuations on the interaction of turbulence with a shock wave," *J. Fluid Mech.* **334**, 353 – 379.

[99] Mahesh, K., Moin, P., and Lele, S. K., ????, *The interaction of a shock wave with a turbulent shear flow*, Tech. Rep. TF-69

[100] di Mare, L., Klein, M., Jones, W. P., and Janicka, J., 2006, "Synthetic turbulence inflow conditions for large-eddy simulation," *Phys. Fluids* **18**, 025107.

[101] Massa, L., and Jha, P., 2012, "Linear analysis of the richtmyer-meshkov instability in shock-flame interactions," *Phys. Fluids* **24**, 056101.

[102] Mattsson, K., 2003 Feb, "Boundary procedures for summation-by-parts operators," *J. Sci. Comput.* **18**, 133 – 153.

[103] Mattsson, K., and Nordström, J., 2004, "Summation by parts operators for finite difference approximations of second derivatives," *J. Comput. Phys.* **199**, 503 – 540.

[104] Mattsson, K., Svärd, M., and Nordström, J., 2004 Aug, "Stable and accurate artificial dissipation," *J. Sci. Comput.* **21**, 57 – 79.

[105] McKenzie, J. F., and Westphal, K. O., 1968, "Interaction of Linear Waves with Oblique Shock Waves," *Phys. Fluids* **11**, 2350 – 2362.

[106] Miller, G. H., and Ahrens, T. J., 1991 Oct, "Shock-wave viscosity measurement," *Rev. Mod. Phys.* **63**, 919 – 948.

[107] Mittal, A., and Girimaji, S. S., 2019 Apr, "Mathematical framework for analysis of internal energy dynamics and spectral distribution in compressible turbulent flows," *Phys. Rev. Fluids* **4**, 042601.

[108] Moore, F. K., 1954, *Unsteady oblique interaction of a shock wave with a plane disturbance*, Tech. Rep. NACA TR 1165 (NACA).

[109] Mostert, W., Pullin, D. I., Samtaney, R., and Wheatley, V., 2018, "Singularity formation on perturbed planar shock waves," *J. Fluid Mech.* **846**, 536–562.

[110] Mostert, W., Pullin, D. I., Samtaney, R., and Wheatley, V., 2018, "Spontaneous singularity formation in converging cylindrical shock waves," *Phys. Rev. Fluids* **3**, 071401.

[111] Moyal, J. E., 1952, "The spectra of turbulence in a compressible fluid; eddy turbulence and random noise," *Math. Proc. Camb. Phil. Soc.* **48**, 329–344.

[112] Pasha, A. A., and Sinha, K., 2008, "Shock-unsteadiness model applied to oblique shock wave/turbulent boundary-layer interaction," *Int. J. Comput. Fluid Dyn.* **22**, 569–582.

[113] Pasha, A. A., and Sinha, K., 2012, "Simulation of Hypersonic Shock/Turbulent Boundary-Layer Interactions Using Shock-Unsteadiness Model," *J. Propuls. Power* **28**, 46 – 60.

[114] Pirozzoli, S., 2002, "Conservative Hybrid Compact - WENO Schemes for Shock - Turbulence Interaction," *J. Comput. Phys.* **178**, 81 – 117.

[115] Poinsot, T. J., and Lele, S. K., 1992, "Boundary conditions for direct simulations of compressible viscous flows," *J. Comput. Phys.* **101**, 104 – 129.

[116] Pope, S. B., 2000, *Turbulent flows* (Cambridge University Press. Cambridge, UK).

[117] Quadros, R., and Sinha, K., 2016, "Modelling of turbulent energy flux in canonical shock-turbulence interaction," *Int. J. Heat Fluid Flow* **61, Part B**, 626 – 635.

[118] Quadros, R., Sinha, K., and Larsson, J., 2016, "Kovasznay Mode Decomposition of Velocity-Temperature Correlation in Canonical Shock-Turbulence Interaction," *Flow, Turbul. and Combust.* **97**, 787 – 810.

[119] Quadros, R., Sinha, K., and Larsson, J., 2016, “Turbulent energy flux generated by shock/homogeneous-turbulence interaction,” *J. Fluid Mech.* **796**, 113 – 157.

[120] Raje, P., and Sinha, K., 2016, “A physically consistent and numerically robust $k-\epsilon$ model for computing turbulent flows with shock waves,” *Comput. Fluids* **136**, 35 – 47.

[121] Rawat, P., and Zhong, X., 2010, “Numerical Simulation of Shock-Turbulence Interactions Using High-Order Shock-Fitting Algorithms,” in *48th AIAA Aerosp. Sci. Meet. Incl. New Horizons Forum Aerosp. Expo.*, Aerospace Sciences Meetings No. AIAA 2010-114 (Orlando, FL, USA).

[122] Rawat, P., and Zhong, X., 2011, “Direct Numerical Simulations of Turbulent Flow Interactions with Strong Shocks Using Shock-Fitting Method,” in *49th AIAA Aerosp. Sci. Meet. Incl. New Horizons Forum Aerosp. Expo.*, Aerospace Sciences Meetings No. AIAA 2011-649 (Orlando, FL, USA).

[123] Ribner, H. S., 1954, *Convection of a pattern of vorticity through a shock wave*, Tech. Rep. NACA TR 1164 (NACA).

[124] Ribner, H. S., 1955, *Shock-turbulence interaction and the generation of noise*, Tech. Rep. NACA TR 1233 (NACA).

[125] Ribner, H. S., 1969, “Acoustic energy flux from shock-turbulence interaction,” *J. Fluid Mech.* **35**, 299âĂŞ310.

[126] Ribner, H. S., 1985, “Cylindrical sound wave generated by shock-vortex interaction,” *AIAA J.* **23**, 1708 – 1715.

[127] Ribner, H. S., 1987, “Spectra of noise and amplified turbulence emanating from shock-turbulence interaction,” *AIAA J.* **25**, 436 – 442.

[128] Ristorcelli, J. R., and Blaisdell, G. A., 1997, “Consistent initial conditions for the DNS of compressible turbulence,” *Phys. Fluids* **9**, 4 – 6.

[129] Robinet, J.-C., and Casalis, G., 2001, “Critical interaction of a shock wave with an acoustic wave,” *Phys. Fluids* **13**, 1047–1059.

[130] Rosenhead, L., 1954, “Introduction - the second coefficient of viscosity: a brief review of fundamentals,” *Proc. Royal Soc. A* **226**, 1–6.

[131] Roy, S., Pathak, U., and Sinha, K., 2018, “Variable Turbulent Prandtl Number Model for Shock / Boundary - Layer Interaction,” *AIAA J.* **56**, 342–355.

[132] Ryu, J., and Livescu, D., 2014, "Turbulence structure behind the shock in canonical shock-vortical turbulence interaction," *J. Fluid Mech.* **756**, R1–1 – R1–13.

[133] Sagaut, P., and Cambon, C., 2018, *Homogeneous Turbulence Dynamics* (Springer International Publishing).

[134] Samtaney, R., Pullin, D. I., and Kosović, B., 2001, "Direct numerical simulation of decaying compressible turbulence and shocklet statistics," *Phys. Fluids* **13**, 1415–1430.

[135] Sandham, N. D., Schülein, E., Wagner, A., Willems, S., and Steelant, J., 2014, "Transitional shock-wave/boundary-layer interactions in hypersonic flow," *J. Fluid Mech.* **752**, 349 – 382.

[136] Sarkar, S., Erlebacher, G., Hussaini, M. Y., and Kreiss, H. O., 1991, "The analysis and modelling of dilatational terms in compressible turbulence," *J. Fluid Mech.* **227**, 473–493.

[137] Sasoh, A., Harasaki, T., Kitamura, T., Takagi, D., Ito, S., Matsuda, A., Nagata, K., and Sakai, Y., 2014, "Statistical behavior of post-shock overpressure past grid turbulence," *Shock Waves* **24**, 489 – 500.

[138] Schülein, E., 2006, "Skin-Friction and Heat Flux Measurements in Shock / Boundary-Layer Interaction Flows," *AIAA J.* **44**, 1732 – 1741.

[139] Schwarzkopf, J. D., Livescu, D., Gore, R. A., Rauenzahn, R. M., and Ristorcelli, J. R., 2011, "Application of a second-moment closure model to mixing processes involving multicomponent miscible fluids," *J. Turbul.* **12**, 1–35.

[140] Sekundov, A. N., 1974, "Turbulence in a supersonic flow and its interaction with a shock wave," *Fluid Dyn.* **9**, 166 – 172.

[141] Sesterhenn, J., Dohogne, J. F., and Friedrich, R., 2005, "Direct numerical simulation of the interaction of isotropic turbulence with a shock wave using shock-fitting," *C. R. Méc.* **333**, 87 – 94.

[142] Sethuraman, Y. P. M., Sinha, K., and Larsson, J., 2018, "Thermodynamic fluctuations in canonical shock–turbulence interaction: effect of shock strength," *Theor. Comput. Fluid Dyn.* **32**, 629 – 654.

[143] Sherman, F. S., 1955, *A low-density wind-tunnel study of shock-wave structure and relaxation phenomena in gases*, Tech. Rep. NACA TN 3298 (University of California).

[144] Sinha, K., 2012, "Evolution of enstrophy in shock/homogeneous turbulence interaction," *J. Fluid Mech.* **707**, 74 – 110.

[145] Sinha, K., Mahesh, K., and Candler, G. V., 2003, "Modeling shock unsteadiness in shock/turbulence interaction," *Phys. Fluids* **15**, 2290 – 2297.

[146] Sinha, K., Mahesh, K., and Candler, G. V., 2005, "Modeling the Effect of Shock Unsteadiness in Shock/ Turbulent Boundary-Layer Interactions," *AIAA J.* **43**, 586 – 594.

[147] Smits, A., and Dussauge, J., 2005, *Turbulent Shear Layers in Supersonic Flow* (Springer-Verlag. New York, USA).

[148] Soulard, O., Griffond, J., and Souffland, D., 2012, "Pseudocompressible approximation and statistical turbulence modeling: Application to shock tube flows," *Phys. Rev. E* **85**, 026307.

[149] Souverein, L. J., Bakker, P. G., and Dupont, P., 2013, "A scaling analysis for turbulent shock-wave/boundary-layer interactions," *J. Fluid Mech.* **714**, 505 – 535.

[150] Strand, B., 1994, "Summation by parts for finite difference approximations for d/dx," *J. Comput. Phys.* **110**, 47 – 67.

[151] Swanson, R. C., and Turkel, E., 1992, "On central-difference and upwind schemes," *J. Comput. Phys.* **101**, 292 – 306.

[152] Takagi, D., Matsuda, A., Sasoh, A., Ito, S., Nagata, K., and Sakai, Y., 2010, "Pressure Modulation of Weak Shock Waves Through Turbulent Flows," in *40th Fluid Dynamics Conference and Exhibit*, Fluid Dynamics and Co-located Conferences No. AIAA 2010-4472 (Chicago, IL, USA).

[153] Takashima, N., and Lewis, M. J., 1992, "Navier-stokes computations of a viscous optimized waverider," in *30th Aerosp. Sci. Meet. Exhib.*, AIAA-92-0305 (Reno, NV, USA).

[154] Tanaka, K., Watanabe, T., Nagata, K., Sasoh, A., Sakai, Y., and Hayase, T., 2018, "Amplification and attenuation of shock wave strength caused by homogeneous isotropic turbulence," *Phys. Fluids* **30**, 035105.

[155] Taulbee, D., and VanOsdol, J., 1991, "Modeling Turbulent Compressible Flows: The Mass Fluctuating Velocity and Squared Density," in *29th Aerosp. Sci. Meet.*, Aerospace Sciences Meetings No. AIAA-91-0524 (Reno, NV, USA).

[156] Tavoularis, S., Bennett, J. C., and Corrsin, S., 1978, "Velocity-derivative skewness in small Reynolds number, nearly isotropic turbulence," *J. Fluid Mech.* **88**, 63.

[157] Thompson, K. W., 1987, "Time dependent boundary conditions for hyperbolic systems," *J. Comput. Phys.* **68**, 1 – 24.

[158] Thompson, P. A., 1984, *Compressible-Fluid Dynamics* (McGraw-Hill Inc. New York, USA).

[159] Tian, Y., Jaberi, F. A., Li, Z., and Livescu, D., 2017, "Numerical study of variable density turbulence interaction with a normal shock wave," *J. Fluid Mech.* **829**, 551–588.

[160] Trolier, J. W., and Duffy, R. E., 1985, "Turbulence Measurements in Shock-Induced Flows," *AIAA J.* **23**, 1172 – 1178.

[161] Tumin, A., 2009, "Comment on "Interaction of small perturbations with shock waves" [Phys. Fluids 16, 4489 (2004)]," *Phys. Fluids* **21**, 079101.

[162] Urzay, J., 2018, "Supersonic combustion in air-breathing propulsion systems for hypersonic flight," *Annu. Rev. Fluid Mech.* **50**, 593–627.

[163] Veera, V. K., and Sinha, K., 2009, "Modeling the effect of upstream temperature fluctuations on shock/homogeneous turbulence interaction," *Phys. Fluids* **21**, 025101.

[164] Wang, J., Shi, Y., Wang, L. P., Xiao, Z., He, X. T., and Chen, S., 2012, "Effect of compressibility on the small-scale structures in isotropic turbulence," *J. Fluid Mech.* **713**, 588–631.

[165] Wouchuk, J. G., Huete Ruiz de Lira, C., and Velikovich, A. L., 2009, "Analytical linear theory for the interaction of a planar shock wave with an isotropic turbulent vorticity field," *Phys. Rev. E* **79**, 066315.

[166] Xanthos, S., Briassulis, G., and Andreopoulos, Y., 2002, "Interaction of Decaying Freestream Turbulence with a Moving Shock Wave: Pressure Field," *J. Propuls. Power* **18**, 1289 – 1297.

[167] Xiao, X., Edwards, J. R., and Hassan, H. A., 2004, "Blending Functions in Hybrid Large-Eddy / Reynolds-Averaged Navier-Stokes Simulations," *AIAA J.* **42**, 2508 – 2515.

[168] Xiao, X., Hassan, H. A., Edwards, J. R., and Gaffney Jr., R. L., 2007, "Role of Turbulent Prandtl Numbers on Heat Flux at Hypersonic Mach Numbers," *AIAA J.* **45**, 806 – 813.

[169] Xiong, Z., Nagarajan, S., and Lele, S. K., 2004, "Simple Method for Generating Inflow Turbulence," *AIAA J.* **42**, 2164 – 2166.

[170] Zang, T. A., Hussaini, M. Y., and Bushnell, D. M., 1984, "Numerical Computations of Turbulence Amplification in Shock-Wave Interactions," *AIAA J.* **22**, 13 – 21.

[171] Zank, G. P., Zhou, Y., Matthaeus, W. H., and Rice, W. K. M., 2002, "The interaction of turbulence with shock waves: A basic model," *Phys. Fluids* **14**, 3766 – 3774.

[172] Zuckerwar, A. J., and Ash, R. L., 2006, "Variational approach to the volume viscosity of fluids," *Phys. Fluids* **18**, 047101.

# List of Publications

**Journals:**

1. **Sethuraman, Y. P. M.**, Sinha, K., & Larsson, J. (2018) Thermodynamic fluctuations in canonical shock-turbulence interaction: effect of shock strength. *Theor. Comput. Fluid Dyn.* **32**, pp. 629 – 654.

2. **Sethuraman, Y. P. M.** & Sinha, K. (2019) Effect of turbulent Mach number on the thermodynamic fluctuations generated by canonical shock-turbulence interaction. *submitted to Comp. Fluids*.

3. **Sethuraman, Y. P. M.** & Sinha, K. (2019) Modeling of thermodynamic fluctuations in canonical shock-turbulence interaction. *Manuscript in preparation*.

**Conference proceedings:**

1. Sinha, K. & **Yogesh Prasaad, M. S.** (2019) Analysis and modeling of thermodynamic fluctuations generated by shock-turbulence interaction, *AIAA 2019 SCITECH Forum*, **AIAA Paper 2019-2155**, San Diego, CA, USA.

2. **Yogesh Prasaad, M. S.**, Sinha, K., & Larsson, J. (2017) Thermodynamic fluctuations in canonical shock-turbulence interaction, *Tenth Int. Symp. on Turbul. and Shear Flow Phenom. (TSFP10)*, Chicago, IL, USA, pp. 8C – 4.

3. Sashittal, P. A., **Yogesh Prasaad, M. S.**, Larsson, J., & Sinha, K. (2014) Study of unsteady shock motion in shock/turbulence interaction, *AIAA 2014 AVIATION Forum*, **AIAA Paper 2014-3341**, Atlanta, GA, USA.

**Reports:**

1. **Yogesh Prasaad, M. S.** & Sinha, K. (2017) Effect of turbulent Mach number on the thermodynamic field generated by a shock wave, *Proc. of the 2017 Summer Progr.*, Munich, Germany, July - August, 2017. pp. 195 – 207.

The author of this dissertation wrote these papers, manuscripts and reports in part or in full, performed the required numerical simulations, and analyzed the results of the simulations. The co-authors on these works provided feedback during these studies, assisted in editing the manuscripts, and were instrumental in determining the model problem and solution procedures.

# Acknowledgements

I would like to express my deep sense of gratitude to my advisor, Prof. Krishnendu Sinha, Dept. of Aerospace Engg., Indian Institute of Technology (IIT) Bombay, Mumbai, India, for his invaluable help and guidance. I am highly indebted to him for giving his critiques on my work and for the thought provoking discussions. His guidance during the model development was immense, and is duly appreciated.

I would like to express my special gratitude to Prof. Johan Larsson, Dept. of Mechanical Engg., University of Maryland (UMD), College Park, USA, for providing his *Hybrid* package which contains the solver and the post-processing codes used in this study. I am also thankful to him for mentoring me via e-mails and Skype calls on the numerical simulations, data analysis, scientific writing, and many more. His timely response to my numerous questions, however, trivial they are, is greatly appreciated. His teachings on the subjects of *Compressible turbulence* and *Numerical methods* via e-mails and skype sessions, the thorough explanations to very hard questions and the subtle hints to the questions for which I should have known the answers, greatly moulded my knowledge.

The comments and suggestions of Profs. Aniruddha Sinha and Amitabh Bhattacharya (members of my research panel committee) over the years, especially the tough ones, greatly helped me not only in my research, but also in my pursuit of knowledge. I deeply appreciate their advices towards the improvement of my presentation skills and their suggestions for my future career.

Majority of the computational resources used for the simulations and for the processing of the large datasets were provided by the *NPSF PARAM YUVA-II facility* in *C-DAC, Pune, India*. I thank the support personnel at C-DAC, for arranging additional storage space to my account and for their timely assistance in many of the issues that arose during this work. I am thankful to Prof. Amitabh Bhattacharya, for mediating with C-DAC and arranging this facility.

I acknowledge SpaceTime-2 supercomputing facility at IIT Bombay for the computing time, which was very helpful during the last stages of my Ph.D. for performing some of the simulations and for post-processing.

I thank the entire faculty and staff of the Dept. of Aerospace Engg., IIT Bombay (past and present) who have supported me directly and indirectly during my PhD tenure. The courses of Profs. Avijit Chatterjee (*Aerodynamics* and *Numerical methods*) and Aniruddha Sinha (*Aeroacoustics* and *Hydrodynamic instabilities*) were very interesting, and I was able to relate some of the concepts that I learned in their classes to my research. The course on *Turbulence* by Prof. Amitabh Bhattacharya, was directly useful for my research, and I truly appreciate his help in addressing my doubts, both related to the course and to my research work.

I thank my fellow lab mates (past and present), Drs. Russell and Bijaylakshmi, Kannan, Anand, Palash, Ashwin, Rachit, Yeshwanth, Devadutta, Jagadish, Naveen Rohilla, Naveen Himthani, Vishnu, Pratik, Subhajit, Utkarsh, Pranav, and Nitin for their help and support. Special thanks are due to our lab secretary, Mukesh, running errands for me during this long tenure of mine. I thank my dear friends, Drs. Marisamynathan, Karthikeyan, Sangeeth, and Amit Katoch, and to be Drs. Sankarganesh, Shaafi, and Satheesh, and Santhanabharathy for their amazing support during my Ph.D. There are many others whom I have not mentioned here, but I thank them all for their helping over the years.

Special thanks are due to Palash Sashittal, an undergraduate student in the Department (2014 batch), from whom I learned a lot during his stay in the Hypersonic CFD lab. It was thanks to him, I was able to contact Prof. Johan Larsson. I also enjoyed the many nights spent discussing technical as well as life lessons with Jagadish over 'enormous' amount of coffee. A huge thanks to the open-source community for obvious reasons.

I am thankful to Prof. Christian Stemmer, Prof. Nikolaus Adams, and the staff of the Institute for Aerodynamics and Fluid Mechanics, Technical University of Munich (TUM), Munich, Germany, for hosting me during the 4$^{th}$ *SFB TRR40 Summer Program 2017* with financial support. I am also thankful to all of the participants of the program for the scintillating discussions and the brainstorming sessions. A portion of the computations carried out in this work were performed at LRZ: Leibniz Supercomputing Centre, Munich, Germany during the summer program, and I am thankful for their support. I relish the time that I spent with Zhang Bo, Sidharth, Giacomo, Umut and Nathalie during the program. I would also like to thank the staff at the TUM for their support and hospitality.

Last but not the least, I thank my parents and brothers for their continuous support and encouragement during my Ph.D. at IIT Bombay. Their contribution in every aspect of my education and life, cannot be overstated.

Financial support was provided as Ph.D. Teaching Assistantship by the Ministry of Human Resources and Development (MHRD) from July, 2012 to July, 2017. Additional financial support was availed from the Industrial Research & Consultancy Centre, IIT Bombay during the period of September, 2017 to February, 2018, and during August, 2018 to October, 2018.

***Yogesh Prasaad M. S.***
IIT Bombay
2019